



Innovative Technologies for Exploration, Extinction and Monitoring of Coal Fires in North China

Geophysical Surveys over the Wuda Coal Fire Area

Work Package 3210 Helicopter geophysical survey, 3220 Ground geophysical survey



**Prepared by: Gerlinde Schaumann, Bernhard Siemon, Gernot
Reitmayr, Wolfgang Voß**

Date: 05.04.2007



Executive Summary

Within the framework of the Sino-German Research Initiative „Innovative Technologies for Exploration, Extinction and Monitoring of Coal Fires in North China” the China Aero Geophysical Survey & Remote Sensing Centre for Land and Resources (AGRS) assisted by the German Federal Institute for Geosciences and Natural Resources (BGR) performed a helicopter survey over the coal fire area of Wuda, Inner Mongolia Autonomous Region, in 2004. The methods applied were electromagnetics and magnetics. In the following year ground surveys were carried out in selected parts of the area concerned. The main ground methods were transient electromagnetics (TEM) carried out by BGR and magnetics executed by AGRS and DMT (Deutsche Montan Technologie).

The objective of the geophysical surveys was to detect and delineate areas affected by coal seam fires. That is possible if the physical parameters such as the electrical conductivity and the magnetic susceptibility are altered over the burning and the already burnt coal seams. The methods based on electromagnetics reveal areas of lower resistivity and the magnetic surveys clearly display increased amplitudes of the magnetic field intensity in the areas affected by coal seam fires.

As the changes of the physical parameters measured over the fire zones are obviously rather small in most cases, ground geophysical surveys are more sensitive to locate coal seam fires than airborne geophysical surveys. However, areas of coal seam fires are not always accessible on ground, so that airborne surveys are necessary. Because of the small signals to be expected caused by coal seam fires, high resolution and high quality data are essential. That requires a low survey altitude and very dense coverage as well as high-precision measuring devices and sophisticated processing and interpretation tools.



Index

1	Introduction.....	19
1.1	Scientific State	20
1.2	Geology of the Wuda area	23
2	Airborne survey	27
2.1	Survey over the entire Wuda Area.....	27
2.2	Geophysical equipment.....	31
	Electromagnetic system.....	31
2.3	Data Processing.....	33
2.4	Map Production and Results	39
2.5	Digital Elevation Model.....	40
3	Results of the airborne electromagnetic survey	42
3.1	Results from the entire survey area.....	42
3.2	Results from the northern part of fire zone no. 8.....	58
3.3	Results from fire zone no. 3.2.....	66
3.4	Results from fire zones within the southern surroundings of fire zone no. 3.2	73
3.5	Results from fire zone no. 7 in the centre of the syncline.....	78
4	Results of the airborne magnetic survey.....	113
4.1	Results from the entire survey area.....	113
4.2	Results from fire zone no. 8.....	116
4.3	Results from fire zone no. 3.2.....	118
4.4	Results from fire zones within the southern surroundings of fire zone no. 3.2	119
4.5	Results from fire zone no. 7 in the centre of the syncline.....	121
4.6	Results from fire zone no. 11 and the southern part of the syncline.....	122
5	Ground electromagnetic surveys	123
5.1	Transient electromagnetics ground survey	123
	5.1.1 Results from fire zone no. 8.....	124
	5.1.3 Results from other sites	146
5.2	Horizontal Loop and VLF ground surveys	150
6	Ground magnetic surveys over fire zones no. 8 and no. 3.2.....	160



7	Conclusions.....	169
8	References.....	169
	Suggested Additional Reading	171
	Acknowledgements.....	171

Figures

Figure 1: Location of the coal mining area of Wuda, Inner Mongolia Autonomous Region, Northern China.	20
Figure 2: Principle scheme of the expected parameter variations gained by the electromagnetic and magnetic methods.	23
Figure 3: Geology of the Wuda syncline and its surroundings, Gielisch (2005).	24
Figure 4: Section of the geological map (see Fig. 5, same key) for the Wuda syncline. The red rectangle roughly marks the area of the airborne survey.....	25
Figure 5: Geology of Fire Zone no. 8, superimposed a quickbird satellite image, after Gielisch & Kahlen (2003). Quickbird satellite image by DLR, 2003 (Gielisch & Kuenzer, 2003). ..	25
Figure 6: Geology of Fire Zone no. 3.2, superimposed a quickbird satellite image, after Gielisch & Kahlen (2003). Quickbird satellite image by DLR, 2003 (Gielisch & Kuenzer, 2003). ..	26
Figure 7: Hydrogeological map of the area of Wuda, Gielisch (2005). The course of the Yellow River is shown in the eastern part of the map.	27
Figure 8: View from the helicopter over the survey area.	28
Figure 9: Quickbird satellite image (projection UTM 48 S / WGS84) of the coal mining area of Wuda in Inner Mongolia, Northern China by DLR (Gielisch & Kuenzer 2003). Bold solid red line outside the satellite image: helicopter survey area, bold solid red rectangles inside: areas of fire zones no. 8 and no. 3.2 (part of no. 3), light blue lines inside: areas of colder coal seam fires, light red lines inside: areas of hotter coal seam fires. Also numbers of further fire zones and mapped polygons from several years are given.	29
Figure 10: Principle of the airborne electromagnetic and magnetic survey system.	33
Figure 11: Helicopter at the airport of Wuhai.	33



- Figure 12: Digital elevation model derived from the helicopter survey over the Wuda area. Colour shading from N-E.42
- Figure 13: Map of the apparent resistivity ρ_{oa} [Ohm*m] at a frequency of 23250 Hz, derived from the helicopter survey over the entire Wuda area. Blue and red polygons show fire zones mapped in 2004, the black dots show single fire points mapped in 2005 (by DLR). Fire zones no. 3.2 and no. 8 are marked by red rectangles. Colour shading from N-E.45
- Figure 14: Map of the apparent resistivity ρ_{oa} [Ohm*m] at a frequency of 23250 Hz, derived from the helicopter survey over the entire Wuda area. Blue and red polygons show fire zones mapped in 2004, the black dots show single fire points mapped in 2005 (by DLR). The colour scale is the same as in Fig. 13 but without shading. Fire zones no. 3.2 and no. 8 are marked by red rectangles.46
- Figure 15: Map of the apparent resistivity ρ_{oa} [Ohm*m] at a frequency of 23250 Hz, derived from the helicopter survey over the entire Wuda area. Blue and red polygons show fire zones mapped in 2004, the black dots show single fire points mapped in 2005 (by DLR). The map is the same as in Fig. 14 but another colour scale was used to emphasize the sites of lower apparent resistivity within the syncline. Fire zones no. 3.2 and no. 8 are marked by red rectangles.47
- Figure 16: Map of the centroid depth at a frequency of 23250 Hz, derived from the helicopter survey over the entire Wuda area. Fire zones no. 3.2 and no. 8 are marked by red rectangles.48
- Figure 17: Map of the apparent resistivity ρ_{oa} [Ohm*m] at a frequency of 4650 Hz, derived from the helicopter survey over the entire Wuda area. Blue and red polygons show fire zones mapped in 2004, the black dots show single fire points mapped in 2005 (by DLR). Colour shading from N-E. Fire zones no. 3.2 and no. 8 are marked by red rectangles.49
- Figure 18: Map of the apparent resistivity ρ_{oa} [Ohm*m] at a frequency of 4650 Hz, derived from the helicopter survey over the entire Wuda area. Blue and red polygons show fire zones mapped in 2004, the black dots show single fire points mapped in 2005 (by DLR). The colour bar is the same as in Fig. 17 but without shading. Fire zones no. 3.2 and no. 8 are marked by red rectangles.50
- Figure 19: Map of the apparent resistivity ρ_{oa} [Ohm*m] at a frequency of 4650 Hz, derived from the helicopter survey over the entire Wuda area. Blue and red polygons show fire zones mapped in 2004, the black dots show single fire points mapped in 2005 (by DLR).



The map is the same as in Fig. 18 but another colour scale was used to emphasize the sites of lower apparent resistivity within the syncline. Fire zones no. 3.2 and no. 8 are marked by red rectangles.....51

Figure 20: Map of the centroid depth at a frequency of 4650 Hz, derived from the helicopter survey over the entire Wuda area. Fire zones no. 3.2 and no. 8 are marked by red rectangles.....52

Figure 21: Map of the apparent resistivity ρ_{oa} [$\text{Ohm}\cdot\text{m}$] at a frequency of 930 Hz, derived from the helicopter survey over the entire Wuda area. Blue and red polygons show fire zones mapped in 2004, the black dots show single fire points mapped in 2005 (by DLR). Colour shading from N-E. Fire zones no. 3.2 and no. 8 are marked by red rectangles.....53

Figure 22: Map of the apparent resistivity ρ_{oa} [$\text{Ohm}\cdot\text{m}$] at a frequency of 930 Hz, derived from the helicopter survey over the entire Wuda area. Blue and red polygons show fire zones mapped in 2004, the black dots show single fire points mapped in 2005 (by DLR). The colour scale is the same as in Fig. 21 but without shading. Fire zones no. 3.2 and no. 8 are marked by red rectangles.....54

Figure 23: Map of the apparent resistivity ρ_{oa} [$\text{Ohm}\cdot\text{m}$] at a frequency of 930 Hz, derived from the helicopter survey over the entire Wuda area. Blue and red polygons show fire zones mapped in 2004, the black dots show single fire points mapped in 2005 (by DLR). The map is the same as in Fig. 22 but another colour scale was used to emphasize the sites of lower apparent resistivity within the syncline. Fire zones no. 3.2 and no. 8 are marked by red rectangles.....55

Figure 24: Map of the centroid depth at a frequency of 930 Hz, derived from the helicopter survey over the entire Wuda area. Fire zones no. 3.2 and no. 8 are marked by red rectangles.....56

Figure 25: Quickbird satellite map (see Fig. 10) superimposed on the apparent resistivity map at a frequency of 930 Hz, derived from the helicopter survey over the entire Wuda area (see Fig. 22). Blue and red polygons show fire zones mapped in 2004, black dots show single fire points mapped in 2005 (by DLR). Sites from the TEM ground survey are marked by violet squares. The course of the Yellow River (light black lines) is roughly shown east of the map beyond the survey area. Fire zones no. 3.2 and no. 8 are marked by red rectangles.57



Figure 26: Map of the apparent resistivity ρ_{oa} [Ohm*m] at a frequency of 23250 Hz, derived from the helicopter survey over and in the vicinity of fire zone no. 8. Black squares show the sites of the TEM soundings, orange lines show the VLF and HL survey lines. Blue and red polygons indicate the burning zones in 2004, light blue and violet polygons and black dots indicate the burning zones in 2005, light black lines mark cracks (mapped by DLR).60

Figure 27: Map of the centroid depth [m] at a frequency of 23250 Hz, derived from the helicopter survey over and in the vicinity of fire zone no. 8. Black squares show the sites of the TEM soundings, orange lines show the VLF and HL survey lines. Blue and red polygons indicate the burning zones in 2004, light blue and violet polygons and black dots indicate the burning zones in 2005, light black lines mark cracks (mapped by DLR)......61

Figure 28: Map of the apparent resistivity ρ_{oa} [Ohm*m] at a frequency of 4650 Hz, derived from the helicopter survey over and in the vicinity of fire zone no. 8. Black squares show the sites of the TEM soundings, orange lines show the VLF and HL survey lines. Blue and red polygons indicate the burning zones in 2004, light blue and violet polygons and black dots indicate the burning zones in 2005, light black lines mark cracks (mapped by DLR).62

Figure 29: Map of the centroid depth [m] at a frequency of 4650 Hz, derived from the helicopter survey over and in the vicinity of fire zone no. 8. Black squares show the sites of the TEM soundings, orange lines show the VLF and HL survey lines. Blue and red polygons indicate the burning zones in 2004, light blue and violet polygons and black dots indicate the burning zones in 2005, light black lines mark cracks (mapped by DLR).63

Figure 30: Map of the apparent resistivity ρ_{oa} [Ohm*m] at a frequency of 930 Hz, derived from the helicopter survey over and in the vicinity of fire zone no. 8. Black squares show the sites of the TEM soundings, orange lines show the VLF and HL survey lines. Blue and red polygons indicate the burning zones in 2004, light blue and violet polygons and black dots indicate the burning zones in 2005, light black lines mark cracks (mapped by DLR).64

Figure 31: Map of the centroid depth [m] at a frequency of 930 Hz, derived from the helicopter survey over and in the vicinity of fire zone no. 8. Black squares show the sites of the TEM soundings, orange lines show the VLF and HL survey lines. Blue and red polygons indicate the burning zones in 2004, light blue and violet polygons and black dots indicate the burning zones in 2005, light black lines mark cracks (mapped by DLR).65

Figure 32: Map of the apparent resistivity ρ_{oa} [Ohm*m] at a frequency of 23250 Hz derived from the helicopter survey over and in the vicinity of fire zone no. 3.2. Black squares show



the sites of the TEM soundings. Blue and red polygons indicate the burning zones in 2004, the black dots indicate burning spots in 2005, light black lines mark cracks (mapped by DLR).....67

Figure 33: Map of the centroid depth [m] at a frequency of 23250 Hz derived from the helicopter survey over and in the vicinity of fire zone no. 3.2. Black squares show the sites of the TEM soundings. Blue and red polygons indicate the burning zones in 2004, the black dots indicate burning spots in 2005, light black lines mark cracks (mapped by DLR).68

Figure 34: Map of the apparent resistivity ρ_a [Ohm*m] at a frequency of 4650 Hz derived from the helicopter survey over and in the vicinity of fire zone no. 3.2. Black squares show the sites of the TEM soundings. Blue and red polygons indicate the burning zones in 2004, the black dots indicate burning spots in 2005, light black lines mark cracks (mapped by DLR).....69

Figure 35: Map of the centroid depth [m] at a frequency of 4650 Hz derived from the helicopter survey over and in the vicinity of fire zone no. 3.2. Black squares show the sites of the TEM soundings. Blue and red polygons indicate the burning zones in 2004, the black dots indicate burning spots in 2005, light black lines mark cracks (mapped by DLR).....70

Figure 36: Map of the apparent resistivity ρ_a [Ohm*m] at a frequency of 930 Hz derived from the helicopter survey over and in the vicinity of fire zone no. 3.2. Black squares show the sites of the TEM soundings. Blue and red polygons indicate the burning zones in 2004, the black dots indicate burning spots in 2005, light black lines mark cracks (mapped by DLR).....71

Figure 37: Map of the centroid depth [m] at a frequency of 930 Hz derived from the helicopter survey over and in the vicinity of fire zone no. 3.2. Black squares show the sites of the TEM soundings. Blue and red polygons indicate the burning zones in 2004, the black dots indicate burning spots in 2005, light black lines mark cracks (mapped by DLR).....72

Figure 38: Map of the apparent resistivity ρ_a [Ohm*m] at a frequency of 23250 Hz, derived from the helicopter survey south of fire zone no. 3.2. Names of fire zones are shown by black numbers. Green polygons mark the fire zones in 2002, light black polygons mark the fire zones in 2003, blue and red polygons indicate the burning zones in 2004, violet polygons and black dots indicate burning spots in 2005 (mapped by DLR).....74



- Figure 39: Map of the apparent resistivity ρ_{oa} [Ohm*m] at a frequency of 4650 Hz, derived from the helicopter survey south of fire zone no. 3.2. Green polygons mark the fire zones in 2002, light black polygons mark the fire zones in 2003, blue and red polygons indicate the burning zones in 2004, violet polygons and black dots indicate burning spots in 2005 (mapped by DLR).....75
- Figure 40: Map of the apparent resistivity ρ_{oa} [Ohm*m] at a frequency of 930 Hz, derived from the helicopter survey south of fire zone no. 3.2. Green polygons mark the fire zones in 2002, light black polygons mark the fire zones in 2003, blue and red polygons indicate the burning zones in 2004, violet polygons and black dots indicate burning spots in 2005 (mapped by DLR).....76
- Figure 41: Map of the centroid depth [m] at a frequency of 4650 Hz, derived from the helicopter survey south of fire zone no. 3.2. Green polygons mark the fire zones in 2002, light black polygons mark the fire zones in 2003, blue and red polygons indicate the burning zones in 2004, violet polygons and black dots indicate burning spots in 2005 (mapped by DLR)...77
- Figure 42: Map of the apparent resistivity ρ_{oa} [Ohm*m] at a frequency of 23250 Hz, derived from the helicopter survey in the vicinity of fire zone no. 7. Orange lines indicate the profiles of the VLF survey. Blue and red polygons indicate the burning zones in 2004, the black dots indicate burning spots in 2005 (mapped by DLR).79
- Figure 43: Map of the apparent resistivity ρ_{oa} [Ohm*m] at a frequency of 4650 Hz, derived from the helicopter survey in the vicinity of fire zone no. 7. Orange lines indicate the profiles of the VLF survey. Blue and red polygons indicate the burning zones in 2004, the black dots indicate burning spots in 2005 (mapped by DLR).80
- Figure 44: Map of the apparent resistivity ρ_{oa} [Ohm*m] at a frequency of 930 Hz, derived from the helicopter survey in the vicinity of fire zone no. 7. Orange lines indicate the profiles of the VLF survey. Blue and red polygons indicate the burning zones in 2004, the black dots indicate burning spots in 2005 (mapped by DLR).81
- Figure 45: Map of the centroid depth [m] at a frequency of 4650 Hz, derived from the helicopter survey in the vicinity of fire zone no. 7. Orange lines indicate the profiles of the VLF survey. Blue and red polygons indicate the burning zones in 2004, the black dots indicate burning spots in 2005 (mapped by DLR).82
- Figure 46: Map of the apparent resistivity ρ_{oa} [Ohm*m] at a frequency of 23250 Hz, derived from the helicopter survey in the southern part of the syncline. Names of fire zones are



shown by black numbers, from fire zone no. 8 the southern part is shown. Green polygons mark the fire zones in 2002, light black polygons mark the fire zones in 2003, blue and red polygons indicate the burning zones in 2004, violet polygons and black dots indicate burning spots in 2005 (mapped by DLR).....84

Figure 47: Map of the apparent resistivity ρ_{oa} [$\Omega \cdot m$] at a frequency of 4650 Hz, derived from the helicopter survey in the southern part of the syncline. Green polygons mark the fire zones in 2002, light black polygons mark the fire zones in 2003, blue and red polygons indicate the burning zones in 2004, violet polygons and black dots indicate burning spots in 2005 (mapped by DLR).....85

Figure 48: Map of the apparent resistivity ρ_{oa} [$\Omega \cdot m$] at a frequency of 930 Hz, derived from the helicopter survey in the southern part of the syncline. Green polygons mark the fire zones in 2002, light black polygons mark the fire zones in 2003, blue and red polygons indicate the burning zones in 2004, violet polygons and black dots indicate burning spots in 2005 (mapped by DLR).....86

Figure 49: Map of the centroid depth [m] at a frequency of 4650 Hz, derived from the helicopter survey in the southern part of the syncline. Green polygons mark the fire zones in 2002, light black polygons mark the fire zones in 2003, blue and red polygons indicate the burning zones in 2004, violet polygons and black dots indicate burning spots in 2005 (mapped by DLR).....87

Figure 50: Path of the selected flight lines crossing fire zone no. 8. Light black squares show the sites of the TEM ground survey, green polygons mark the fire zones in 2002, light black polygons mark the fire zones in 2003, blue and red polygons indicate the burning zones in 2004, light blue and violet polygons and black dots indicate burning spots in 2005 (mapped by DLR).....90

Figure 51: Path of the selected flight lines crossing fire zone no. 3.2. Black squares show the sites of the TEM ground survey, green polygons mark the fire zones in 2002, light black polygons mark the fire zones in 2003, blue and red polygons indicate the burning zones in 2004 and black dots indicate burning spots in 2005 (mapped by DLR).91

Figure 52: Path of the selected flight lines crossing fire zones no. 11, no. 12, no. 13 and no. 14. Green polygons mark the fire zones in 2002, light black polygons mark the fire zones in 2003, blue and red polygons indicate the burning zones in 2004 and black dots indicate burning spots in 2005 (mapped by DLR).....91



Figure 53: Path of the selected flight lines crossing fire zone no. 7. Orange lines mark the HL survey lines, green polygons mark the fire zones in 2002, light black polygons mark the fire zones in 2003, blue and red polygons indicate the burning zones in 2004 and black dots indicate burning spots in 2005 (mapped by DLR).....92

Figure 54: Inphase and quadrature values at three frequencies, vertical apparent resistivity section, 1-D vertical resistivity section and misfit along profile 2220, crossing fire zone no. 8.....93

Figure 55: Inphase and quadrature values at three frequencies, vertical apparent resistivity section, 1-D vertical resistivity section and misfit along profile 2240, crossing fire zone no. 8.....94

Figure 56: Inphase and quadrature values at three frequencies, vertical apparent resistivity section, 1-D vertical resistivity section and misfit along profile 2270, crossing fire zone no. 8.....95

Figure 57: Inphase and quadrature values at three frequencies, vertical apparent resistivity section, 1-D vertical resistivity section and misfit along profile 2280, crossing fire zone no. 8.....96

Figure 58: Inphase and quadrature values at three frequencies, vertical apparent resistivity section, 1-D vertical resistivity section and misfit along profile 2290, crossing fire zone no. 8.....97

Figure 59: Inphase and quadrature values at three frequencies, vertical apparent resistivity section, 1-D vertical resistivity section and misfit along profile 2390, crossing fire zone no. 8.....98

Figure 60: Inphase and quadrature values at three frequencies, vertical apparent resistivity section, 1-D vertical resistivity section and misfit along profile 3110, crossing fire zone no. 3.2.....99

Figure 61: Inphase and quadrature values at three frequencies, vertical apparent resistivity section, 1-D vertical resistivity section and misfit along profile 3120, crossing fire zone no. 3.2.....100

Figure 62: Inphase and quadrature values at three frequencies, vertical apparent resistivity section, 1-D vertical resistivity section and misfit along profile 3130, crossing fire zone no. 3.2.....101



Figure 63: Inphase and quadrature values at three frequencies, vertical apparent resistivity section, 1-D vertical resistivity section and misfit along profile 3140, crossing fire zone no. 3.2.....102

Figure 64: Inphase and quadrature values at three frequencies, vertical apparent resistivity section, 1-D vertical resistivity section and misfit along profile 1680, crossing the fire zones no. 12, no. 13 and no. 14.103

Figure 65: Inphase and quadrature values at three frequencies, vertical apparent resistivity section, 1-D vertical resistivity section and misfit along profile 1700, crossing the fire zones no. 12, no. 13 and no. 14.104

Figure 66: Inphase and quadrature values at three frequencies, vertical apparent resistivity section, 1-D vertical resistivity section and misfit along profile 1720, crossing the fire zones no. 12, no. 13 and no. 14.105

Figure 67: Inphase and quadrature values at three frequencies, vertical apparent resistivity section, 1-D vertical resistivity section and misfit along profile 1740, crossing the fire zones no. 12, no. 13 and no. 14.106

Figure 68: Inphase and quadrature values at three frequencies, vertical apparent resistivity section, 1-D vertical resistivity section and misfit along profile 2490, crossing fire zone no. 7.....107

Figure 69: Inphase and quadrature values at three frequencies, vertical apparent resistivity section, 1-D vertical resistivity section and misfit along profile 2500, crossing fire zone no. 7.....108

Figure 70: Inphase and quadrature values at three frequencies, vertical apparent resistivity section, 1-D vertical resistivity section and misfit along profile 2510, crossing fire zone no. 7.....109

Figure 71: Inphase and quadrature values at three frequencies, vertical apparent resistivity section, 1-D vertical resistivity section and misfit along profile 2540, crossing fire zone no. 7.....110

Figure 72: Inphase and quadrature values at three frequencies, vertical apparent resistivity section, 1-D vertical resistivity section and misfit along profile 2050, crossing fire zone no. 11.....111



- Figure 73: Inphase and quadrature values at three frequencies, vertical apparent resistivity section, 1-D vertical resistivity section and misfit along profile 2120, crossing coal seams no. 6 and 7. 112
- Figure 74: Anomalies of the total magnetic field dT [nT] over the whole Wuda syncline, derived from the airborne magnetic data at an average flight altitude of 60 m and a line separation of about 50 m. Bold solid red rectangles indicate the areas of fire zones no. 8 and no. 3.2. In general fire zones are marked by blue and red polygons (by DLR, 2002 to 2005)..... 114
- Figure 75: Anomalies of the total magnetic field dT [nT] over the whole Wuda syncline, derived from the airborne magnetic data at an average flight altitude of 60 m and a line separation of about 50 m. Bold solid red rectangles indicate the areas of fire zones no. 8 and no. 3.2. In general fire zones are marked by blue and red polygons (by DLR, 2002 to 2005). Colour shading from N-E..... 115
- Figure 76: Section of the map of the anomalies of the total magnetic field dT [nT] for fire zone no. 8 derived from the airborne magnetic data at an average flight altitude of 60 m and a line separation of about 50 m. Blue and red polygons indicate the burning zones in 2004, light blue and violet polygons and black dots indicate the burning zones in 2005 (mapped by DLR). The sites of the TEM ground survey are shown by black squares (see Fig. 82). 117
- Figure 77: Section of the map of the anomalies of the total magnetic field dT [nT] for the surroundings of fire zone no. 8 derived from the airborne magnetic data at an average flight altitude of 60 m and a line separation of about 50 m. Blue and red polygons indicate the burning zones in 2004, light blue and violet polygons and black dots indicate the burning zones in 2005, green lines mark the burning zone in 2002 and light black lines in 2003 (mapped by DLR). The sites of the TEM ground survey are shown by black squares (see Fig. 82)..... 118
- Figure 78: Section of the map of the anomalies of the total magnetic field dT [nT] for fire zone no. 3.2 derived from the airborne magnetic data at an average flight altitude of 60 m and a line separation of about 50 m. Blue and red polygons indicate the burning zones in 2004, black dots indicate the burning zones in 2005, green lines mark the burning zone in 2002 and light black lines in 2003 (mapped by DLR). The sites of the TEM ground survey are shown by black squares. 119

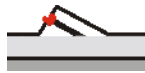


Figure 79: Section of the map of the anomalies of the total magnetic field dT [nT] for the southern surroundings of fire zone no. 3.2 derived from the airborne magnetic data at an average flight altitude of 60 m and a line separation of about 50 m. Blue and red polygons indicate the burning zones from 2002 to 2004, violet polygons and black dots indicate the burning zones in 2005, green lines mark the burning zones in 2002 and light black lines in 2003 (mapped by DLR)..... 120

Figure 80: Section of the map of the anomalies of the total magnetic field dT [nT] over fire zone no. 7 derived from the airborne magnetic data at an average flight altitude of 60 m and a line separation of about 50 m. Blue and red polygons indicate the burning zones from 2004, black dots indicate the burning zones in 2005, green lines in 2002 and light black lines in 2003 (mapped by DLR). Profiles no. 6 and no. 7 from the VLF and ground magnetic survey are shown as orange lines..... 121

Figure 81: Section of the map of the anomalies of the total magnetic field dT [nT] for fire zone no. 11 and the southern part of the syncline derived from the airborne magnetic data at an average flight altitude of 60 m and a line separation of about 50 m. Blue and red polygons indicate the burning zones in 2004, green polygons mark the burning zones from 2002 and black dots indicate the burning zones in 2005. Green lines show the burning zones in 2002 and light black lines in 2003 (mapped by DLR). 122

Figure 82: Map of the location of the TEM sites (black squares) crossing fire zone no. 8 (profiles no. 3 to no. 9) and at various other sites in the desert, west and east of one of the big hills in the south and over coal seams 6 and 7. Profiles no. 1, 2, 3 and 4 (orange lines) show the sites of the HL and the VLF measurements. The polygons of the burning zones (blue resp. light blue for colder fires and red resp. violet for hotter fires) were mapped in 2004 resp. 2005 by DLR. 125

Figure 83: Quickbird satellite image of fire zone no. 8 (DLR, 2003) with location of the TEM ground survey sites (black squares). Orange lines show the profile lines of the HL and the VLF measurements. Blue and red polygons show the burning zones in 2004 and light blue and violet polygons show the burning zones in 2005. Black dots mark burning spots in 2005 (mapped by DLR). Cracks are marked by light black lines. 126

Figure 84: Apparent resistivity curves from TEM data along profile no. 3. Crosses: data, lines: model curve. 129

Figure 85: Apparent resistivity versus apparent depth from TEM data along profile no. 3..... 130



Figure 86: Vertical resistivity section derived from TEM data along profile no. 3. The burning zone is marked by a dashed red line. 130

Figure 87: Apparent resistivity curves from TEM data along profile no. 6. Crosses: data, lines: model curve. 131

Figure 88: Apparent resistivity versus apparent depth from TEM data along profile no. 6. 131

Figure 89: Vertical resistivity section derived from TEM data along profile no. 6. The burning zone is marked by a dashed red line. The conductor is dipping northwards from about 25 m to 50 m depth. 132

Figure 90: Apparent resistivity curves from TEM data along profile no. 7. Crosses: data, lines: model curve. 132

Figure 91: Vertical resistivity section derived from TEM data along profile no. 7. 133

Figure 92: Apparent resistivity curves from TEM data along the western part of profile no. 5. Crosses: data, lines: model curve. 133

Figure 93: Apparent resistivity curves from TEM data along the eastern part of profile no. 5. Crosses: data, lines: model curve. 134

Figure 94: Apparent resistivity versus apparent depth from TEM data along profile no. 5. 135

Figure 95: Vertical resistivity section derived from TEM data along profile no. 5. The burning zone is marked by a dashed red line. The eastwards dipping shallow conductor correlates with the burning part of fire zone no. 8. 135

Figure 96: Apparent resistivity curves from TEM data along profile no. 4. Crosses: data, lines: model curve. 136

Figure 97: Vertical resistivity section derived from TEM data along profile no. 4. The burning zone is marked by a dashed red line. This profile crosses profile no. 6 at site 1. 137

Figure 98: Apparent resistivity curves from TEM data along profile no. 8. Crosses: data, lines: model curve. 137

Figure 99: Vertical resistivity section derived from TEM data along profile no. 8. This profile crosses profile no. 6 at site 8. 138

Figure 100: Apparent resistivity curves from TEM data along profile no. 9. Crosses: data, lines: model curve. 138



Figure 101: Vertical resistivity section derived from TEM data along profile no. 9 in the northern part of fire zone no. 8..... 139

Figure 102: TEM survey at fire zone no. 3.2, site no. 24. View to the south-east. 140

Figure 103: Quickbird satellite image of fire zone no. 3.2 (DLR, 2003) with location of the TEM ground survey sites (black squares). The red and blue polygons show burning zones in 2004 and black dots show the burning spots in 2005 (mapped by DLR). Cracks are marked by light black lines. 141

Figure 104: Apparent resistivity curves from TEM data along profile no. 12. Crosses: data, lines: model curve. 142

Figure 105: Vertical resistivity section derived from TEM data along profile no. 12. Site 51 is situated about 370 m apart west of profile no. 12. 143

Figure 106: Apparent resistivity curves from TEM data along profile no. 11. Crosses: data, lines: model curve. 143

Figure 107: Vertical resistivity section derived from TEM data along profile no. 11. 144

Figure 108: Apparent resistivity curves from TEM data along profile no. 10. Crosses: data, lines: model curve. 145

Figure 109: Vertical resistivity section derived from TEM data along profile no. 10. 146

Figure 110: Apparent resistivity curves from TEM data at coal seams no. 6 and no. 7..... 147

Figure 111: 1D inversion models derived from TEM data for two sites outside the burning zones over the not burning coal seams no. 6 and no. 7 in the central part of the Wuda syncline..... 147

Figure 112: Apparent resistivity curves from TEM data at sites in the desert north beyond the Wuda syncline. 148

Figure 113: Vertical resistivity section derived from TEM data outside the burning zones in the desert area north of the Wuda syncline. 148

Figure 114: Apparent resistivity curves from TEM data at two sites in the southern part of the Wuda syncline. 149

Figure 115: Vertical resistivity section from TEM data outside the burning zones in the southern part of the Wuda syncline. Site 38 is located west of one of the big hills in the south and site 39 east of it..... 149



Figure 116: VLF and HL data along profile no. 1 in the western part of the Wuda syncline, fire zone no. 8. The red marked parts of the profile line show the data over burning spots within the fire zone..... 151

Figure 117: HL data along profile no. 2 in the eastern part of fire zone no. 8. 152

Figure 118: 1-D model from HL data for profiles no. 1 and no. 2. 153

Figure 119: VLF and HL data along profile no. 3, crossing fire zone no. 8. The red marked parts of the profile show the data over active parts of the fire zone..... 154

Figure 120: VLF and HL data along profile no. 4, crossing fire zone no. 8 close to the hot burning part at the southern end of the plateau. The red tagged sections mark anomalies. 156

Figure 121: VLF and HL data along profile no. 5, crossing fire zone no. 8 south of the collapsed area. The red coloured sections mark areas over the burning part of this fire zone. 157

Figure 122: Location of the VLF profiles no. 6 and no. 7 at fire zone no. 7..... 158

Figure 123: VLF and magnetic data along profile no. 6 within the central part of the Wuda syncline in the vicinity of fire zone no. 7, marked in red. 159

Figure 124: VLF and magnetic data along profile no. 7 over fire zone no. 7 within the central part of the Wuda syncline. The red stripes again mark the burnt fire zone..... 159

Figure 125: Areas with baked rocks at fire zone no. 8: 1) Area south of the hot burning zone with collapsed overburden, view to the east, 2) Western slope below the water basin, view to the north. TEM site no. 18 was situated in the small flat area below the hill..... 161

Figure 126: Anomalies of the magnetic field T derived from the ground magnetic survey, conducted by AGRS in 2005 over fire zone no. 8. Blue resp. light blue and red resp. violet lines outline areas of colder and hotter coal seam fires, mapped by DLR in 2004 and 2005. Black dots mark burning spots mapped in 2005. For a better orientation the TEM survey sites from profiles no. 3 and no. 5 are shown as light black squares. Light solid black lines show the survey lines. 162

Figure 127: Anomalies of the magnetic field T derived from the ground magnetic survey, conducted by AGRS in 2005 over fire zone no. 3.2. Blue and red lines outline areas of colder and hotter coal seam fires, mapped by DLR in 2004. Black dots mark burning spots mapped in 2005. For a better orientation the TEM survey sites from profiles no. 10, 11 and 12 are shown as black squares..... 163



Figure 128: Ground magnetic measurements at fire zone no. 8: 1) at the southern end of the plateau close to the cracks, view to the west, 2) within the southern part of the collapsed zone, view to the north (Photos by AGRS).164

Figure 129: Anomalies of the magnetic field ΔT derived from the ground magnetic surveys, conducted by DMT in 2005 over fire zone no. 8. Blue resp. light blue and red resp. violet lines outline areas of colder and hotter coal seam fires, mapped by DLR in 2004 and 2005. Black dots mark burning spots mapped in 2005. The light black lines show the route of the survey. For a better orientation the TEM survey sites from profiles no. 3 and no. 5 are shown as light black squares.166

Figure 130: Anomalies of the magnetic field ΔT derived from the ground magnetic surveys, conducted by AGRS and DMT in 2005 over fire zone no. 8. Blue resp. light blue and red resp. violet lines outline areas of colder and hotter coal seam fires, mapped by DLR in 2004 and 2005. Black dots mark burning spots mapped in 2005. For a better orientation the TEM survey sites from profiles no. 3 and no. 5 are shown as light black squares. The light black lines show the route of the surveys.167

Figure 131: Anomalies of the magnetic field ΔT derived from the ground magnetic survey, conducted by DMT in 2005 over fire zone no. 3.2. Blue and red lines outline areas of colder and hotter coal seam fires, mapped by DLR in 2004. Black dots mark burning spots mapped in 2005. The light black lines show the route of the survey. For a better orientation the TEM survey sites from profiles no. 10, 11 and 12 are shown as black squares.168

Tables

Tab 1: Survey parameters.....29

Tab 2: Data Format34



1 Introduction

Within the framework of the BMBF (German Federal Ministry of Education and Research) funded Sino-German Research Initiative „Innovative Technologies for Exploration, Extinction and Monitoring of Coal Fires in North China” the China Aero Geophysical Survey & Remote Sensing Centre for Land and Resources (AGRS) assisted by the Federal Institute for Geosciences and Natural Resources (BGR) performed a helicopter survey using electromagnetics (HEM) and magnetics over the coal fire area of Wuda, Inner Mongolia Autonomous Region, in 2004. In the following year ground surveys were carried out in selected parts of the area concerned, conducting especially transient electromagnetics (TEM) done by BGR and magnetics done by AGRS and DMT (Deutsche Montan Technologie). The objective of the geophysical surveys was to detect areas affected by coal seam fires by means of physical parameters acquired over the burning and burnt coal seams, such as the electrical conductivity (resp. the resistivity, its reciprocal) and the magnetic susceptibility.

The survey area is covered mainly by sandstones; below up to 18 mined coal seams extend to greater depths varying from a few metres down to several hundreds of metres below surface. In the areas affected by coal seam fires several testing areas were selected. Within these areas especially two fire zones (no. 3.2 and no. 8) were of great interest and became object of the geophysical studies. Several Chinese and German partners from various geoscientific fields of work participated in the investigations of the coal fire area of Wuda (location see Fig. 1).

The helicopter-borne survey should reveal the electrical properties and anomalies of the total magnetic field at sites related to coal seam fires. Besides that a general overview of the geological situation of the whole area can be gained. The ground surveys were conducted in selected parts of the airborne survey area. Numerous ground electromagnetic measurements, especially transient electromagnetics (TEM), were performed by BGR across the fire zones and were extended to areas not affected by coal seam fires. A ground magnetic survey done by AGRS covered most parts of one of the fire zones (fire zone no. 8) and was supplemented by DMT (Deutsche Montan Technologie). Satellite supported maps (Voigt et al. 2004, Kuenzer et al. 2005) of the burning areas conducted by DLR (German Aerospace Center) complemented the survey in order to distinguish between coal seam fire affected areas and unaffected areas. Further investigations with respect to geological, micropetrographical, thermal and geochemical aspects of the Wuda coal fire area are introduced by other authors within the volumes of the project reports and the articles of the ERSEC Ecological Book Series - 4 on Coal Fire Research (e.g. Schloemer et al. 2006, Kus et al. 2006).



Figure 1: Location of the coal mining area of Wuda, Inner Mongolia Autonomous Region, Northern China.

1.1 Scientific State

Only a few publications are known about geophysical measurements, especially electromagnetics, over burning coal seams. The behaviour of coal samples under high temperature was investigated in the laboratory by Duba (1977, 1983). The properties of the coal (e.g. the maturity or rank of carbonization) influence the measured physical parameters in the field, e.g. the electrical conductivity. If influences like enhanced temperature take place, the processes are more complex. The influences of burning coal seams on the local total magnetic field intensity are well known. Publications about this topic can be found by Hooper (1987) and Thomas (2002).

Duba (1977, 1983) described changes of the electrical conductivity of coal samples and its products by pyrolysis. Heating water-saturated coal samples increased their conductivity from an initial value of 10^{-3} Sm^{-1} (resistivity: $1000 \text{ Ohm}\cdot\text{m}$) at 24°C (when the coal is saturated with formation water) to 100 Sm^{-1} ($0.01 \text{ Ohm}\cdot\text{m}$) for char samples, recovered after pyrolysis to 800°C . After a large initial decrease owing to water loss on drying to 110°C the conductivity continues to decrease on heating from 110°C to 300°C and then begins to increase slowly with heating to 515°C and after which it increases rapidly. The large increase in the conductivity of the char recovered after pyrolysis at temperatures greater than 600°C is probably related to the increased carbon content of the char. Duba (1977) suggests the electrical conductivity of coal and its pyrolysis products as a mean to locate and identify regions of different physical properties during in situ coal gasification. His data indicate that there is an enormous change in the conductivity of coal during pyrolysis. So it may be exploited for locating and monitoring the underground reaction zone. Char as a product of pyrolysis could increase the conductivity of the ash zone.

Jödicke (1991) showed that the carbon content of coal is determining the electrical conductivity. Enhanced carbon content means more graphitic-like properties of the coal. Temperature plays an important role within the processes of ranking of coal.

Powell & Schofield (1939) investigated the electrical conductivities of carbon and graphite at high temperatures. They found that the electrical conductivity increased with an increase in



thermal conductivity and that the process of graphitization of carbon also increases the electrical conductivity.

King (1987) described transient electromagnetic measurements above cindered coal seams in Australia, which showed significantly lower resistivities. These seams were detected by resistivity lows on the sounding curves.

Van Krevelen (1981) described a rapid rise in electrical conductivity with coal rank due to the increasing graphitoid character of coal by the phenomenon of free moving electrons. A graphitization of the carbon atoms involves an increase in electrical conductance.

Bartel (1982) described CSAMT (Controlled Source Audiomagnetotelluric) measurements above abandoned coal mine fires. In all surveys resistivity anomalies associated with the area on fire were observed. He showed model calculations with unaffected coal seams and pillars with a resistivity of about 500 Ohm*m and pillars on fire with a resistivity of about 1 Ohm*m. Furthermore he reports laboratory measurements which show that coal undergoes drastic electrical resistivity changes during the combustion process. While coal in its virgin state has a resistivity of approximately 100 to 500 Ohm*m (depending on water saturation, pore water resistivity, porosity and permeability) it gets a very high resistivity (up to 105 Ohm*m) by drying and subjected to temperatures up to 450°C. During the pyrolysis process at temperatures greater than approximately 650°C coal becomes highly conductive with a resistivity of approximately 1 Ohm*m. In situ resistivity measurements made on coked coal from an in-situ coal gasification experiment show that coked (carbonized) coal at ambient temperature is highly conductive with a resistivity in the order of 1 Ohm*m. Heat from burning coal will increase the temperature of the pore water adjacent to the fire leading to a decrease in electrical resistivity of the pore water. He suggests due to of these drastic resistivity changes electrical and electromagnetic techniques to be appropriate to map and monitor the progress of the combustion front in burning coal. The observed low resistivity values may be due to several causes which include burning or coked coal, increased porosity due to subsidence, increased water saturation due to groundwater encroachment (if present) or condensed steam, increased salinity of the pore water due to leaching, heated pore water and increased effective permeability due to subsidence cracks with fire present or not. High values of observed resistivity may be due to several causes which include pillars not on fire with a low water saturation, areas of low water saturation and low porosity and empty rooms (Bartel 1982).

An airborne survey by FAS (Fugro Airborne Surveys, Canada) was carried out in Wyoming for investigations of a coal fire affected area. Apparent resistivity lows were found over burnt coal in the area (Hodges, pers. comm., 2003). The host rock above the burnt coal shows an increase of the magnetic susceptibility and of the electrical resistivity. For researching the possibility of detecting an active burning front, it is assumed that it will be very conductive compared to the coal (Hodges, pers. comm., 2006).

Jongmans et al. (2000) described electrical tomography measurements at a carboniferous shale heap, of which the core was burning. They found high resistivity spots close to the surface at places where heat flows are observed.

Heffern & Coates (2004) described coal-bed fires ignited by natural processes that have baked and fused overlying sediments to form clinker. The resulting clinker forms a rim along the exposed edge of the coal bed. Clinker outcrops can be found in the Powder River basin in Wyoming and Montana.



Hooper (1987) investigated the magnetic properties of baked rock samples in Wyoming. As they are usually quite distinct from the properties of the surrounding sedimentary rocks, baked rocks can be located by magnetic surveys. He reported baked siltstones with larger magnetic susceptibility than baked sandstones and shales of similar iron oxide content and thermal alteration history. While the magnetic susceptibility of unbaked rocks was quite low, the magnetic susceptibility of baked samples was variable. In most rocks the magnetic susceptibility is proportional to the magnetite content. So high magnetic susceptibilities were directly correlated with high magnetite content. Besides some iron oxides already present in the unbaked rocks, most of the hematite and magnetite in baked rocks are derived from the thermal alteration of sedimentary minerals. Baked siltstones are routinely more magnetic than coexisting sandstones and shales (Hooper 1987).

The most common magnetic mineral occurring in the earth's crust is magnetite. It can occur in large concentrations or can be finely distributed through sedimentary rocks. The presence of this magnetic mineral besides some other minerals which occur to a much lesser extent (e.g. pyrrhotite and ilmenite) causes deviations from the normally existing earth's magnetic field and provides the basis for a magnetic prospecting method. Magnetic anomalies of the earth's magnetic field are caused by induced and remanent magnetism. While the induced magnetism depends on the intensity of the present day earth's field, the remanent magnetism of rocks is due to the remanent magnetism of their constituent ferromagnetic grains. The magnetic susceptibility is a measure of the degree to which a material may be magnetised. It is defined as the ratio of the intensity of the magnetization to the magnetic field intensity. That means the larger the susceptibility the greater the intensity of magnetization and hence the bigger the anomaly produced relative to the earth's magnetic field (Roux 1978). The amount of magnetic minerals which possess remanent magnetism is responsible for the strength of the remanent magnetism, which may dominate the induced magnetism. The remanent magnetism is due to the earth's magnetic field by cooling down after heating beyond the Curie temperature and keeps the strength and direction of the earth's magnetic field at that time. Therefore outcrop magnetic susceptibility measurements detect magnetic mineral variations, i.e. magnetic mineral enrichment, because of their greater remanent magnetism. A difficulty may occur when the cooling down took place at a time with distinct different magnetic field intensity or direction. Then the preserved remanent magnetism may weaken or even oppose the present magnetic field. This is not expected in the Wuda area, because the processes of heating and cooling down of rocks took place during the last years or decades.

The magnetic properties of rocks may differ by several orders of magnitude. The magnetic susceptibility of a rock depends primarily on the amount of ferromagnetic minerals, its magnetite content, but it is reduced by weathering in general and measurements in the field give not necessarily a bulk susceptibility of the formation. In general sedimentary rocks have the lowest average susceptibility and coal bearing sequences have the lowest magnetic susceptibility within the sedimentary suite. In the delineation of burnt zones in coal seams, the magnetic susceptibility of unbaked sedimentary rocks is quite low, whilst the magnetic susceptibility of the baked rocks is variable (Thomas 2002, Hooper 1987). Most of the magnetite in the baked rocks is derived from the thermal alteration of sedimentary minerals. Iron enrichment in some baked areas is possible, because iron is mobile during thermal metamorphism and can be redeposited in the baked rocks. On heating, siltstones undergo a reduction in volume. The sediments around the edges of a burnt seam may contain more magnetite if the coal fire is extinguished due to the lack of oxygen, which reduces more iron



oxides and hydroxides to magnetite. In these cases larger magnetite anomalies may be expected along the margins of the baked zones (Thomas 2002, Hooper 1987).

Sternberg & Lippincott (2004) presented a study about magnetic surveys over clinkers and coal seam fires in the United States. They found enhanced magnetic susceptibility at burning coal seams altering the overlying sedimentary rocks including clinker formations.

Baked siltstones have larger magnetic susceptibilities than baked sandstones and shales of similar iron oxide content and thermal alteration history (Hooper 1987).

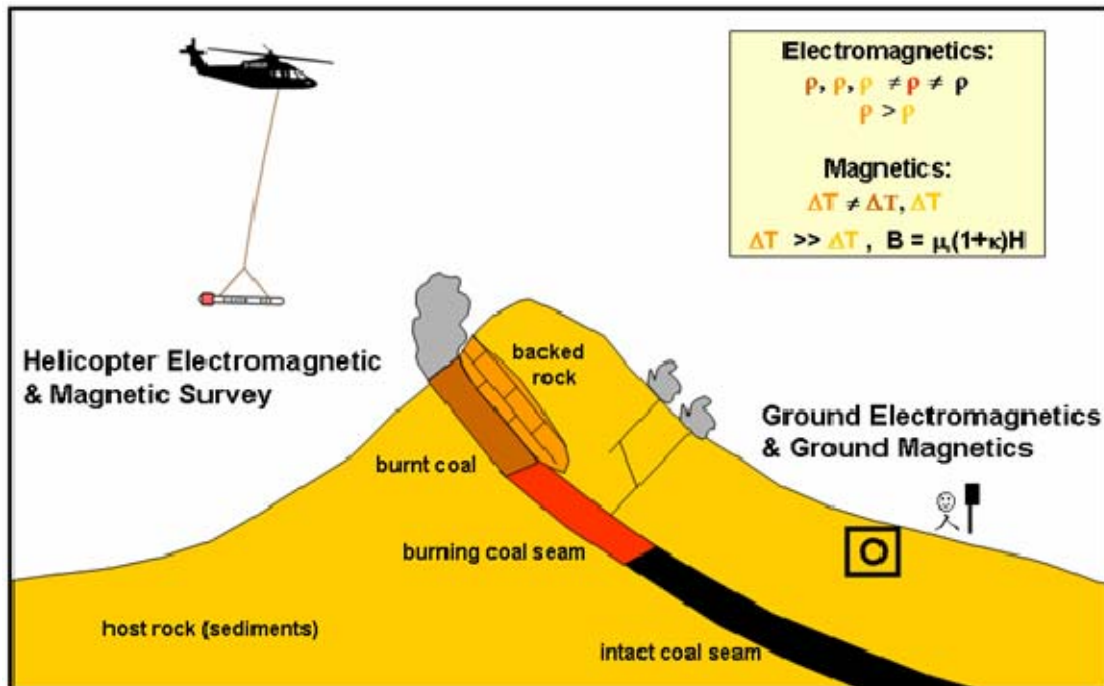


Figure 2: Principle scheme of the expected parameter variations gained by the electromagnetic and magnetic methods.

Due to these aspects the zones affected by coal seam fires in the Wuda area were investigated with regard to changes in electrical conductivity (respectively the resistivity, its reciprocal) of the subsurface and local anomalies of the magnetic field. Figure 2 shows a principle scheme of the expected parameter variations gained by the electromagnetic and magnetic methods.

1.2 Geology of the Wuda area

The Wuda area represents a Permian coal deposit with 18 coal seams. The strata are made up of a mixed layer sedimentary sequences by clastic sediments ranging from claystones, siltstones to conglomeratic sandstones and coal seams. The coal seams are embedded in the clastic sediments. This sequence forms a syncline, cut off in their centre by a system of faults. East of the Wuda syncline, a system of faulted blocks is made up by intensely folded marine carbonates. Alluvial sediments of the Yellow River can be found covering the older formations. The northern part of the coalfield is covered by postglacial loess and eolian quicksands of the Gobi Desert, which extends west of the syncline. An overview of the geology of the Wuda syncline and its surroundings is given in Fig. 5 and 6. The Yellow River flows about 10 km east of the Wuda syncline. West of fire zone no. 3.2, which is located in



**Innovative Technologies for Exploration, Extinction and Monitoring of Coal Fires in North China
Final Report Phase A Part B**

the north-western part of the Wuda syncline, the outcropping Permo-Carboniferous strata form the outer rim of the structure. The main burning coal seam is no. 9. The thickness of this seam is not determined. Directly north of the test area no. 3.2 eolian sediments of the desert cover the Palaeozoic strata of the Wuda syncline. In fire zone no. 8 in the western part of the centre of the syncline the coal seams no. 9 and no. 10 are burning very heavily. The overburden has collapsed at parts of the area where the seams are burning intensely. The thickness of the coal seams is about a few metres. The geological section of this burning zone can be correlated with the corresponding series in burning zone no. 3.2. The strata are generally dipping into an easterly direction. The outcropping series is destroyed by cracks (Gielisch & Kahlen 2003). Figures 7 and 8 show the geology of the mentioned fire zones in detail.

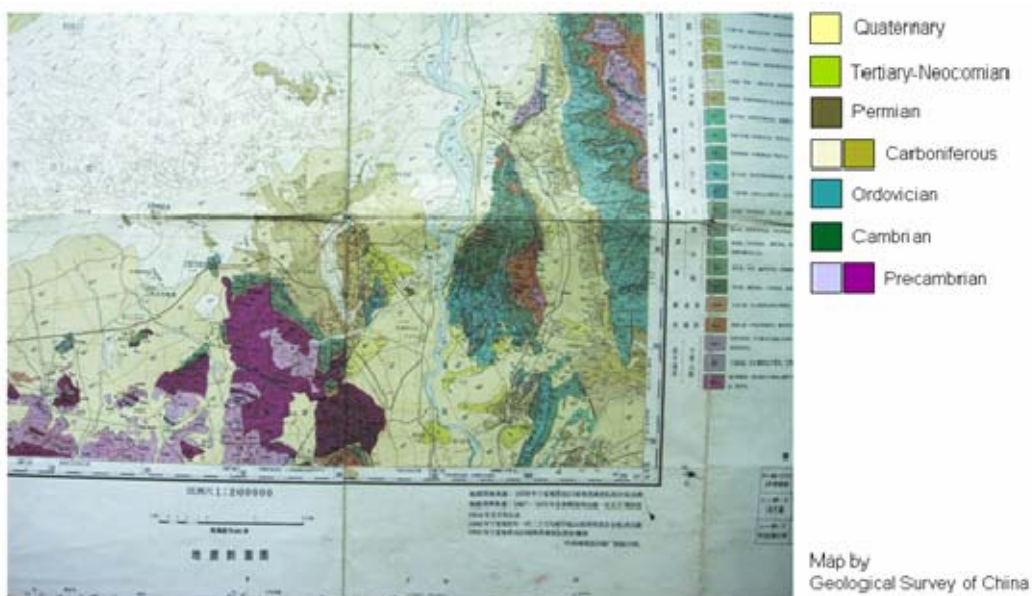


Figure 3: Geology of the Wuda syncline and its surroundings, Gielisch (2005).



Innovative Technologies for Exploration, Extinction and Monitoring of Coal Fires in North China
Final Report Phase A Part B

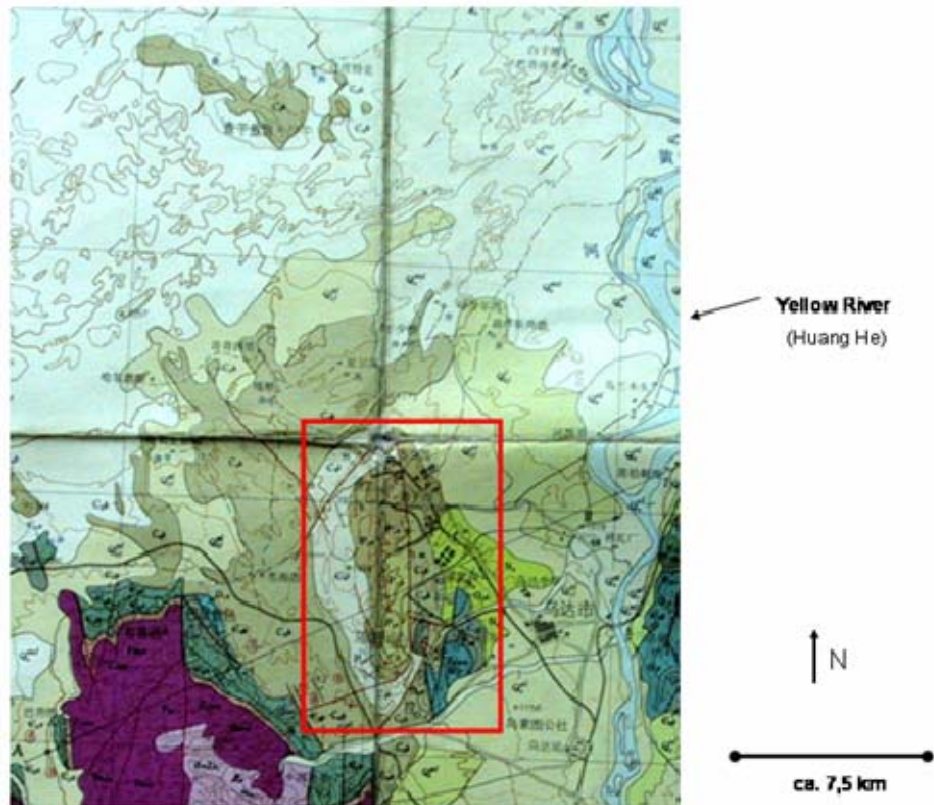


Figure 4: Section of the geological map (see Fig. 5, same key) for the Wuda syncline. The red rectangle roughly marks the area of the airborne survey.

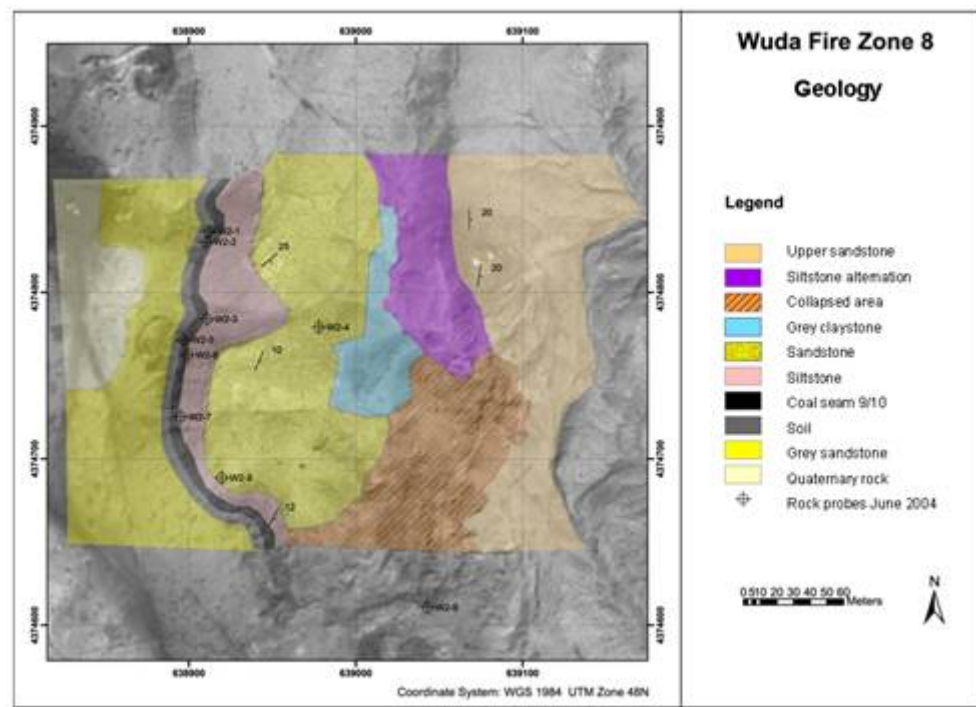


Figure 5: Geology of Fire Zone no. 8, superimposed a quickbird satellite image, after Gielisch & Kahlen (2003). Quickbird satellite image by DLR, 2003 (Gielisch & Kuenzer, 2003).



Innovative Technologies for Exploration, Extinction and Monitoring of Coal Fires in North China
Final Report Phase A Part B

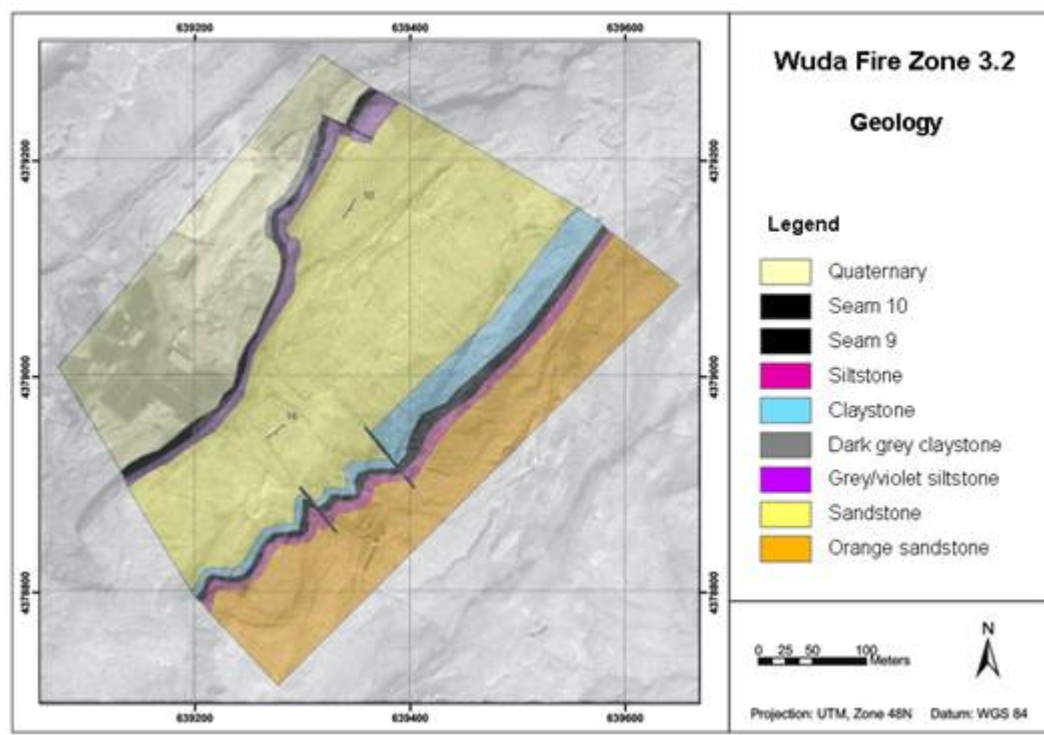


Figure 6: Geology of Fire Zone no. 3.2, superimposed a quickbird satellite image, after Gielisch & Kahlen (2003). Quickbird satellite image by DLR, 2003 (Gielisch & Kuenzer, 2003).

Figure 7 shows the hydrogeological map of the area of Wuda. It displays the potential groundwater deliverability for the investigated area. For more details see the report of Gielisch (2005).



Innovative Technologies for Exploration, Extinction and Monitoring of Coal Fires in North China
Final Report Phase A Part B

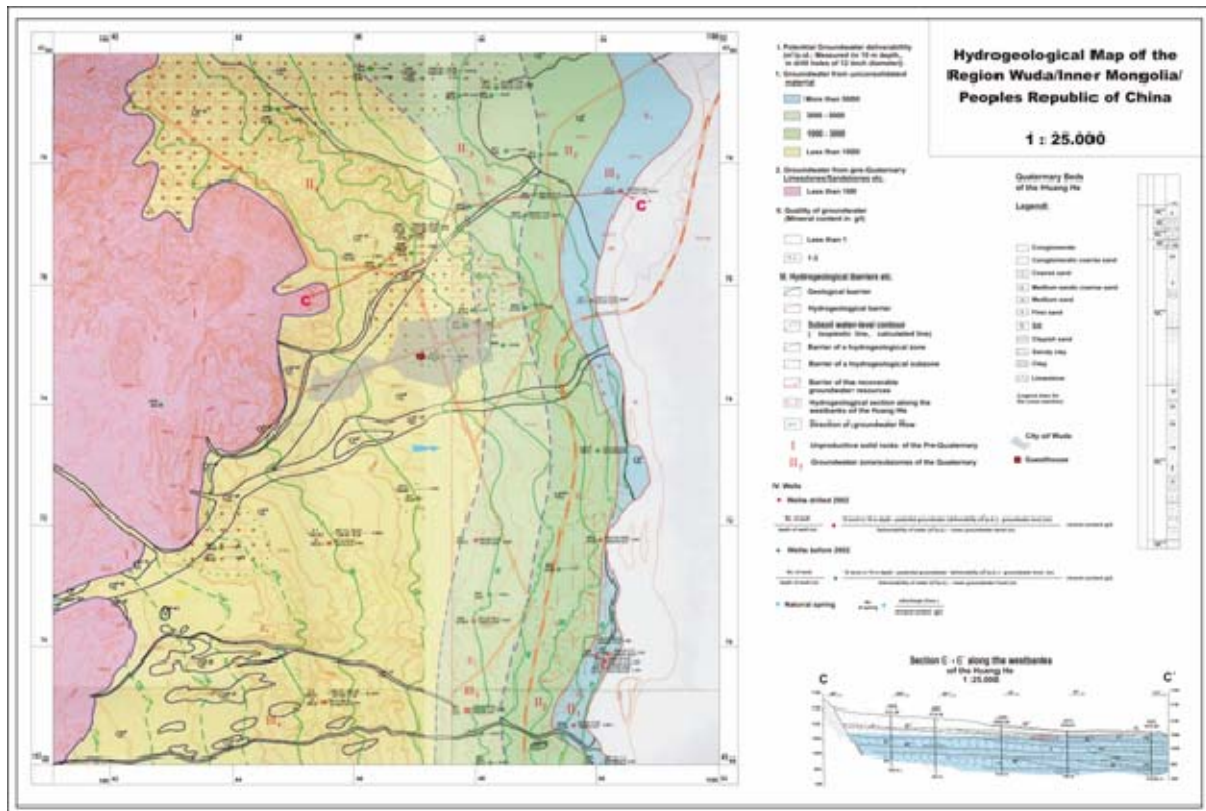


Figure 7: Hydrogeological map of the area of Wuda, Gielisch (2005). The course of the Yellow River is shown in the eastern part of the map.

2 Airborne survey

2.1 Survey over the entire Wuda Area

The China Aero Geophysical Survey & Remote Sensing Centre for Land and Resources (AGRS) performed the first helicopter-borne survey by Chinese Geophysicists in China. AGRS is a substitute of the Chinese Geological Survey (CGS) and thus the Ministry of Land and Resources. AGRS is a partner in the Sino-German Coal Fire Research Initiative and engaged in geophysical measurements together with its counterpart, the German Federal Institute for Geosciences and Natural Resources (BGR). The survey was flown from August 12th 2004 to September 6th 2004. It started from the airport of Wuhai; about 25 km north of the test area.

About 2575 line kilometres on 319 survey lines were flown with a single engine Squirrel helicopter hired by AGRS from a Chinese company. The spacing of the flight lines was 50 m and the spacing of the cross lines (tie lines) was 250 m. The size of the survey area is about 120 km². The survey area includes all known coal fire locations and for the first time complex airborne geophysical equipment has been used to verify the coal fire locations with helicopter-borne methods in China. A six-frequency coplanar/coaxial electromagnetic system built by AEROQUEST, Canada was used for the HEM measurements and a caesium sensor built by SCINTREX, Canada, was used for the total magnetic field measurements. The output sampling rate was 30 Hz resulting in about 1.2 m sampling distance for the electromagnetic



signals, and 10 Hz for the magnetic signal resulting in about 3.8 m sampling distance for an average flight velocity of 140 km/h.

Figure 8 shows a view from the helicopter over the survey area. In Fig. 9 a quickbird satellite image of the whole coal mining area of Wuda is shown (Gielisch & Kuenzer 2003). The bold solid red polygon marks the area of the helicopter survey. It extends about 8 km from west to east and about 15 km from north to south and covers the entire syncline of Wuda. Parts of the settlements of the city of Wuda are situated in the eastern part of the survey area. In the western and central part of the survey area spurs of the Gobi desert extend. The study areas from fire zones no. 3.2 and no. 8, which were investigated by ground geophysical surveys, are marked by bold red rectangles. The coal seam fire zones mapped by DLR in 2004 were outlined in blue (colder fires, mainly less than 150°C) and red (hotter fires, mainly more than 150°C) polygons, depending on the temperatures of the burning coal seams. Polygons were marked light blue for colder fires and violet for hotter fires mapped in 2005. Besides that at several fire zones single hot burning spots mapped in 2005 were marked by black dots. These polygons for 2004 and 2005 are also displayed on several thematic maps. Older polygons mapped in 2002 are generally marked by light green or dark green lines or by light black lines, mapped in 2003. The areas mapped as burning zones do not reflect the precise outline of the underground fires, they can only approximate the burning conditions underground (Kuenzer et al. 2006).



Figure 8: View from the helicopter over the survey area.

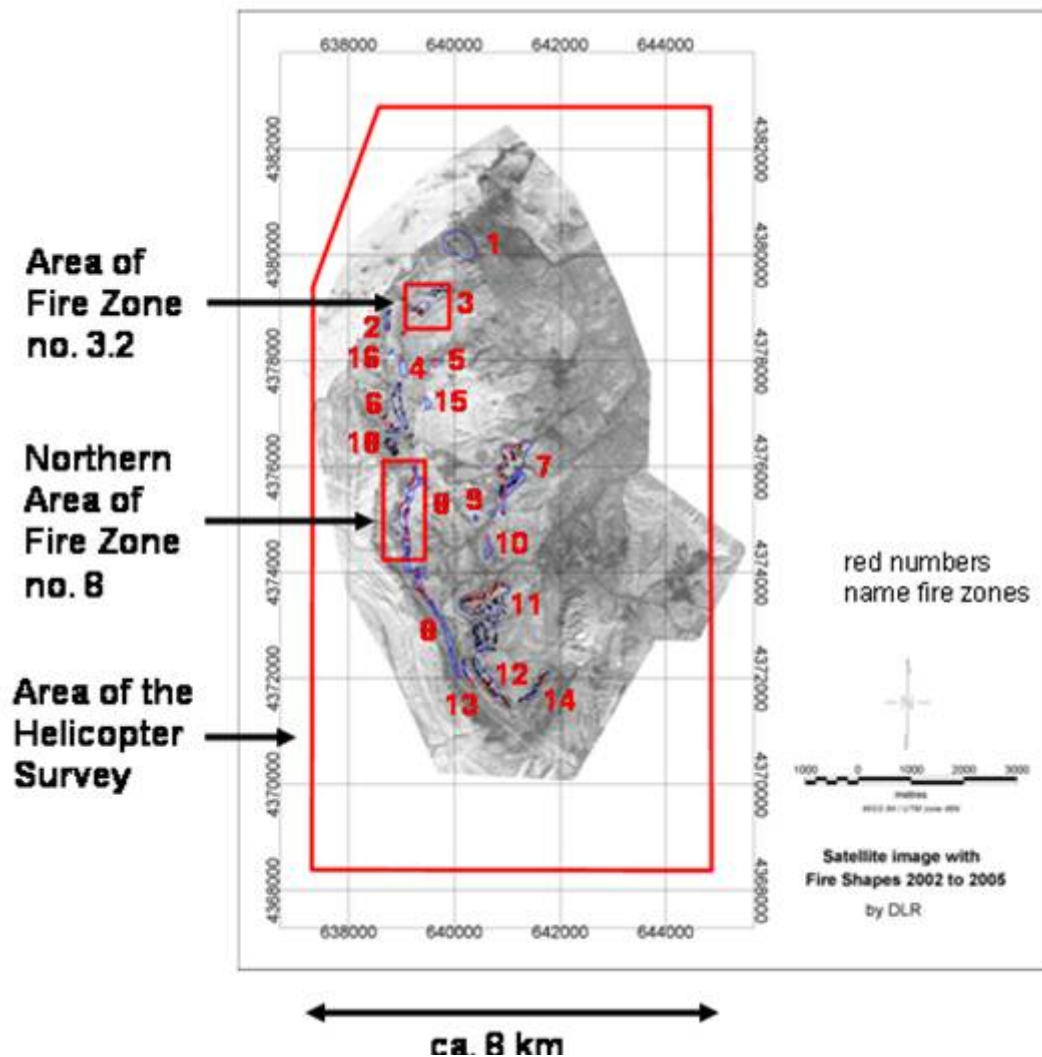


Figure 9: Quickbird satellite image (projection UTM 48 S / WGS84) of the coal mining area of Wuda in Inner Mongolia, Northern China by DLR (Gielisch & Kuenzer 2003). Bold solid red line outside the satellite image: helicopter survey area, bold solid red rectangles inside: areas of fire zones no. 8 and no. 3.2 (part of no. 3), light blue lines inside: areas of colder coal seam fires, light red lines inside: areas of hotter coal seam fires. Also numbers of further fire zones and mapped polygons from several years are given.

Survey Parameters

Tab 1: Survey parameters

Location:	west of the city of Wuda and 25 to 40 km south of the city of Wuhai
Size:	about 8 km in E-W direction and about 15 km in N-S direction
Number of profile lines:	289



**Innovative Technologies for Exploration, Extinction and Monitoring of Coal Fires in North China
Final Report Phase A Part B**

Separation of profile lines:	50 m
Length of profile lines:	about 8 km
Direction of profile lines:	E-W; W-E
Number of tie lines:	30
Separation of tie lines:	250 m
Length of tie lines:	about 15 km
Direction of tie lines:	N-S; S-N
Time period of survey flights:	August, 12th, 2004 – September, 6th, 2004
Number of survey flights:	25
Profile line km:	2125
Tie line km:	450
Total line km:	2575

The survey area includes all known coal fires in the area of Wuda. Base of the survey is the airport of Wuhai.

Besides the survey of the coal fire area of Wuda, where coal fires in the subsurface should be precisely located, it has been the goal of this project for AGRS to train the pilots from the China Flying Dragoon Company as well as the scientists and engineers from AGRS in handling such an aero geophysical helicopter survey. Therefore, the whole operation was accompanied by two German experts from BGR who supported the AGRS team during the survey, checked the results of the flights and processed, together with the expert from AGRS, the data. As a result preliminary resistivity maps of the survey area could be made available at the end of the survey.

As survey base the airport of Wuhai was used. The survey area itself, situated at about 1100 m a.s.l. (above sea level) and with its southern boundary about 40 km south of the airport, is hilly with very sparse vegetation. Without the great number of small and medium power lines which are all over the area, the survey flights would have been more easy. In addition, these power lines produce a lot of noise especially in the lowest frequency of the coplanar coil system of the HEM system. Besides that the data were harmed by atmospheric noise (sferics). Electrical discharges of the atmosphere influenced the HEM system mainly in the afternoon.



Sometimes the noise, caused by these sferics especially in the coaxial coil system, was too high for a successful survey flight. Many flights suffered under these influences and led to very noisy data sets.

2.2 Geophysical equipment

In Fig. 10 a principle scheme of the airborne electromagnetic and magnetic measurements is shown.

The airborne geophysical equipment carried by a Squirrel helicopter, type 350 B2 (Fig. 11), consists of the following instruments:

- six-frequency electromagnetic system
- magnetometer
- data acquisition system
- analog chart recorder
- power distribution box
- radar altimeter
- barometric altimeter
- navigation system with a GPS/GLONASS receiver

Electromagnetic system

An IMPULSE 2 Electro Magnetic system developed by Aeroquest, Canada, was used for this survey. A towed “bird” with a length of 7.62 m (excluding the end caps) and a diameter of 0.76 m contains two different coil systems each operating at three different frequencies. The coil axis of the COAXIAL system is horizontal and parallel to the bird axis, the coil axis of the COPLANAR system is vertical orientated.

The signals picked up by the receiver coils are converted to inphase and quadrature phase components for each of the six frequencies (referred to the transmitted signal), digitized and transmitted to the data acquisition system in binary form 30 times per second.

Frequencies and deflection of coils

Coaxial system	Frequency	Coil deflection
F1	870 Hz	50 ppm
F2	4350 Hz	50 ppm
F3	21750 Hz	50 ppm
Coplanar system		
F4	930 Hz	100 ppm
F5	4650 Hz	100 ppm
F6	23250 Hz	100 ppm



Cable length between helicopter and “bird”: 30 m

Distance between receiver coil and transmitter coil (for both coil systems): 6.5 m

Magnetometer

The magnetometer sensor, a CS-3 Caesium sensor manufactured by Scintrex, Canada, has been installed at the rear end of the “bird”. The output signal of the sensor is the Larmor frequency which is proportional to the field strength of the total magnetic field. The frequency of the Larmor signal is determined by a counter, converted to nano-Tesla [nT], the unit of the magnetic field strength, and 10 times per second transmitted to the data acquisition system.

Navigation system

The navigation system, developed by AGRS, China, uses an Ashtech GG24 GPS/GLONASS receiver which simultaneously receives the information of the American GPS and the Russian GLONASS navigation satellites. It calculates the actual position of the helicopter as well as the other data required by the navigation system to give the pilot all the information needed to fly a survey line as exact as possible. Besides the position data together with the GPS time are transmitted once per second to the data acquisition system. The horizontal position error of the GPS/GLONASS receiver should be less than 10 m, provided that enough Russian satellites are available.

Radar altimeter

The radar altimeter is part of the helicopter equipment (not of the geophysical equipment). It is a French altimeter (type: AHV-8) with an analogue output signal.

Barometric altimeter

The barometric altimeter is a Rosemount altimeter, type 1241 B, with an analogue output signal. It is also part of the helicopter equipment.

Data acquisition system

The data acquisition system DS-3 is a computer based system, developed by AGRS, China. Analog signals from the radar and barometric altimeter are digitized and, together with the digital data from the HEM, the magnetometer, the GPS and the internal clock of the DS-3, once per second formed to data blocks. At the end of a survey flight the stored survey data are transferred to a memory stick by the operator.

Base station

A Helium magnetometer was used as a base station magnetometer which has been developed and manufactured by AGRS. The magnetometer data are recorded on an analogue chart recorder as well as once per second in digital form on a DS-3 data acquisition system together with the internal time of the DS-3.

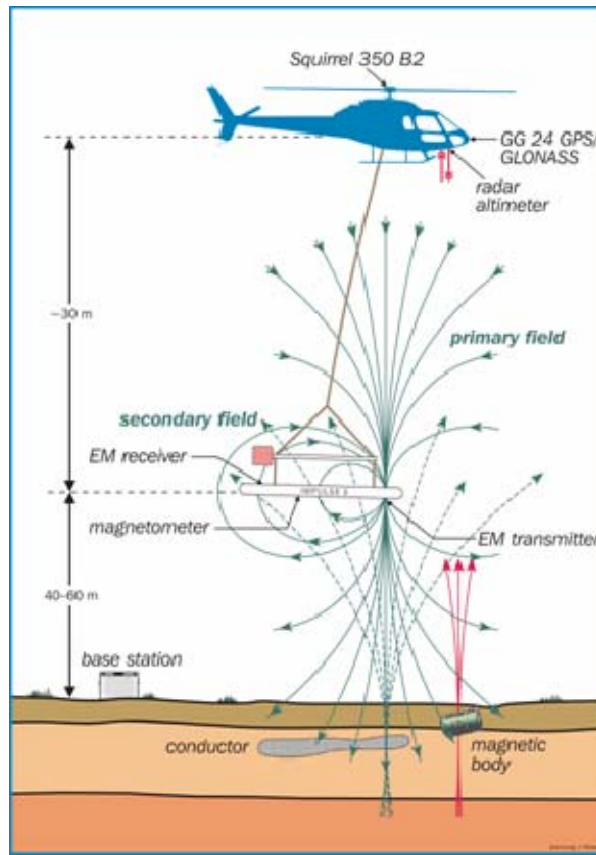


Figure 10: Principle of the airborne electromagnetic and magnetic survey system.



Figure 11: Helicopter at the airport of Wuhai.

2.3 Data Processing

Data processing was carried out using the Geosoft OASIS montaj software (Valleau 2000, Whitehead 2002). The flight data, mainly ASCII, binary and BCD coded, sampled by the



**Innovative Technologies for Exploration, Extinction and Monitoring of Coal Fires in North China
Final Report Phase A Part B**

Data Acquisition System (DAS) were transferred to a USB memory stick, and were finally copied to an ASCII file ready for use with Geosoft Oasis montaj.

Data Format

The digital data of a survey flight were processed by an AGRS-own programme to be compatible with the Geosoft data format. These ASCII data handed over to the German side have the following format:

Tab 2: Data Format

Fid:	numbering of each data block, starting with 0 (once per second)
Date:	date of the flight (ymmdd / once per second)
Time:	internal time (hh:mm:ss,ss / once per second)
Line:	line number (xxxx / once per second)
GPSTime:	time of the GPS system, converted to seconds, starting with 0 seconds at 00:00:00 (sssss:ss / once per second)
GPS_lat:	xx.xxxxxx (once per second)
GPS_lon:	xxx.xxxxxx (once per second)
HDOP:	quality factor of GPS (xxx / once per second)
GPS_ALT:	GPS-altitude in m (xxxx.xxxx / once per second)
GPS_ERR:	±xx.xxx (once per second)
Baro:	barometric altitude in m (xxxx / once per second)
Mag:	value of the total magnetic field in nT (mmmmm.mmmm / 10 times per second)
AI1-3	12 channels with electromagnetic information in ppm (parts per million)
AQ1-3	A = coaxial coil configuration, P = coplanar coil configuration
PI1-3	I = inphase, Q = quadrature phase
PQ1-3	1 = low, 2 = medium, 3 = high frequency (xxxx.xxx / 30 times per second)

The main tasks of data processing and data analysis can be briefly summarized as follows:

a) Data processing:

- Input of the acquired data to the Geosoft programme.
- Flight by flight processing and creation of a flight data base for more detailed processing.



**Innovative Technologies for Exploration, Extinction and Monitoring of Coal Fires in North China
Final Report Phase A Part B**

- Linear interpolation of all channels that need to be interpolated because of the different sampling rates in these channels.
- Remove non-geological noise from the raw data using appropriate filters.
- Apply drift corrections (picking of zero levels at high altitude flight segments). Remove system and instrumentation drift from all EM channels.
- Mag: Calculation of IGRF (International Geomagnetic Reference Field).
- Splitting the flight data piecewise into survey lines, clipping the high flight segments and the data acquired while travelling into the survey area and during the return to the airport.

b) Data analysis:

- Calculation of the apparent resistivity ($R_{\rho a}$) and calculation of the apparent depth below ground level (d_a) for each frequency
- choose anomalies for conductive target body location.
- investigate anomaly targets – may require apparent conductance and depth to conductors.
- Presentation of results and reports; various combination of:
 - Standard maps – like survey line map etc.;
 - Apparent resistivity and depth maps;
 - Profile maps of in-phase and out-of-phase, resistivity, depth, etc.;
 - Detailed multi channel profile plots for each survey line;
 - Vertical resistivity distribution (VRD) plots for each survey line;
 - Horizontal resistivity maps for selected depth below surface or sea level;
 - HEM anomaly report;
 - dT (anomalies of the total magnetic field) map;
 - Calculation of derivatives of dT in any possible direction;
 - Analytic gradient calculation along profiles and from the dT grid;
 - MAG anomaly report;
 - Combine HEM and MAG data with Remote Sensing imagery.
 - Combine HEM and MAG with Geological maps.
 - Combine HEM and MAG with Topographic maps.

General considerations about data processing and data base creation

After the main processing of each survey flight had been finished and the amount of all flight data had been reduced to profile data, the profiles were copied to a subset database receiving only the data along profiles according to the coordinate setup of the pre-defined survey area. A polygon file is used to keep the data inside the survey area. All other data outside the



survey area were clipped. Later, this subset data base has been copied to a final survey data base containing all pre-processed profiles of all flights within the survey area.

HEM Processing Details

A flight by flight processing followed immediately after the return of the helicopter from a survey flight using a field processing station (Laptop) at Wuhai airport. The main purpose was to inspect the digital data verifying the quality and the formal correctness of the data before the start of the next flight. The results were discussed with the flight operator and the geophysical team mainly to adjust (if necessary) the tasks of the operator during the survey flights.

A copy of the digital data was transferred to the BGR working group immediately after the flights for further processing. The processing was done separately from both groups using their own version of GEOSOFT Oasis montaj. It includes the helicopter electromagnetic extension tools namely HEMRES1 and HEMRES2 (Cheeseman 1988). HEMRES is the abbreviation for Helicopter based Electromagnetic Resistivity calculation, HEMRES1 is using a pseudo-layer resistivity (Fraser 1978) algorithm and HEMRES2 is using the amplitude-altitude approach. Both methods are used for the inversion of inphase and out-of-phase (quadrature) data to calculate the resistivities and depth below the bird. Several other tools for filtering the data or for picking of zero levels are integrated.

The main tasks of processing the HEM data require the following steps:

1. Input the survey data to the appropriate software programme.
2. Inspect the data by visualizing all channels.
3. Interpolate the data to receive the same amount of data in all channels according to the sampling rate of the HEM channels. The HEM channels are recorded 30 times per second, the MAG channel is recorded 10 times per second and the GPS altitude and other channels are recorded only once a second. The missing values between the outputs records have to be interpolated.
4. Calculate a set of new x, y coordinates from the WGS84 Latitude/Longitude values recorded with the GPS navigation system during the survey flights. The new coordinates are transformed to the Chinese Datum (Beijing 1954) using the Krassowski ellipsoid and Geoid constants from 1940, followed by a local datum shift. The new x, y coordinates are comparable with the coordinate system grid mapped onto the actual topographic maps in China.
5. Calculate a set of new WGS84 coordinates from the WGS84 Latitude/Longitude values using WGS84 ellipsoid Geoid constants followed by a datum transformation using UTM zone 48N. This new set of x, y coordinates is compatible with available remote sensing data. Landsat TM data of the Wuda area are available to the project and maps comparing airborne geophysical results with the remote sensing data are produced during the course of this survey. (In this study only WGS84 coordinates related to the WGS84 datum are used to produce the thematic maps.)
6. De-spike the altitude channels including radar altitude, barometric altitude and GPS altitude. Due to sampling errors in the data acquisition system these channels



sometimes are inferred by spikes which can be easily visualized in the digital data and which have to be removed before further processing.

7. Calculate the bird altitude channel from the radar altimeter value subtracting the length of the tow cable of the bird. Tow cable length is assumed to be 30 m overall (pers. communication, Mr. Wang, AGRS) and this value was subtracted from the radar altimeter channel. The bird altitude channel is used for the calculation of resistivity and depth values in one of the following steps of the processing sequence.
8. Carefully filter the in-phase and out-of-phase (quadrature) data channels mainly to de-noise the channels to clean them from non-geological noise. In the first step a non-linear filter is used to de-spike the data from so called sferics (atmospheric disturbances in the air); which usually influences the coaxial data; but frequently the coplanar data were influenced by sferics as well.
In the next step a low-pass filter is used to smooth the data. The cut-off value and the length of the filter window are set by the data processing engineer or geophysicist according to the amount of sferics and other noise in the specific channel of interest. In this study a nonlinear filter was applied to all EM channels to remove spikes. This was followed by a low-pass filter. Examination of the filtered data against the original deemed satisfactory and the power-line noise and the influence of sferics were significantly removed.
9. Zero-level picking is performed in the high flight segments of the survey flights. High flight segments are also used for the internal calibration of the electromagnetic system. International standard is to have a minimum of three or more intervals at each flight, one before the beginning of the survey profiles, one or more during the survey flight and one at the end after the last survey line has been completed on the way back to the airport. The flight altitude of these segments should be higher than 400 m above ground to avoid any influence of the subsurface especially in areas with low resistivities. Only at this altitude the amplitudes of the in-phase and out-of-phase channels are assumed to be very small – at least they should have a value close to zero ppm. Most of the time the survey altitude in high flight segments was higher than 400 m according to the standard procedures mentioned above. But, especially in the beginning of the survey period the high flight altitude was sometimes less than 400 m and zero level picking was difficult.

Due to temperature effects cool air in the high flight segments cools the electronic system and strongly affects the in-phase and quadrature values. Again the system is affected while moving into the survey area reducing the altitude of the helicopter. Especially the coaxial component of flight seven shows a non-linear drift from the beginning to the end of the flight which has to be removed by data processing. As known from our experience, usually in the beginning of the flight the drift changes dramatically and decreases less dramatically during the duration of the flight. To remove the dramatic change of EM data due to drift problems in the beginning of a survey flight, a high flight segment after the first or second survey profile is recommended acting as an “early” zero level picking point. At this point the amplitudes are set to zero. From now on, the drift changes are commonly smooth compared to the start of the flight and can be removed more easily from the last sentence of the survey data.



10. Adjust the level of the data according to the picked levels. This is done using a pick-up table created in the processing step described above. The author prefers to have two pick-up tables, one for the coaxial, one for the coplanar amplitudes, mainly to set the pick-up point for the two coil systems very precisely.
11. Calculate the resistivity and depth values for each frequency. Geosoft supports the user with two different methods to perform this specific task. One approach, the monogram approach, uses the coil separation, the survey frequencies and the coil geometry as input parameters and creates specific monograms of resistivity, conductivity and depth according to the system parameters. The generation of these monograms is based on a homogeneous half-space model. Input values are the in-phase and quadrature data, while apparent resistivity and apparent distance to the half-space are outputs. The second method uses the amplitude-altitude approach. EM signal amplitudes and bird altitude are the input, and the apparent resistivity is the output. No depth or distance information to the half-space is achieved with this method. For the calculation of the resistivities and depth values, presented in this report, the BGR own software was used which calculates apparent resistivities, apparent depths, and centroid depths. The apparent depth (d_a) is derived from the apparent distance (D_a) of the bird from the top of the conductive half-space minus the bird height (h). In addition, the centroid depth (z^*) values are obtained from $z^* = d_a - p_a/2$ (Sengpiel 1988, Siemon 2001), where $p_a = 505.3 (\text{Rho}_a/f)^{-1/2}$ is the apparent skin depth.
12. Clip the survey lines from the whole flight data. In the set-up phase of the Wuda survey AGRS has created a navigation map showing the nominal survey lines of the survey. The data of the navigation map were used to create a polygon file containing the surrounding points of the survey area. This file was used to clip all data outside the polygon remaining only the data inside the polygon which are the survey lines.
13. The final data base (reduced to survey lines for the specific flights of interest) was used to create a subset data base that was exported to a new GEOSOFT compatible xyz-data file acting as input for a survey profile data base containing all profiles of the survey.
14. of the HEM data and careful inspection of the resulting grids precedes the next step (which sometimes is leveling). Gridding was performed uniformly with a grid spacing of 25 m in the x and y direction for each channel. With the Geosoft software grids of Rho_{a1cp} , Rho_{a2cp} , Rho_{a3cp} , Rho_{a1cx} , Rho_{a2cx} and Rho_{a3cx} and the corresponding apparent depth d_{a1cp} , d_{a2cp} , d_{a3cp} , d_{a1cx} , d_{a2cx} and d_{a3cx} for the coplanar (index cp) and the coaxial (index cx) system were calculated. For creating the grids all profiles of the final data base were used, excluding the profiles which had been repeated due to significant noise or the influence of sferics during the course of this survey.
15. Apparent resistivities and centroid depths are displayed as images as mentioned above. Examples showing the resistivity distribution and the corresponding depths are presented in this report in chapter 3.
16. Microleveling of resistivity data for final grids can sometimes be successfully used for aesthetic purposes, but requires careful consideration because of the nonlinear relationship between the in-phase and out-of-phase channels and the calculated resistivities. Microleveling was applied in accordance with the specifications given in



Geosoft's Technical Note: Microleveling Using FFT Decorrugation. The paper defines: "microleveling" might be "filtering a gridded dataset to reduce or remove non-geological effects caused by long-wavelength noise along survey lines". Such noise manifests itself as apparent data shifts from one survey line to the next, often creating bust or streaky looking images. The OASIS montaj MAGMAP module was used to apply a decorrugation filter in the space domain to microlevel the HEM resistivity and depth values.

17. The final HEM data is inverted to layered half-space models using a Marquardt inversion procedure (Sengpiel & Siemon 2000).

The maps showing apparent resistivity and centroid depths for all three frequencies over the entire survey area (Chapter 3) were calculated by using a pseudo-layer half-space model (Siemon 2001).

MAG processing details

1. Despite the MAG channel. The caesium magnetometer used is sited in the rear of the electromagnetic sensor system and is very sensitive for shifts during survey flights. At the end of each line the helicopter turns to the next survey line and during this turn the signal of the magnetometer breaks down, accusing severe spikes in the digital channel.
2. Calculate the IGRF value for the specific date of the flight using the bird altitude, Latitude and Longitude values as input, receiving the IGRF value in [nT], declination and inclination values of the main magnetic field in the survey area in [°] as output. IGRF model coefficients for the year 2000, epoch 2004.x (x = date of the actual flight) were used to calculate the IGRF field value. A medium value of the IGRF for the survey area for August 22nd 2004 calculates to about 55363 nT.
3. Anomalies of the total magnetic field (dT) are finally received subtracting a) the IGRF values and b) the processed diurnal MAG values from the spike and noise free original MAG values.
4. Gridding and mapping has been performed using the same conditions as for the HEM grids and maps.
5. A grid trend removal technique was used to remove the magnetic gradient from the preliminary dT grid (Whitehead & Musselman 2002).
6. Microleveling technique was applied to remove line busts. BGR uses the MAGMAP FFT Decorrugation method provided by the OASIS software.
7. Several filters in the space domain were applied to the microleveled dT grid to calculate the derivatives in the x, y and z direction. Laplace filter techniques were used to calculate the 2nd vertical derivative of the preliminary TMI and the analytic signal and edge detection filters (like Sobel and Prewitt) were applied to support the interpretation.

2.4 Map Production and Results

From the finally processed data, several maps were produced. Map production was performed using the map plot facilities of Oasis montaj. Prior to plotting any map the channel displayed has to be gridded. The grids were produced using grid cell size dx/dy of 25 m in the x and y



direction. A cell size of 25 m was selected a) to receive maps with sufficient details and b) according to the flight line spacing of 50 m. The cell size of about half of the flight line spacing is a compromise between averaging along line and interpolation across line.

At the time of the survey a topographic map of the survey area was not available. A topographic map showing towns, roads, railway systems etc. in one layer together with the geophysical map on top as a second layer is very useful for the interpretation of anomalies caused by man-made installations.

No interpretation of the measurements with the coaxial coil configuration was carried out, because most of these data were very noisy. Only the coplanar data recorded at three frequencies were used for the interpretation (cf. chapter 3).

2.5 Digital Elevation Model

Digital Elevation Models (DEM) can be derived from difference of the GPS or barometric (BARO) elevation and the radar altitude of the helicopter. The main purpose of the DEM is to represent the topographic elevation in the survey area and it is useful for 3D visualisation of geophysical parameters, e.g. draping a measured channel over the 3D model.

$$\text{DEM_GPS [m a.m.s.l.]} = \text{GPS elevation [m a.m.s.l.]} - \text{radar altitude [m]}$$

$$\text{DEM_BARO [m a.m.s.l.]} = \text{BARO elevation [m a.m.s.l.]} - \text{radar altitude [m]}$$

The quality of the altitude data, with respect to the “real” elevation of the terrain in the survey area, mainly depends on the quality of the GPS, the barometric elevation and the radar altitude readings. AGRS is using an Ashtech GPS/GLONASS receiver for the GPS elevation measurements (GPS_Z). The instrument receives the signals from the American GPS and the Russian GLONASS satellites simultaneously. Former tests at BGR, using the same instrument, and at the airport at Wuhai have shown that the GPS elevation at ground significantly drifts with time and can vary about several tens of metres at the same point. The technical papers of the Ashtech instrument specify that the accuracy in the x, y coordinates is about ± 10 m in each direction from the original data point and the accuracy in GPS_Z may vary about three times the x, y resolution, so the accuracy in the z-component may be only about ± 30 m.

Reliable GPS_Z values may only be received using differential GPS (DGPS) instruments, like the DGPSmax© GPS receiver which enables on-line differential measurements of the x, y coordinates yielding also more precise z values of the aircraft above m.s.l.

A second argument related to the quality of the measurements of the GPS_Z is due to the sampling rate of this channel. During the survey the measurements were taken once per second. Assuming the survey speed of the helicopter ranges from 100 – 140 km/h, the distance between two measured points (i.e. the resolution on ground) for the sampling interval of 1/s is in the range of 28 – 39 m. The actual sampling rate therefore is probably insufficient to resolve many details at ground.

The barometric elevation is related to the barometric pressure at the day of the survey flight. Due to rapid changes of meteorological conditions affecting also the situation in the survey area, the air pressure varies significantly during the day and may also vary significantly during the duration of survey flights. Under these conditions the measurements of the barometric elevation are only “relative” elevation values and are without any relation to a



**Innovative Technologies for Exploration, Extinction and Monitoring of Coal Fires in North China
Final Report Phase A Part B**

known or constant base level elevation. The elevation values should be adjusted to a given or constant absolute elevation. As no base station pressure history records exist, the elevation of the airfield used for the survey has to be used to correct the barometric elevation measurements (Wuhai airport is about 1102 m a.s.l.).

For this, the reading of the barometric value before the start to a survey flight and after landing is necessary and should be noticed on the operator's flight schedule. Both readings represent the given elevation of 1102 m at Wuhai airport related to the actual air pressure before and after the flight and the difference of the readings can be used to correct the barometric altitude measurements received during the flight by linear interpolation.

The discussion about the sampling rate and the ground resolution are still valid for the barometric elevation.

Non-linear variations, particularly highs and lows, during a survey flight, however, are not recorded resulting in possibly inaccurate barometric values.

From the view of data processing it is strongly recommended to adjust the sampling rate to at least 5 or 10 or even more readings per second for the analogue signals like barometric and radar altitude. The AD converter as integrated part of the Data Acquisition System (DAS) used by AGRS should be checked or reconfigured according to these necessities.

A change of the sampling rate of the radar altimeter to at least 10 samplings per second meets the international standard and is recommended for the calculation of the important value "bird altitude".

$$\text{BIRD altitude} = \text{Radar altitude} - \text{Tow cable length (30 m)} \text{ [m a.g.l.]}$$

The value given in metres above ground level [m a.g.l.] is one of the actual input parameter for the resistivity and depth calculation with the HEMRES software mentioned earlier. The actual sampling rate of 1 reading per second is probably insufficient for precise calculations of resistivity and depth. The comment about ground resolution is also still valid for the radar altimeter.

Figure 12 shows the map of the topographic elevation (DEM) derived from the GPS_Z subtracting the altitude of the sensor above ground for the helicopter-borne survey over the entire Wuda area. The elevation is displayed with a colour shading effect from N-E. Clearly visible are the hills in the west, which bound the syncline and extend from north to south. In the east a flat area extends down to the Yellow River, which flows about 15 km east of the city of Wuda. Remarkable are also the big hills elevating in the south-east. They belong to the Ordovician strata.

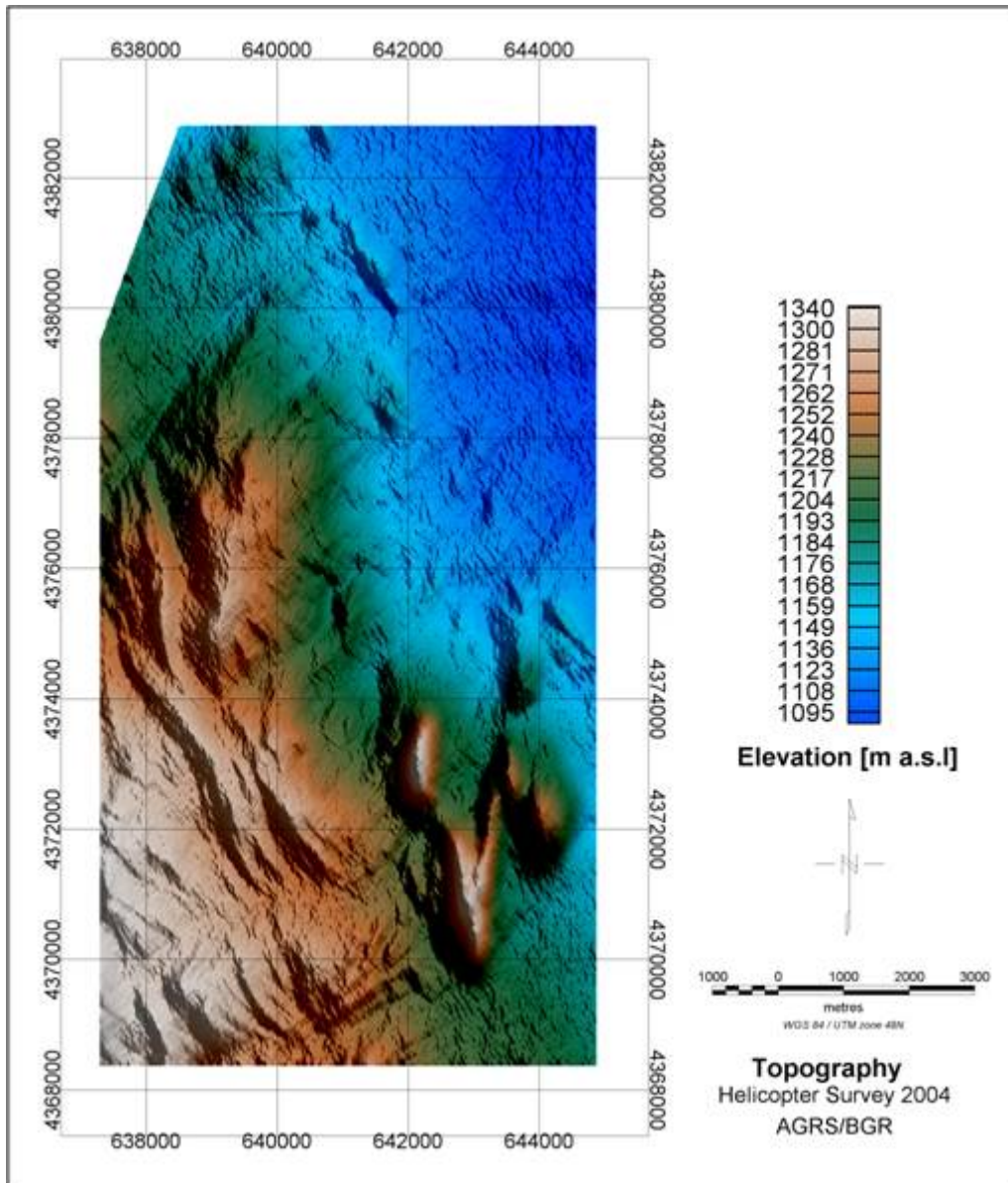


Figure 12: Digital elevation model derived from the helicopter survey over the Wuda area. Colour shading from N-E.

3 Results of the airborne electromagnetic survey

3.1 Results from the entire survey area

Apparent resistivities (R_{ho}) as well as centroid depth (z^*) values were calculated using a pseudo-layer half-space model (Siemon 2001). The following maps show these apparent resistivities and centroid depths for all three frequencies over the entire survey area. Every apparent resistivity value corresponds to a centroid depth value and both parameters should be considered together. The centroid depth is a measure for the centre of a homogeneous half-space model.



**Innovative Technologies for Exploration, Extinction and Monitoring of Coal Fires in North China
Final Report Phase A Part B**

For a better orientation on all apparent resistivity maps the shapes of the fire zones are shown. A comparison of the apparent resistivities for all three frequencies is done to point out results of interest. For all apparent resistivities the maps are shown with and without shading effects (from north-east, i.e. 45°) and the apparent resistivities are also displayed using different colour scales. This clarifies the representation and makes some special details more clearly visible. The second colour scale is mainly used for the presentation of the apparent resistivity maps of the fire zones selected. This colour scale emphasizes the places of higher conductivity and allows regarding the burning zones in more detail with a better resolution for the apparent resistivity. Sections of interest from the fire zones are shown below.

Figures 13 to 24 show apparent resistivities and centroid depths for all frequencies. Clearly mapped are the big hills of Ordovician strata in the south east at all three frequencies. They are highly resistive (500 Ohm*m and more) and the centroid depth is more than 120 m for the lowest frequency (Fig. 22 and 24).

The centre of the syncline with the Permian strata is also characterized by highly resistive strata, but not as resistive as the Ordovician hills. The apparent resistivities are in a medium range, about 100 to 250 Ohm*m, but some single sites with low apparent resistivities can be found. The centroid depth is in the range of 5 m to 190 m, depending on the frequency. In general the centroid depth of the highest frequency shows more details. Down to greater depths the area with these resistive strata becomes bigger. While at a frequency of 23250 Hz the area affected by coal seam fire at the southern end of the syncline corresponds very clearly to the resistive strata, the same area is more widened at the lower frequencies. Fire zones no. 7 and no. 11 are situated very close to the eastern resp. southern boundary of these Permian strata. This can be seen very well at all map sections for the apparent resistivity of fire zone no. 7 (Fig. 42-45).

East of the central part of the syncline the alluvial sediments covering the marine carbonates can be found in an area being flatter than the syncline itself. The alluvial sediments are characterized by an extended area of low apparent resistivity, mostly about 10 Ohm*m or below. The lower the frequency the smaller the areas with higher conductivities situated east of the syncline. That means that the portion of the alluvial sediments reduces with depths. At the frequencies 4650 Hz and 930 Hz a sharp boundary corresponding to the transition of the Permian strata and the alluvial sediments can be found on the centroid depth maps. The centroid depth in general in this part of the area ranges from 5 m to 50 m. Most parts of this area are covered by settlements which extend in northerly and easterly direction.

In the western part of the survey area the quicksands from the Gobi desert correlate with low apparent resistivities, but not as low as those of the alluvial sediments. They are in the range of 10 to 30 Ohm*m. At a frequency of 4650 Hz the boundary between the outcropping carboniferous strata within the syncline and the Gobi desert can be found very sharply shaped in the north west of fire zone no. 3.2. In the whole area west of the syncline low apparent resistivities occur. They restrict the centroid depth to a range of 10 m to 40 m. Clearly shown are also the hills which bound the western part of the syncline extending from north-westerly direction to the south-east. Along these hills the outcropping strata with several coal seams, e.g. coal seams no. 9 and no. 10, can be found. Fire zones no. 2, 18, 8, 13 and 12 are located along this structure. Fire zone no. 14 is situated at the eastern boundary in the southernmost part of the syncline.



**Innovative Technologies for Exploration, Extinction and Monitoring of Coal Fires in North China
Final Report Phase A Part B**

The apparent resistivities resp. centroid depths reveal the general geological structure at all three frequencies. Figures 15, 19 and 23 display the same apparent resistivity maps using another colour scale (3-150 Ohm*m instead of 1-1000 Ohm*m) to exaggerate the sites of lower apparent resistivities.

Many fire zones within the syncline correspond to spots of higher conductivity resp. lower apparent resistivity. Several sites with lower apparent resistivities can be found, a few of them correspond to the fire shapes mapped. Especially at fire zones no. 7 and no. 11, situated in the centre of the syncline, there are distinct spots of lower apparent resistivity fitting to the burning shapes mapped. These features at the selected sites appear on the apparent resistivity maps at every frequency. This can also be seen at fire zones no. 6, no. 8, no. 12 and no. 14, although not as clear as at the two fire zones mentioned above. These fire zones are situated in the western part of the syncline and need to be viewed in detail, see below.

There are a few features on the apparent resistivity maps which may be of anthropogenic origin or are caused by bad data quality. These features occur in the very south of the survey area, in the north-eastern part of the survey area and at a few spots west of the big hills in the south. They are visible best at the map of the centroid depth at a frequency of 930 Hz (Fig. 24). It has to be kept in mind that many factories, mining facilities and power lines are located within the survey area. Therefore every site of interest has to be investigated very carefully to select disturbing influences on the data.

For a general overview of many features of the survey area Fig. 25 shows the 930 Hz apparent resistivity map with a superimposed quickbird satellite map of the area. For better orientation the blue and red polygons which outline the mapped fire zones in 2004 and black dots showing single fire points in 2005 (by DLR) are shown. Sites from the TEM ground survey are marked by violet squares. The course of the Yellow River (light black lines) is roughly shown east of the map beyond the survey area. The fire zones no. 3.2 and no. 8 are marked by red rectangles.

Figure 25 resp. Fig. 22 and 23 showing the apparent resistivity for the lowest frequency together with hydrogeological map (Fig. 7) may suggest potential groundwater storing areas.



Innovative Technologies for Exploration, Extinction and Monitoring of Coal Fires in North China
Final Report Phase A Part B

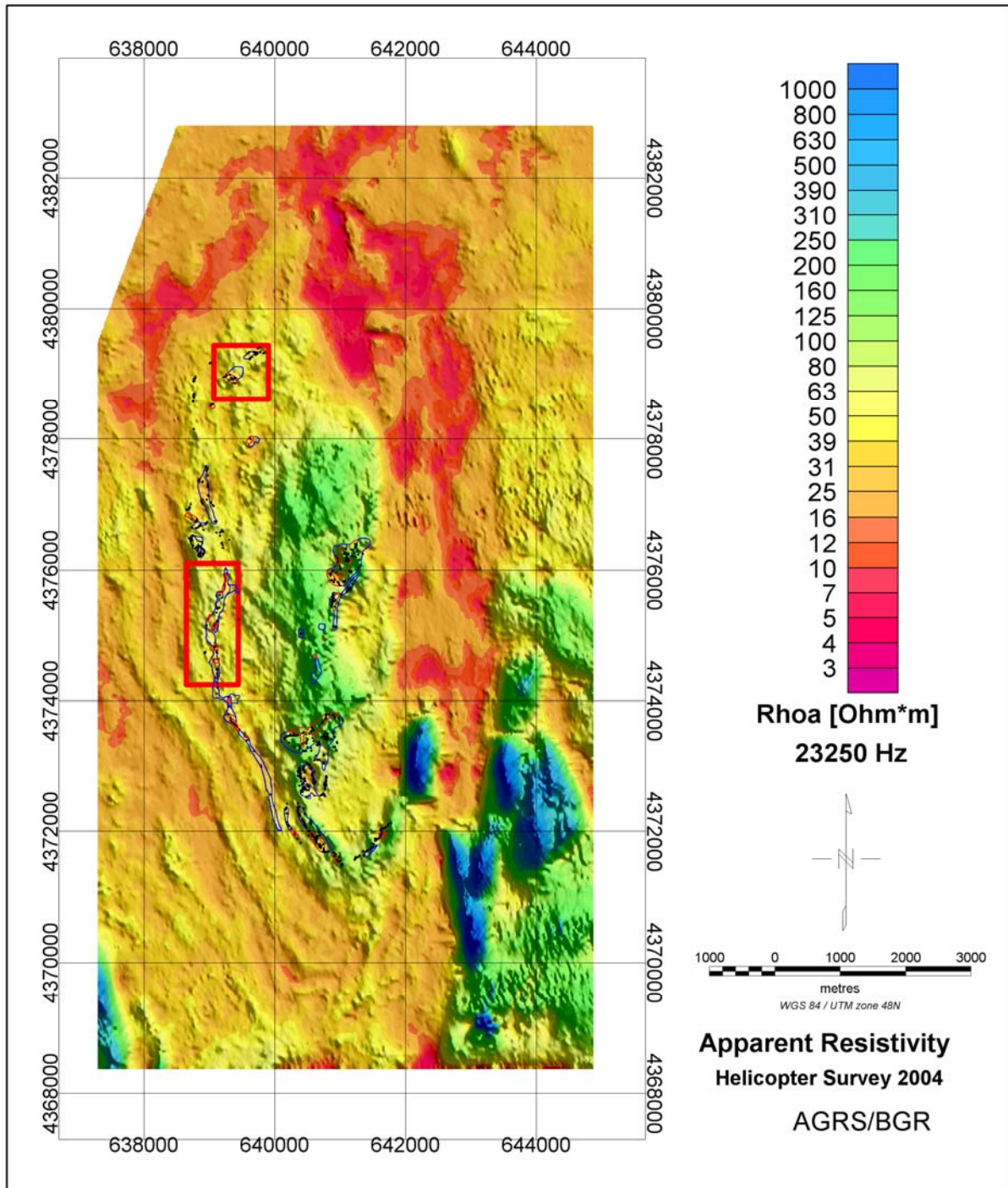


Figure 13: Map of the apparent resistivity Rho_a [Ohm*m] at a frequency of 23250 Hz, derived from the helicopter survey over the entire Wuda area. Blue and red polygons show fire zones mapped in 2004, the black dots show single fire points mapped in 2005 (by DLR). Fire zones no. 3.2 and no. 8 are marked by red rectangles. Colour shading from N-E.



Innovative Technologies for Exploration, Extinction and Monitoring of Coal Fires in North China
Final Report Phase A Part B

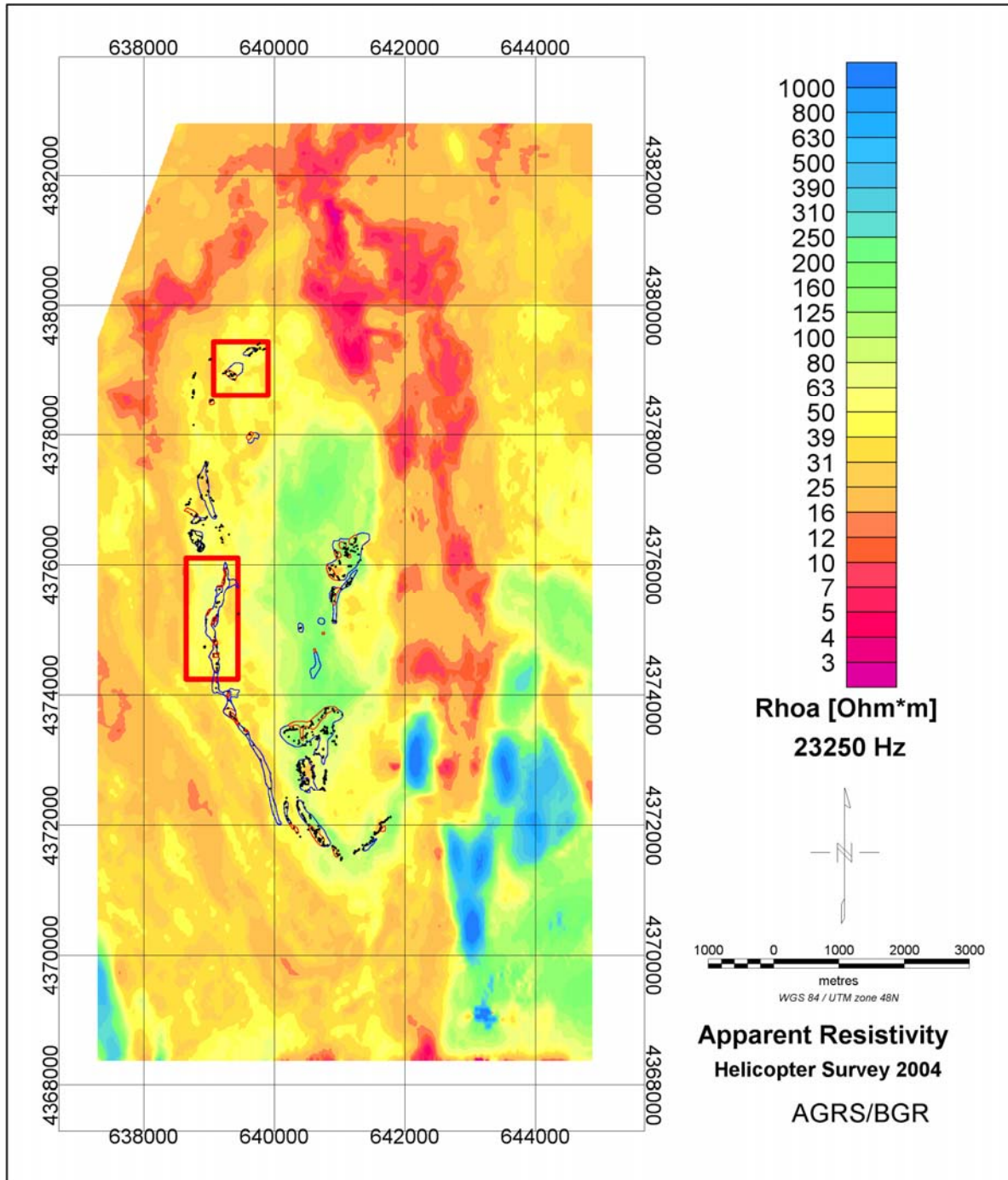


Figure 14: Map of the apparent resistivity Rho_a [Ohm*m] at a frequency of 23250 Hz, derived from the helicopter survey over the entire Wuda area. Blue and red polygons show fire zones mapped in 2004, the black dots show single fire points mapped in 2005 (by DLR). The colour scale is the same as in Fig. 13 but without shading. Fire zones no. 3.2 and no. 8 are marked by red rectangles.

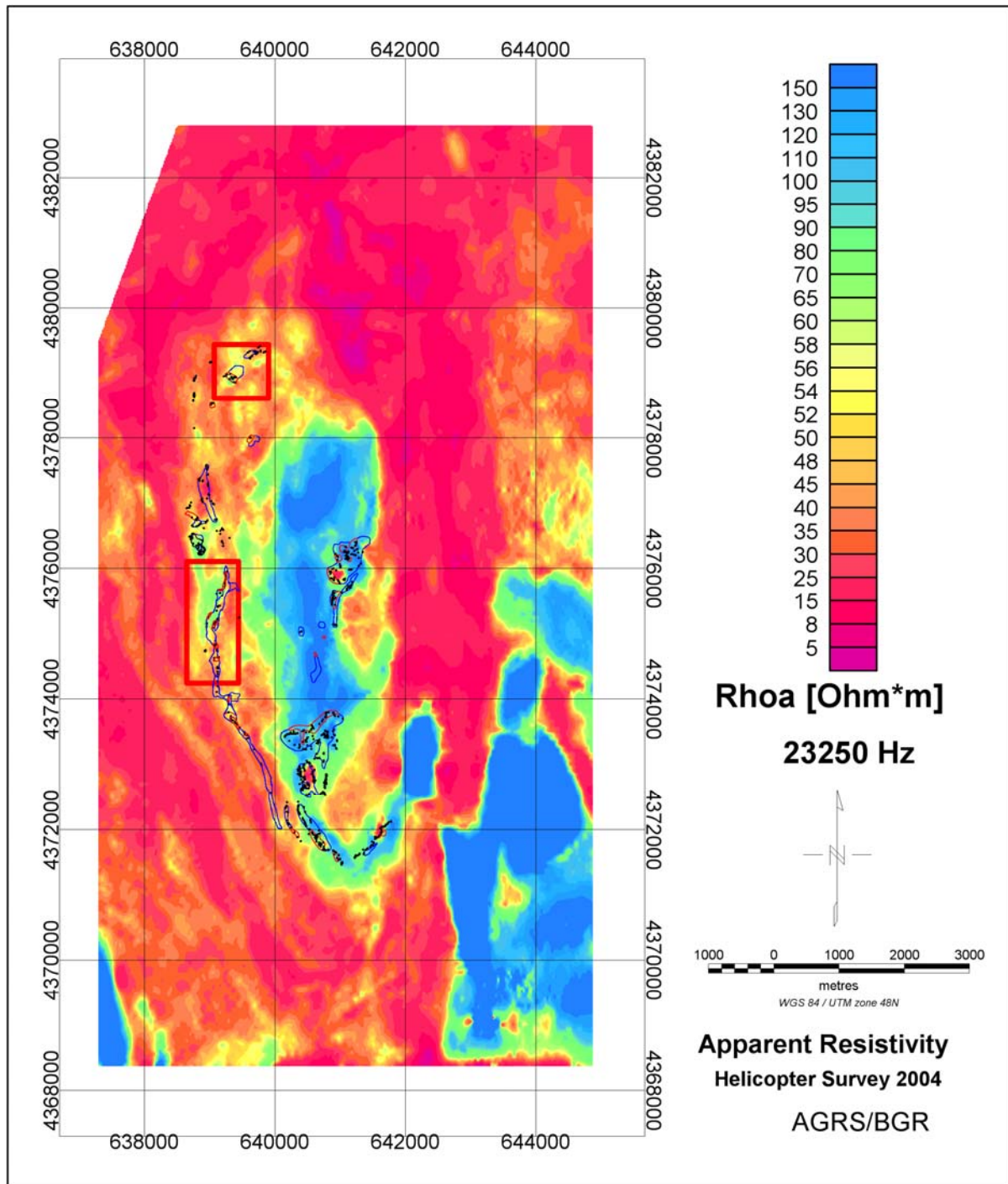


Figure 15: Map of the apparent resistivity Rhoa [Ohm*m] at a frequency of 23250 Hz, derived from the helicopter survey over the entire Wuda area. Blue and red polygons show fire zones mapped in 2004, the black dots show single fire points mapped in 2005 (by DLR). The map is the same as in Fig. 14 but another colour scale was used to emphasize the sites of lower apparent resistivity within the syncline. Fire zones no. 3.2 and no. 8 are marked by red rectangles.



Innovative Technologies for Exploration, Extinction and Monitoring of Coal Fires in North China
Final Report Phase A Part B

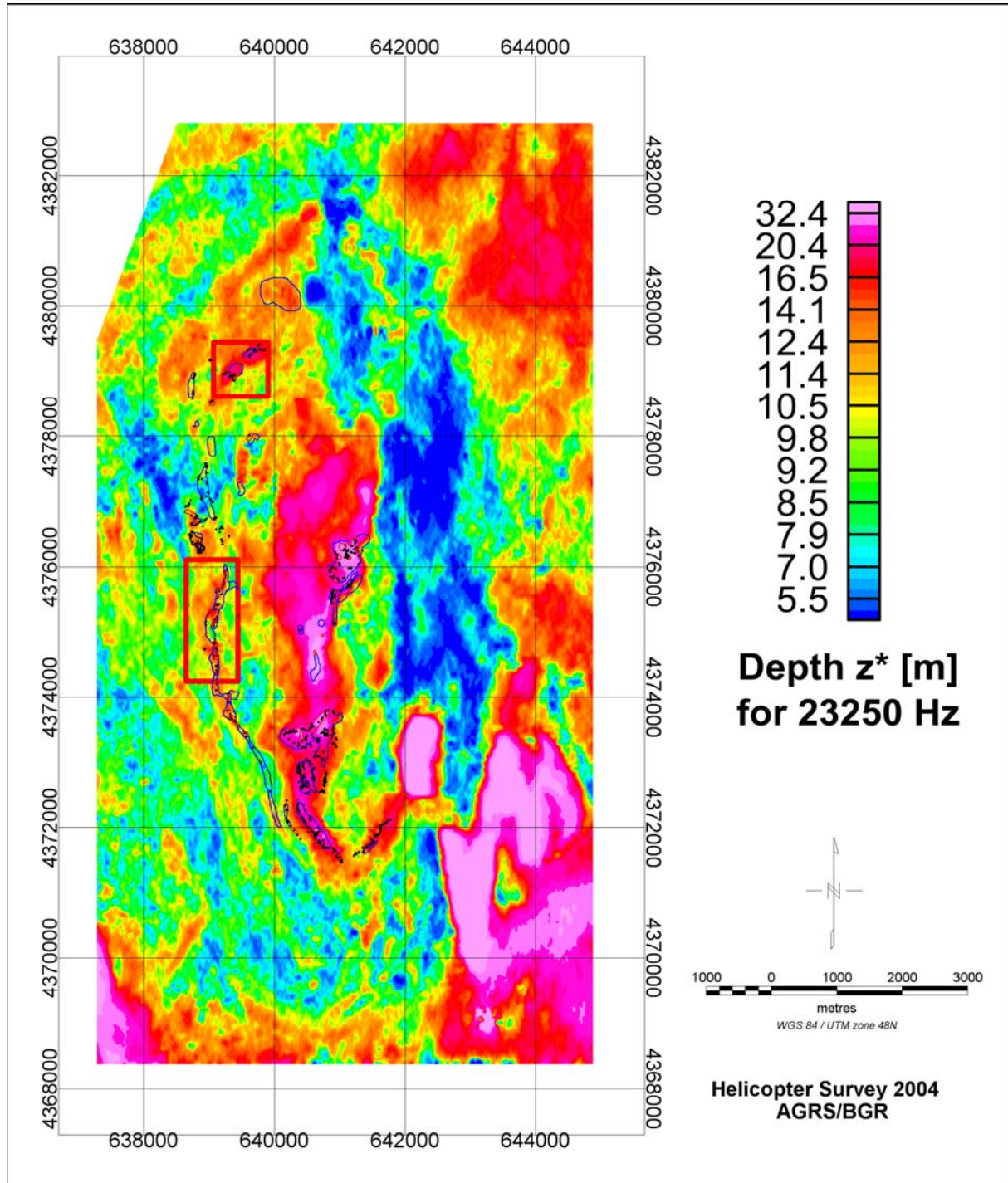


Figure 16: Map of the centroid depth at a frequency of 23250 Hz, derived from the helicopter survey over the entire Wuda area. Fire zones no. 3.2 and no. 8 are marked by red rectangles.



Innovative Technologies for Exploration, Extinction and Monitoring of Coal Fires in North China
Final Report Phase A Part B

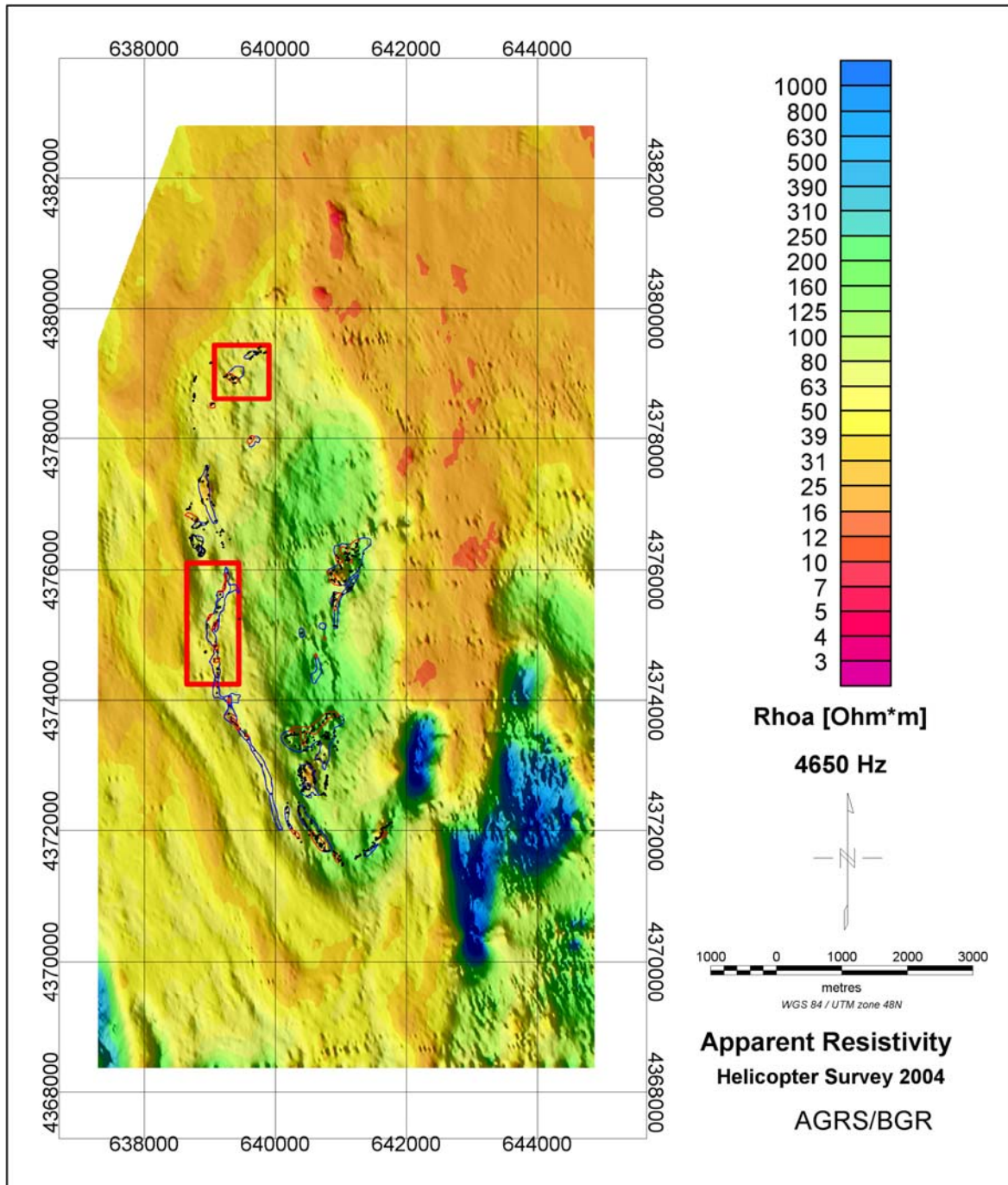


Figure 17: Map of the apparent resistivity Rhoa [Ohm*m] at a frequency of 4650 Hz, derived from the helicopter survey over the entire Wuda area. Blue and red polygons show fire zones mapped in 2004, the black dots show single fire points mapped in 2005 (by DLR). Colour shading from N-E. Fire zones no. 3.2 and no. 8 are marked by red rectangles.



Innovative Technologies for Exploration, Extinction and Monitoring of Coal Fires in North China
Final Report Phase A Part B

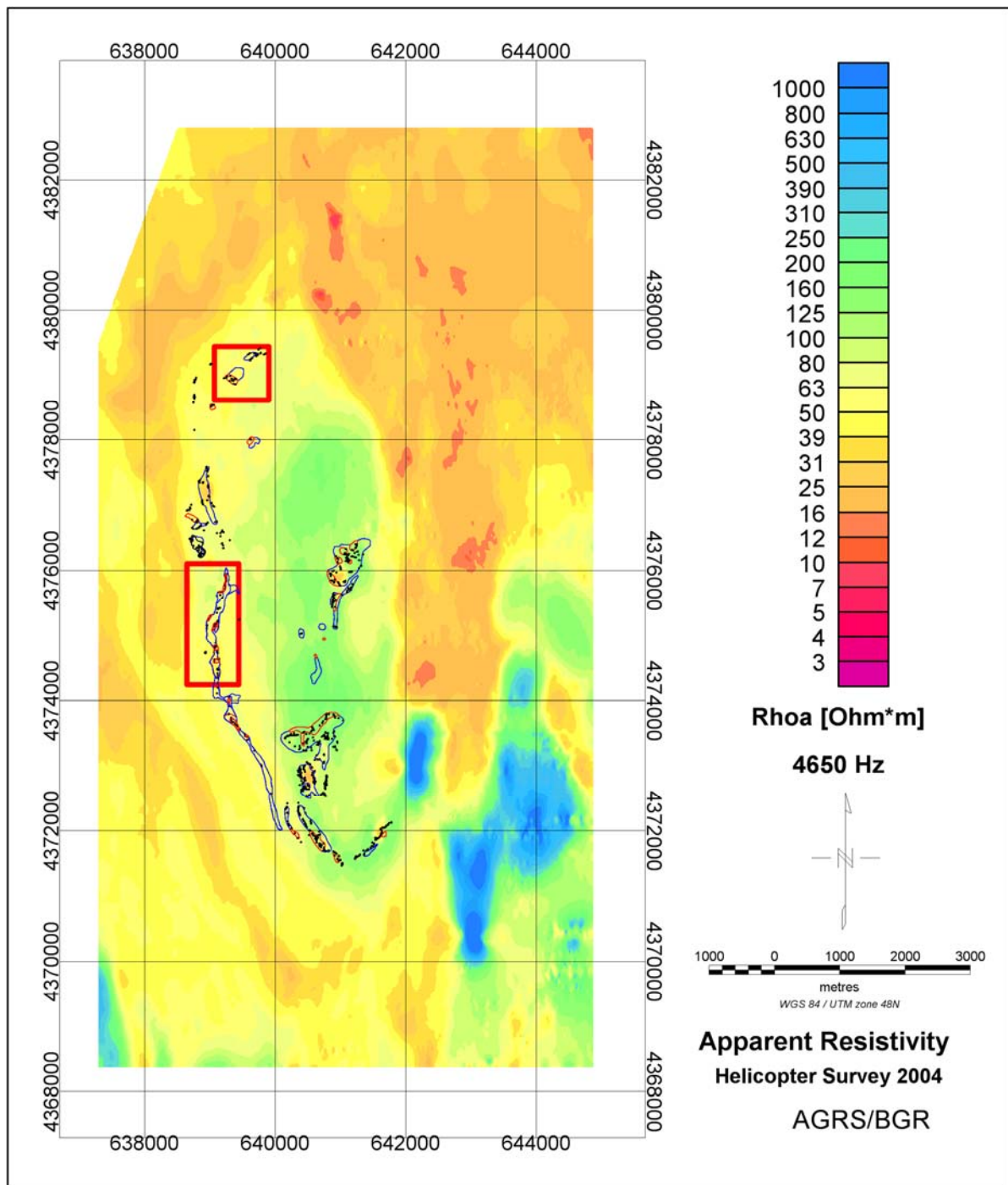


Figure 18: Map of the apparent resistivity Rhoa [Ohm*m] at a frequency of 4650 Hz, derived from the helicopter survey over the entire Wuda area. Blue and red polygons show fire zones mapped in 2004, the black dots show single fire points mapped in 2005 (by DLR). The colour bar is the same as in Fig. 17 but without shading. Fire zones no. 3.2 and no. 8 are marked by red rectangles.

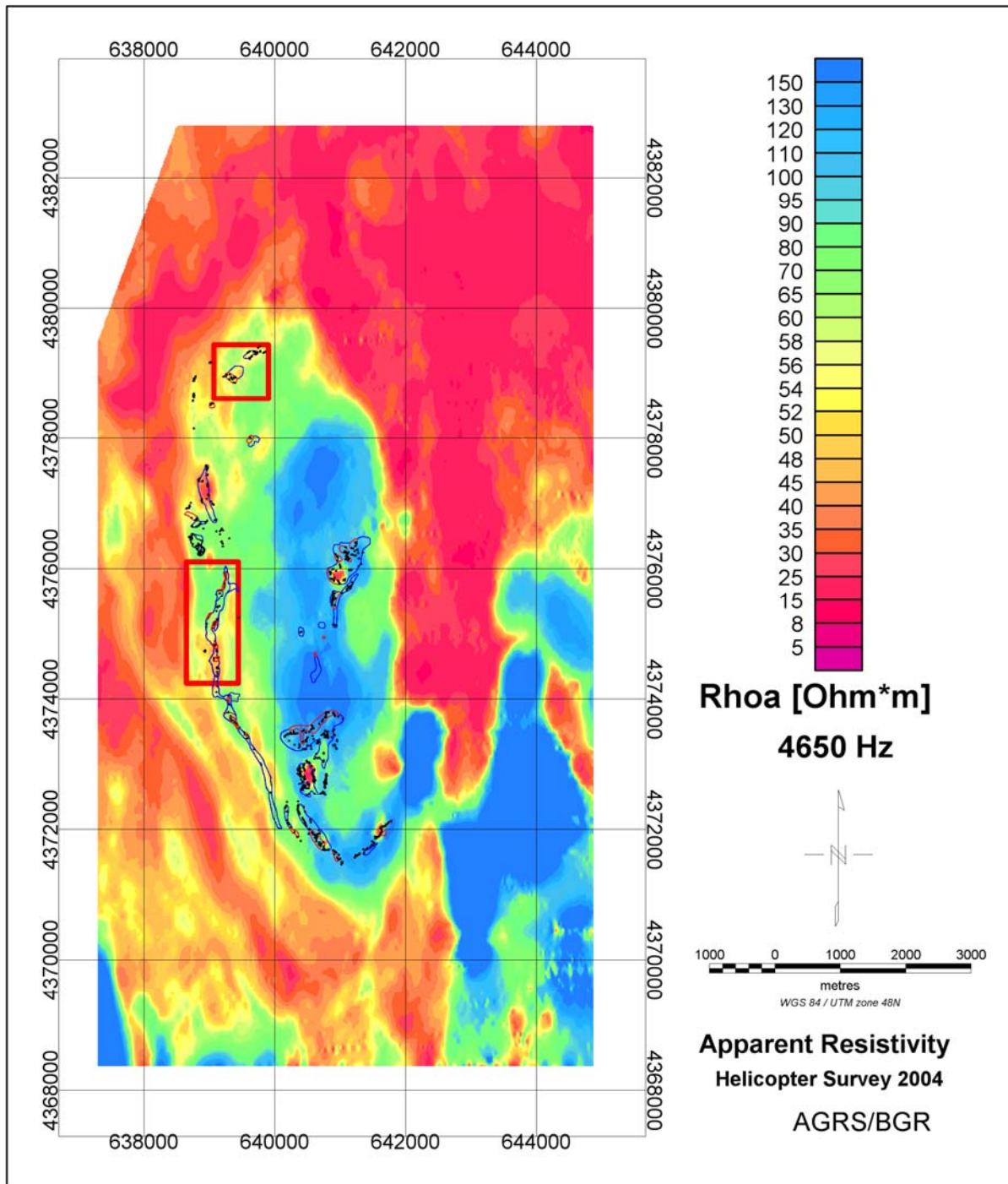


Figure 19: Map of the apparent resistivity Rho_a [Ohm*m] at a frequency of 4650 Hz, derived from the helicopter survey over the entire Wuda area. Blue and red polygons show fire zones mapped in 2004, the black dots show single fire points mapped in 2005 (by DLR). The map is the same as in Fig. 18 but another colour scale was used to emphasize the sites of lower apparent resistivity within the syncline. Fire zones no. 3.2 and no. 8 are marked by red rectangles.



Innovative Technologies for Exploration, Extinction and Monitoring of Coal Fires in North China
Final Report Phase A Part B

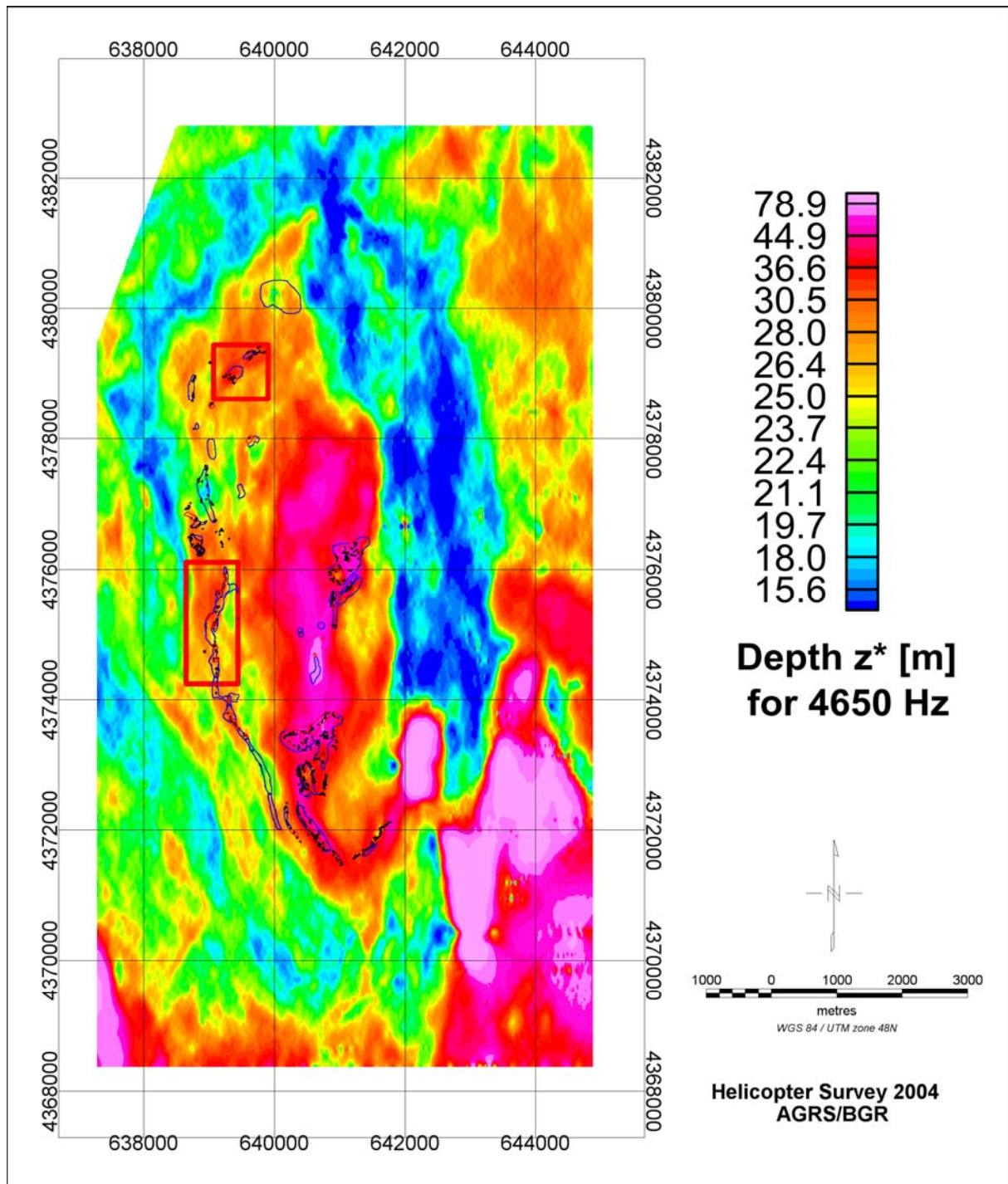


Figure 20: Map of the centroid depth at a frequency of 4650 Hz, derived from the helicopter survey over the entire Wuda area. Fire zones no. 3.2 and no. 8 are marked by red rectangles.



Innovative Technologies for Exploration, Extinction and Monitoring of Coal Fires in North China
Final Report Phase A Part B

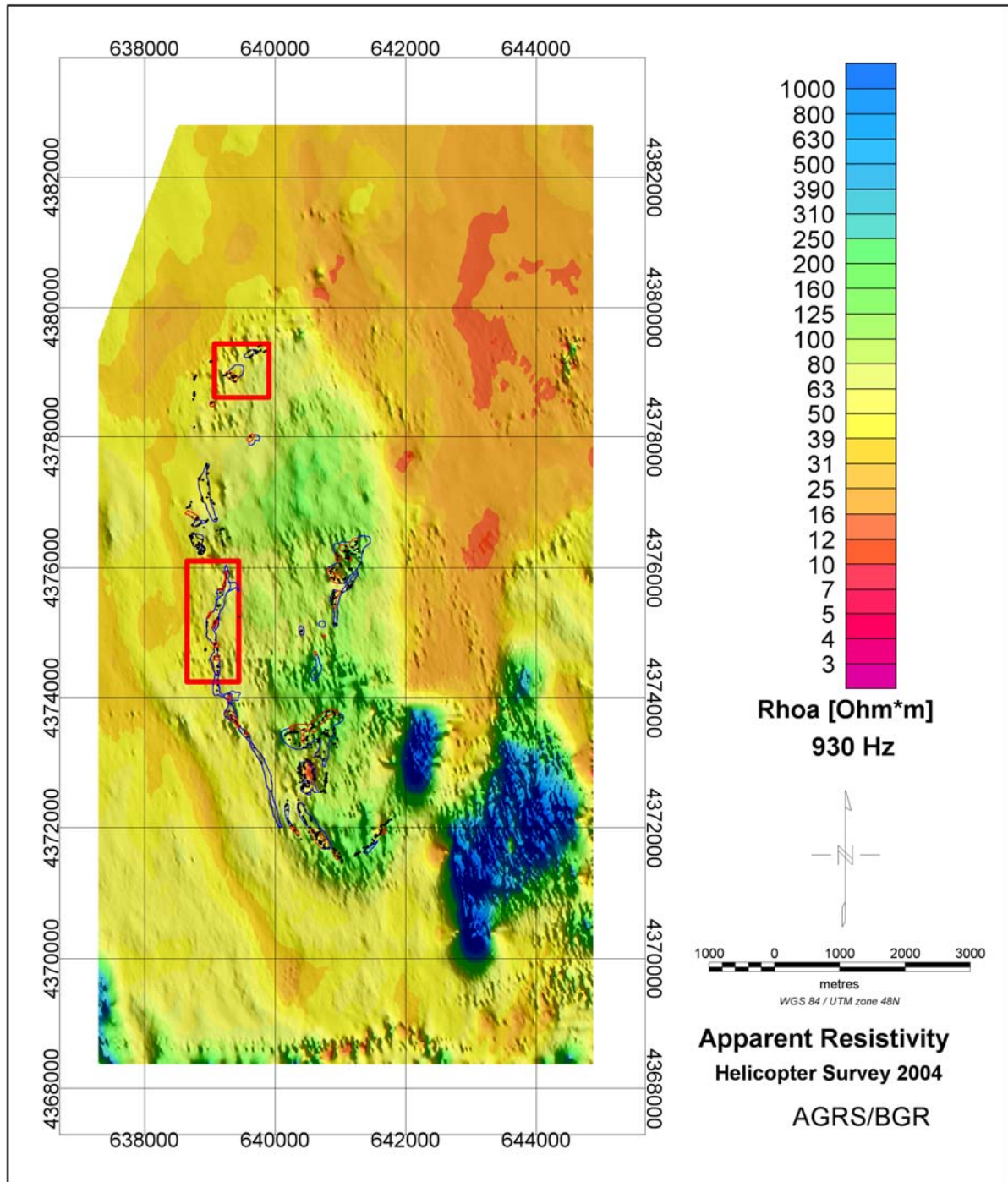


Figure 21: Map of the apparent resistivity Rho_a [Ohm*m] at a frequency of 930 Hz, derived from the helicopter survey over the entire Wuda area. Blue and red polygons show fire zones mapped in 2004, the black dots show single fire points mapped in 2005 (by DLR). Colour shading from N-E. Fire zones no. 3.2 and no. 8 are marked by red rectangles.



Innovative Technologies for Exploration, Extinction and Monitoring of Coal Fires in North China
Final Report Phase A Part B

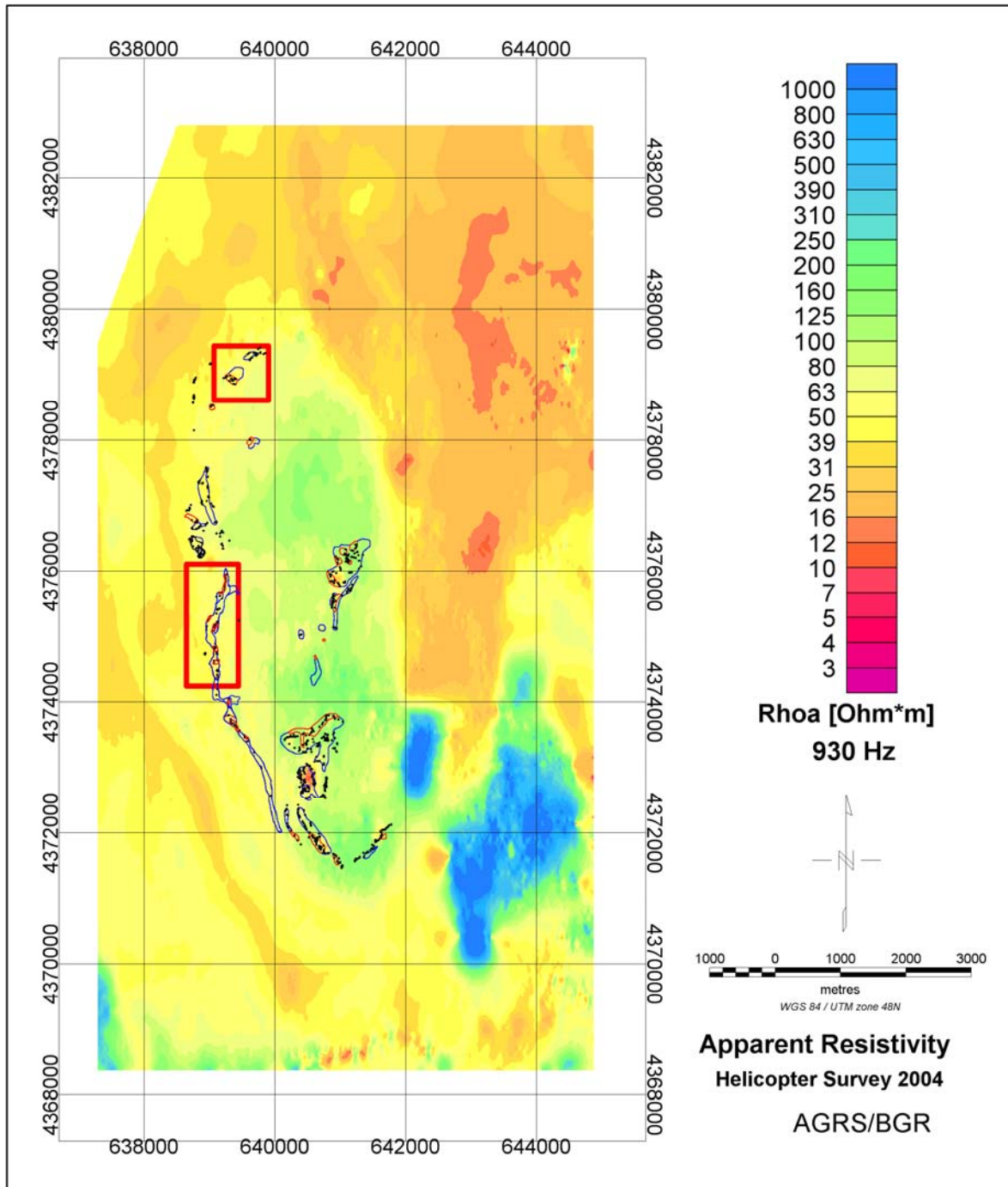


Figure 22: Map of the apparent resistivity Rhoa [Ohm*m] at a frequency of 930 Hz, derived from the helicopter survey over the entire Wuda area. Blue and red polygons show fire zones mapped in 2004, the black dots show single fire points mapped in 2005 (by DLR). The colour scale is the same as in Fig. 21 but without shading. Fire zones no. 3.2 and no. 8 are marked by red rectangles.

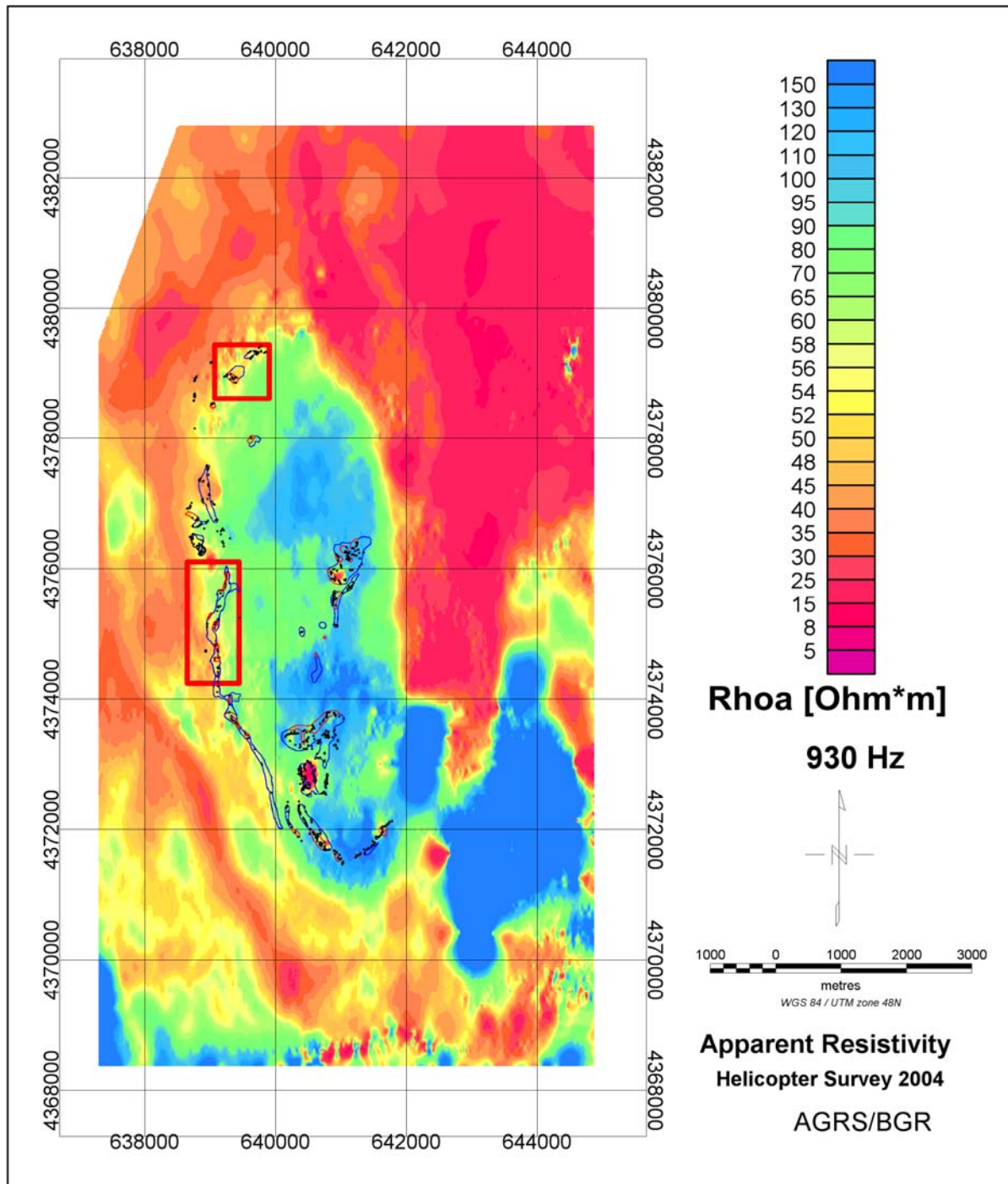


Figure 23: Map of the apparent resistivity Rhoa [Ohm*m] at a frequency of 930 Hz, derived from the helicopter survey over the entire Wuda area. Blue and red polygons show fire zones mapped in 2004, the black dots show single fire points mapped in 2005 (by DLR). The map is the same as in Fig. 22 but another colour scale was used to emphasize the sites of lower apparent resistivity within the syncline. Fire zones no. 3.2 and no. 8 are marked by red rectangles.

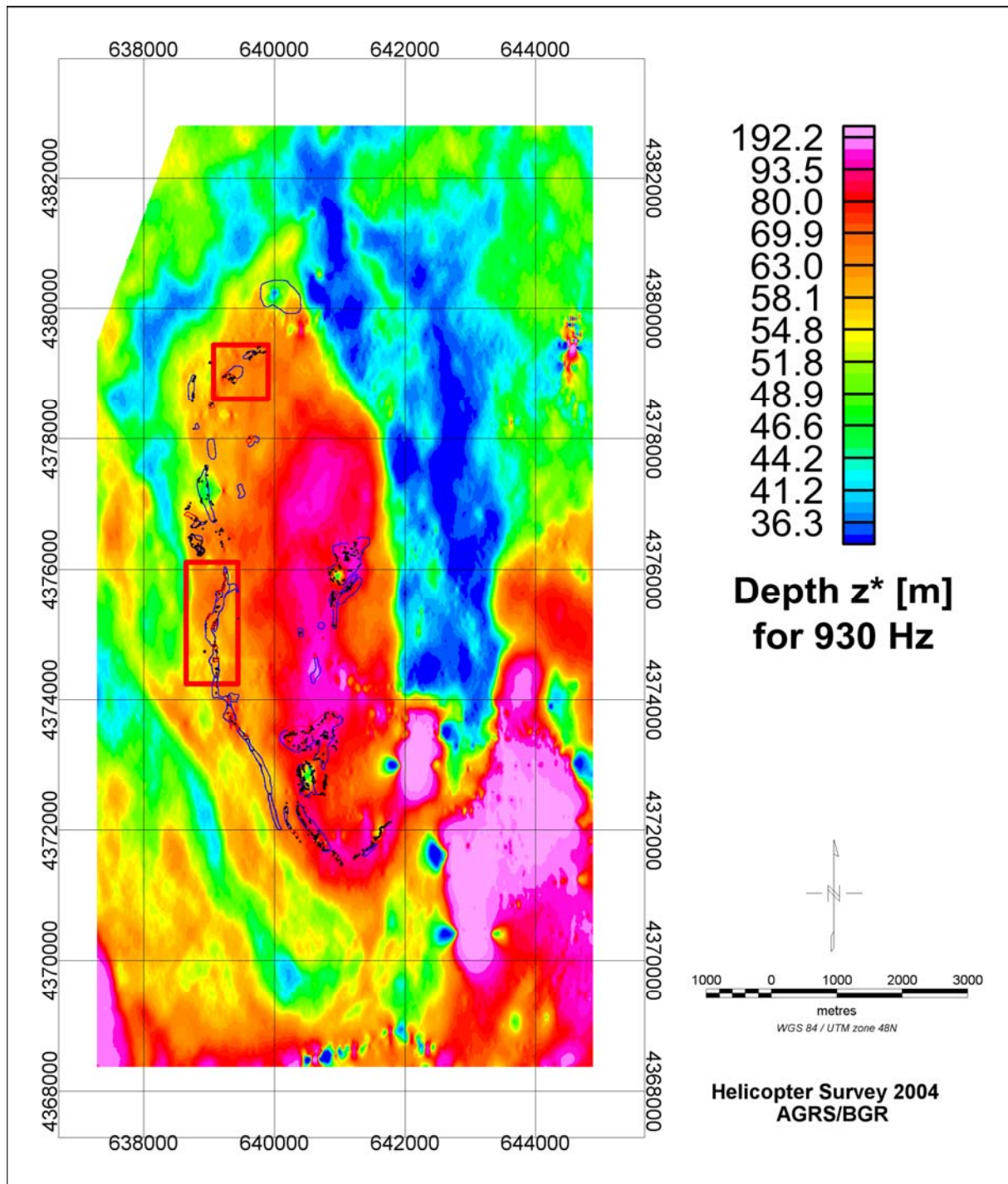


Figure 24: Map of the centroid depth at a frequency of 930 Hz, derived from the helicopter survey over the entire Wuda area. Fire zones no. 3.2 and no. 8 are marked by red rectangles.



Innovative Technologies for Exploration, Extinction and Monitoring of Coal Fires in North China
Final Report Phase A Part B

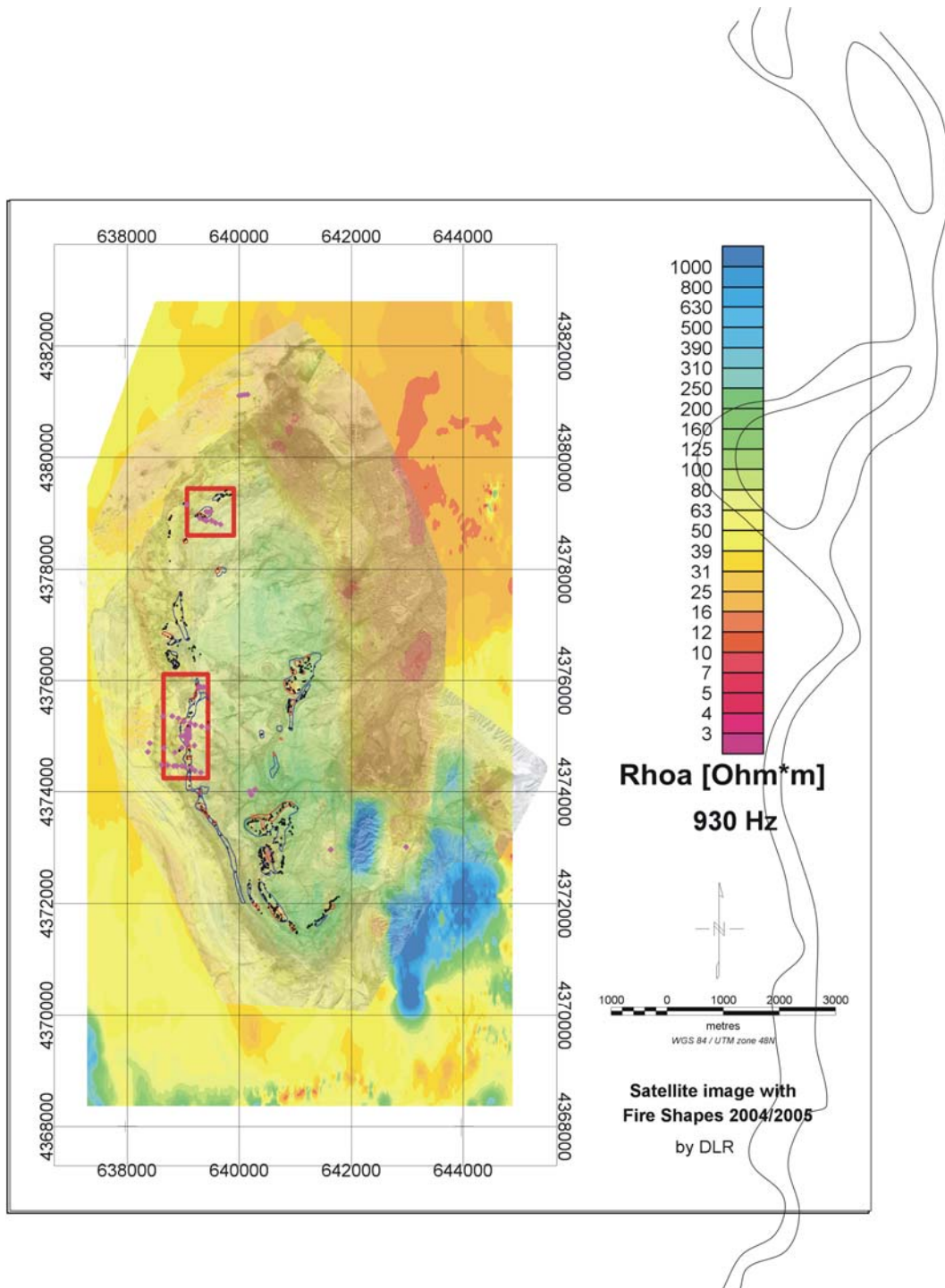


Figure 25: Quickbird satellite map (see Fig. 10) superimposed on the apparent resistivity map at a frequency of 930 Hz, derived from the helicopter survey over the entire Wuda area (see Fig. 22). Blue and red polygons show fire zones mapped in 2004, black dots show single fire points mapped in 2005 (by DLR). Sites from the TEM ground survey are marked by violet squares. The course of the Yellow River (light black lines) is roughly shown east of the map beyond the survey area. Fire zones no. 3.2 and no. 8 are marked by red rectangles.



3.2 Results from the northern part of fire zone no. 8

For a detailed investigation of the selected fire zones sections of the apparent resistivity maps and of the maps of the centroid depths were produced (Fig. 26 to 31). Sites and profile lines of the ground surveys are also plotted on these maps for comparison of the survey results. Burning zones mapped in 2004 are marked by blue and red polygons, light blue and violet polygons and black dots indicate the burning zones mapped in 2005 (by DLR). The central part of this fire zone was also investigated by the ground geophysical surveys (see Chapter 5). Black squares show the sites of the TEM soundings, orange lines show the VLF and HL survey lines. For a detailed location map of the ground survey sites see Fig. 82. The crack system is described by Gielisch & Kuenzer (2003).

Fire zone no. 8 is located at the western edge of the Wuda syncline. Its northern part, usually named “fire zone no. 8”, extends more than 1 km from north to south and about 200 m from west to east, see Fig. 9. The southern part of this fire zone, extending about several km southwards, is not considered here, but can be partly seen at the section for the southern part of the syncline.

The apparent resistivity maps for all frequencies (Fig. 26, 28 and 30) show areas of low apparent resistivities (below 30 Ohm*m). The low resistive area in the western part extends from depths of about 8 to 10 m for the highest frequency down to about 50 m for the lowest frequency. The low resistivity might be caused by enhanced iron oxide content within the sandstones (Gielisch 2006, pers. comm.).

East of the central part of the fire zone, where the TEM ground survey determined low resistivities at shallow depths at profile no. 3 (Fig. 85 and 86), the helicopter survey reveals a low resistive area. The area north east of the burning zone shows lower resistivities with centroid depths about 8 to 10 m for the highest frequency (Fig. 26), and at the medium frequency, but of smaller extension (Fig. 28). The centroid depth at this frequency is about 20 m (Fig. 29). At the lowest frequency apparent resistivity values of about 50 to 80 Ohm*m allow centroid depths of about 60 m or more (Fig. 31).

The southern part of fire zone no. 8, especially the collapsed area and the area south of it, show also lower resistivities. They correspond to the burning zone as it can be seen best at the frequency of 4650 Hz. The centroid depth is about 30 m there.

North of the collapsed area beginning at the southern part of the plateau, an extension of the area with lower resistivity is observed. It extends in north-easterly direction. At the highest frequency the apparent resistivity in this area is about 40 Ohm*m (Fig. 26), corresponding to a centroid depth of 10 m (Fig. 27). At the medium frequency this extension to north-east is visible best. Here apparent resistivities in the order of 40 Ohm*m occur at centroid depths of about 20 m (Fig. 28 and 29). The collapsed area south of the plateau shows lower resistivities than the area north of it. Especially at the frequency of 4650 Hz at centroid depths of more than 25 m apparent resistivities about 40 Ohm*m occur (Fig. 28 and 29).

At the northern end of the blue polygon a small area with lower apparent resistivity is found at the eastern part of a small hill, best seen on the apparent resistivity maps at the frequencies of 4650 Hz and 930 Hz. TEM profile no. 9 was carried out to investigate this site. Below the westernmost TEM site a mining pit was found by the authors. A burning area is situated directly west of it, extending about 300 m to the south. A very heavily burning site at the western foot of this hill was observed by the authors. This burning area does not show low



**Innovative Technologies for Exploration, Extinction and Monitoring of Coal Fires in North China
Final Report Phase A Part B**

resistivities corresponding to the polygon mapped. About 200 m west of the plateau of fire zone no. 8 (west of TEM profile no. 8) a mining facility was built. It might be the reason for an area of lower resistivity, best seen at the frequency of 930 Hz. Directly at the northern edge of the map section another area with low resistivity values can be found at all three frequencies. This area corresponds to another mining facility.

The location of the colder coal seam fires mapped do not vary distinctly from 2004 to 2005. The hotter coal seam fires show more variation from 2004 to 2005. Some new spots of hotter fires were observed in 2005. They are located in the middle part of fire zone no. 8 at the western edge, in the northern part at the heavily burning hill and at the collapsed area in the south. This new burning spots mapped in 2005 give some more clues for areas of interest.

The centroid depth varies between 20 and 35 m at 4650 Hz. Close to the TEM profiles no. 6 and no. 7 the centroid depth ranges from 20 to 26 m. Several resistivity lows obviously caused by active coal removal or operational activities occur west and north of fire zone no. 8. The conductive area in the western part of the map might be caused by enhanced iron oxide content within the sandstones (Gielisch 2006, pers. comm.).

The classification of this fire zone, made by DLR, characterizes it as “accelerating fire” in 2004 and “consistently burning fire” in 2005 (Kuenzer et al. 2006).

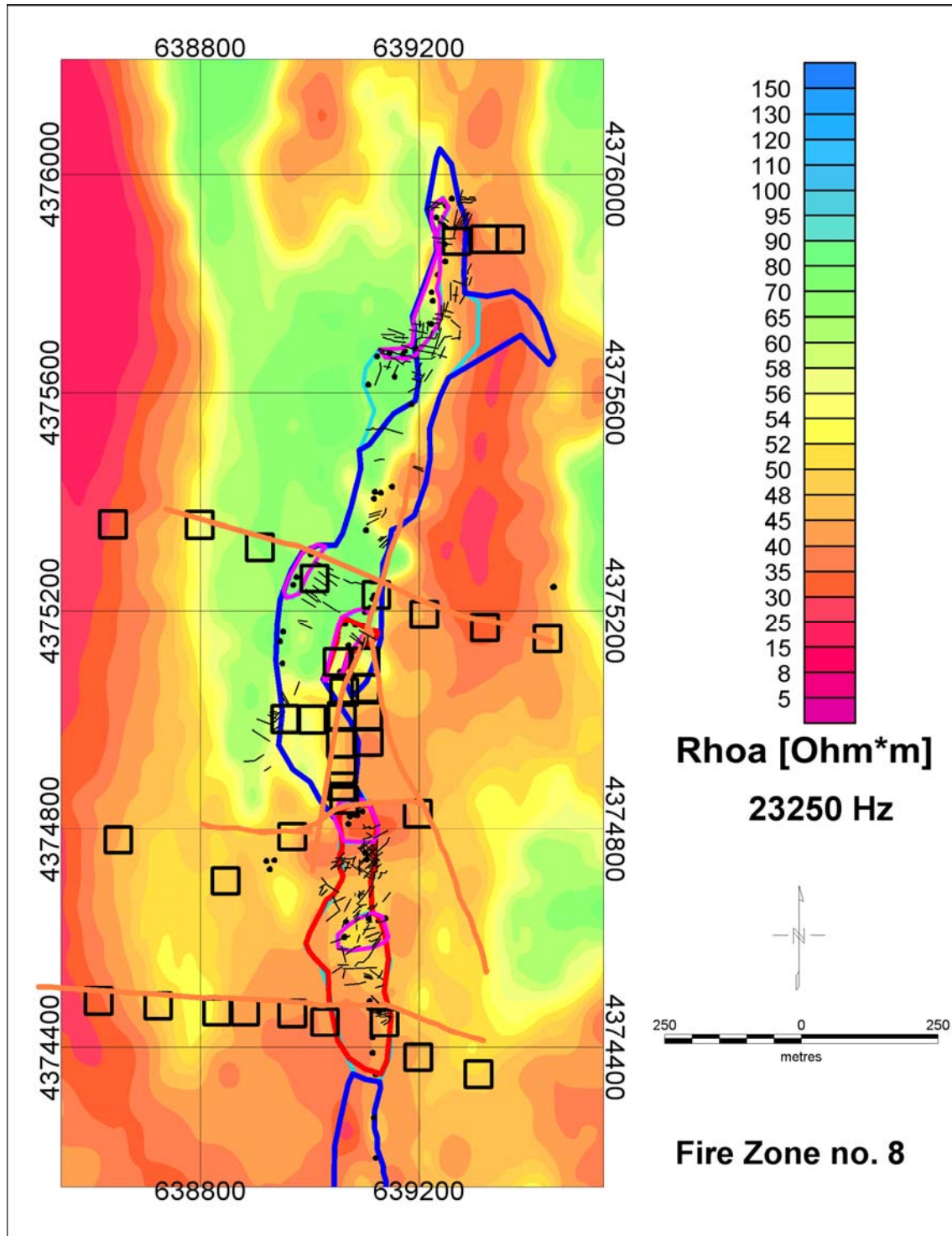


Figure 26: Map of the apparent resistivity R_{hoa} [$\Omega \cdot m$] at a frequency of 23250 Hz, derived from the helicopter survey over and in the vicinity of fire zone no. 8. Black squares show the sites of the TEM soundings, orange lines show the VLF and HL survey lines. Blue and red polygons indicate the burning zones in 2004, light blue and violet polygons and black dots indicate the burning zones in 2005, light black lines mark cracks (mapped by DLR).

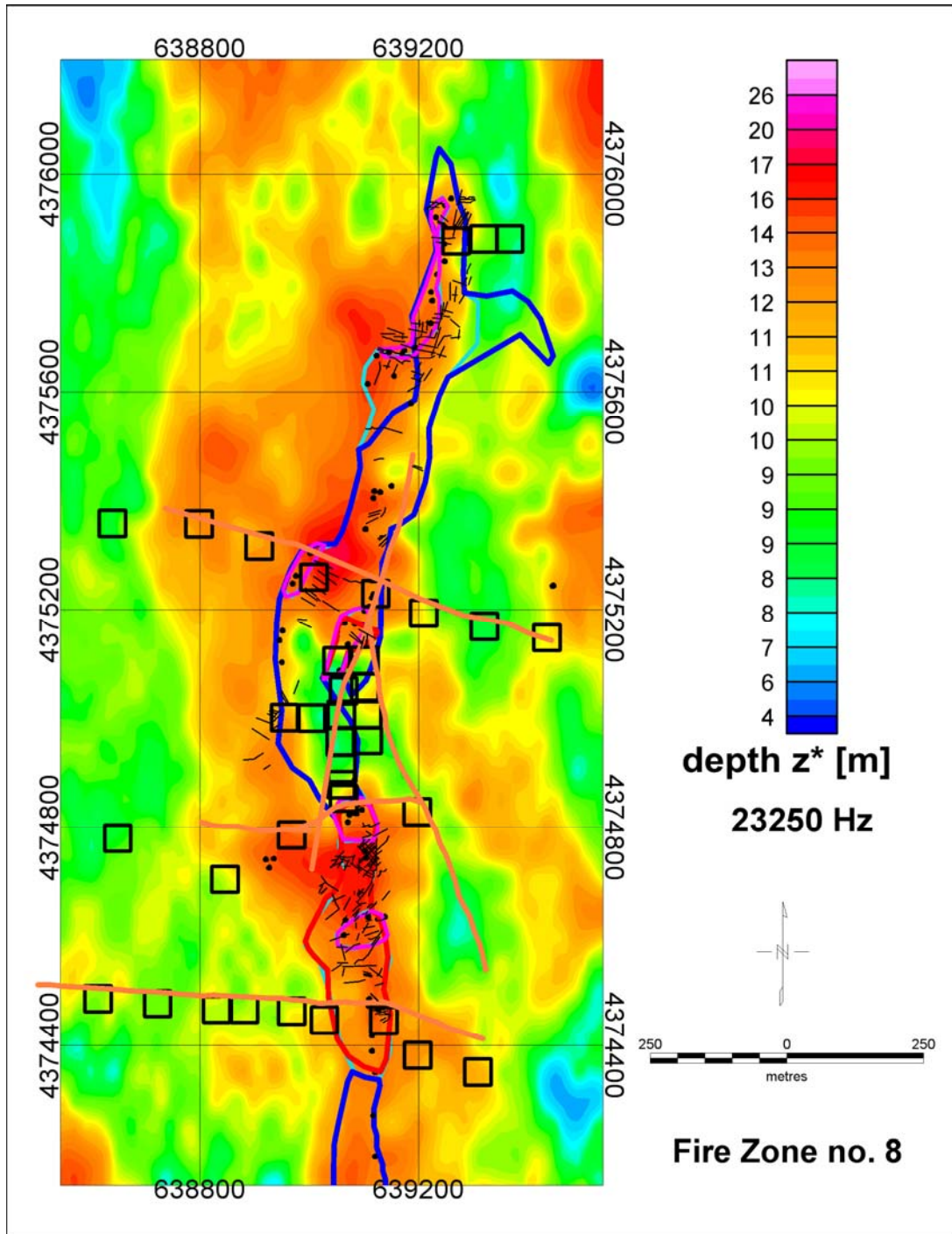


Figure 27: Map of the centroid depth [m] at a frequency of 23250 Hz, derived from the helicopter survey over and in the vicinity of fire zone no. 8. Black squares show the sites of the TEM soundings, orange lines show the VLF and HL survey lines. Blue and red polygons indicate the burning zones in 2004, light blue and violet polygons and black dots indicate the burning zones in 2005, light black lines mark cracks (mapped by DLR).

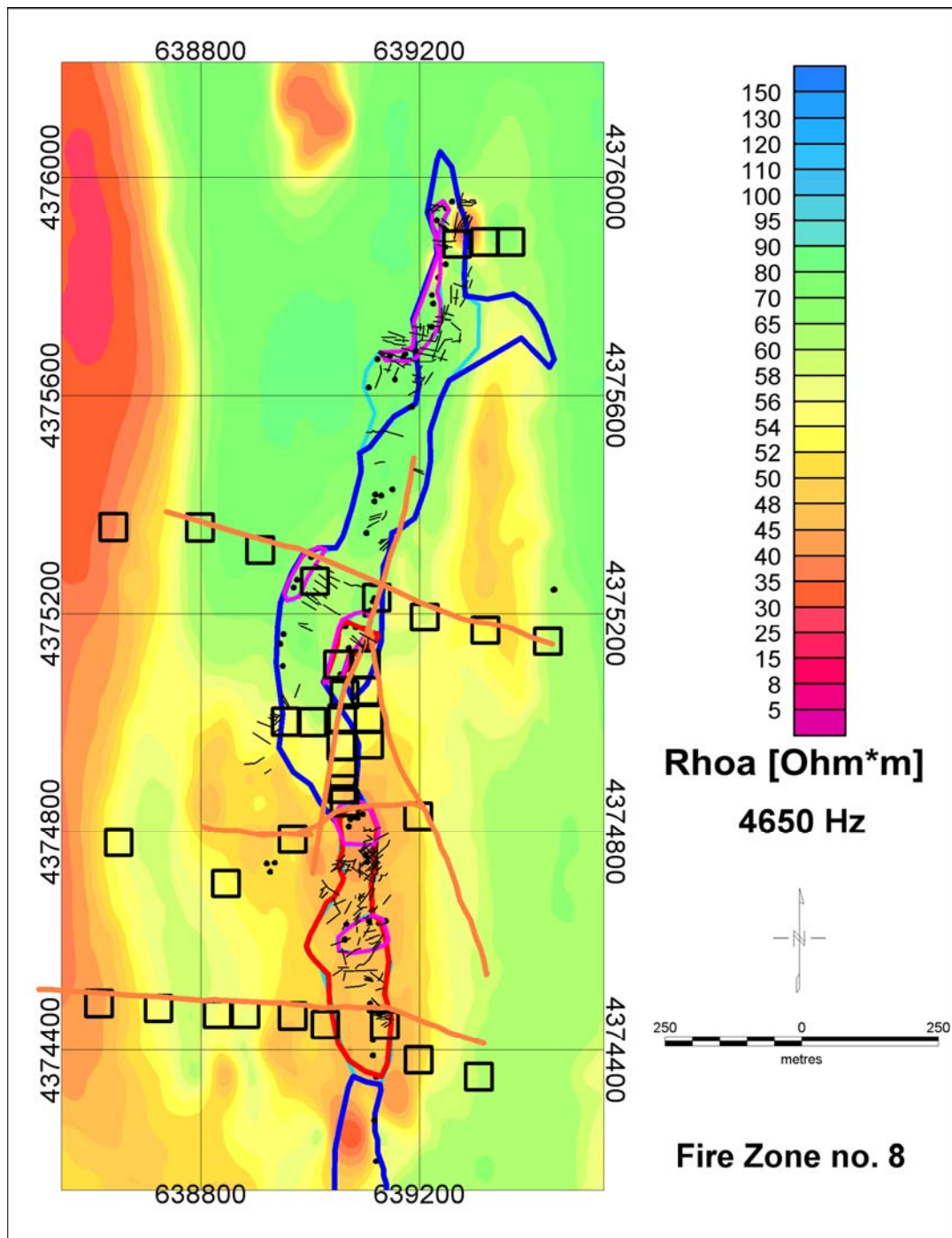


Figure 28: Map of the apparent resistivity Rhoa [Ohm*m] at a frequency of 4650 Hz, derived from the helicopter survey over and in the vicinity of fire zone no. 8. Black squares show the sites of the TEM soundings, orange lines show the VLF and HL survey lines. Blue and red polygons indicate the burning zones in 2004, light blue and violet polygons and black dots indicate the burning zones in 2005, light black lines mark cracks (mapped by DLR).

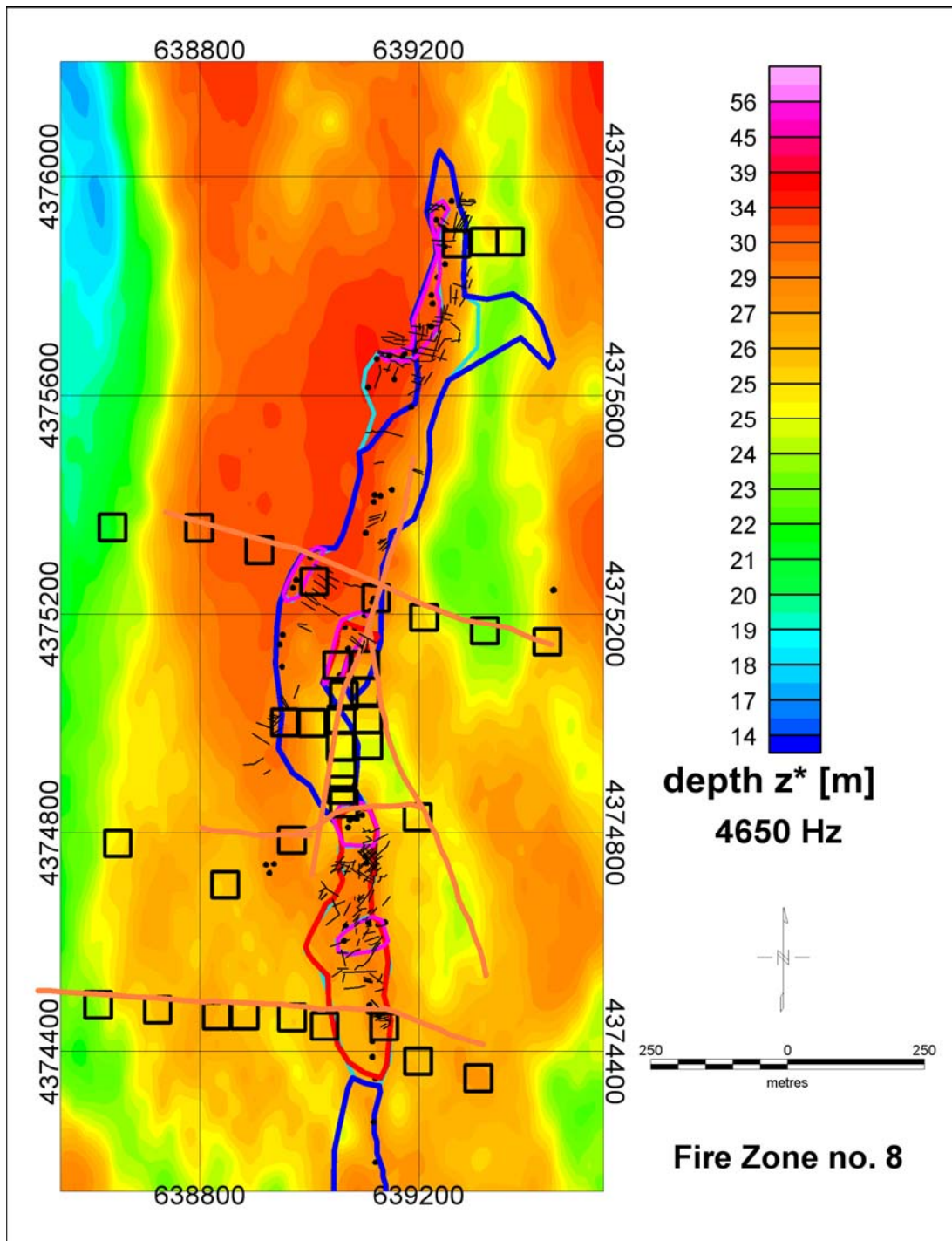


Figure 29: Map of the centroid depth [m] at a frequency of 4650 Hz, derived from the helicopter survey over and in the vicinity of fire zone no. 8. Black squares show the sites of the TEM soundings, orange lines show the VLF and HL survey lines. Blue and red polygons indicate the burning zones in 2004, light blue and violet polygons and black dots indicate the burning zones in 2005, light black lines mark cracks (mapped by DLR).

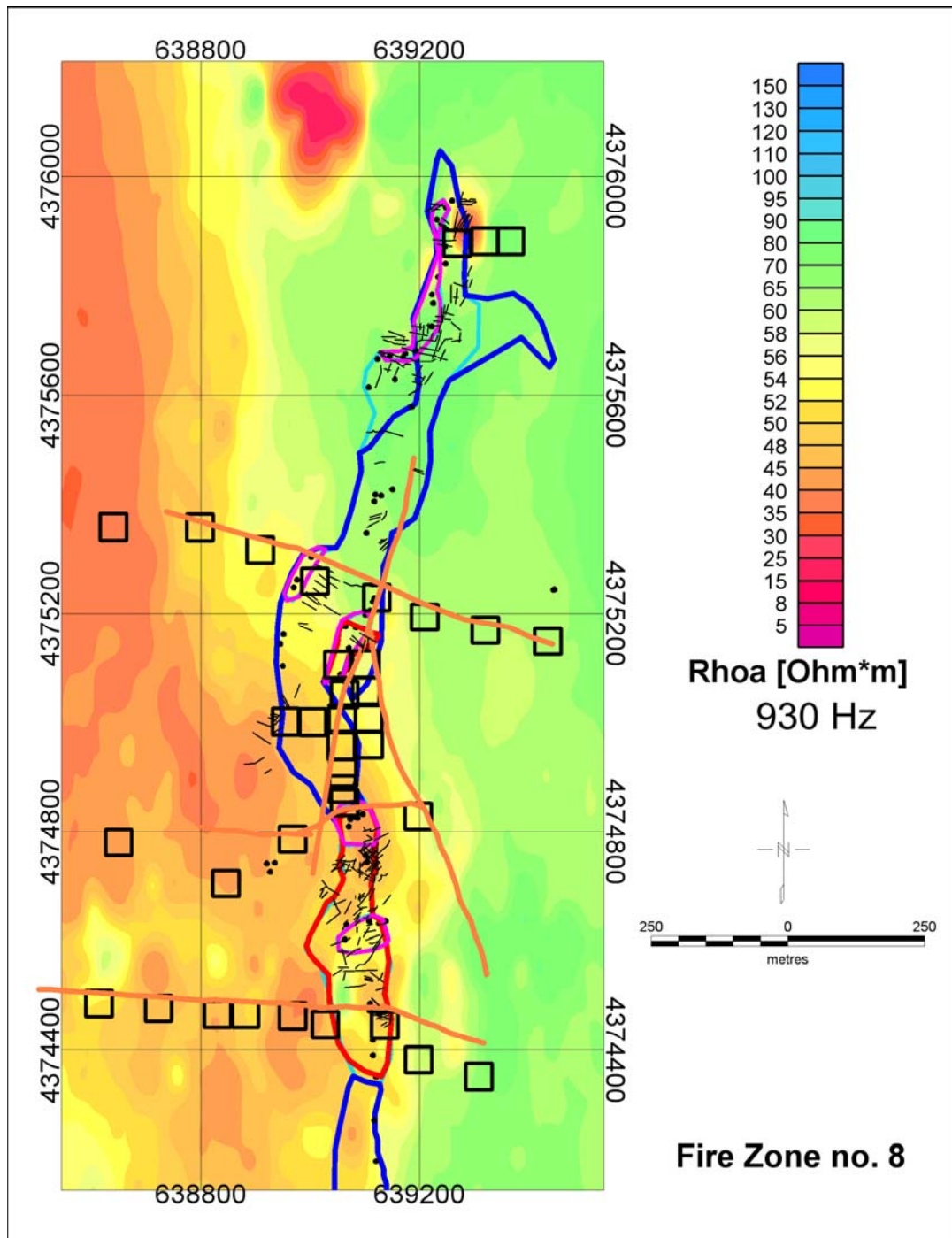


Figure 30: Map of the apparent resistivity R_{hoa} [$\text{Ohm}\cdot\text{m}$] at a frequency of 930 Hz, derived from the helicopter survey over and in the vicinity of fire zone no. 8. Black squares show the sites of the TEM soundings, orange lines show the VLF and HL survey lines. Blue and red polygons indicate the burning zones in 2004, light blue and violet polygons and black dots indicate the burning zones in 2005, light black lines mark cracks (mapped by DLR).

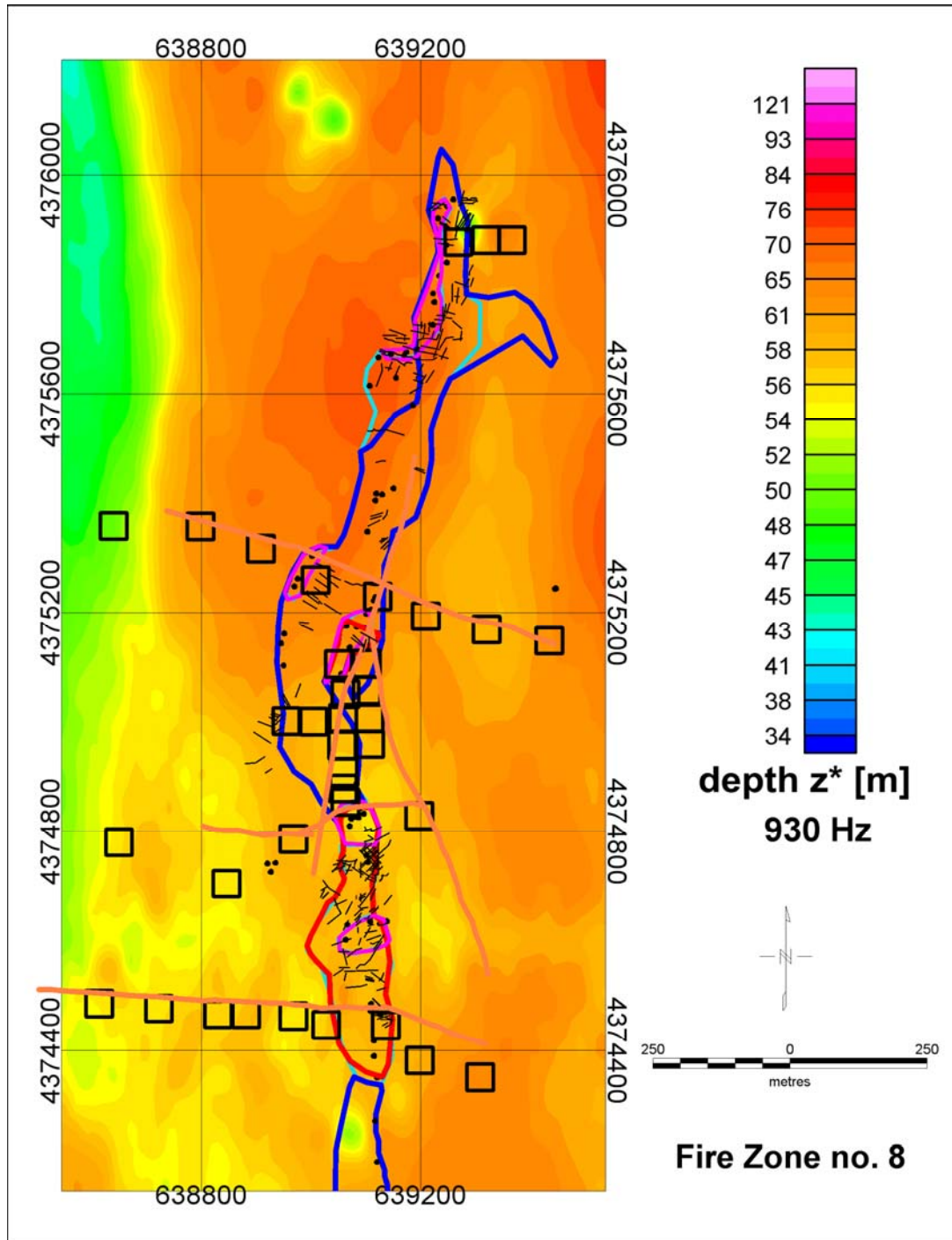


Figure 31: Map of the centroid depth [m] at a frequency of 930 Hz, derived from the helicopter survey over and in the vicinity of fire zone no. 8. Black squares show the sites of the TEM soundings, orange lines show the VLF and HL survey lines. Blue and red polygons indicate the burning zones in 2004, light blue and violet polygons and black dots indicate the burning zones in 2005, light black lines mark cracks (mapped by DLR).



3.3 Results from fire zone no. 3.2

Fire zone no. 3.2 as a part of fire zone no. 3 is located in the north-western part of the Wuda syncline, extending about a few hundreds of metres from south-westerly to north-easterly direction along a valley and about 300 m in width, see Fig. 9. The outcropping coal seams no. 9 and no. 10 are separated by sandstone. In the vicinity of the coal seams siltstones and claystones are present. A burning pillar extends about 200 m in the central part of the valley. The mapped burning zones are shown as described before. The apparent resistivity and centroid depth maps show also the surroundings of this fire zone, including the sites of the TEM ground survey (Fig. 32 to 37). Facilitating the comparison of the ground sites to the maps yielded by the helicopter survey the TEM sites are shown by black squares. About 200 m in north-westerly direction of the fire zone a factory is situated.

At the highest frequency the apparent resistivity map shows values about 50 to 60 Ohm*m for the southern part of this fire zone, slightly lower apparent resistivities about 40 Ohm*m for its north-eastern part. Up to 30 m centroid depth is determined at these sites.

At the medium frequency the fire zone partly shows apparent resistivities of about 40 Ohm*m or slightly higher values. These parts are located in the south-western part, mapped as hot burning zone and in the north-eastern part, where hot burning spots are found. In the middle part of the fire zone, within the polygons mapped at colder parts of the area, where three TEM sites are situated along a flight line, also a small area with apparent resistivities about 40 Ohm*m is located. Centroid depths are about 40 m. These area correlates to the burning pillar in the centre of the valley.

The lowest frequency shows similar apparent resistivities for the same area in the south-western part for centroid depth of about 60 m or more.

The fire zone is situated close to the north-western rim of the syncline. At the medium and the lowest frequencies the Permian strata within the syncline are indicated by higher apparent resistivities and the quicksands from the Gobi desert are indicated by lower resistivities in the area in north-westerly direction beyond the fire zone. At the highest frequency also within the syncline lower resistivities about 40 or 30 Ohm*m are determined. This might respond to an eolian sand cover above the Permian strata caused by the Gobi desert.

The classification of this fire zone by DLR characterizes it as “slowly burning out fire” in 2004 and “consistently burning fire” in 2005 (Kuenzer et al. 2006).



Innovative Technologies for Exploration, Extinction and Monitoring of Coal Fires in North China
Final Report Phase A Part B

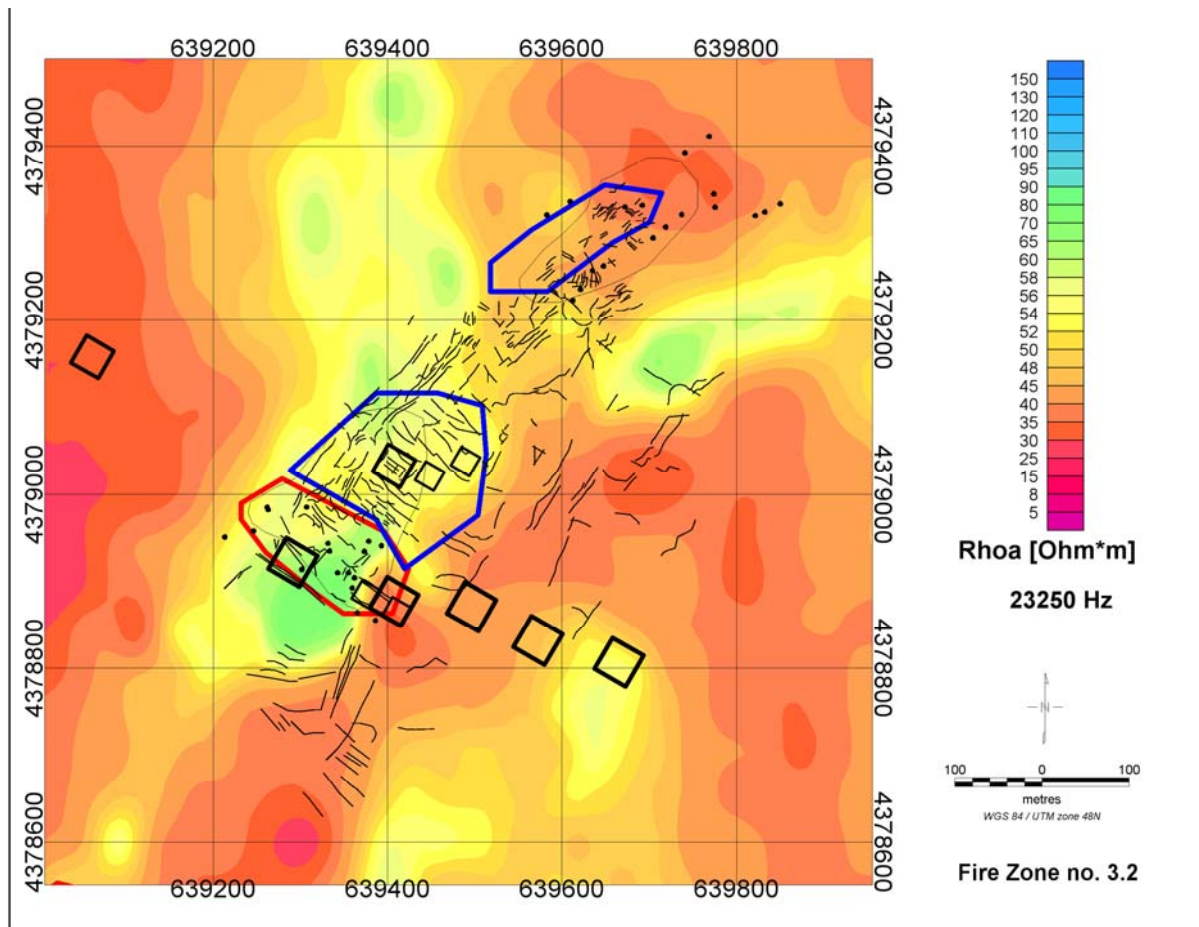


Figure 32: Map of the apparent resistivity $R_{\rho a}$ [Ohm*m] at a frequency of 23250 Hz derived from the helicopter survey over and in the vicinity of fire zone no. 3.2. Black squares show the sites of the TEM soundings. Blue and red polygons indicate the burning zones in 2004, the black dots indicate burning spots in 2005, light black lines mark cracks (mapped by DLR).



Innovative Technologies for Exploration, Extinction and Monitoring of Coal Fires in North China
Final Report Phase A Part B

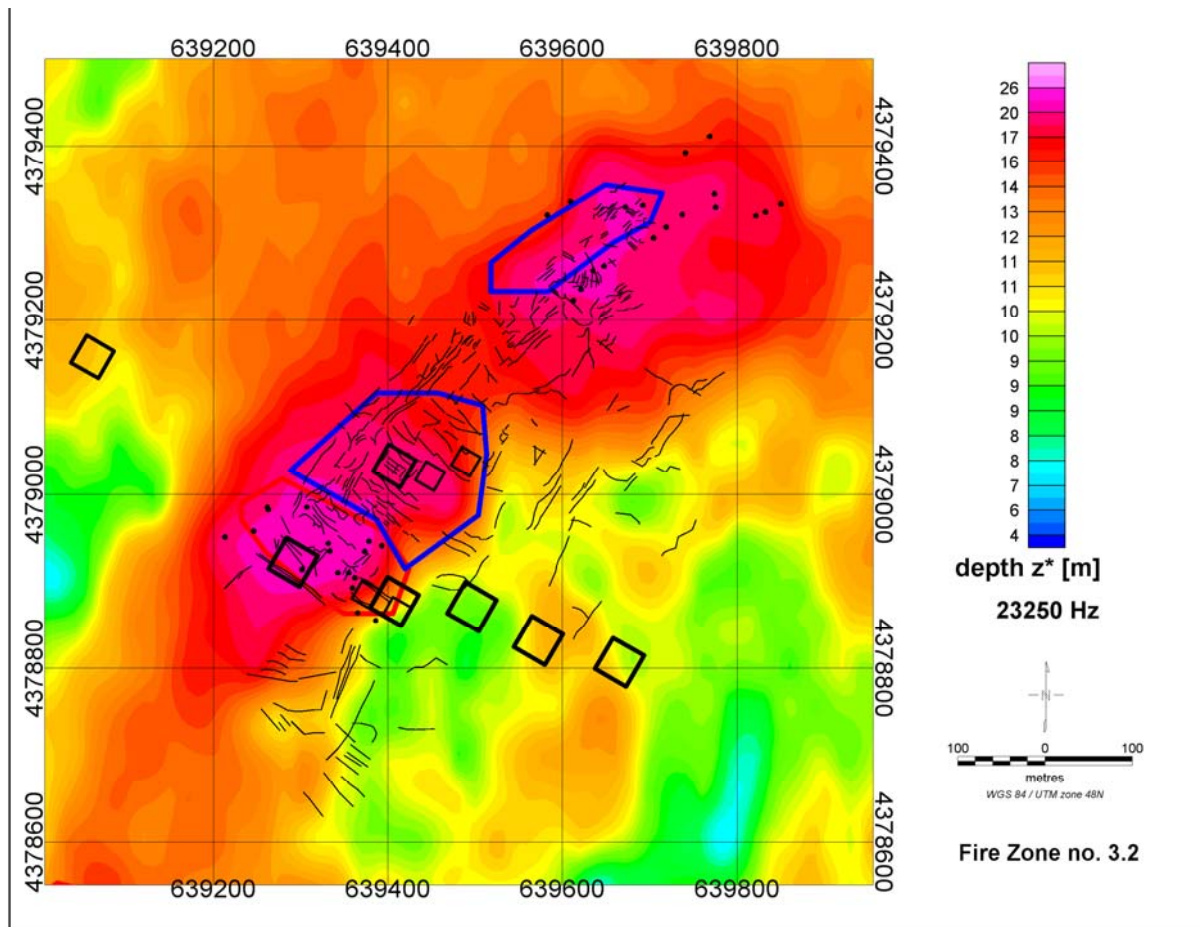


Figure 33: Map of the centroid depth [m] at a frequency of 23250 Hz derived from the helicopter survey over and in the vicinity of fire zone no. 3.2. Black squares show the sites of the TEM soundings. Blue and red polygons indicate the burning zones in 2004, the black dots indicate burning spots in 2005, light black lines mark cracks (mapped by DLR).



Innovative Technologies for Exploration, Extinction and Monitoring of Coal Fires in North China
Final Report Phase A Part B

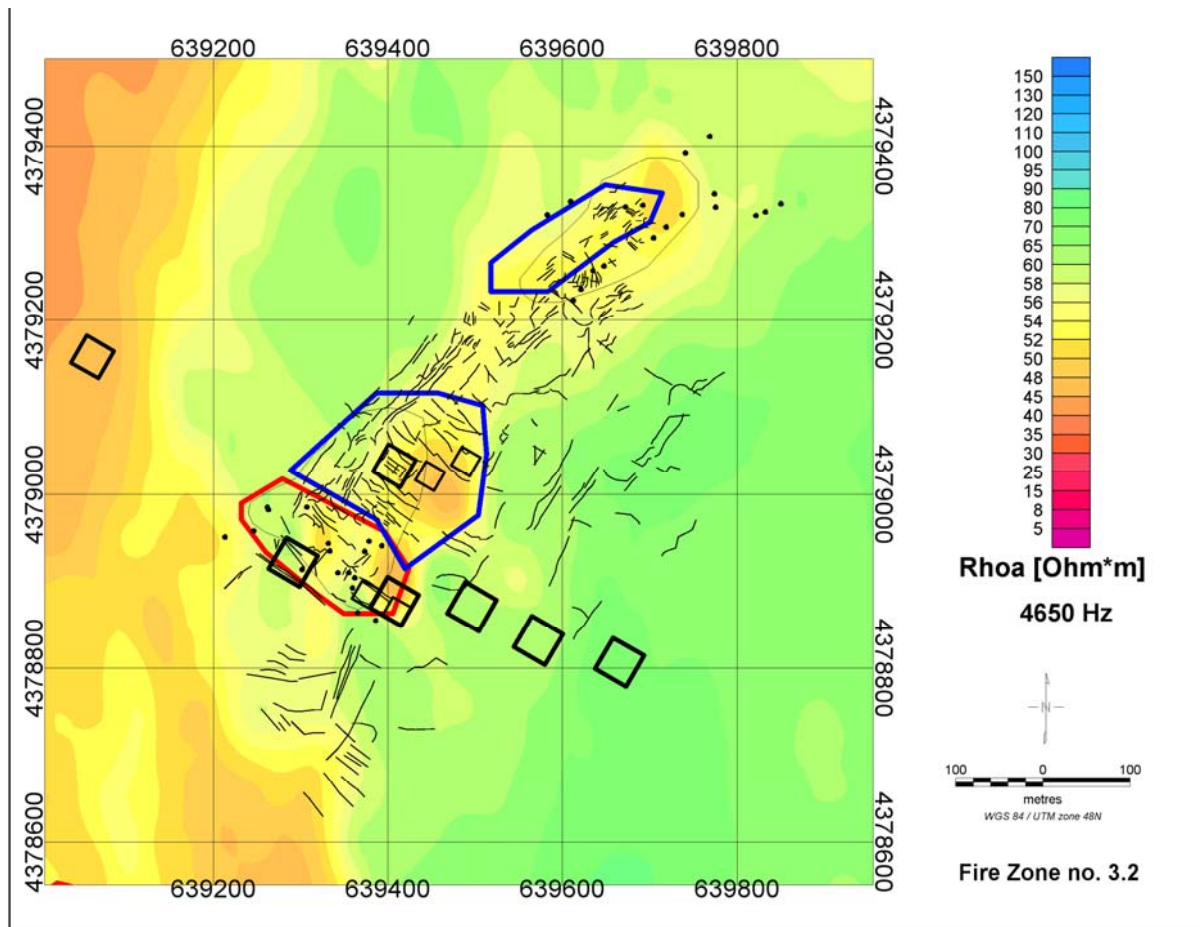


Figure 34: Map of the apparent resistivity Rhoa [Ohm*m] at a frequency of 4650 Hz derived from the helicopter survey over and in the vicinity of fire zone no. 3.2. Black squares show the sites of the TEM soundings. Blue and red polygons indicate the burning zones in 2004, the black dots indicate burning spots in 2005, light black lines mark cracks (mapped by DLR).



Innovative Technologies for Exploration, Extinction and Monitoring of Coal Fires in North China
Final Report Phase A Part B

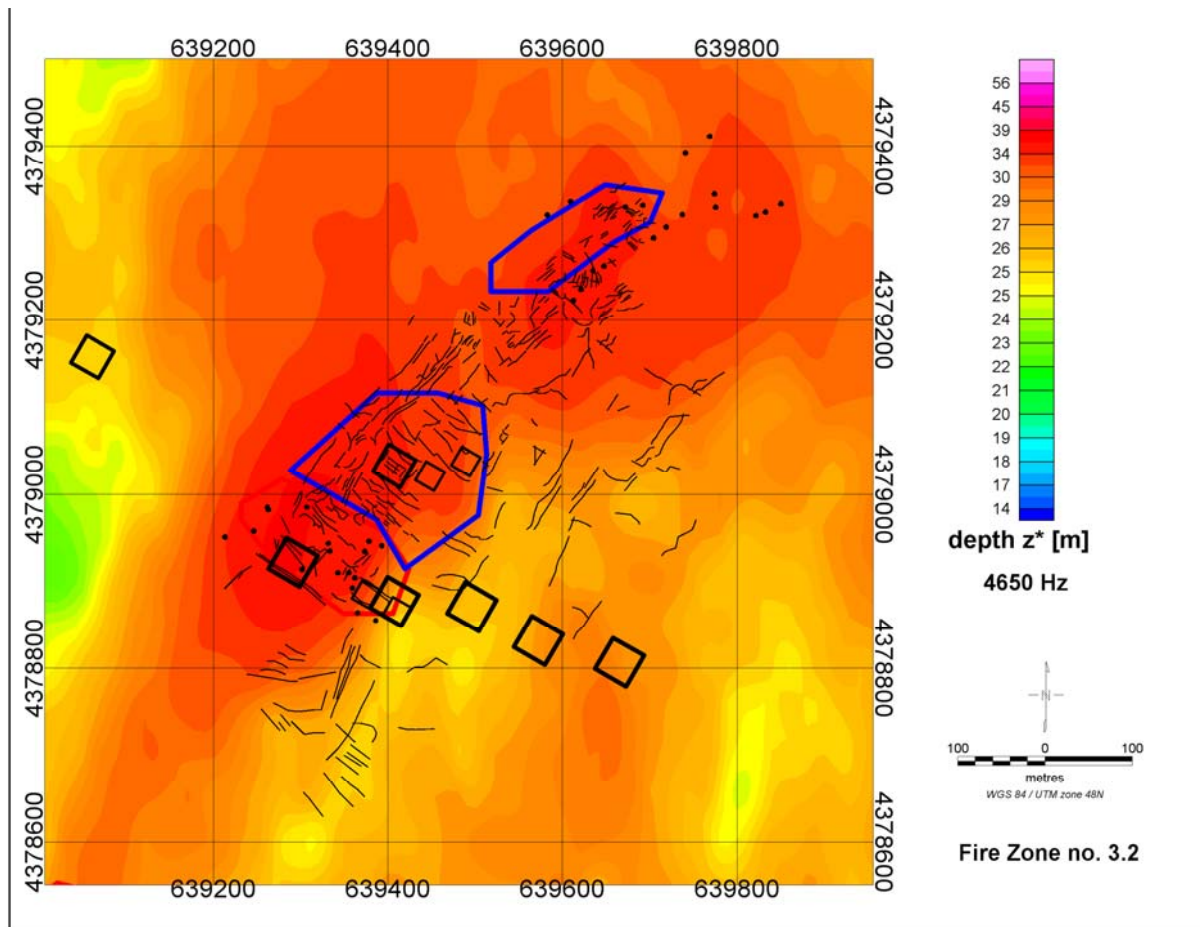


Figure 35: Map of the centroid depth [m] at a frequency of 4650 Hz derived from the helicopter survey over and in the vicinity of fire zone no. 3.2. Black squares show the sites of the TEM soundings. Blue and red polygons indicate the burning zones in 2004, the black dots indicate burning spots in 2005, light black lines mark cracks (mapped by DLR).



Innovative Technologies for Exploration, Extinction and Monitoring of Coal Fires in North China
Final Report Phase A Part B

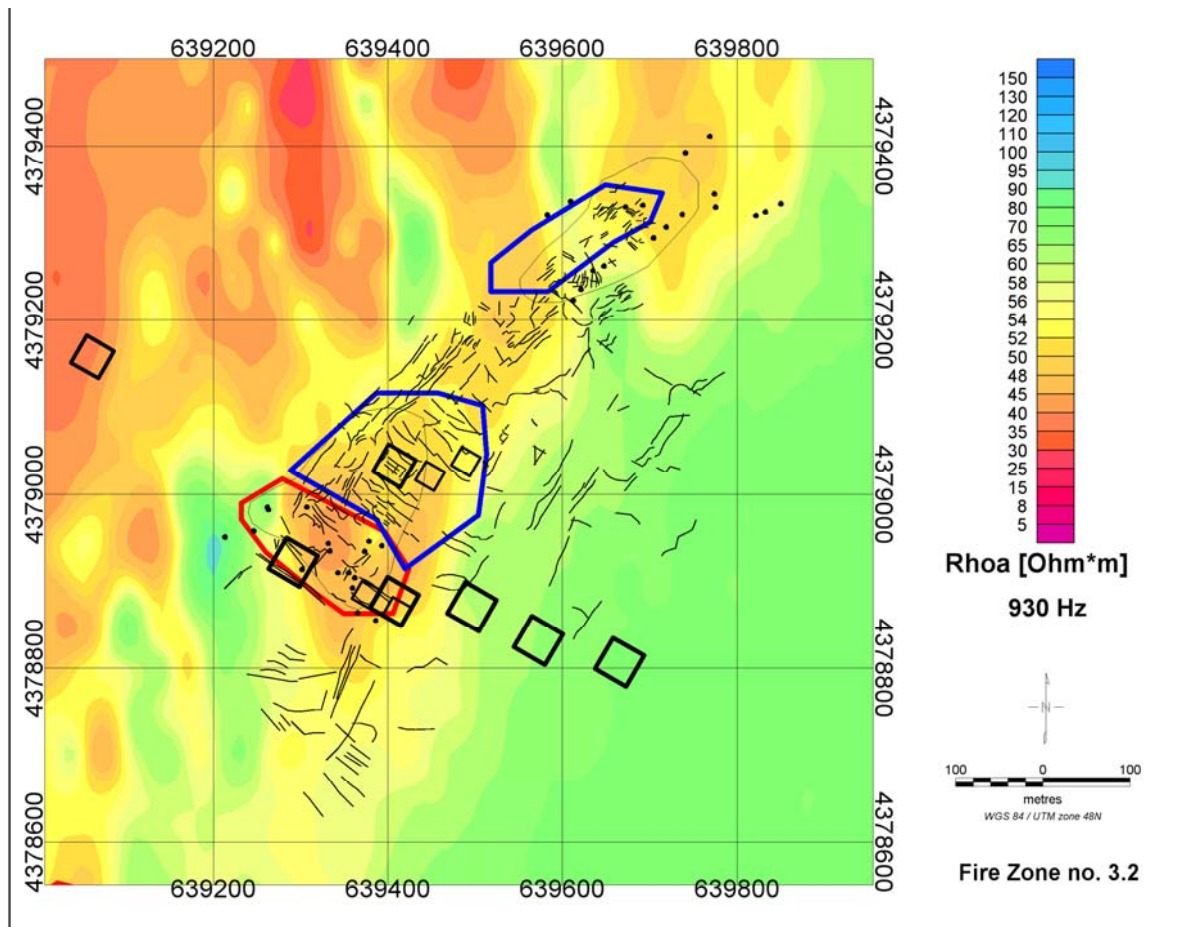


Figure 36: Map of the apparent resistivity R_{hoa} [$\text{Ohm}\cdot\text{m}$] at a frequency of 930 Hz derived from the helicopter survey over and in the vicinity of fire zone no. 3.2. Black squares show the sites of the TEM soundings. Blue and red polygons indicate the burning zones in 2004, the black dots indicate burning spots in 2005, light black lines mark cracks (mapped by DLR).



Innovative Technologies for Exploration, Extinction and Monitoring of Coal Fires in North China
Final Report Phase A Part B

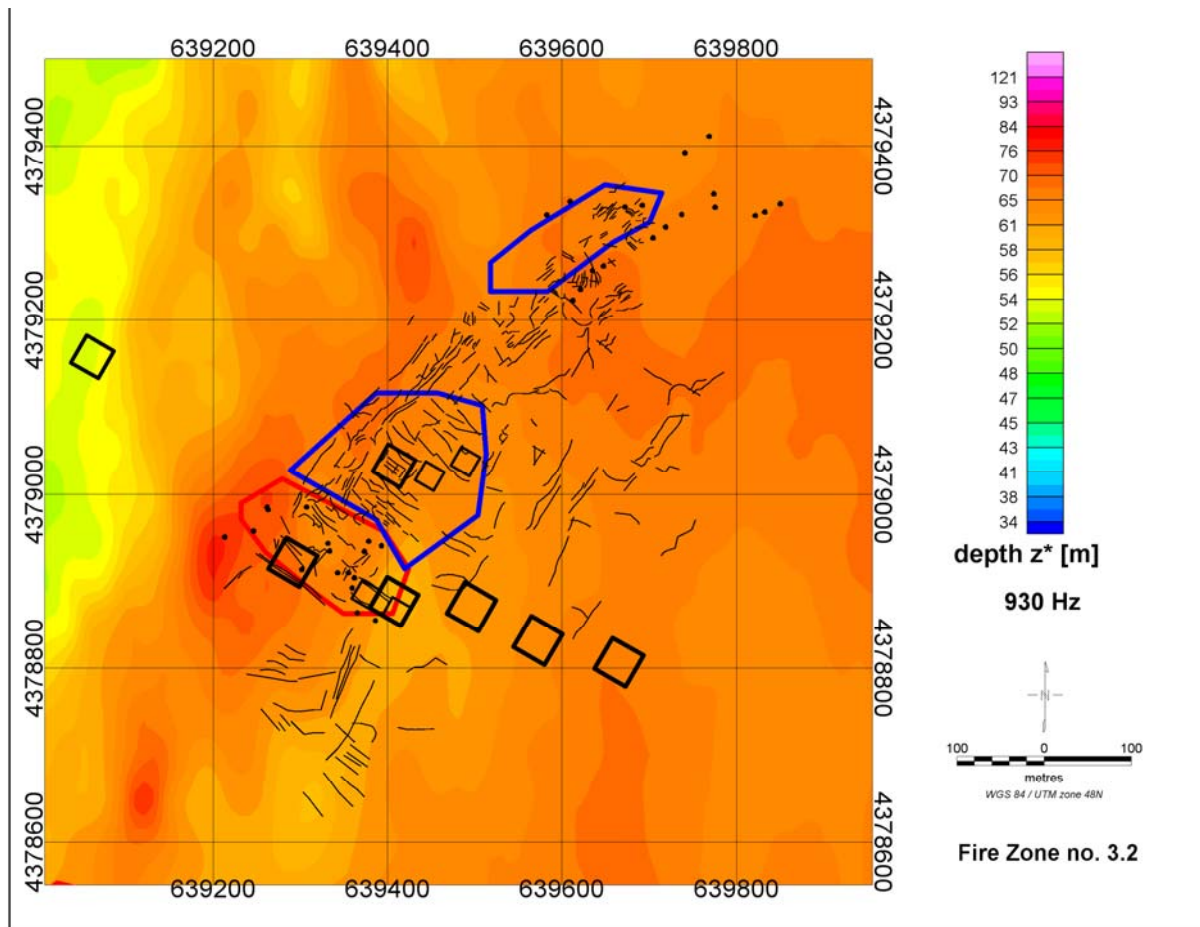


Figure 37: Map of the centroid depth [m] at a frequency of 930 Hz derived from the helicopter survey over and in the vicinity of fire zone no. 3.2. Black squares show the sites of the TEM soundings. Blue and red polygons indicate the burning zones in 2004, the black dots indicate burning spots in 2005, light black lines mark cracks (mapped by DLR).



3.4 Results from fire zones within the southern surroundings of fire zone no. 3.2

For the southern surroundings of fire zone no. 3.2 including fire zones no. 2, further parts of no. 3, no. 4, no. 5, no. 6, no. 15, no. 16 and no. 18 (see Fig. 9, Fig. 38) sections of the apparent resistivity maps are shown (Fig. 38-40). Only for the medium frequency the centroid depth is mapped (Fig. 41). While fire zones no. 3, no. 6 and no. 18 are still burning, fire zones no. 2, no. 4, no. 5, no. 15 and no. 16 are extinct (Kuenzer et al. 2006).

Fire zone no. 6 shows low resistivities at the medium and at the lowest frequencies, while at fire zone no. 18 no striking changes of the apparent resistivity occur.

Clearly visible, especially at the medium frequency, is the difference in resistivity between the low resistive eolian quicksands beyond the syncline and the Permian strata within the syncline.

The classification of this fire zones by DLR characterize fire zone no. 5 as “accelerating fire” in 2004 and “extinct fire” in 2005, fire zone no. 6 as “consistently burning fire” in 2004 and in 2005 and fire zone no. 18 as “accelerating fire” in 2004 and “consistently burning fire” in 2005 (Kuenzer et al. 2006).

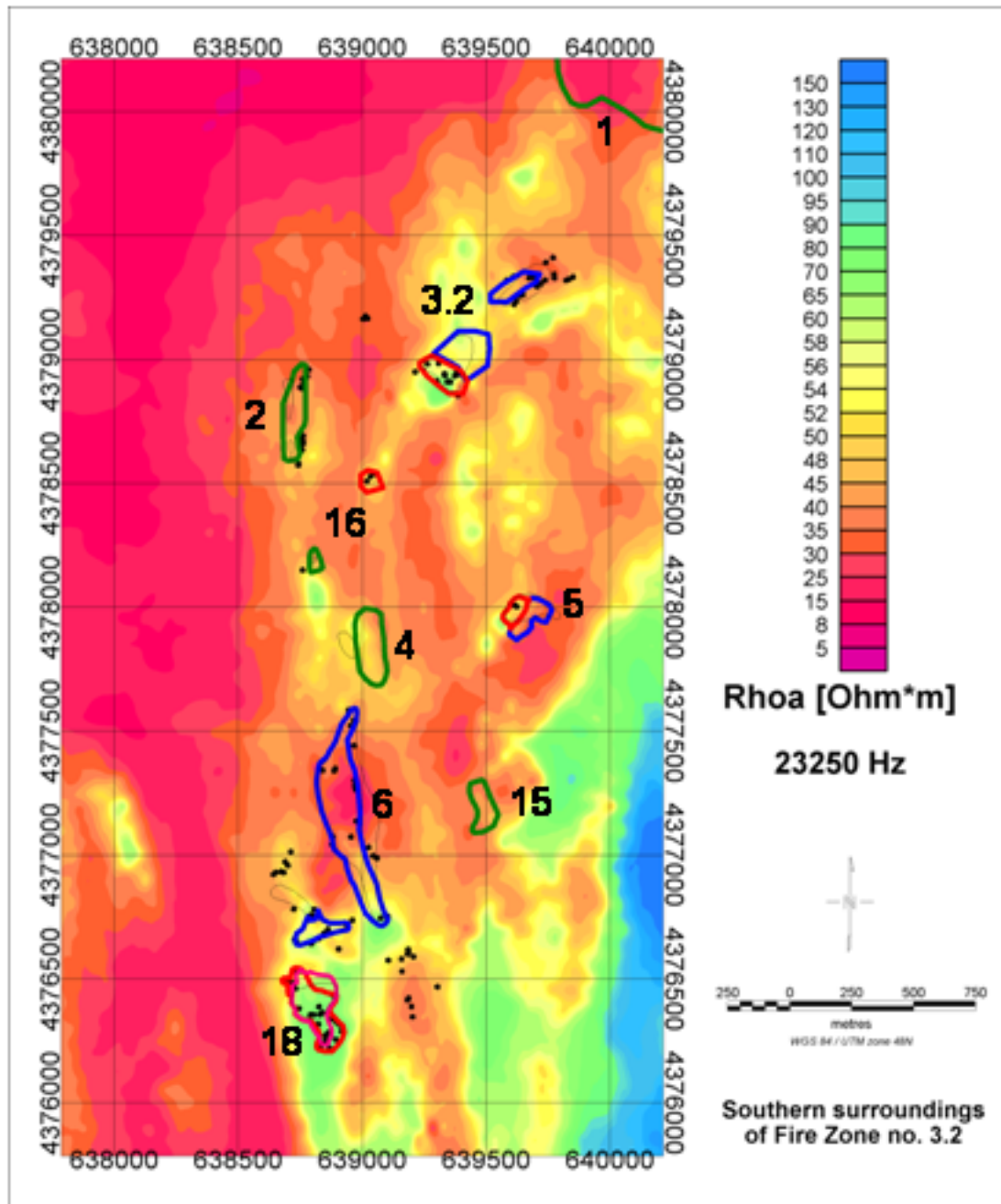


Figure 38: Map of the apparent resistivity R_{ρ} [Ohm*m] at a frequency of 23250 Hz, derived from the helicopter survey south of fire zone no. 3.2. Names of fire zones are shown by black numbers. Green polygons mark the fire zones in 2002, light black polygons mark the fire zones in 2003, blue and red polygons indicate the burning zones in 2004, violet polygons and black dots indicate burning spots in 2005 (mapped by DLR).

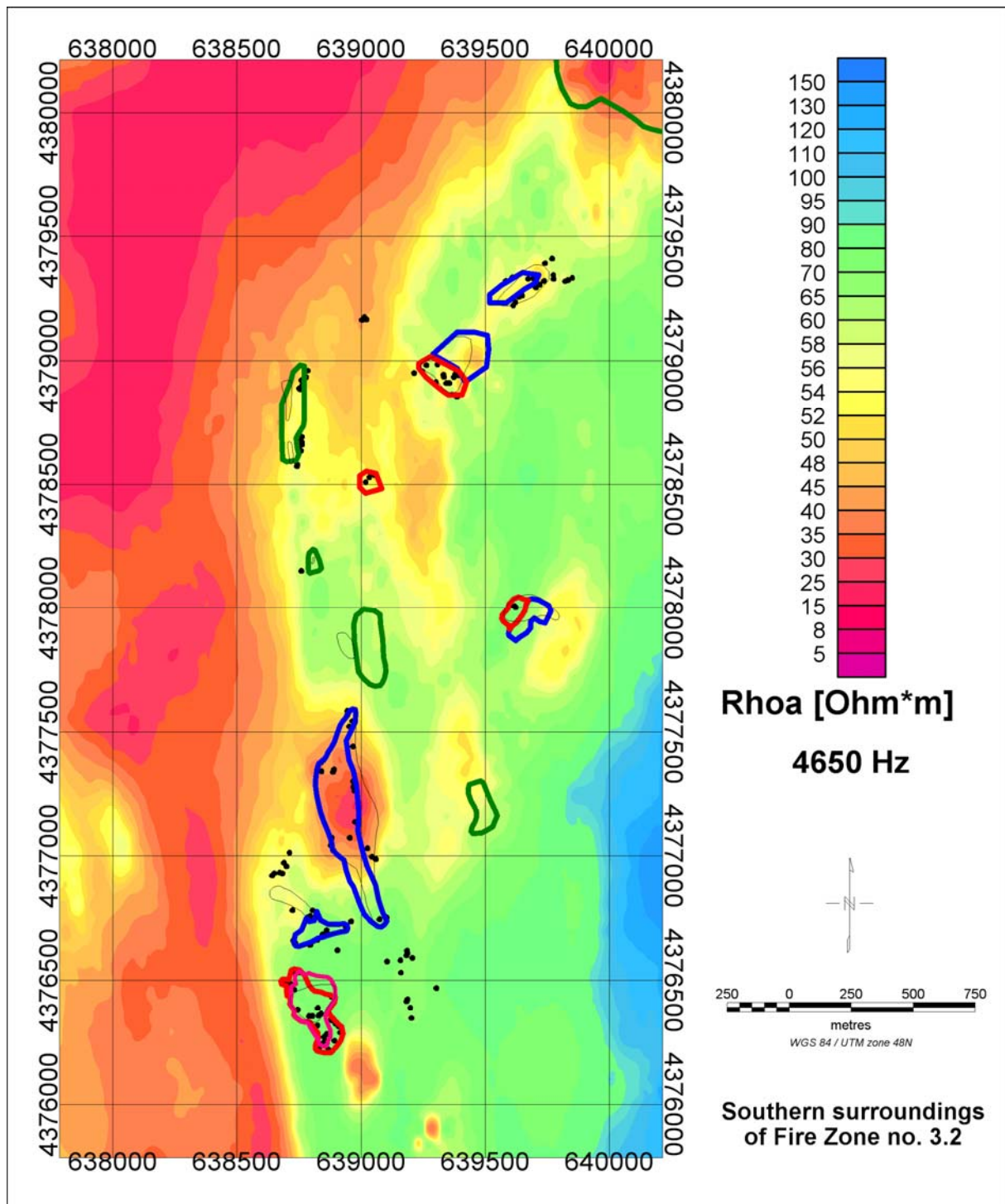


Figure 39: Map of the apparent resistivity Rhoa [Ohm*m] at a frequency of 4650 Hz, derived from the helicopter survey south of fire zone no. 3.2. Green polygons mark the fire zones in 2002, light black polygons mark the fire zones in 2003, blue and red polygons indicate the burning zones in 2004, violet polygons and black dots indicate burning spots in 2005 (mapped by DLR).

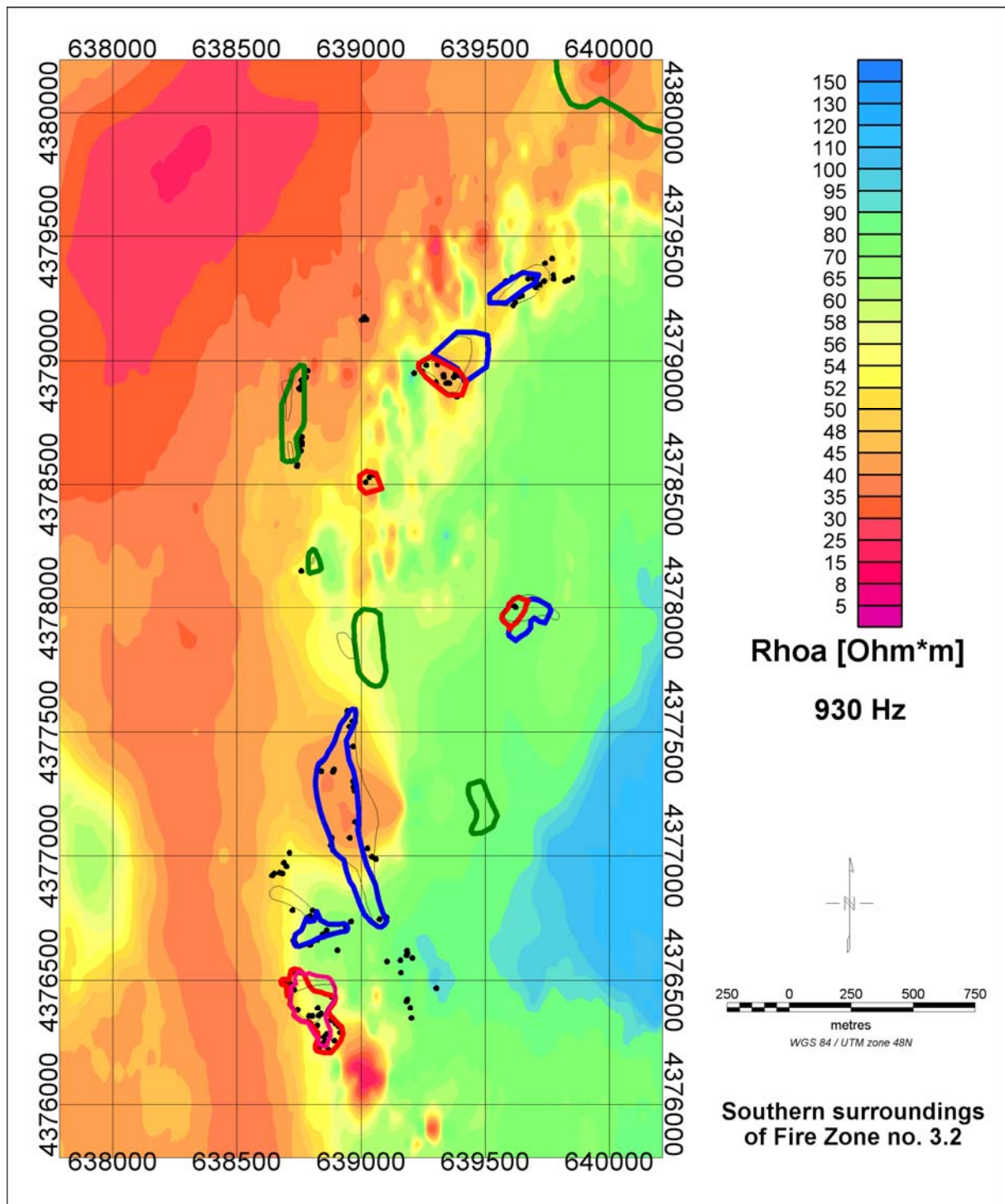


Figure 40: Map of the apparent resistivity Rhoa [Ohm*m] at a frequency of 930 Hz, derived from the helicopter survey south of fire zone no. 3.2. Green polygons mark the fire zones in 2002, light black polygons mark the fire zones in 2003, blue and red polygons indicate the burning zones in 2004, violet polygons and black dots indicate burning spots in 2005 (mapped by DLR).

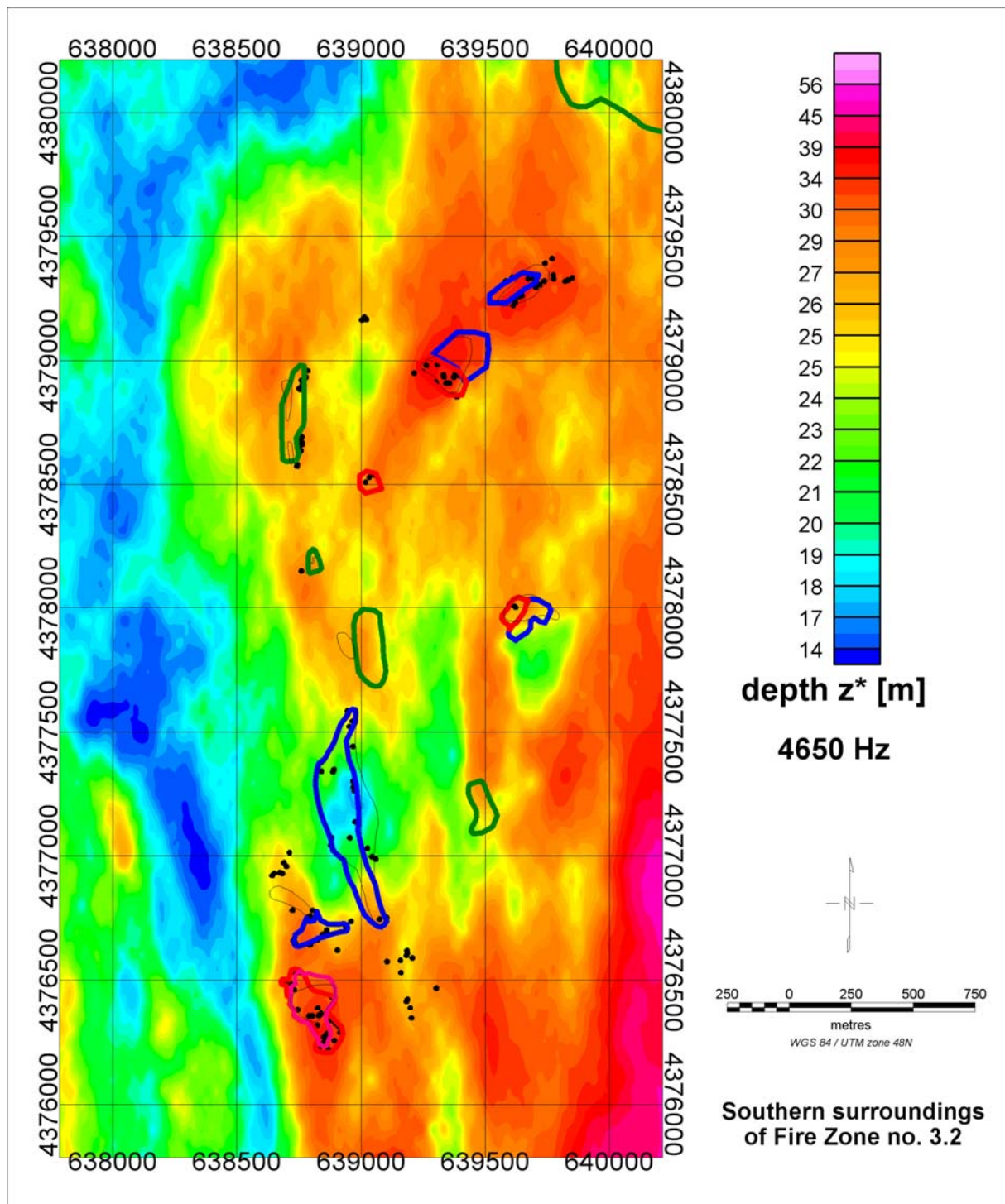


Figure 41: Map of the centroid depth [m] at a frequency of 4650 Hz, derived from the helicopter survey south of fire zone no. 3.2. Green polygons mark the fire zones in 2002, light black polygons mark the fire zones in 2003, blue and red polygons indicate the burning zones in 2004, violet polygons and black dots indicate burning spots in 2005 (mapped by DLR).



3.5 Results from fire zone no. 7 in the centre of the syncline

Fire zone no. 7 is located about 2 km east of fire zone no. 8 in the centre of the syncline. It extends about 1 km in north-south direction and its width is about 200 to 600 m. One part in the centre was inspected by the authors on ground and was investigated by VLF measurements. The results are presented in Chapter 5. This fire zone is located at the structural change in geology in this area.

The apparent resistivity maps (Fig. 42 to 44) show a distinct resistivity low in the centre of the fire zone for all frequencies. About 200 to 400 m in northerly direction, a few sites are hot burning spots (mapped by red polygons). They do not strike by lower resistivity but show higher apparent resistivity in the neighbouring surroundings, as well as the spot mapped as hot burning, located south of the central part of this fire zone.

The apparent resistivities at all three frequencies show clearly a change in the geology between the western part and the south-eastern part. While at the highest frequency the western part is more resistive and the south eastern part shows lower resistivities, the apparent resistivities at the other two frequencies show also a difference between this two areas, but the difference between the apparent resistivities is not as high. Despite this little difference a change of the geology between the two parts is evident. The burning coal seam at this fire zone courses along this change, as it can be found at all three frequencies.

At the medium frequency also the centroid depth is shown for this fire zone (Fig. 45).

The classification of this fire zone by DLR characterizes fire zone no. 7 as “consistently burning fire” in 2004 and “slowly burning out fire” in 2005 (Kuenzer et al. 2006).

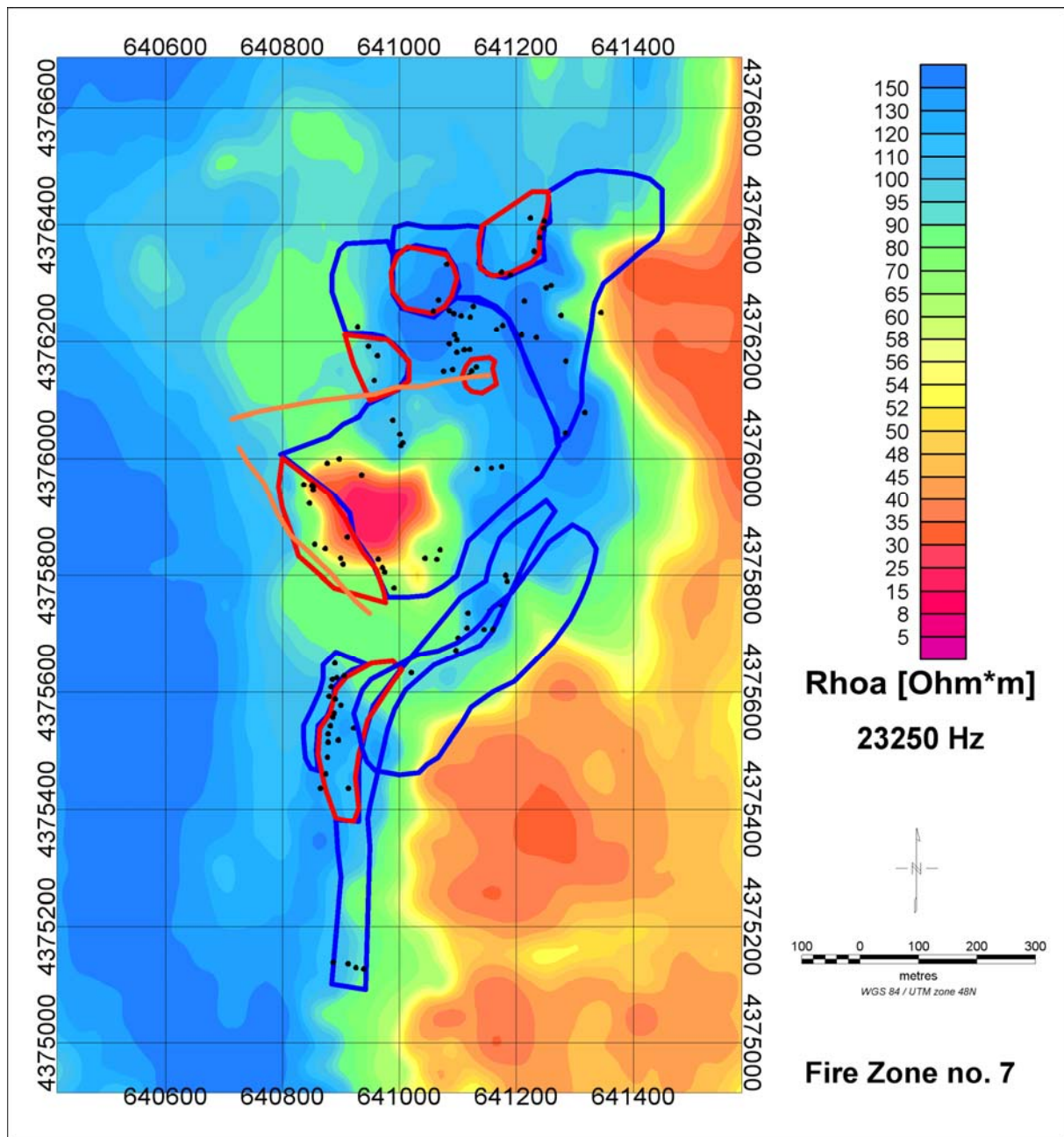


Figure 42: Map of the apparent resistivity R_{ρ} [$\text{Ohm}\cdot\text{m}$] at a frequency of 23250 Hz, derived from the helicopter survey in the vicinity of fire zone no. 7. Orange lines indicate the profiles of the VLF survey. Blue and red polygons indicate the burning zones in 2004, the black dots indicate burning spots in 2005 (mapped by DLR).

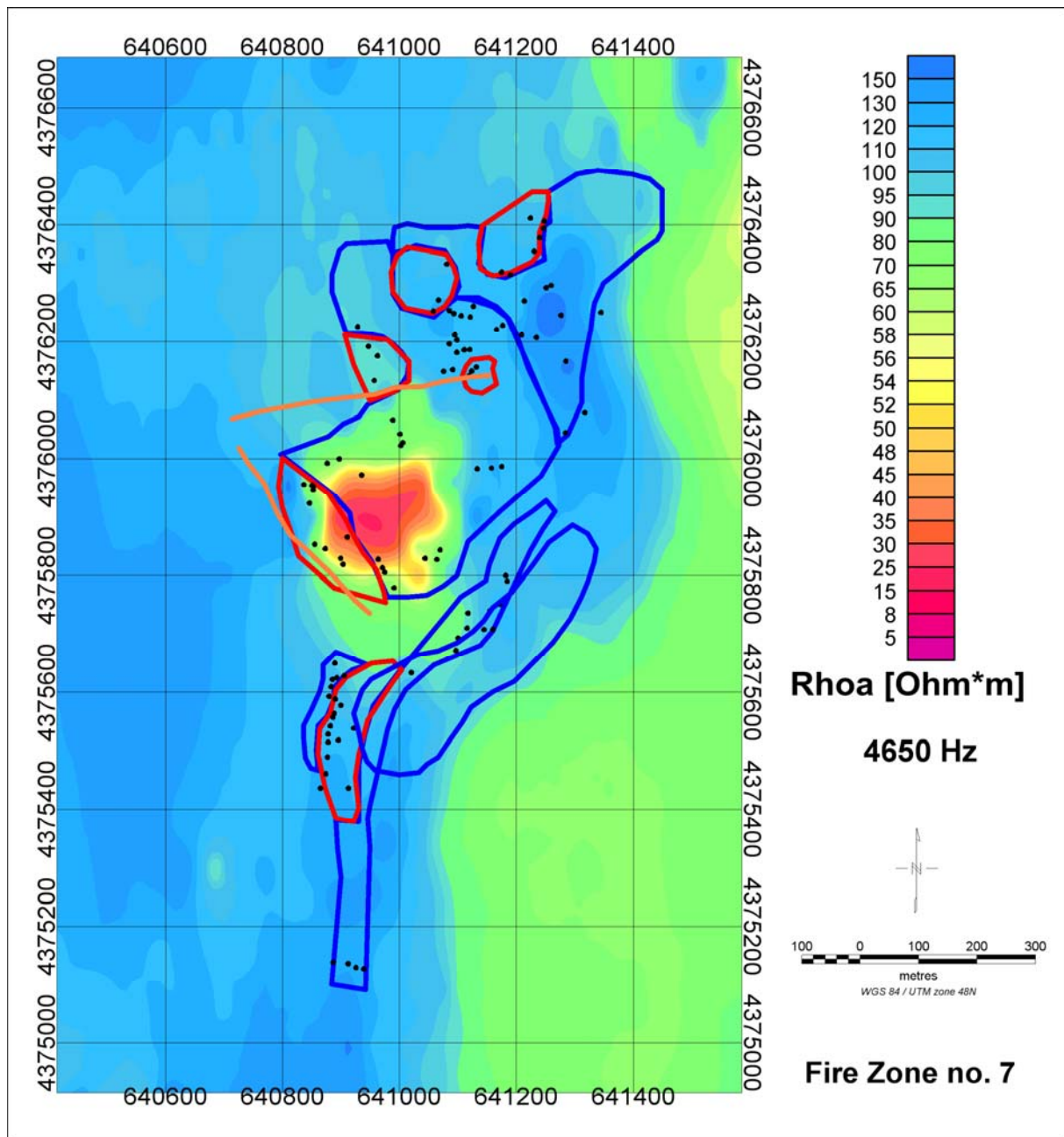


Figure 43: Map of the apparent resistivity R_{hoa} [$\text{Ohm}\cdot\text{m}$] at a frequency of 4650 Hz, derived from the helicopter survey in the vicinity of fire zone no. 7. Orange lines indicate the profiles of the VLF survey. Blue and red polygons indicate the burning zones in 2004, the black dots indicate burning spots in 2005 (mapped by DLR).

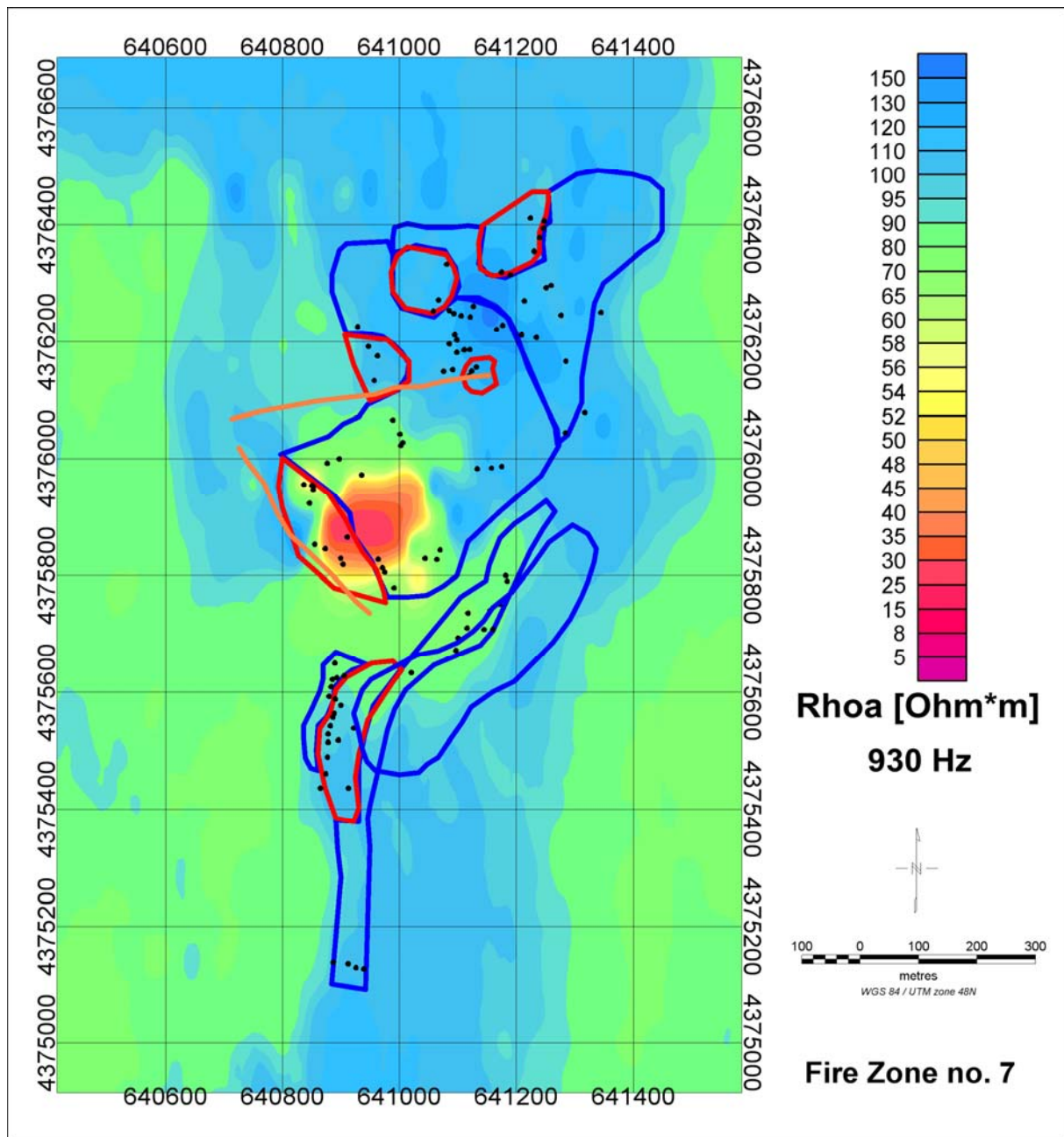


Figure 44: Map of the apparent resistivity R_{hoa} [$\text{Ohm}\cdot\text{m}$] at a frequency of 930 Hz, derived from the helicopter survey in the vicinity of fire zone no. 7. Orange lines indicate the profiles of the VLF survey. Blue and red polygons indicate the burning zones in 2004, the black dots indicate burning spots in 2005 (mapped by DLR).

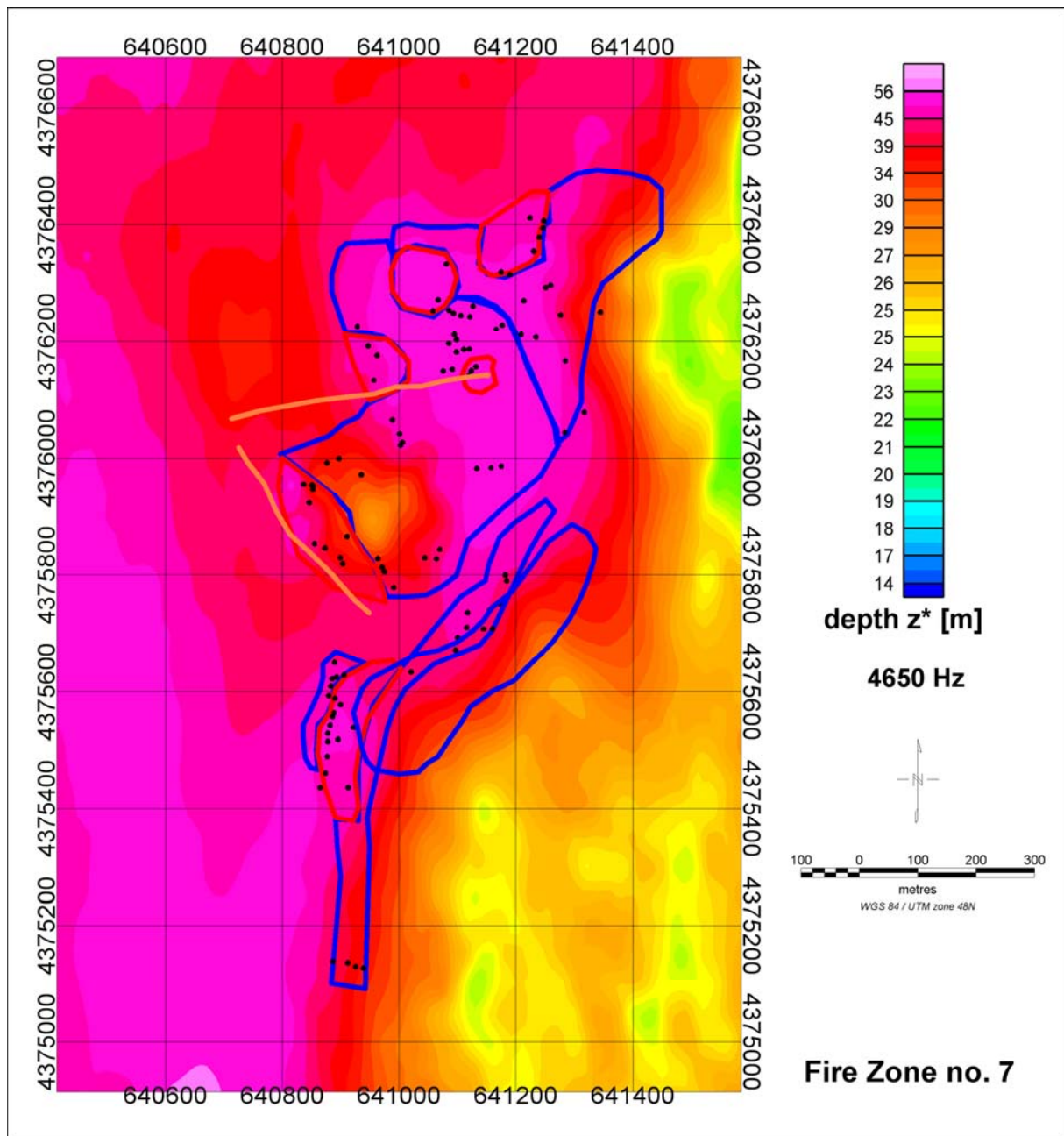


Figure 45: Map of the centroid depth [m] at a frequency of 4650 Hz, derived from the helicopter survey in the vicinity of fire zone no. 7. Orange lines indicate the profiles of the VLF survey. Blue and red polygons indicate the burning zones in 2004, the black dots indicate burning spots in 2005 (mapped by DLR).



3.6 Results from the southern part of the syncline

The locations of fire zones no. 11, no. 12, no. 13, no. 14 and the southern part of no. 8 are shown in Fig. 9 and Fig. 46. They are situated in the southern part of the syncline.

Fire zone no. 11 shows in its southern part a distinct lower resistivity at all frequencies (Fig. 46 to 48). This resistivity low cannot be found in its northern part, also mapped as burning area. The centroid depth at the medium frequency is about 30 m for this area (Fig. 49).

Fire zones no. 12 and no. 14 show sites with lower resistivities at the medium and at the lowest frequency (Fig. 47 and 48). They do not fit exactly to the polygons mapped, but they occur very close to them.

Fire zone no. 13 does not show striking changes in the apparent resistivity within the mapped polygons which could be correlated with coal seam fires.

The very southern part of fire zone no. 8 is also displayed on these apparent resistivity maps. It extends along one of the western rims of the syncline for more than 1 km. At the medium frequency two sites with slightly lower resistivity about 50 Ohm*m occur (Fig. 47). They are located in the neighbourhood to the mapped cold burning zones. The corresponding centroid depth is about 20 m (Fig. 49).

The boundary between the carboniferous strata within the syncline and the low resistive sand cover from the Gobi desert beyond the syncline in westerly direction is clearly mapped at all frequencies (Fig. 46 to 48).

The classification of fire zone no. 11, made by DLR, characterizes it as “slowly burning out fire” in 2004 and “accelerating fire” in 2005, fire zone no. 12 is characterized as “accelerating fire” in 2004 and “consistently burning fire” in 2005, fire zone no. 13 is characterized as “accelerating fire” in 2004 and “consistently burning fire” in 2005 and fire zone no. 14 is



Innovative Technologies for Exploration, Extinction and Monitoring of Coal Fires in North China
Final Report Phase A Part B

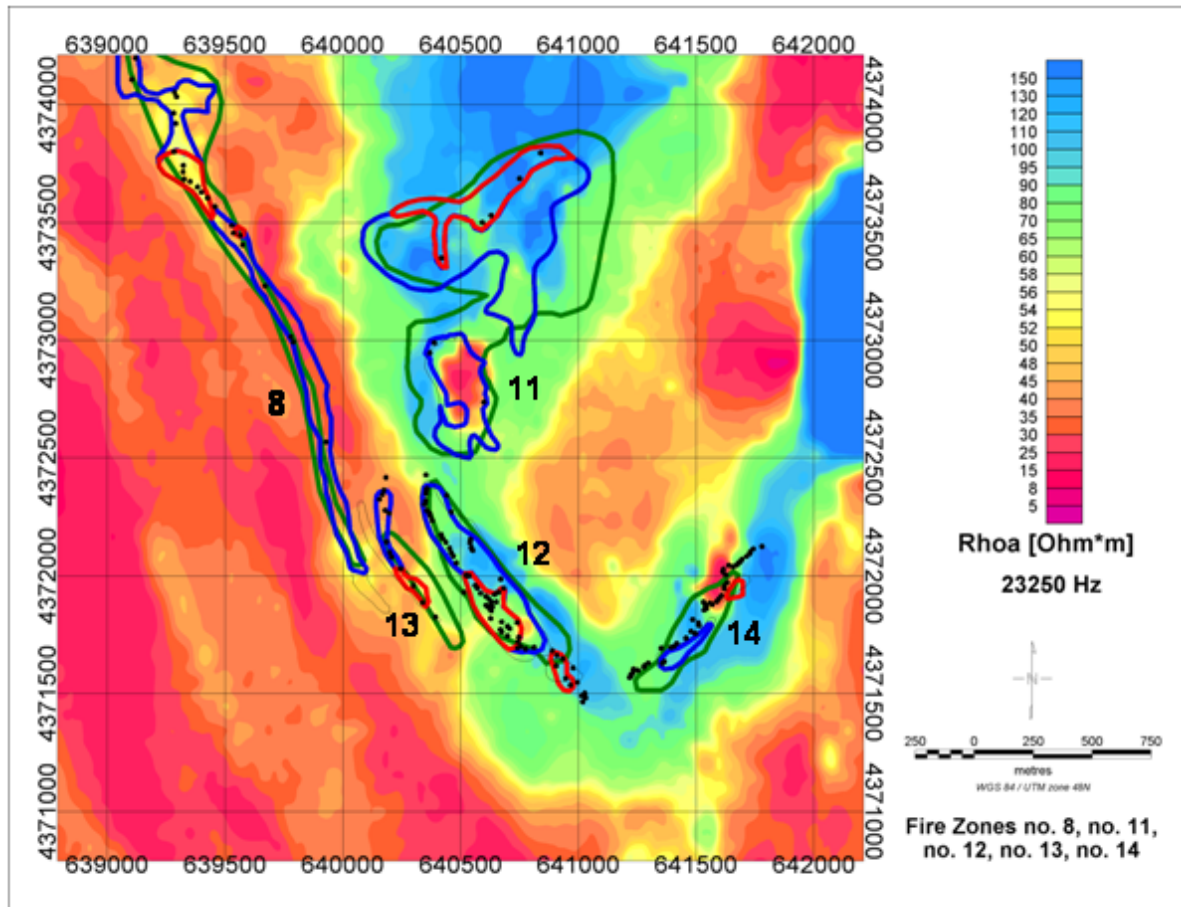


Figure 46: Map of the apparent resistivity Rhoa [Ohm*m] at a frequency of 23250 Hz, derived from the helicopter survey in the southern part of the syncline. Names of fire zones are shown by black numbers, from fire zone no. 8 the southern part is shown. Green polygons mark the fire zones in 2002, light black polygons mark the fire zones in 2003, blue and red polygons indicate the burning zones in 2004, violet polygons and black dots indicate burning spots in 2005 (mapped by DLR).



Innovative Technologies for Exploration, Extinction and Monitoring of Coal Fires in North China
Final Report Phase A Part B

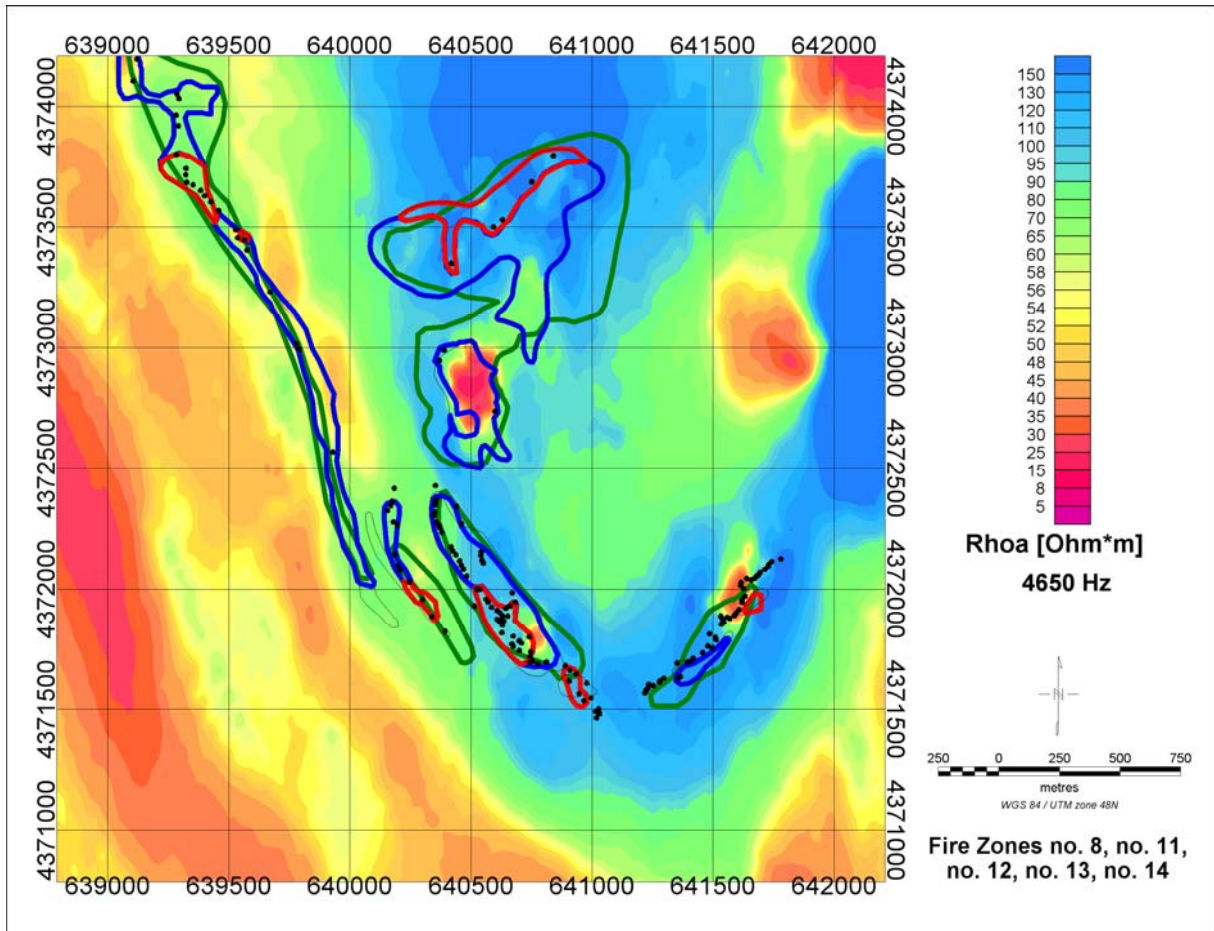


Figure 47: Map of the apparent resistivity Rhoa [Ohm*m] at a frequency of 4650 Hz, derived from the helicopter survey in the southern part of the syncline. Green polygons mark the fire zones in 2002, light black polygons mark the fire zones in 2003, blue and red polygons indicate the burning zones in 2004, violet polygons and black dots indicate burning spots in 2005 (mapped by DLR).



Innovative Technologies for Exploration, Extinction and Monitoring of Coal Fires in North China
Final Report Phase A Part B

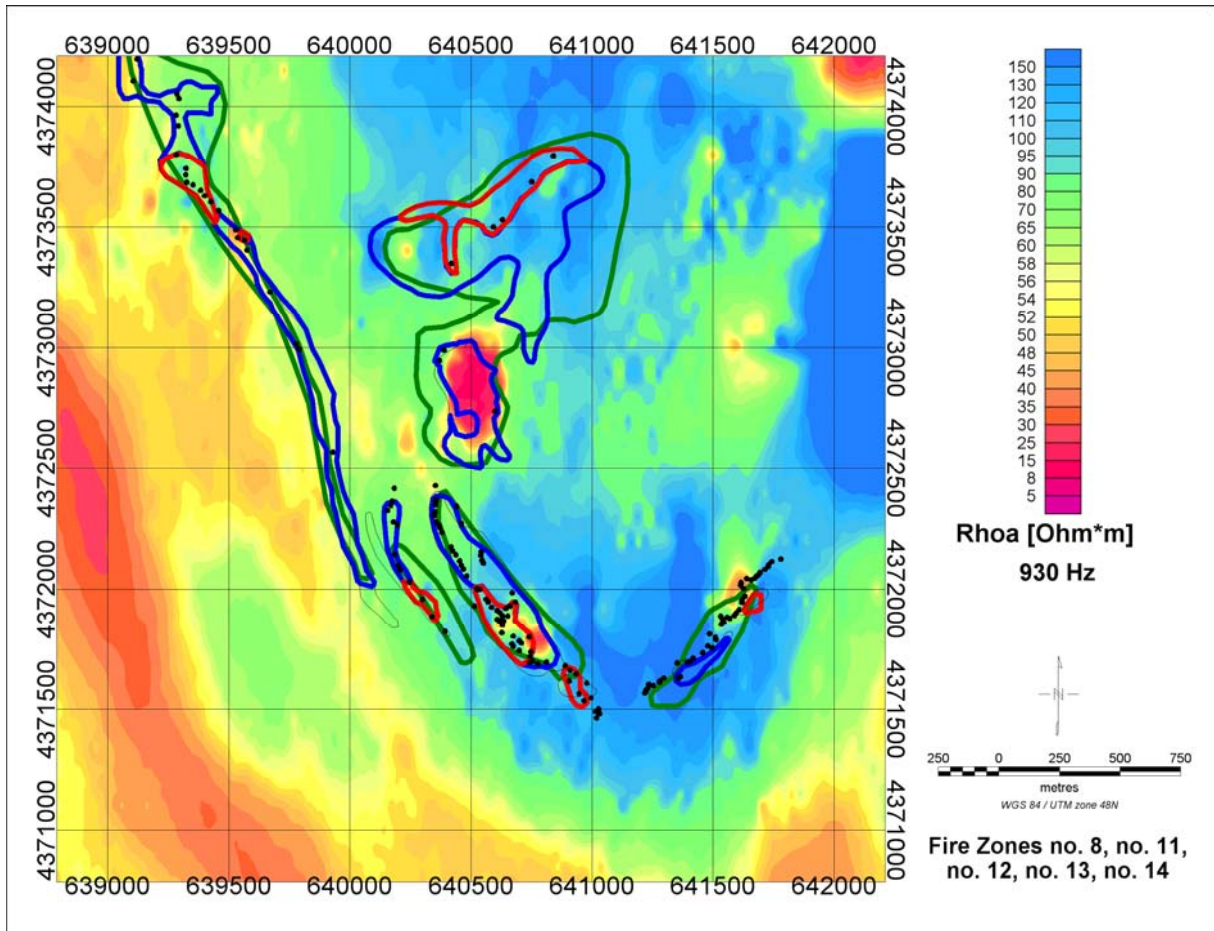


Figure 48: Map of the apparent resistivity Rhoa [Ohm*m] at a frequency of 930 Hz, derived from the helicopter survey in the southern part of the syncline. Green polygons mark the fire zones in 2002, light black polygons mark the fire zones in 2003, blue and red polygons indicate the burning zones in 2004, violet polygons and black dots indicate burning spots in 2005 (mapped by DLR).



Innovative Technologies for Exploration, Extinction and Monitoring of Coal Fires in North China
Final Report Phase A Part B

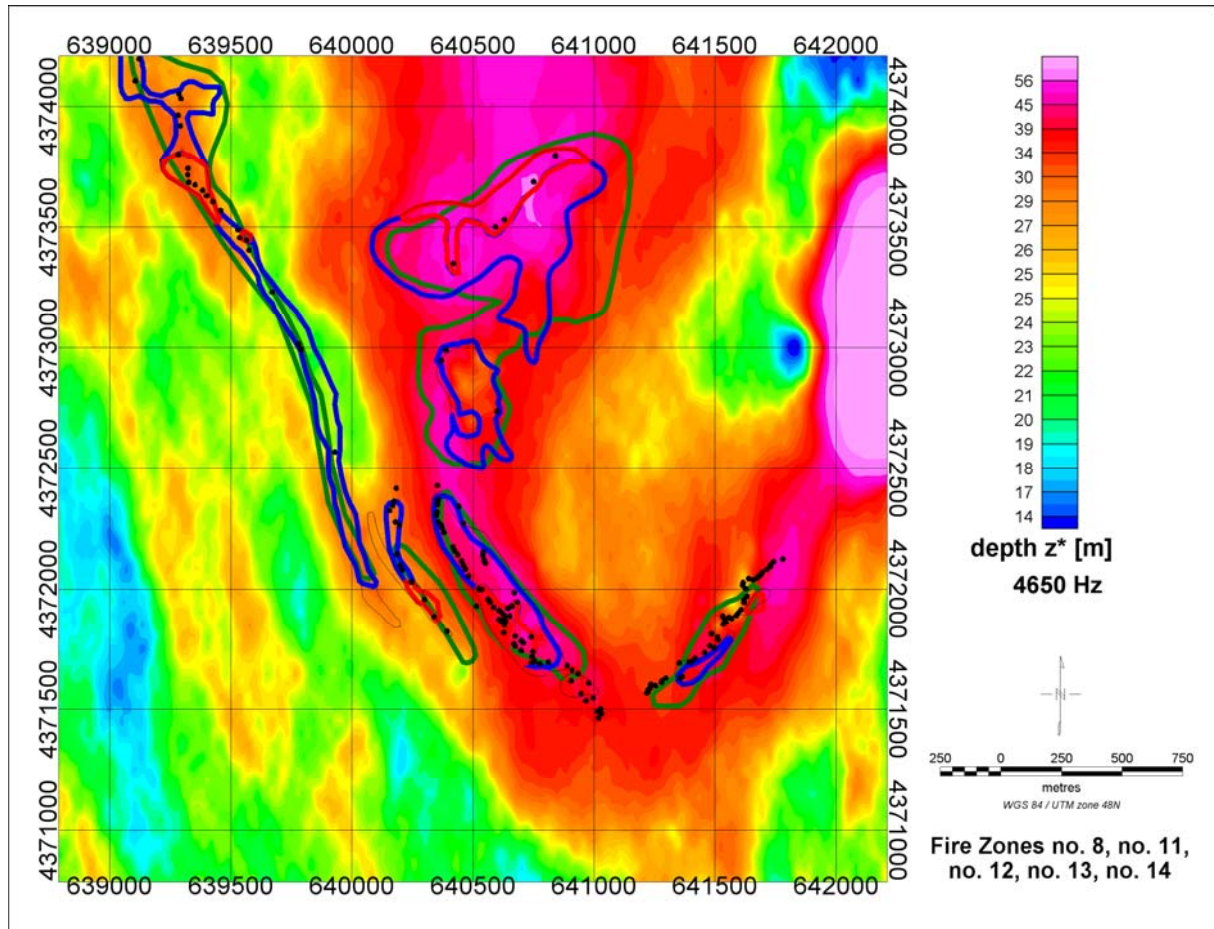


Figure 49: Map of the centroid depth [m] at a frequency of 4650 Hz, derived from the helicopter survey in the southern part of the syncline. Green polygons mark the fire zones in 2002, light black polygons mark the fire zones in 2003, blue and red polygons indicate the burning zones in 2004, violet polygons and black dots indicate burning spots in 2005 (mapped by DLR).



3.7 Vertical sections for selected flight lines over the fire zones

For a few flight lines crossing the fire zones 1-D vertical resistivity sections are presented. Figures 50 to 53 show the path of these selected lines. Figures 54 to 73 show the inphase and quadrature values at three frequencies on a logarithmic scale, the vertical sections of the apparent resistivity and the 1-D inversion models, and misfit of the inversion. All flight lines are plotted from west to east. So the changes of the HEM survey results are observable in south-northerly direction. Although there is only a selection of about 20 lines out of 289 profile lines, the lines display the most important features for the fire zones investigated. The fire zones are marked by vertical black lines. Currently burning parts of the fire zones can be found within this delimitation, in most cases they are much smaller than the sections shown but of unknown lateral and depth extension.

Flight lines 2220, 2240, 2270, 2280, 2290 and 2390 cross fire zone no. 8, (Fig. 50, 54-59). Within the central part of the fire zone a highly resistive cover is determined especially at flight lines 2280 and 2290 (Fig. 57 and 58). These two lines cross the heavily burning part of fire zone no. 8 south of the plateau. Below this resistive cover a zone of lower resistivity is determined (third layer in the model), especially at lines 2270 and 2290 (Fig. 56 and 58). Its depth is estimated about 20 to 30 m and its lateral extension about 200 m or less. Striking at the vertical resistivity sections of all these flight lines is a change in the resistivities of the layers within the centre of the fire zone. It can be seen best at flight lines 2270, 2280, 2290 and 2390.

Flight lines 2220 and 2240, which are located about 200 m south of this currently burning part, show only slightly lower resistivities at this depth (Fig. 54 and 55). They cross the already burnt collapsed part of the fire zone with only single burning spots.

Flight line 2390 crosses fire zone no. 8 further to the north. It also shows a lower resistivity in the third layer at a depth of approximately 50 m (Fig. 59). In the eastern part of the delimited section a lower resistivity is determined, corresponding to the maps of the apparent resistivity for this area. The zones of lower resistivity are very small and similar results are determined along the flight lines at places without known fires. To attach these results to coal seam fires they have to be considered carefully and using all known facts about this area. A striking result can hardly be found, but hints for a correlation of the fires to zones of lower resistivity are determined.

The vertical sections along the flight lines 3110, 3120, 3130 and 3140 (fire zone no. 3.2, Fig. 51) are shown in Fig. 60 to 63. Because of the greater extension of the defined fire zone a second delimitation within is given which marks the currently burning part. A cover of high resistivity is determined on all flight lines within this delimitation. Below this cover a layer with slightly lower resistivity occurs, but it is not very striking. For the part to the east of the active burning zone a highly resistive cover above a layer with lower resistivity is determined at flight lines 3130 and 3140. It cannot be related to burning zones mapped. Similar to fire zone no. 8, a striking change at the vertical resistivity sections of all these flight lines occur within the centre of the fire zone. It can be seen at all vertical resistivity sections presented (Fig. 60 to 63). The correlation of the results from the HEM survey to coal seam fires seems to be difficult at this fire zone.

Flight lines 1680, 1700, 1720 and 1740 cross fire zones no. 12, no. 13 and no. 14 in the southern part of the syncline (Fig. 52). While on flight line 1680 only at fire zone no. 13 a highly resistive cover is determined, it appears at line 1700 for fire zone no. 14 and slightly



**Innovative Technologies for Exploration, Extinction and Monitoring of Coal Fires in North China
Final Report Phase A Part B**

for fire zone no. 12 at line 1740. From lines 1700 to 1740 a low resistivity appears in the second layer below the resistive cover, striking at lines 1700 and 1720. For flight line 1740, which is located to the north of the others, also a slightly lower resistivity for fire zone no. 12 is determined below the resistive cover. The hot burning part of fire zone no. 12 starts a few hundreds of metres further to the north than the hot burning part of fire zone no. 13, mapped by DLR. The estimated depth from the vertical section for the beginning of the conductive layer is about 20 m for fire zone no. 13 and about 20 m for fire zone no. 14 (Fig. 64 to 67). There is little knowledge about these fire zones and no information available about the depths of the fires. Also mining activities can be found in this area and could cause lower resistivities in the subsurface.

Flight line 2050 (Fig. 52) represents a result above fire zone no. 11 (Fig. 72). Although this fire zone is classified as slowly burning out in 2004 when the helicopter survey took place, it was again an active burning zone in 2005. A highly resistive cover is determined almost over the whole part of the fire zone, but zones of lower resistivity can hardly be found. It was not accessible for the ground survey.

Fire zone no. 7 in the centre of the syncline shows striking apparent resistivities at all frequencies at its burning part. Flight line 2490 crosses to the south of the biggest active part of the burning zone and the vertical resistivity section shows a highly resistive cover in the western part of the fire zone. At lines 2500 and 2510 a striking low resistivity below the resistive cover can be found (Fig. 68 to 70). At flight line 2540 this low resistivity is not determined anymore (Fig. 71). It passes just to the north of the biggest active burning part of this fire zone. The described highly conductive layer caused investigations in this area by ground geophysical measurements. Mining activities are located close to this burnt fire zone.

Flight line 2120 crosses coal seams no. 6 and no. 7 (Fig. 50), which are classified as not burning seams. At the point of interest (corresponding to the TEM ground survey) no highly resistive cover and no layer with lower resistivity in the subsurface are determined (Fig. 73).



Innovative Technologies for Exploration, Extinction and Monitoring of Coal Fires in North China
Final Report Phase A Part B

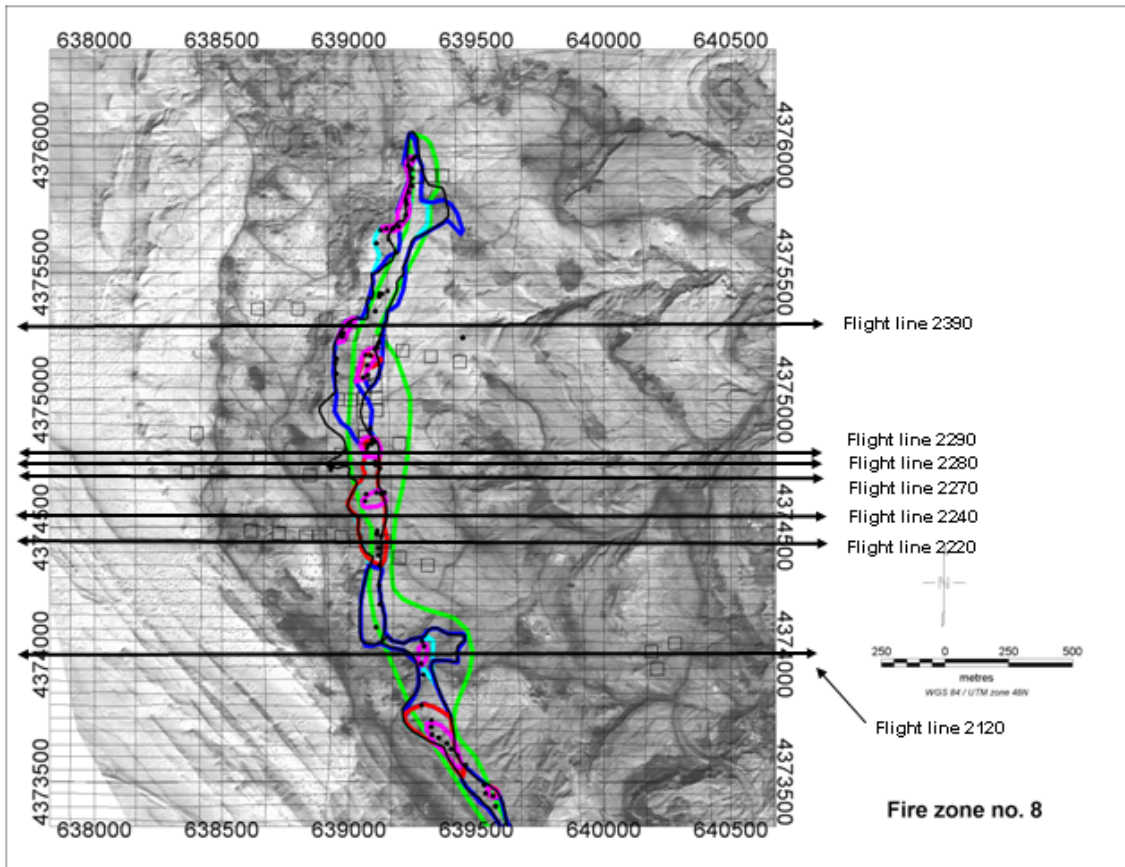


Figure 50: Path of the selected flight lines crossing fire zone no. 8. Light black squares show the sites of the TEM ground survey, green polygons mark the fire zones in 2002, light black polygons mark the fire zones in 2003, blue and red polygons indicate the burning zones in 2004, light blue and violet polygons and black dots indicate burning spots in 2005 (mapped by DLR).



Innovative Technologies for Exploration, Extinction and Monitoring of Coal Fires in North China
Final Report Phase A Part B

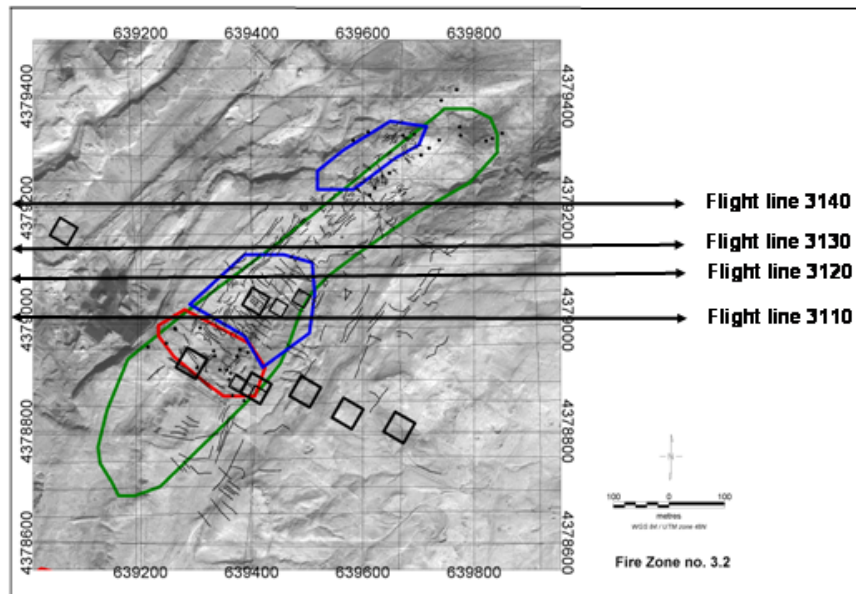


Figure 51: Path of the selected flight lines crossing fire zone no. 3.2. Black squares show the sites of the TEM ground survey, green polygons mark the fire zones in 2002, light black polygons mark the fire zones in 2003, blue and red polygons indicate the burning zones in 2004 and black dots indicate burning spots in 2005 (mapped by DLR).

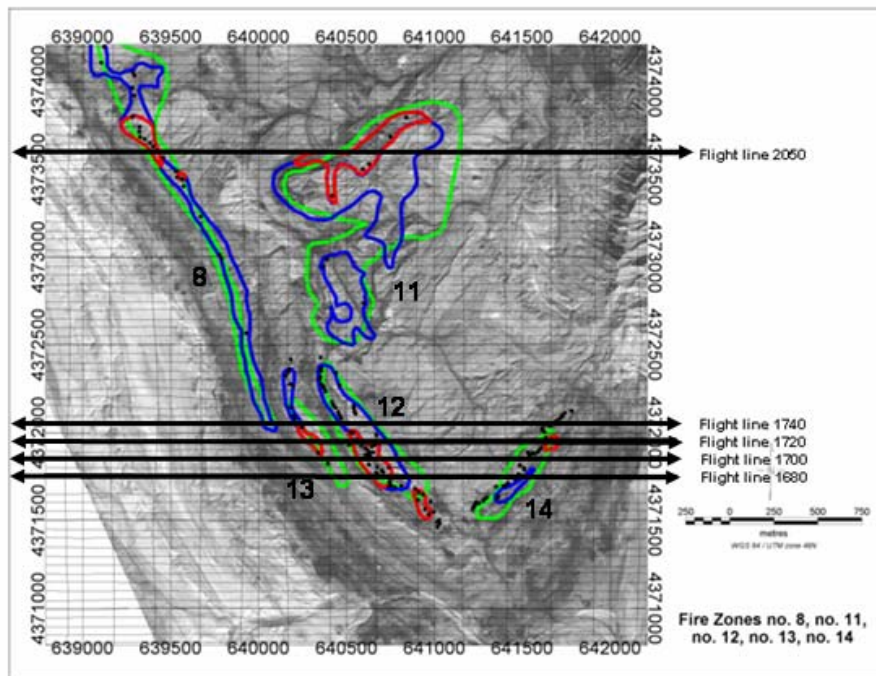


Figure 52: Path of the selected flight lines crossing fire zones no. 11, no. 12, no. 13 and no. 14. Green polygons mark the fire zones in 2002, light black polygons mark the fire zones in 2003, blue and red polygons indicate the burning zones in 2004 and black dots indicate burning spots in 2005 (mapped by DLR).

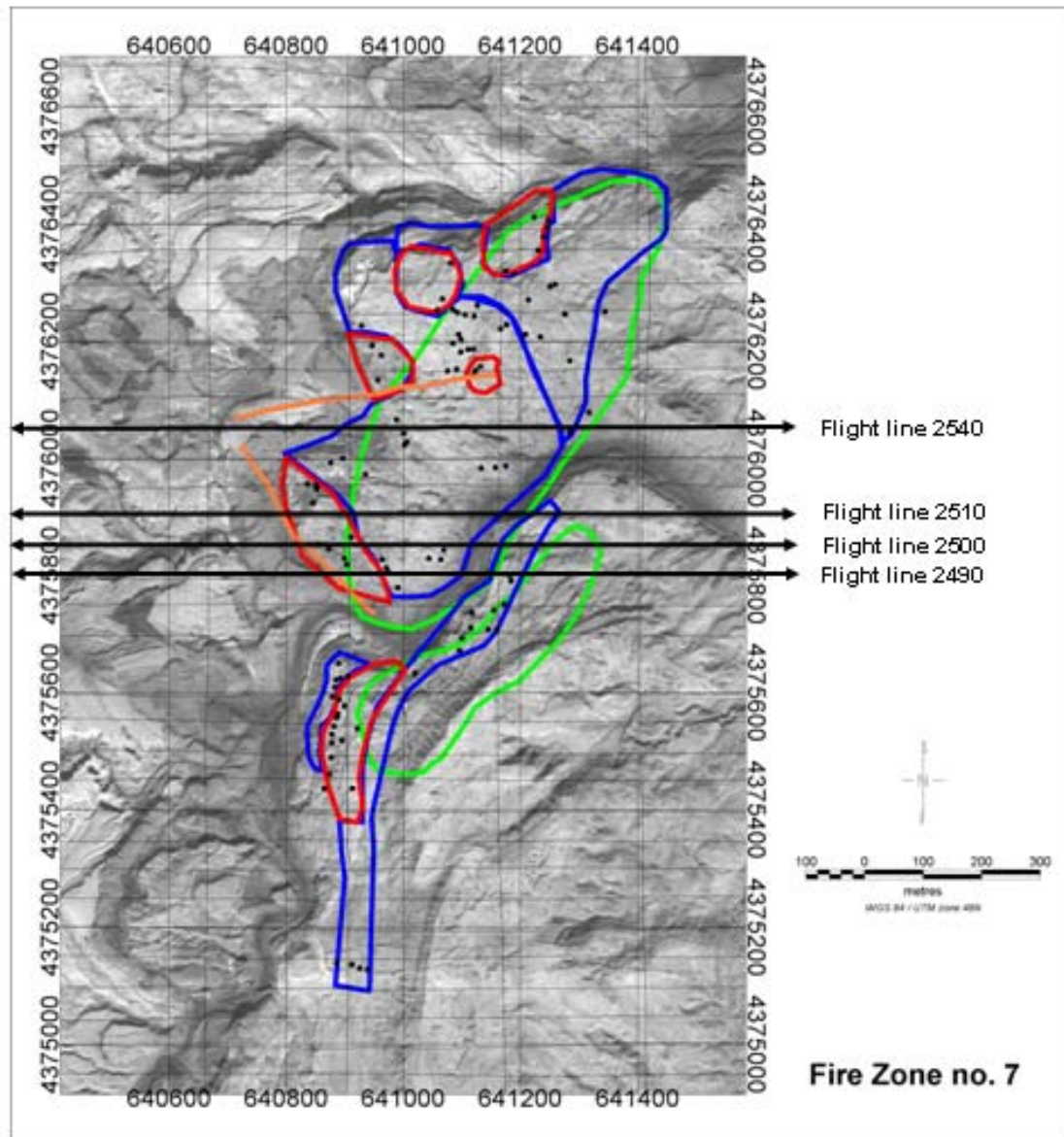


Figure 53: Path of the selected flight lines crossing fire zone no. 7. Orange lines mark the HL survey lines, green polygons mark the fire zones in 2002, light black polygons mark the fire zones in 2003, blue and red polygons indicate the burning zones in 2004 and black dots indicate burning spots in 2005 (mapped by DLR).

At most of the burning sites highly conductive layers below a resistive cover are determined, but this result cannot be generalized for all presented fire zones. The absence of knowledge about most of the introduced fire zones and no or only small information about the depths of the fires makes an interpretation difficult. Mining activities are scattered in the areas close to burning coal seams and can also cause lower resistivities in the subsurface at that places.



Wuda

Profil : L222.0:19914

horizontal-coplanar coil system, $r = 6.50$ m

EM sensor height: 32 – 72 m

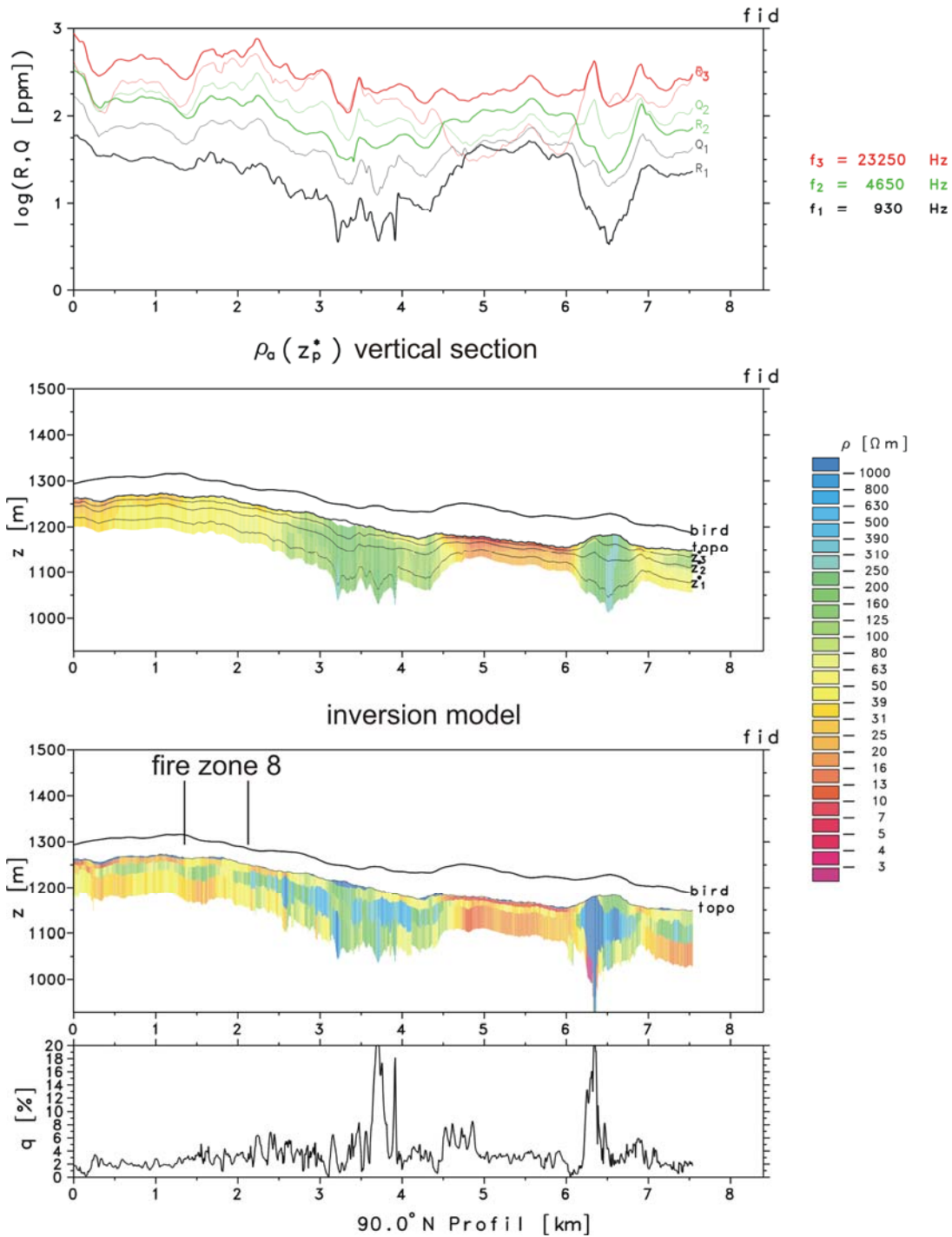


Figure 54: Inphase and quadrature values at three frequencies, vertical apparent resistivity section, 1-D vertical resistivity section and misfit along profile 2220, crossing fire zone no. 8.



Innovative Technologies for Exploration, Extinction and Monitoring of Coal Fires in North China
 Final Report Phase A Part B

Wuda

Profil : L224.0:19915
 horizontal-coplanar coil system, $r = 6.50$ m
 EM sensor height: 37 – 74 m

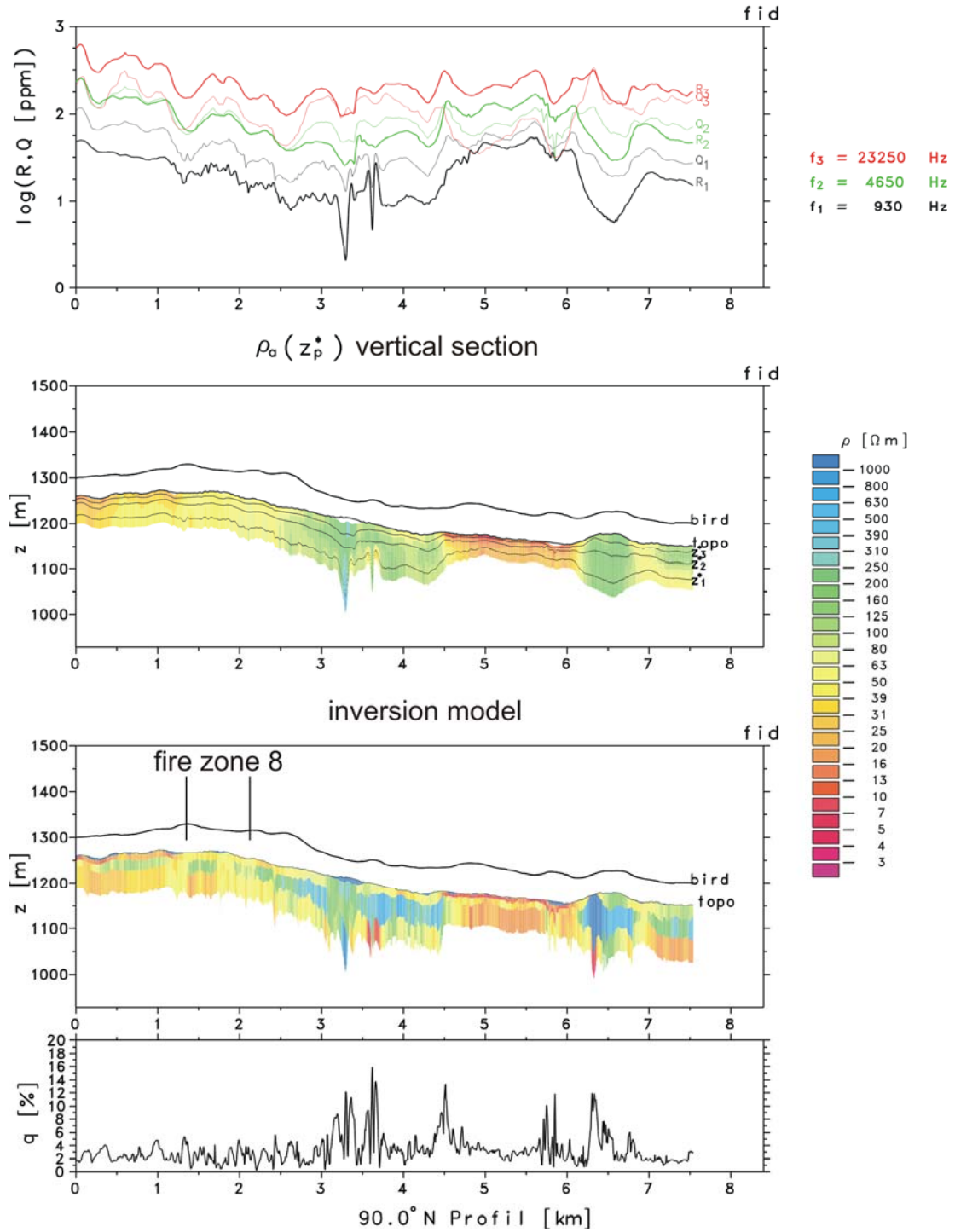


Figure 55: Inphase and quadrature values at three frequencies, vertical apparent resistivity section, 1-D vertical resistivity section and misfit along profile 2240, crossing fire zone no. 8.



Wuda

Profil : L227.0:19915

horizontal-coplanar coil system, $r = 6.50$ m

EM sensor height: 35 – 71 m

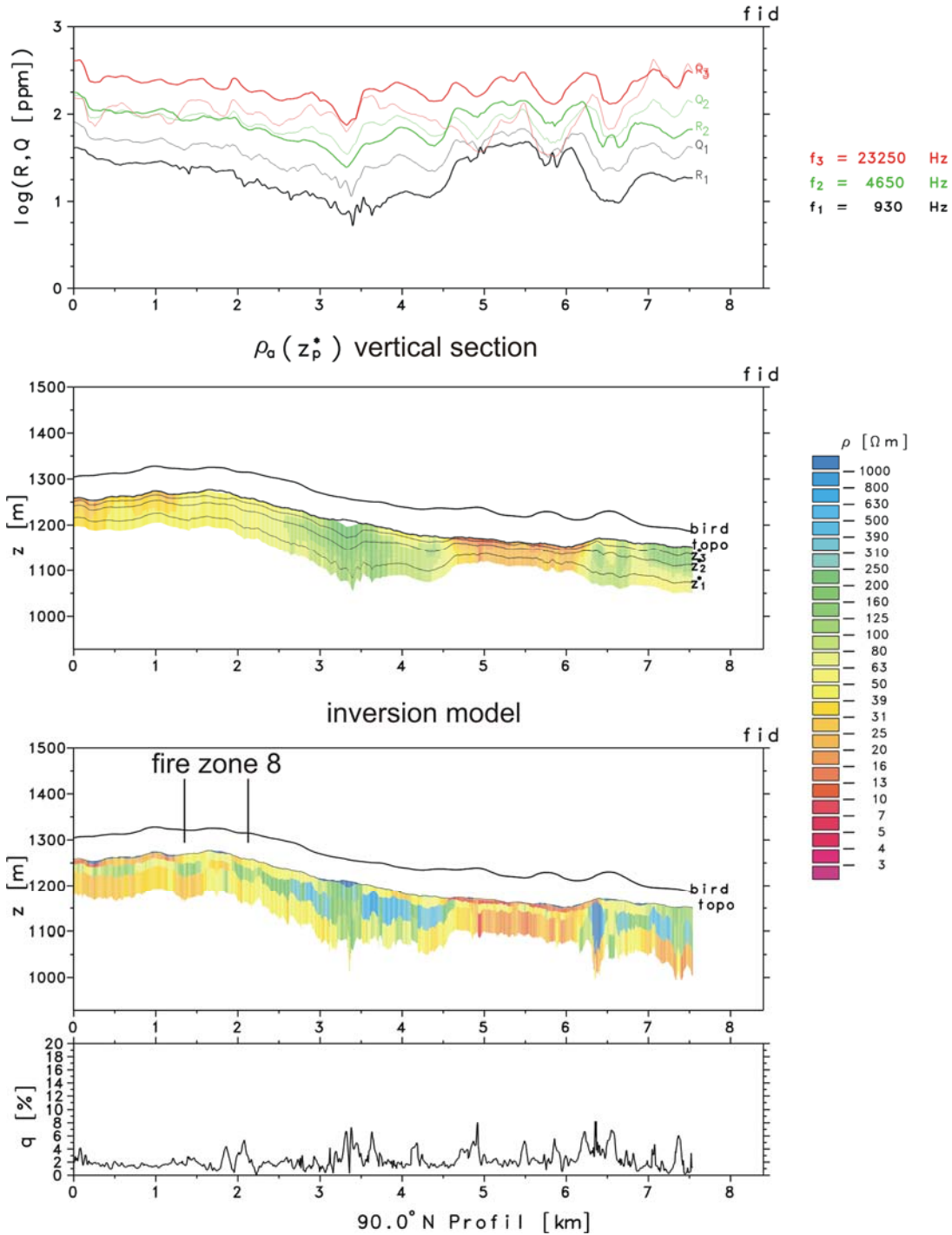


Figure 56: Inphase and quadrature values at three frequencies, vertical apparent resistivity section, 1-D vertical resistivity section and misfit along profile 2270, crossing fire zone no. 8.



Wuda

Profil : L228.0:19915

horizontal-coplanar coil system, $r = 6.50$ m

EM sensor height: 33 – 71 m

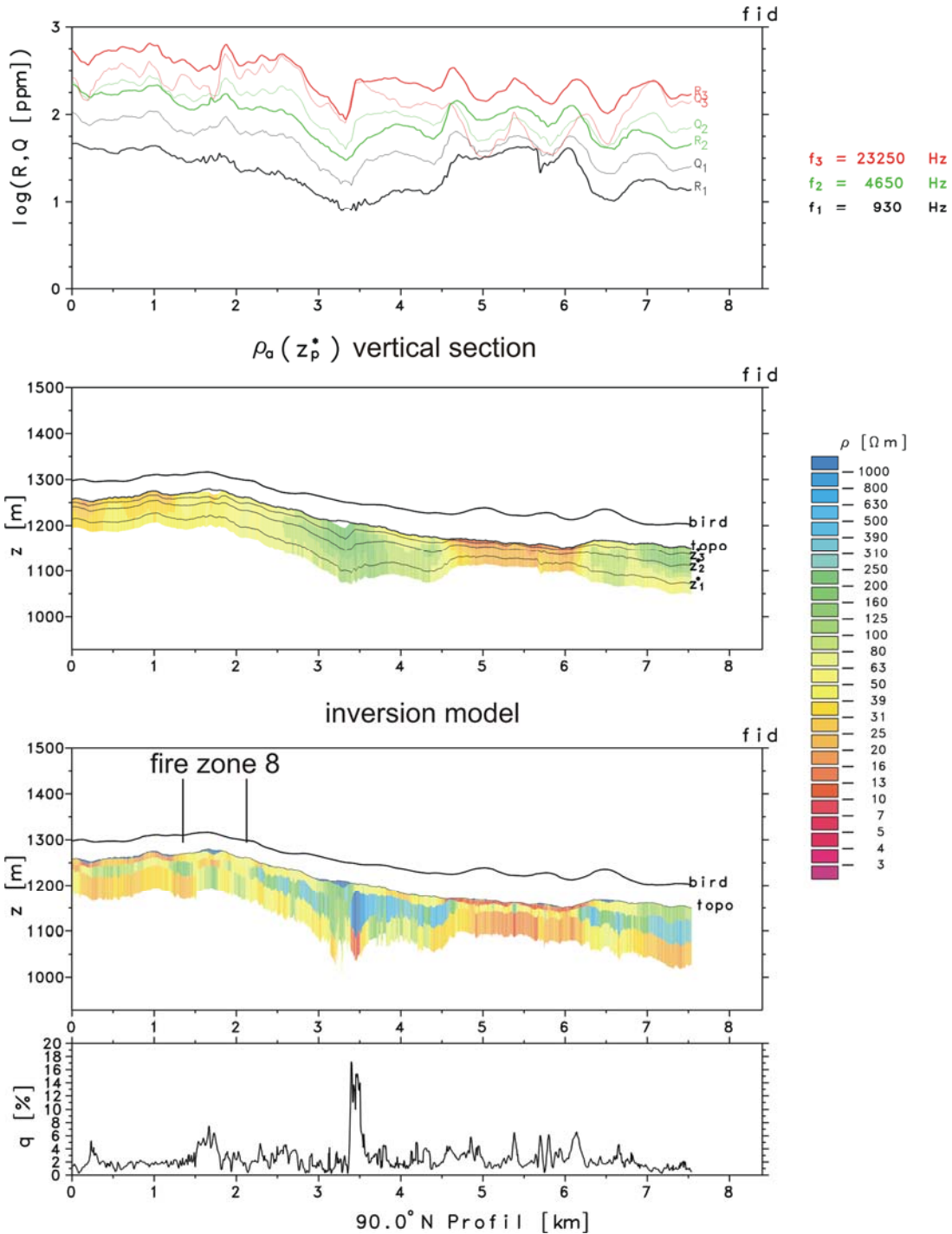


Figure 57: Inphase and quadrature values at three frequencies, vertical apparent resistivity section, 1-D vertical resistivity section and misfit along profile 2280, crossing fire zone no. 8.



Wuda

Profil : L229.0:19915
 horizontal-coplanar coil system, r = 6.50 m
 EM sensor height: 38 – 66 m

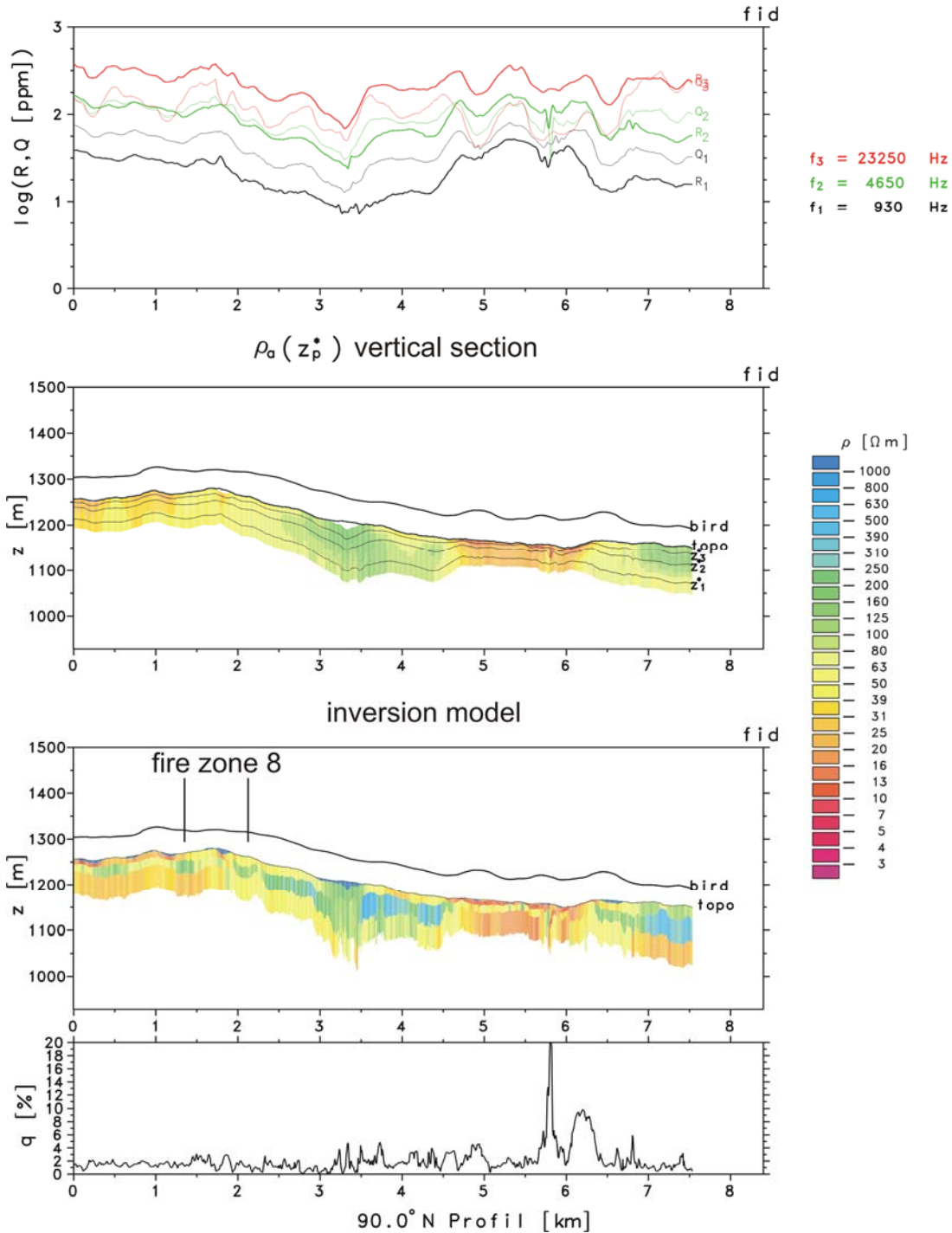


Figure 58: Inphase and quadrature values at three frequencies, vertical apparent resistivity section, 1-D vertical resistivity section and misfit along profile 2290, crossing fire zone no. 8.



Wuda

Profil : L239.0:19915

horizontal-coplanar coil system, r = 6.50 m

EM sensor height: 36 – 73 m

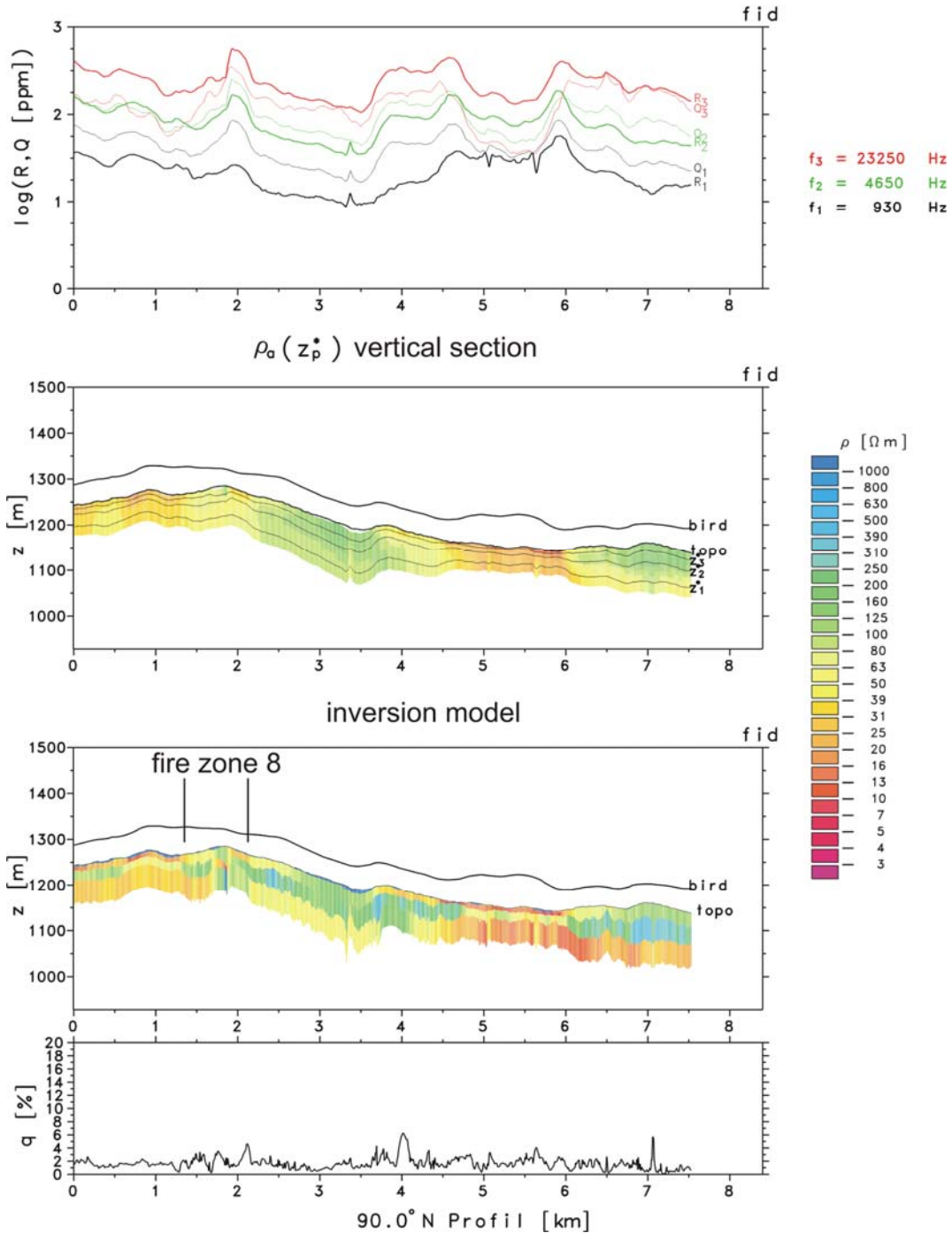


Figure 59: Inphase and quadrature values at three frequencies, vertical apparent resistivity section, 1-D vertical resistivity section and misfit along profile 2390, crossing fire zone no. 8.



Innovative Technologies for Exploration, Extinction and Monitoring of Coal Fires in North China
Final Report Phase A Part B

Wuda

Profil : L311.0:19910

horizontal-coplanar coil system, $r = 6.50$ m

EM sensor height: 33 – 77 m

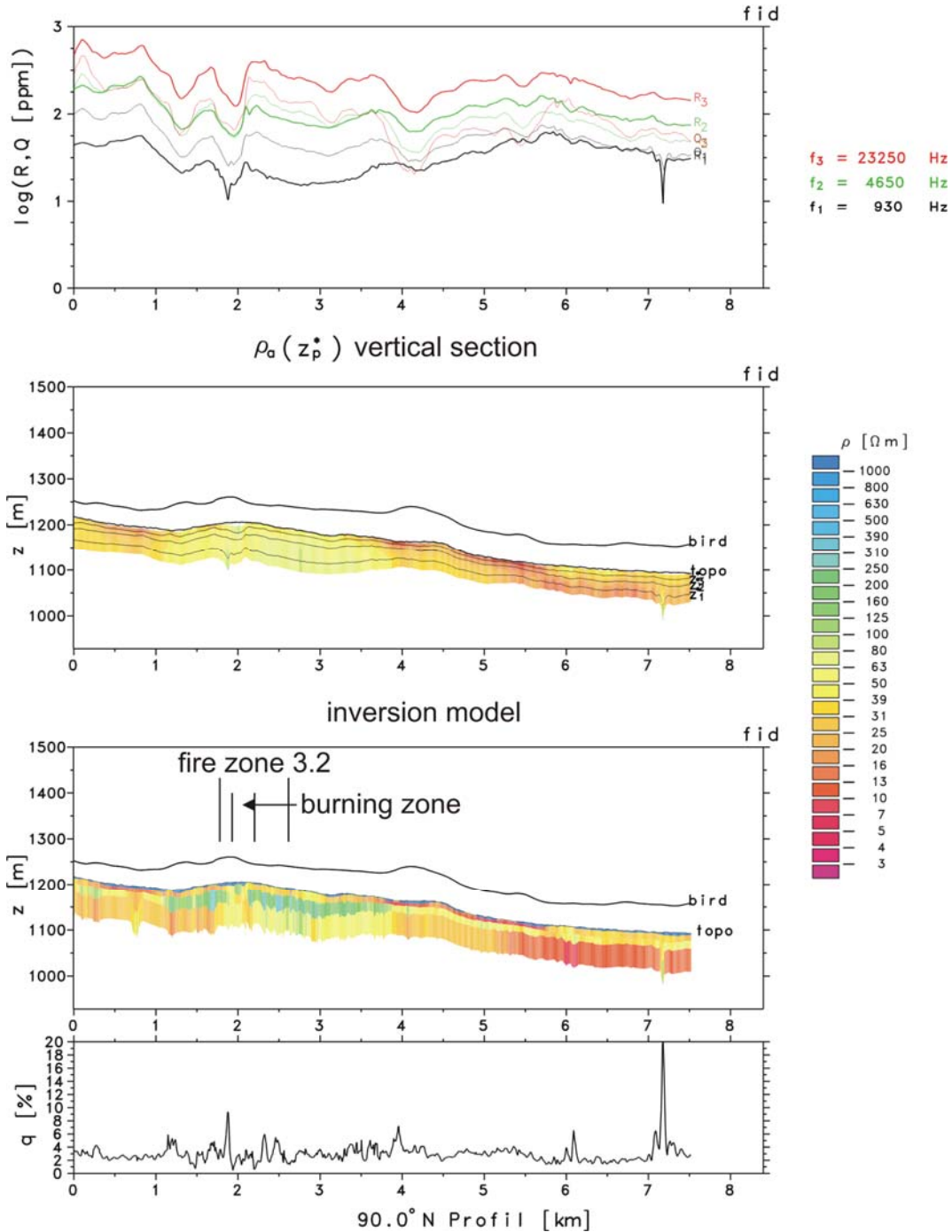


Figure 60: Inphase and quadrature values at three frequencies, vertical apparent resistivity section, 1-D vertical resistivity section and misfit along profile 3110, crossing fire zone no. 3.2.



Wuda

Profil : L312.0:19910
horizontal-coplanar coil system, r = 6.50 m
EM sensor height: 37– 90 m

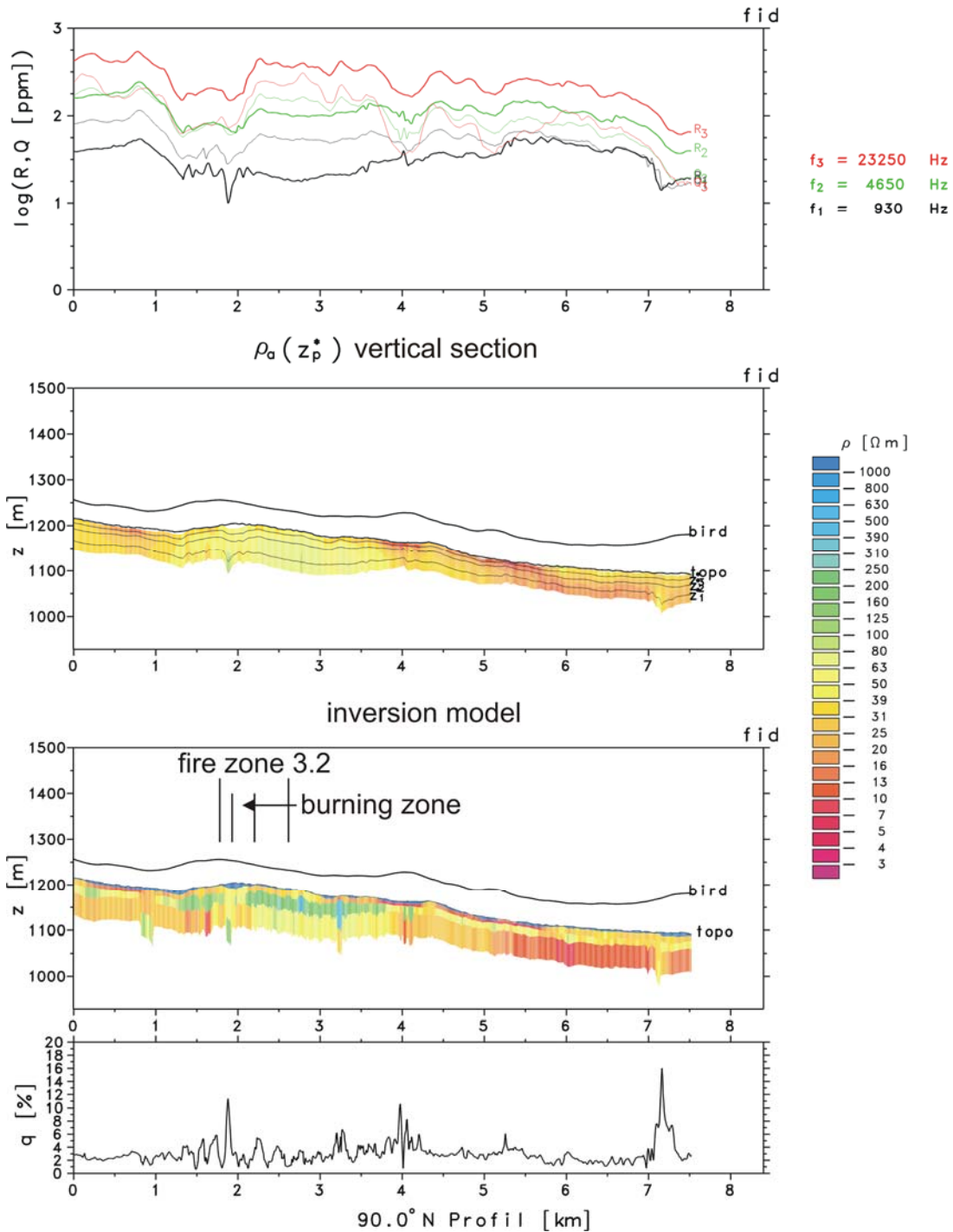


Figure 61: Inphase and quadrature values at three frequencies, vertical apparent resistivity section, 1-D vertical resistivity section and misfit along profile 3120, crossing fire zone no. 3.2.



Innovative Technologies for Exploration, Extinction and Monitoring of Coal Fires in North China
Final Report Phase A Part B

Wuda

Profil : L313.0:19910

horizontal-coplanar coil system, $r = 6.50$ m

EM sensor height: 36 – 75 m

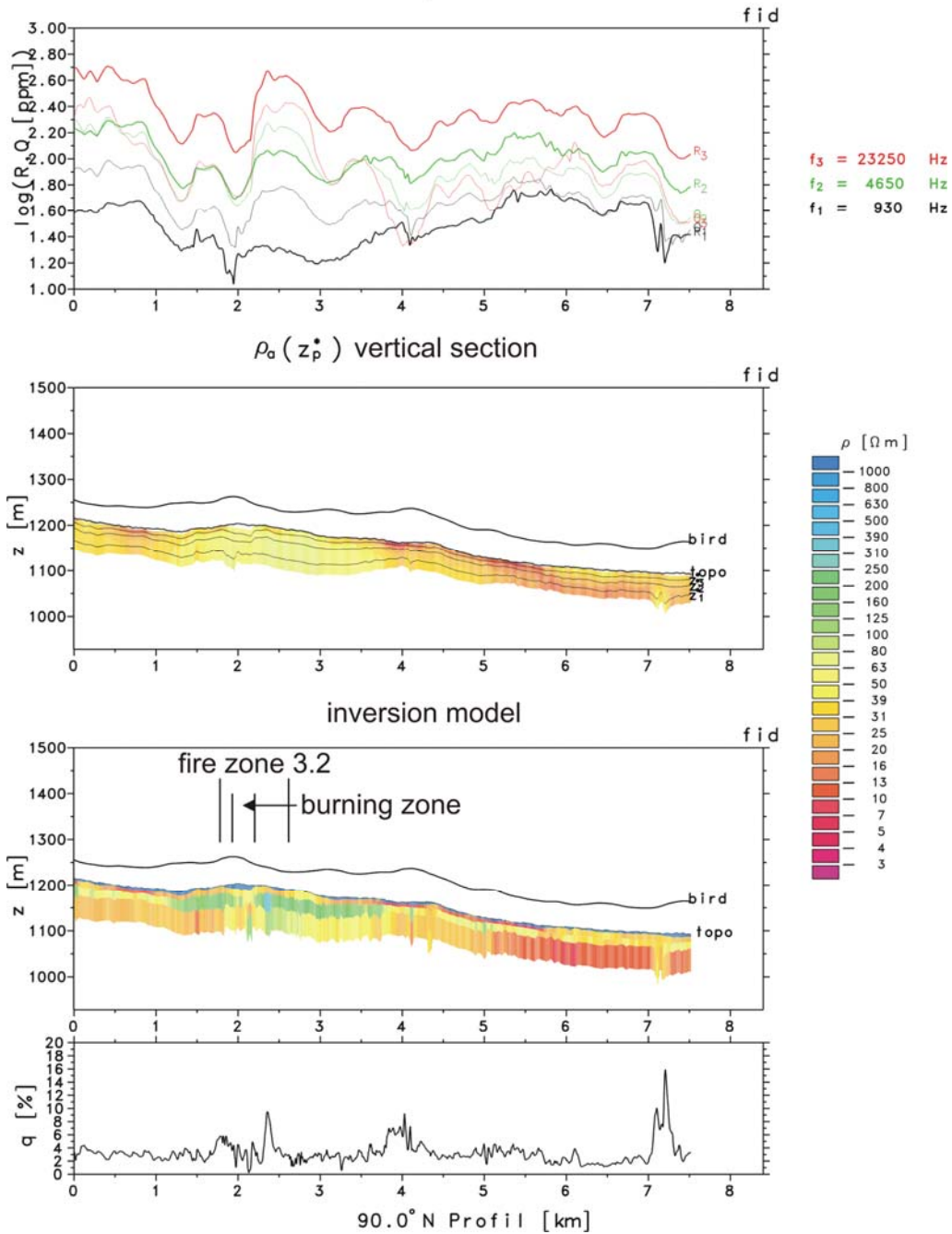


Figure 62: Inphase and quadrature values at three frequencies, vertical apparent resistivity section, 1-D vertical resistivity section and misfit along profile 3130, crossing fire zone no. 3.2.



Innovative Technologies for Exploration, Extinction and Monitoring of Coal Fires in North China
Final Report Phase A Part B

Wuda

Profil : L314.0:19911
horizontal-coplanar coil system, r = 6.50 m
EM sensor height: 31 – 69 m

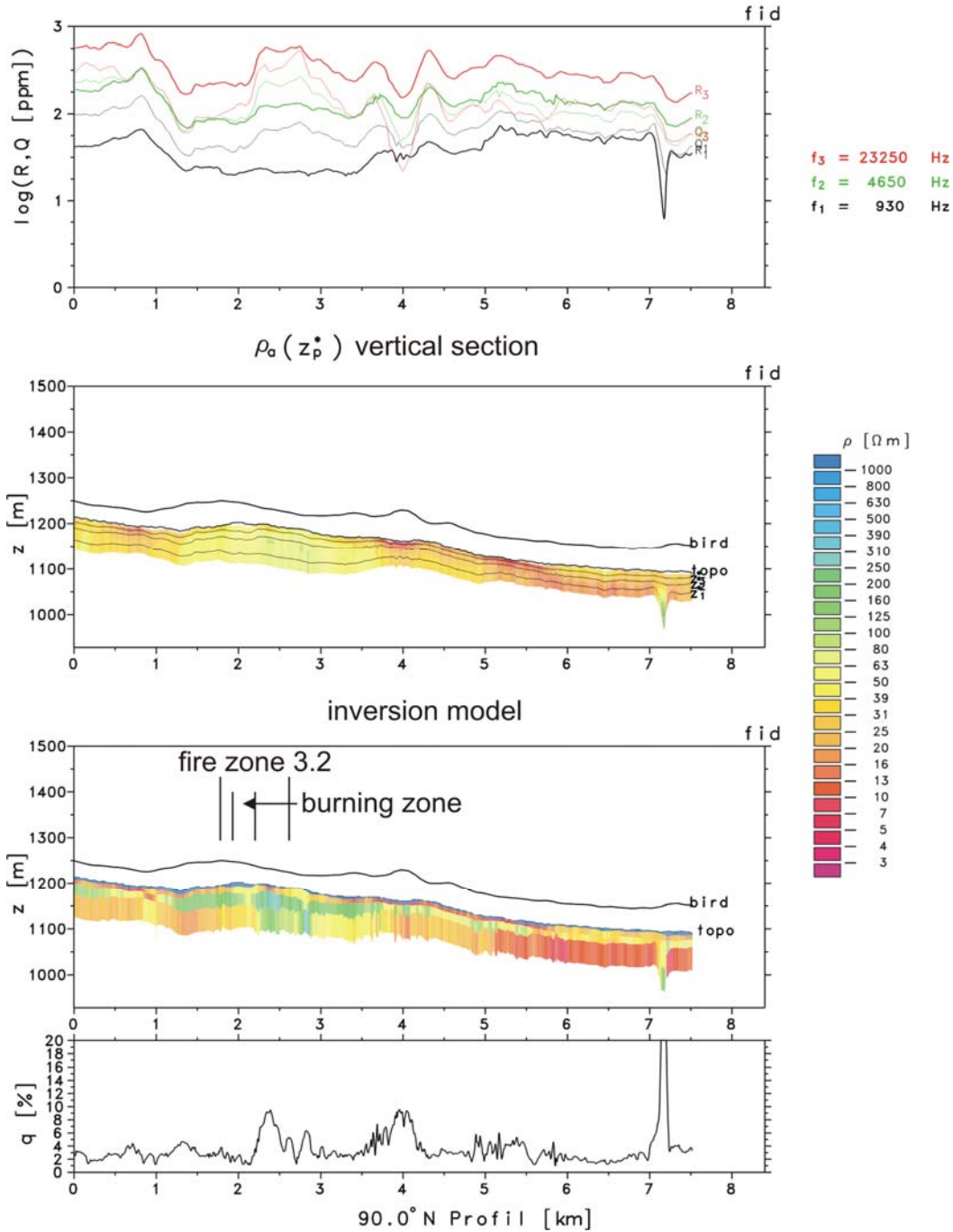


Figure 63: Inphase and quadrature values at three frequencies, vertical apparent resistivity section, 1-D vertical resistivity section and misfit along profile 3140, crossing fire zone no. 3.2.



Innovative Technologies for Exploration, Extinction and Monitoring of Coal Fires in North China
 Final Report Phase A Part B

Wuda

Profil : L170.0:19907
 horizontal-coplanar coil system, $r = 6.50$ m
 EM sensor height: 24 – 100 m

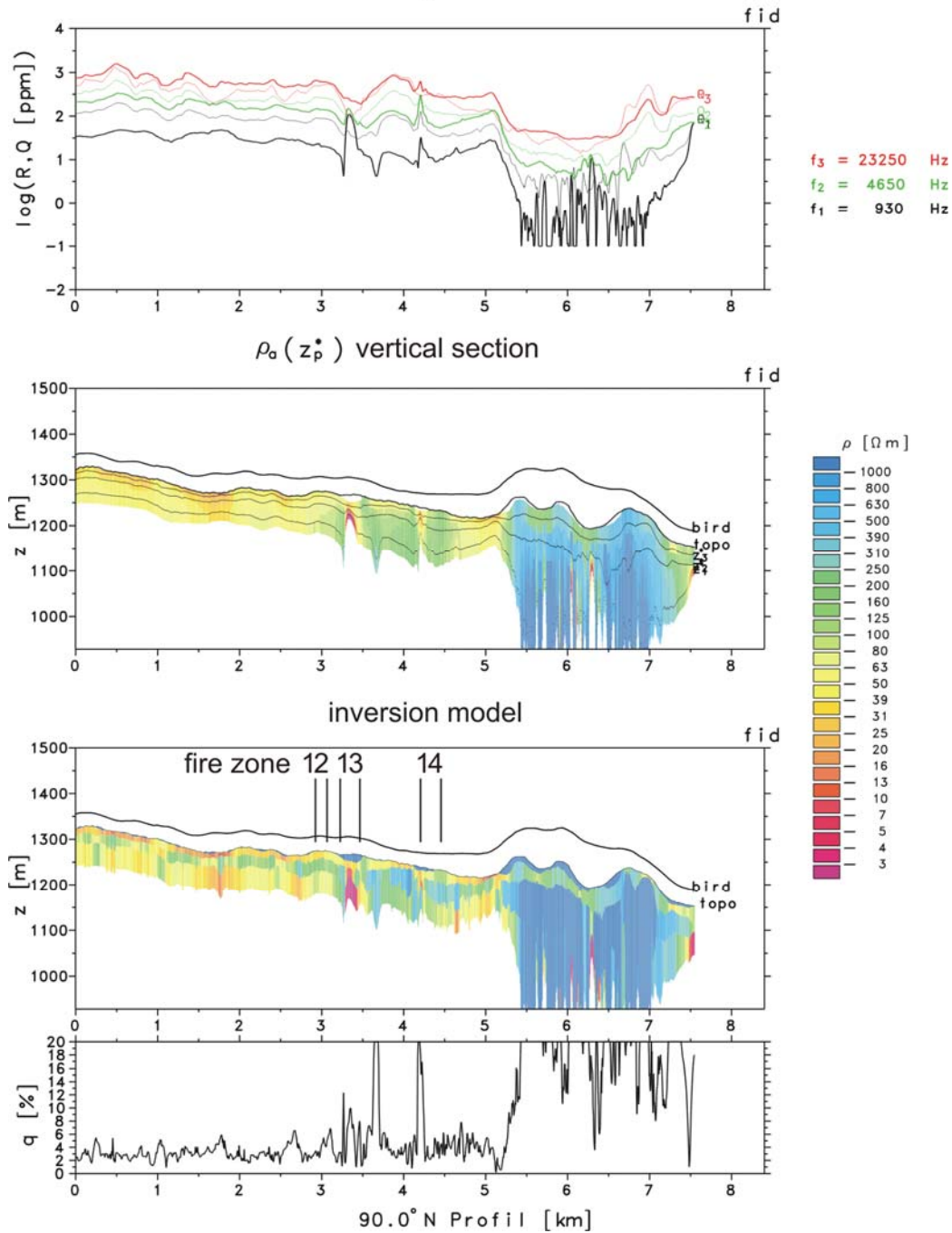


Figure 65: Inphase and quadrature values at three frequencies, vertical apparent resistivity section, 1-D vertical resistivity section and misfit along profile 1700, crossing the fire zones no. 12, no. 13 and no. 14.



Innovative Technologies for Exploration, Extinction and Monitoring of Coal Fires in North China
Final Report Phase A Part B

Wuda

Profil : L172.0:19907

horizontal-coplanar coil system, $r = 6.50$ m

EM sensor height: 24 – 88 m

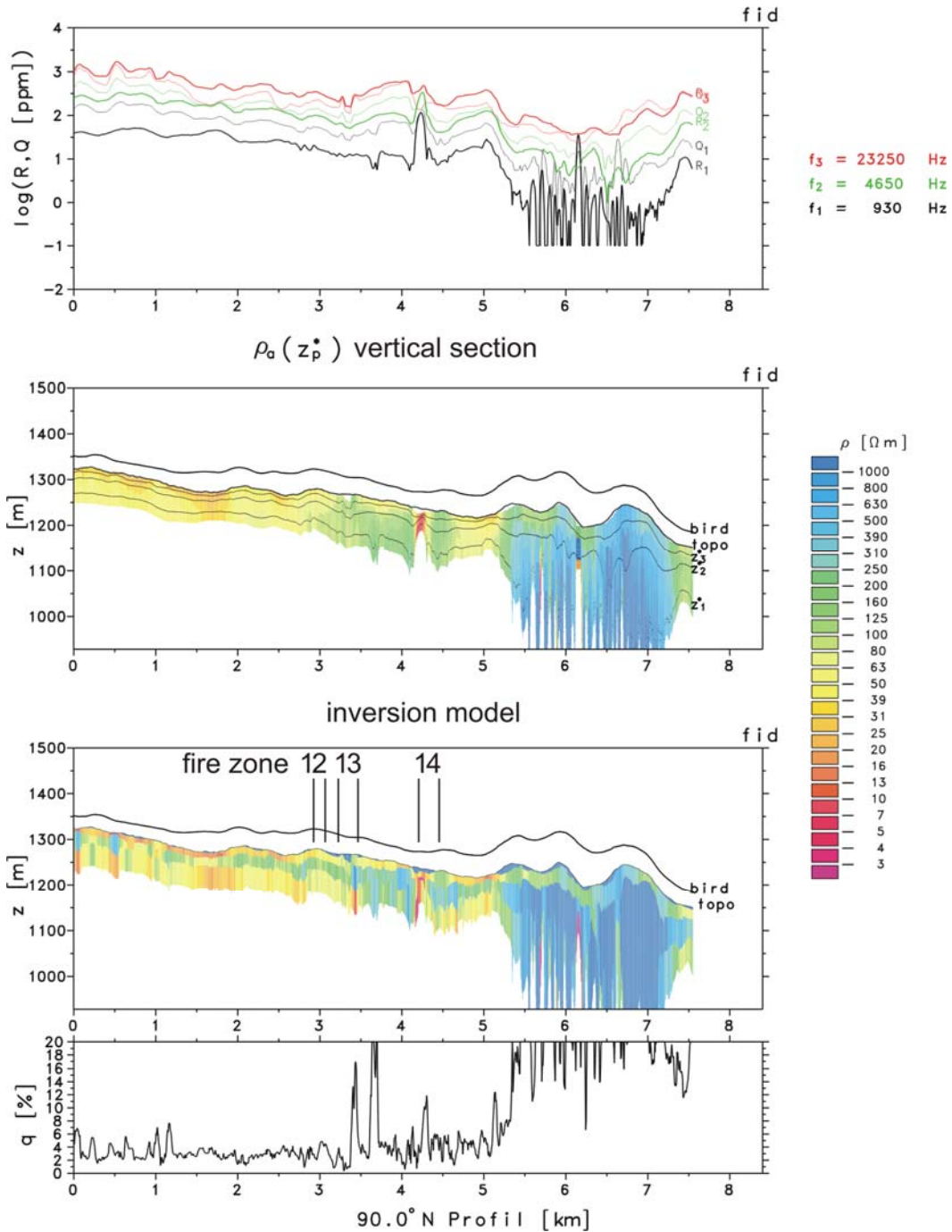


Figure 66: Inphase and quadrature values at three frequencies, vertical apparent resistivity section, 1-D vertical resistivity section and misfit along profile 1720, crossing the fire zones no. 12, no. 13 and no. 14.



Innovative Technologies for Exploration, Extinction and Monitoring of Coal Fires in North China
 Final Report Phase A Part B

Wuda

Profil : L174.0:19908
 horizontal-coplanar coil system, r = 6.50 m
 EM sensor height: 39 – 88 m

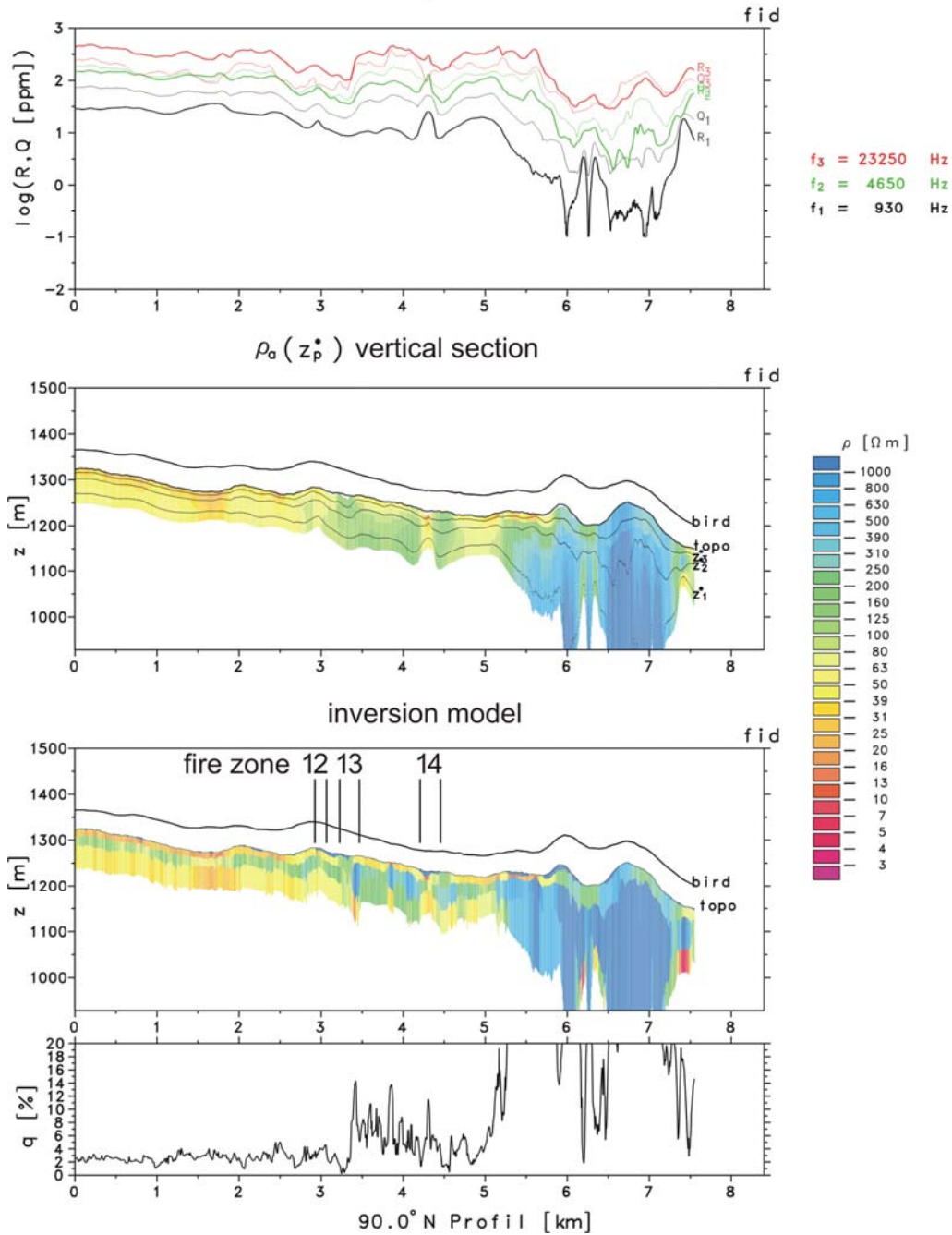


Figure 67: Inphase and quadrature values at three frequencies, vertical apparent resistivity section, 1-D vertical resistivity section and misfit along profile 1740, crossing the fire zones no. 12, no. 13 and no. 14.



Innovative Technologies for Exploration, Extinction and Monitoring of Coal Fires in North China
Final Report Phase A Part B

Wuda

Profil : L250.0:19916
horizontal-coplanar coil system, r = 6.50 m
EM sensor height: 27 – 66 m

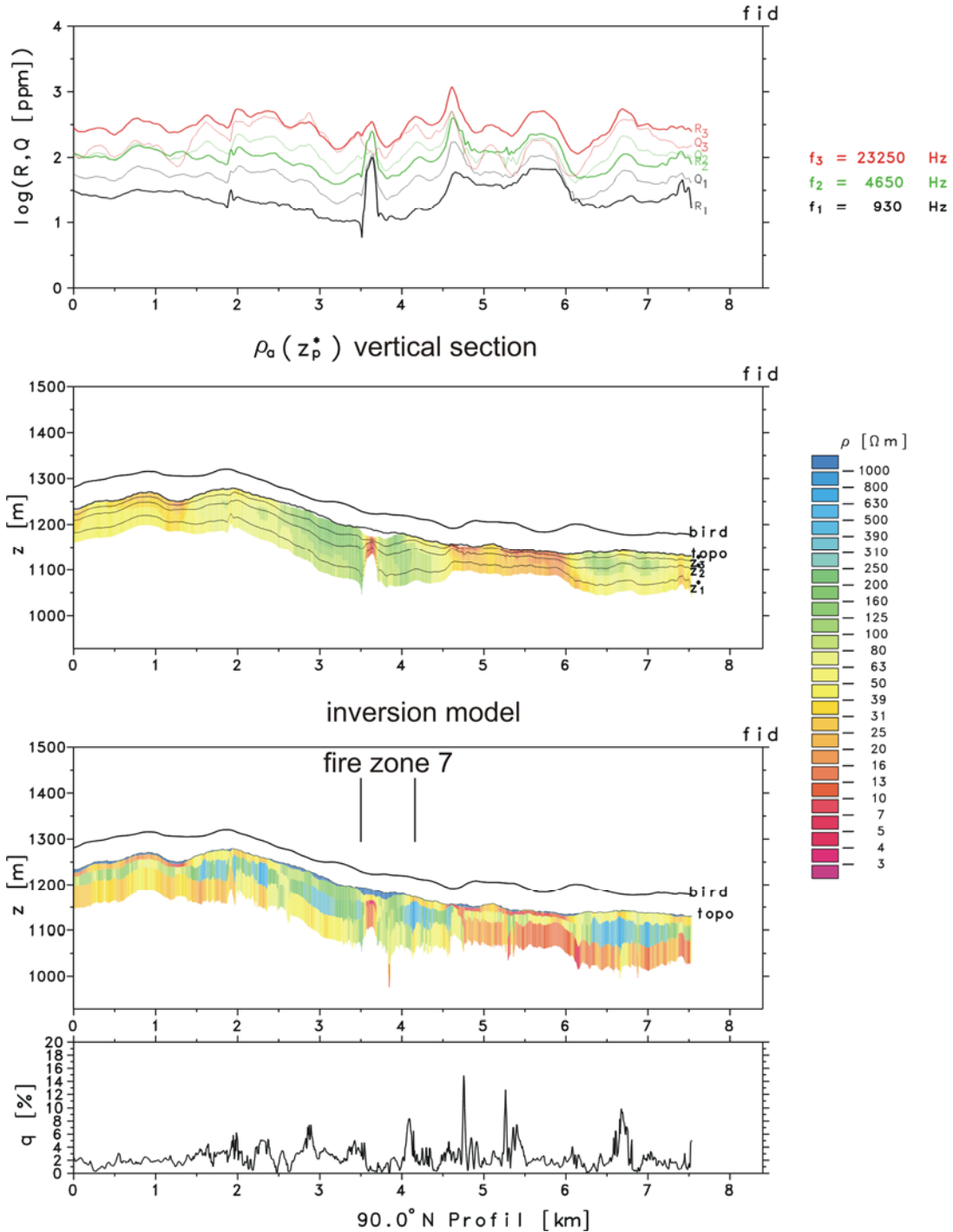


Figure 69: Inphase and quadrature values at three frequencies, vertical apparent resistivity section, 1-D vertical resistivity section and misfit along profile 2500, crossing fire zone no. 7.



Innovative Technologies for Exploration, Extinction and Monitoring of Coal Fires in North China
Final Report Phase A Part B

Wuda

Profil : L251.0:19916

horizontal-coplanar coil system, $r = 6.50$ m
EM sensor height: 35 – 62 m

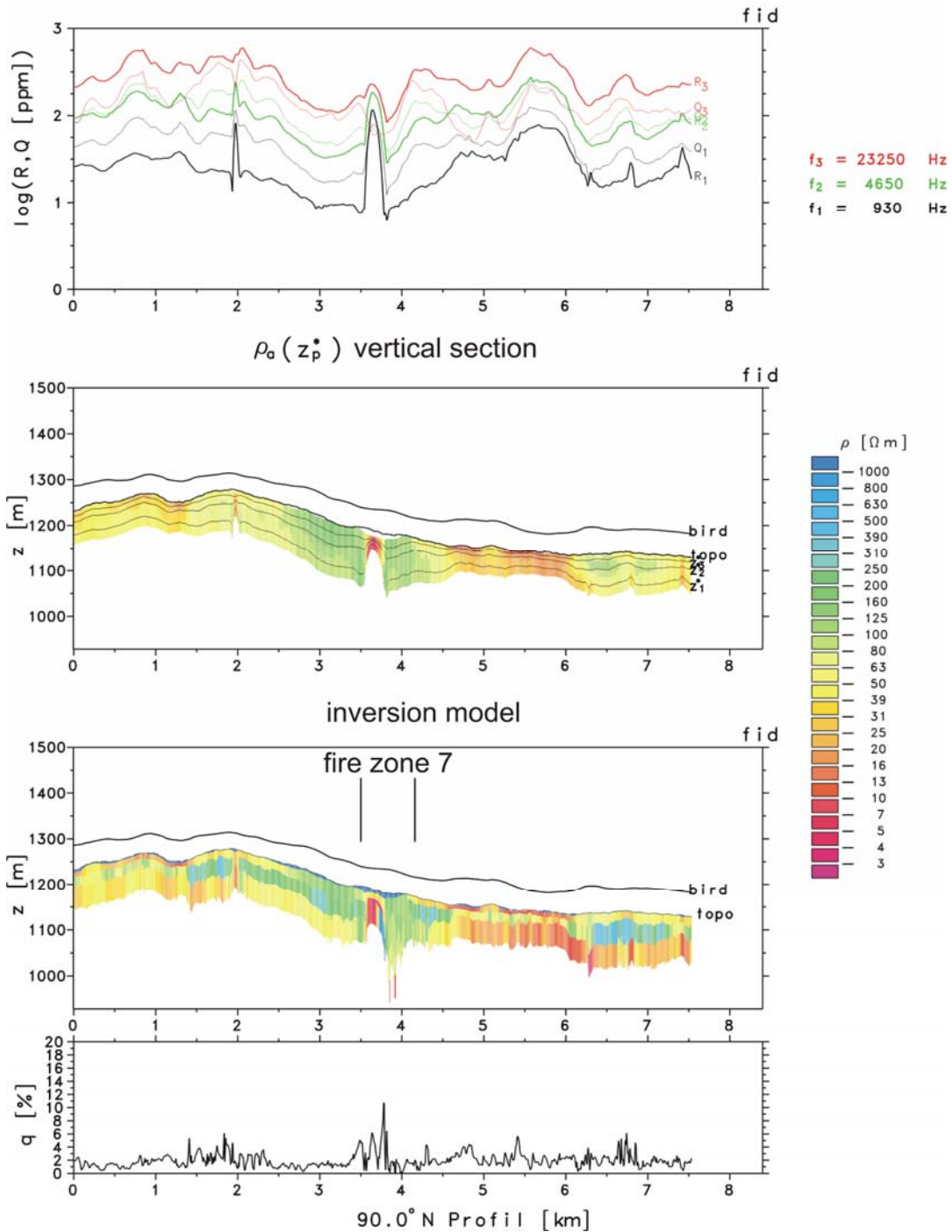


Figure 70: Inphase and quadrature values at three frequencies, vertical apparent resistivity section, 1-D vertical resistivity section and misfit along profile 2510, crossing fire zone no. 7.



Innovative Technologies for Exploration, Extinction and Monitoring of Coal Fires in North China
Final Report Phase A Part B

Wuda

Profil : L205.0:19914

horizontal-coplanar coil system, $r = 6.50$ m

EM sensor height: 38 – 92 m

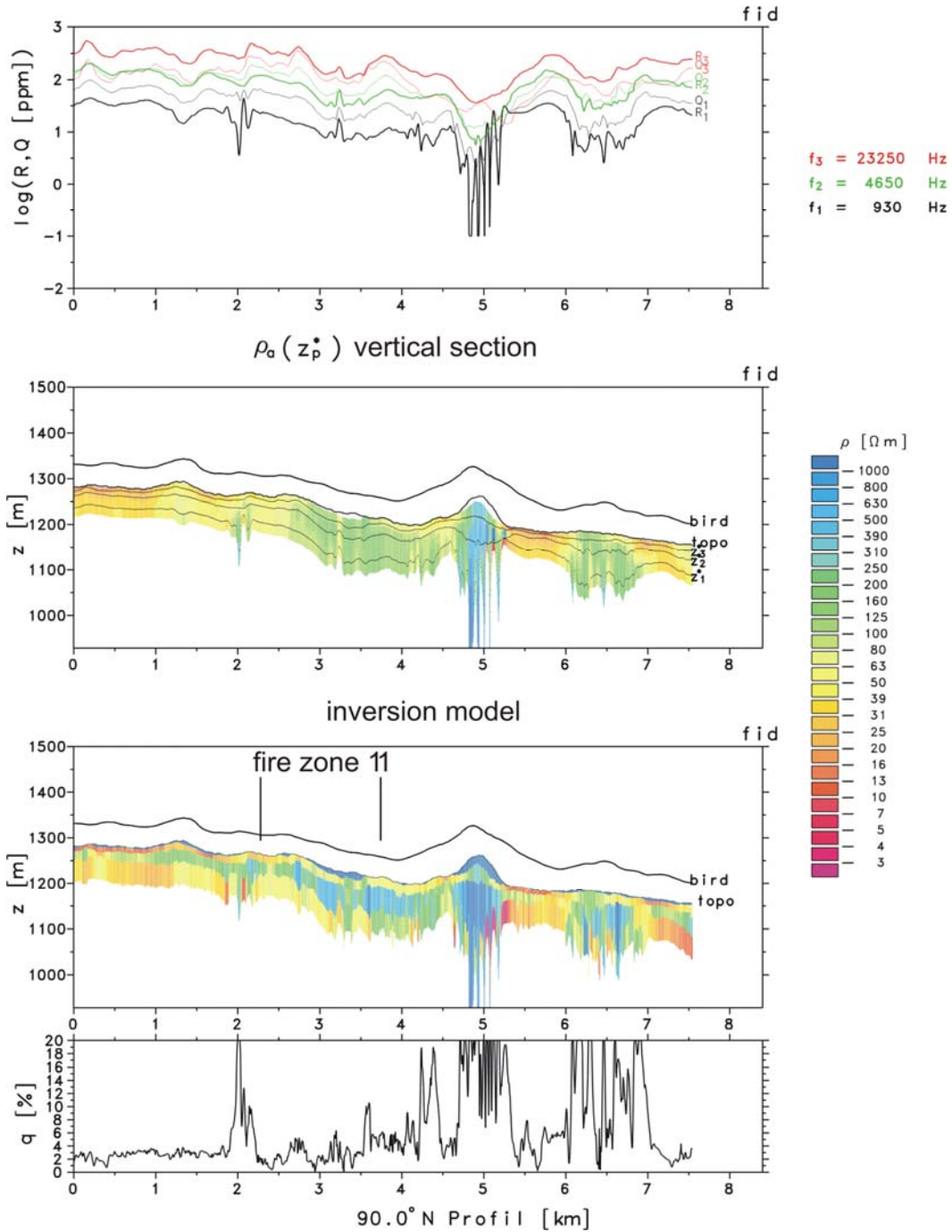


Figure 72: Inphase and quadrature values at three frequencies, vertical apparent resistivity section, 1-D vertical resistivity section and misfit along profile 2050, crossing fire zone no. 11.



Innovative Technologies for Exploration, Extinction and Monitoring of Coal Fires in North China
 Final Report Phase A Part B

Wuda

Profil : L212.0:19914
 horizontal-coplanar coil system, $r = 6.50$ m
 EM sensor height: 40 – 68 m

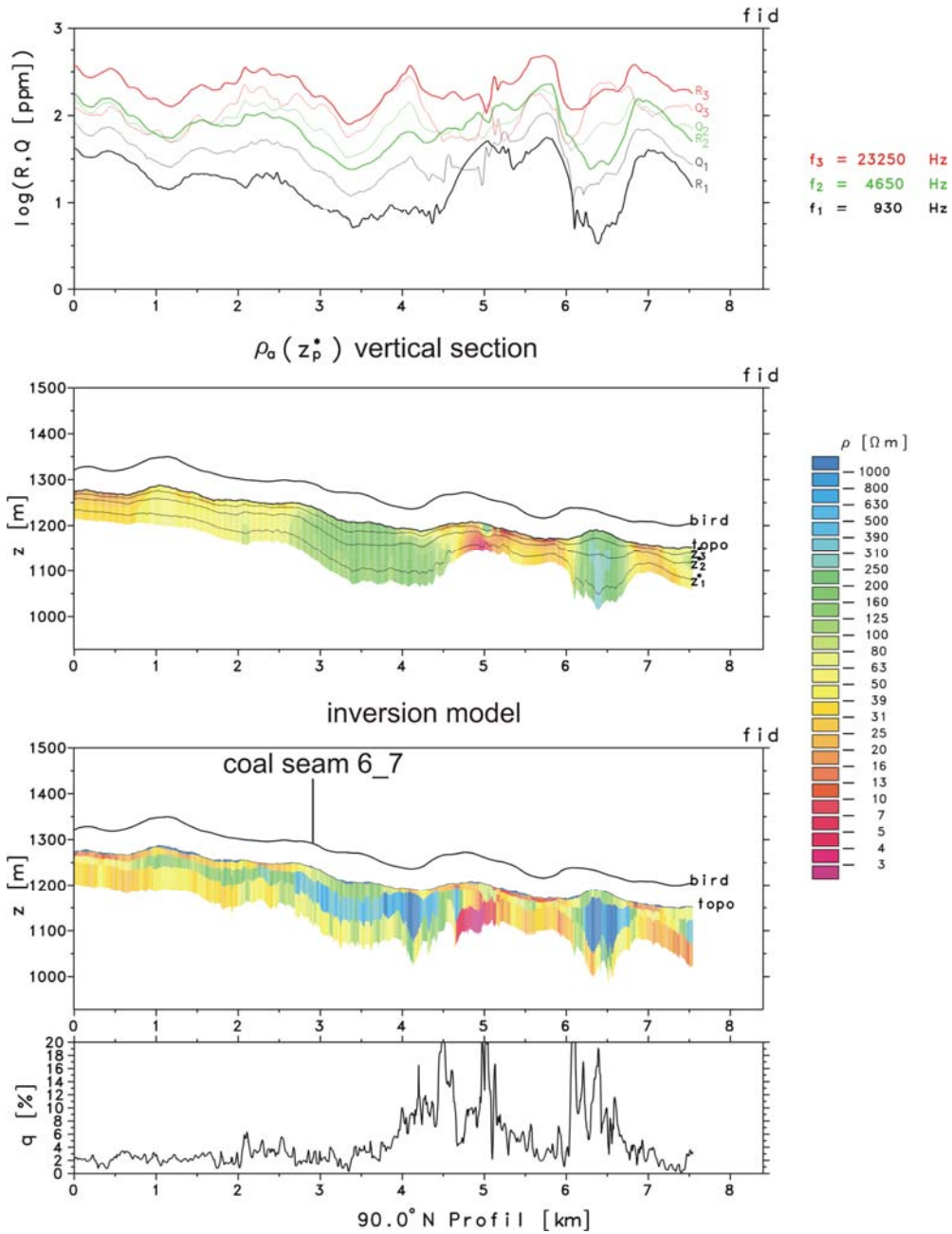


Figure 73: Inphase and quadrature values at three frequencies, vertical apparent resistivity section, 1-D vertical resistivity section and misfit along profile 2120, crossing coal seams no. 6 and 7.



4 Results of the airborne magnetic survey

4.1 Results from the entire survey area

The anomalies of the total magnetic field dT (or T) [nT] derived from the airborne magnetic survey over the entire survey area are shown in Fig. 74 and 75. Figure 75 shows the same map with colour shading for a better visualization of the geological structure. The anomalies are small in general, but reflect the features of the syncline as well. The regional magnetic field is not yet deducted. Due to cubic amplitude reduction of the magnetic field with distance from the source, the amplitudes obtained at a relatively high flight altitude (about 60 m) are smaller and the anomalies are broader than on ground. These anomalies with enhanced positive amplitudes fit to the areas where burning and burnt coal seams are located.

Within the syncline several anomalous regions occur. Although the variations of the magnetic field are small, they extend for several tens or hundreds of metres. The area of fire zone no. 8 with its spurs to the south shows these anomalies at several places. Further fire zones, like fire zone no. 3.2, no. 6, no. 7, no. 10, no. 11, no. 12, no. 13, no. 14, no. 15 and no. 18 show these distinct anomalies, too. Details are discussed below. All these fire zones have in common that most regions with anomalous total magnetic field intensities extend beyond the mapped polygons. As already mentioned, the mapped burning zones do not reflect the precise outline of the underground fires; they can only approximate the burning conditions underground (Kuenzer et al. 2006) at the time of mapping, because temperature data were collected on the surface. Already burnt zones are not included in the mapped regions, but they contribute to the magnetic field anomalies.

Besides that several sites with enhanced total magnetic field values do not show known coal fire activities, e.g. in the north-west of fire zone no. 8. Here a big mining facility is located. Anthropogenic activities may also cause enhanced total magnetic field values. All sites of interest therefore have to be investigated carefully.

The amplitudes of the anomalies of the total magnetic field gained by the airborne survey are smaller than those measured on ground. Therefore the correlation of the fire zones with airborne magnetic anomalies is not as strong as with those discovered by the ground magnetic surveys (see Chapter 6).

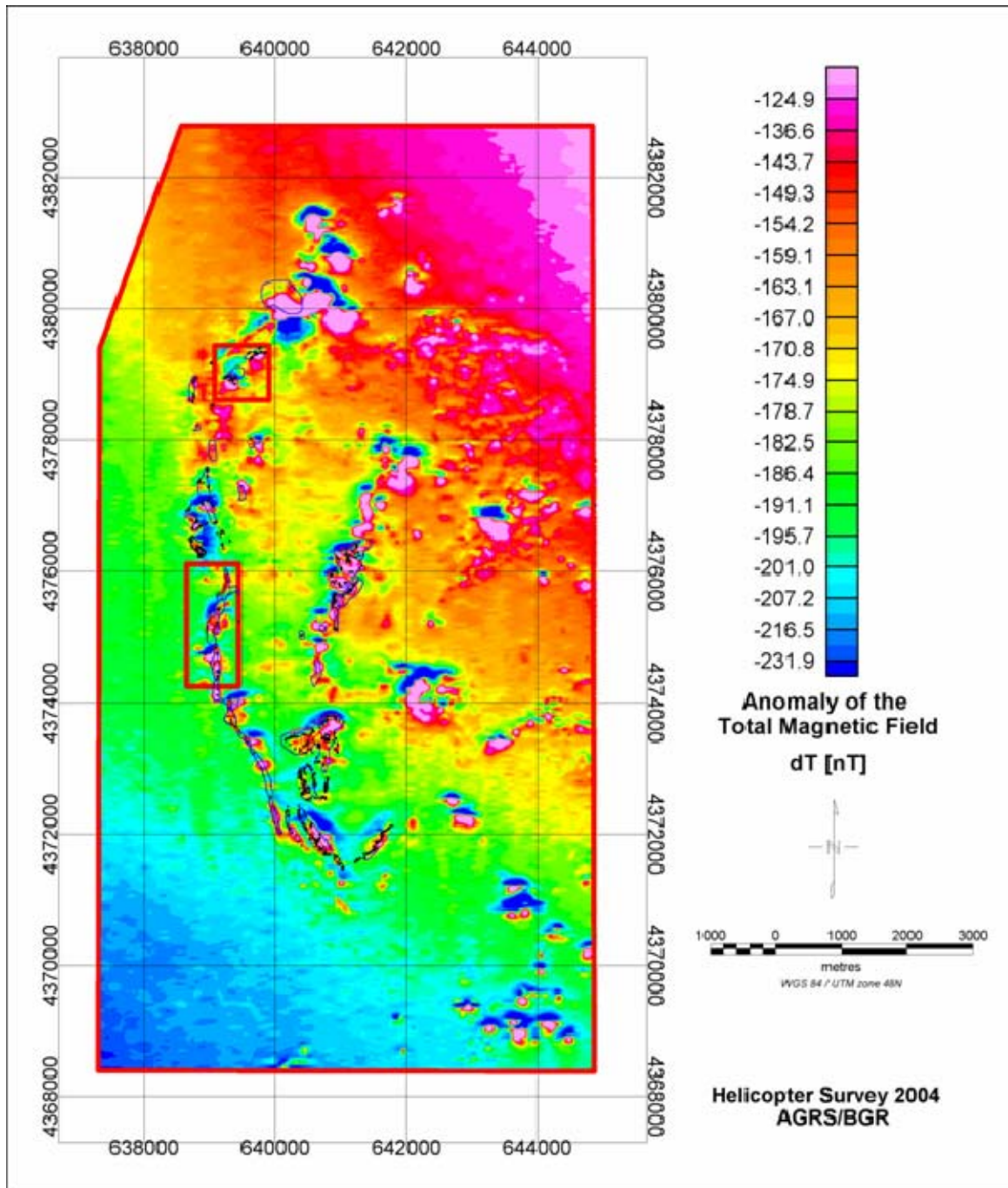


Figure 74: Anomalies of the total magnetic field dT [nT] over the whole Wuda syncline, derived from the airborne magnetic data at an average flight altitude of 60 m and a line separation of about 50 m. Bold solid red rectangles indicate the areas of fire zones no. 8 and no. 3.2. In general fire zones are marked by blue and red polygons (by DLR, 2002 to 2005).

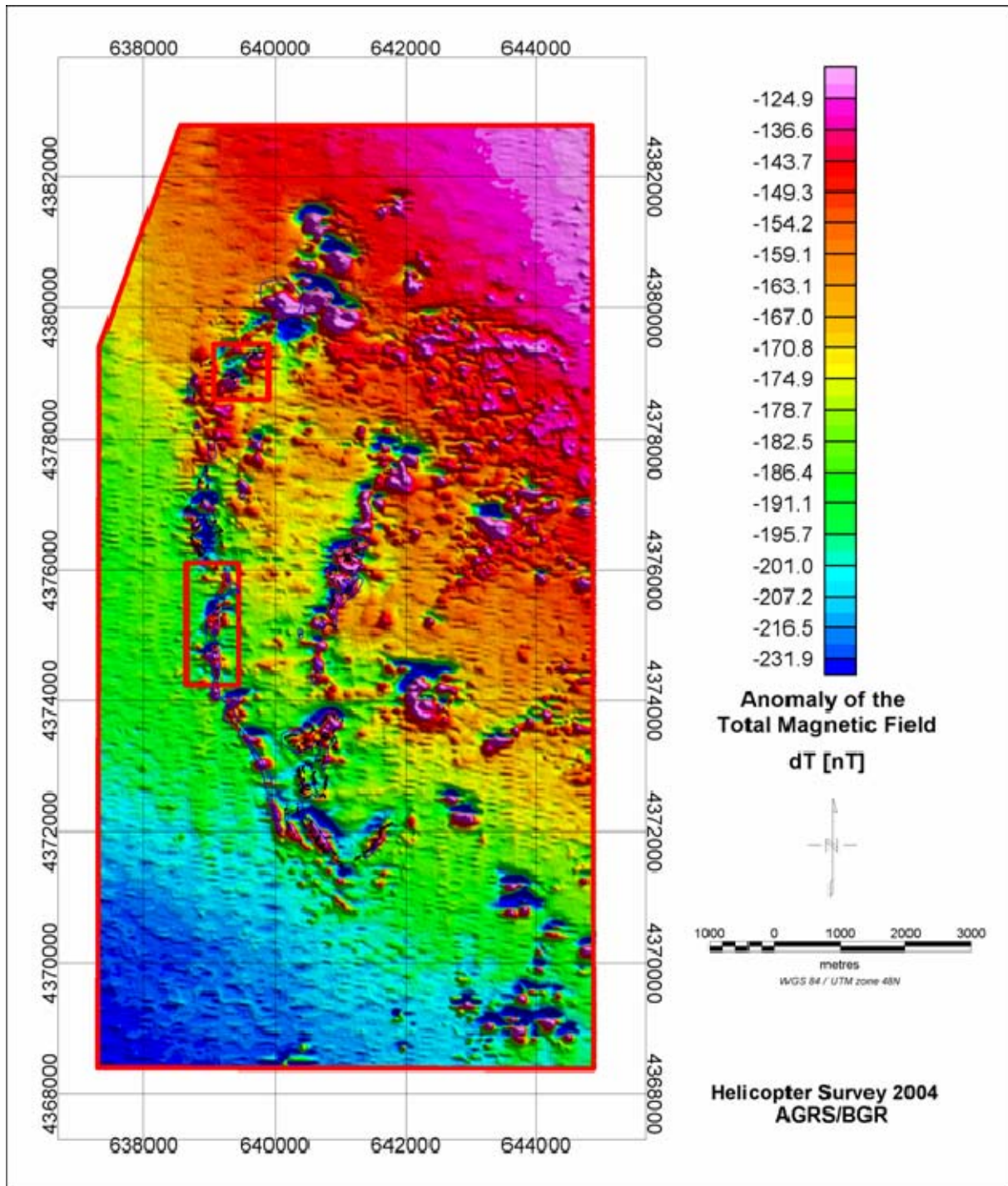


Figure 75: Anomalies of the total magnetic field dT [nT] over the whole Wuda syncline, derived from the airborne magnetic data at an average flight altitude of 60 m and a line separation of about 50 m. Bold solid red rectangles indicate the areas of fire zones no. 8 and no. 3.2. In general fire zones are marked by blue and red polygons (by DLR, 2002 to 2005). Colour shading from N-E.



4.2 Results from fire zone no. 8

Figures 76 and 77 show the anomalies of the total magnetic field for fire zone no. 8 and its surroundings in detail. They can be found at several places within the fire zone, clearly of greater extension than the mapped polygons which mark burning coal seam fires by their temperature effects on the surface. A difference between colder and hotter fires cannot be clearly found in the anomalous magnetic field values. In the very northern part of the fire zone a hot burning area was mapped in 2005 (violet polygons). It shows variations of the magnetic field values, measured in 2004. Mapped by a green line the extension of the burning zone in 2002 is shown (Fig. 77). At the plateau of fire zone no. 8 this line courses further to the east than the mapped lines from 2004. At a site further in the south (located close to coordinates 4374000, 639500) the mapped polygon from 2002 shows a bulge to the east. The area with enhanced values of the total magnetic field also extends to the east at that place. No distinct variations of the burning zones from 2002 to 2003 can be detected.

From literature (see above) it is known that the occurrence of striking anomalies depends on the enrichment of magnetic minerals and on the state of the burning process. Especially burnt coal seam fires in proper geological reality (e.g. high mineral content) show distinct anomalies of the magnetic field. Currently burning fires do not show very striking magnetic anomalies (Elsen 2006, see Chapter 6). This fits to the phenomenon that ferromagnetic material loses nearly all magnetic susceptibility at the Curie temperature.

North-west of fire zone no. 8 a mining facility is situated and contributes to a single anomaly in that region. This anthropogenic source is also observed on the apparent resistivity maps.

The airborne magnetic anomalies correspond to those measured on ground (Chapter 6). This can be seen in the southern collapsed part, in the area close to TEM profile no. 3 and in the northern part of the fire zone.

The location of coal seams no. 6 and no. 7, shown by the squares from the TEM survey (see Fig. 82), do not show striking variations of the magnetic field values (Fig. 77). At this site no coal seam fires are known up to now.

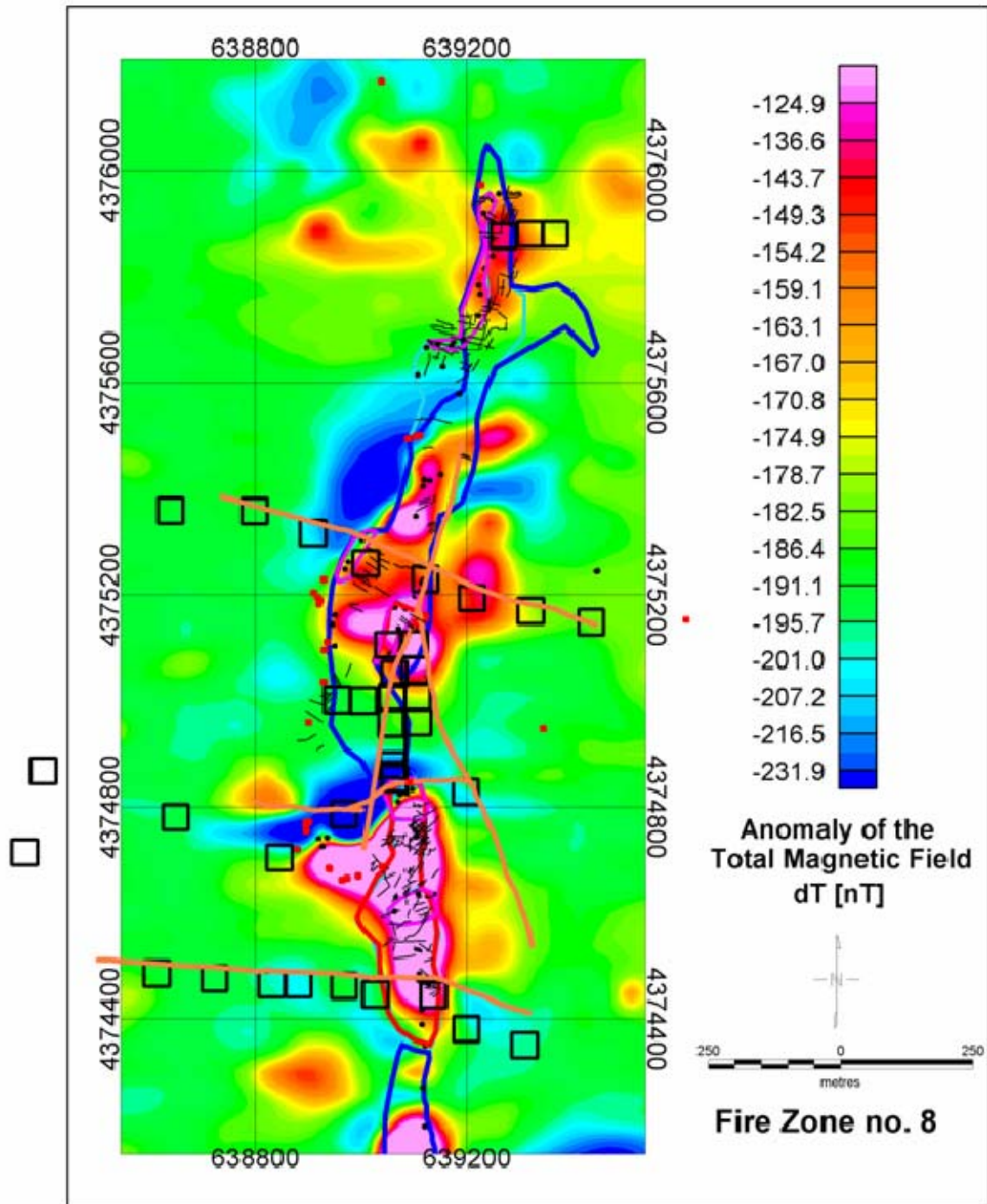


Figure 76: Section of the map of the anomalies of the total magnetic field dT [nT] for fire zone no. 8 derived from the airborne magnetic data at an average flight altitude of 60 m and a line separation of about 50 m. Blue and red polygons indicate the burning zones in 2004, light blue and violet polygons and black dots indicate the burning zones in 2005 (mapped by DLR). The sites of the TEM ground survey are shown by black squares (see Fig. 82).

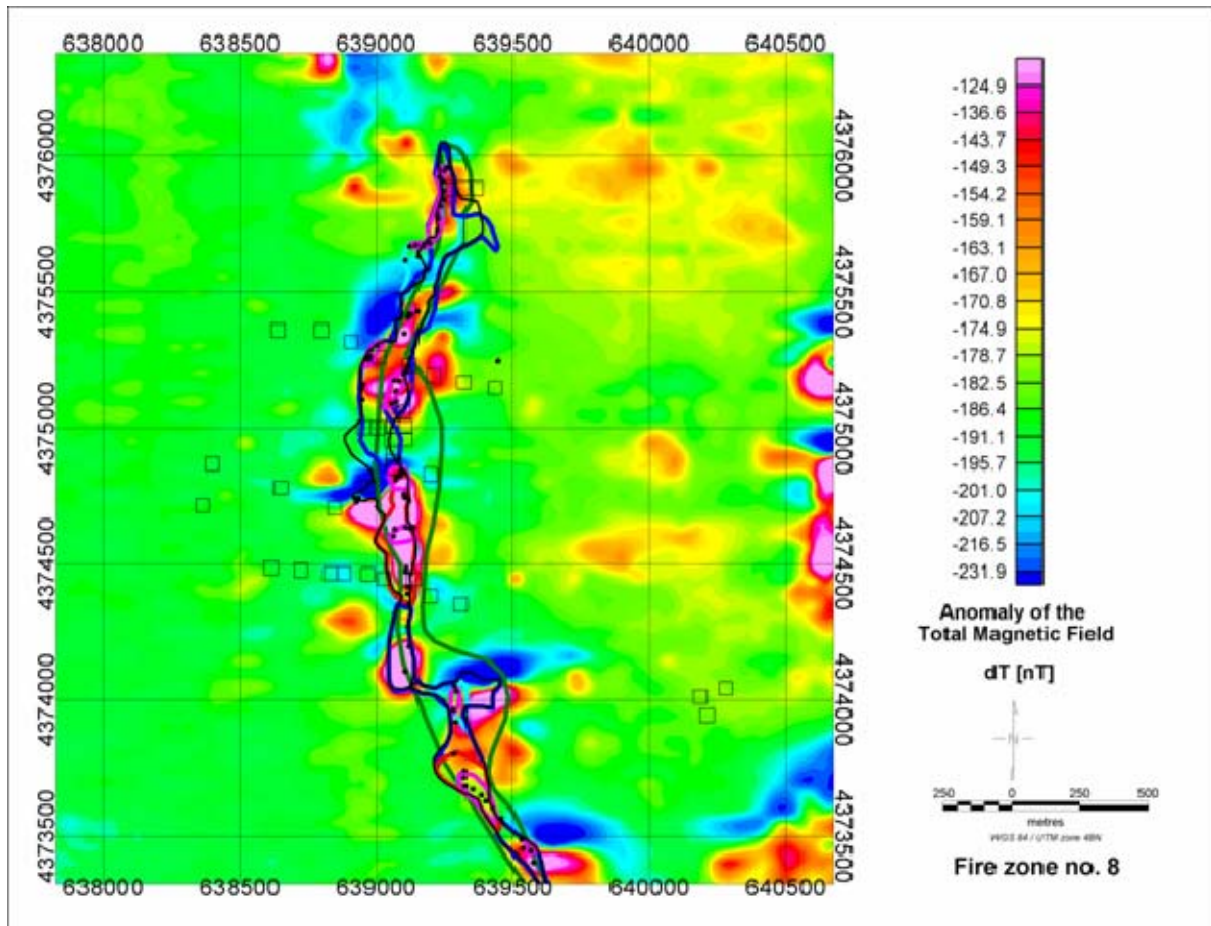


Figure 77: Section of the map of the anomalies of the total magnetic field dT [nT] for the surroundings of fire zone no. 8 derived from the airborne magnetic data at an average flight altitude of 60 m and a line separation of about 50 m. Blue and red polygons indicate the burning zones in 2004, light blue and violet polygons and black dots indicate the burning zones in 2005, green lines mark the burning zone in 2002 and light black lines in 2003 (mapped by DLR). The sites of the TEM ground survey are shown by black squares (see Fig. 82).

4.3 Results from fire zone no. 3.2

The map section of the anomalies of the total magnetic intensity for fire zone no. 3.2 (Fig. 78) shows similar features as the map of the anomalies at fire zone no. 8. The extension of the anomalous region is greater than the polygons mapped in 2004, and it is somewhat displaced. Over the entire area of this fire zone, extending from south west to north east, clearly enhanced values of the magnetic field can be found. They correspond better to polygons mapped in 2002 (green lines) than to those mapped in 2004. The anomalies within the area cannot be correlated clearly to cold or hot burning zones. The burnt out southern part shows higher values of the magnetic field intensity. A small factory west of the hot burning zone is not emphasized in the anomalous field values.

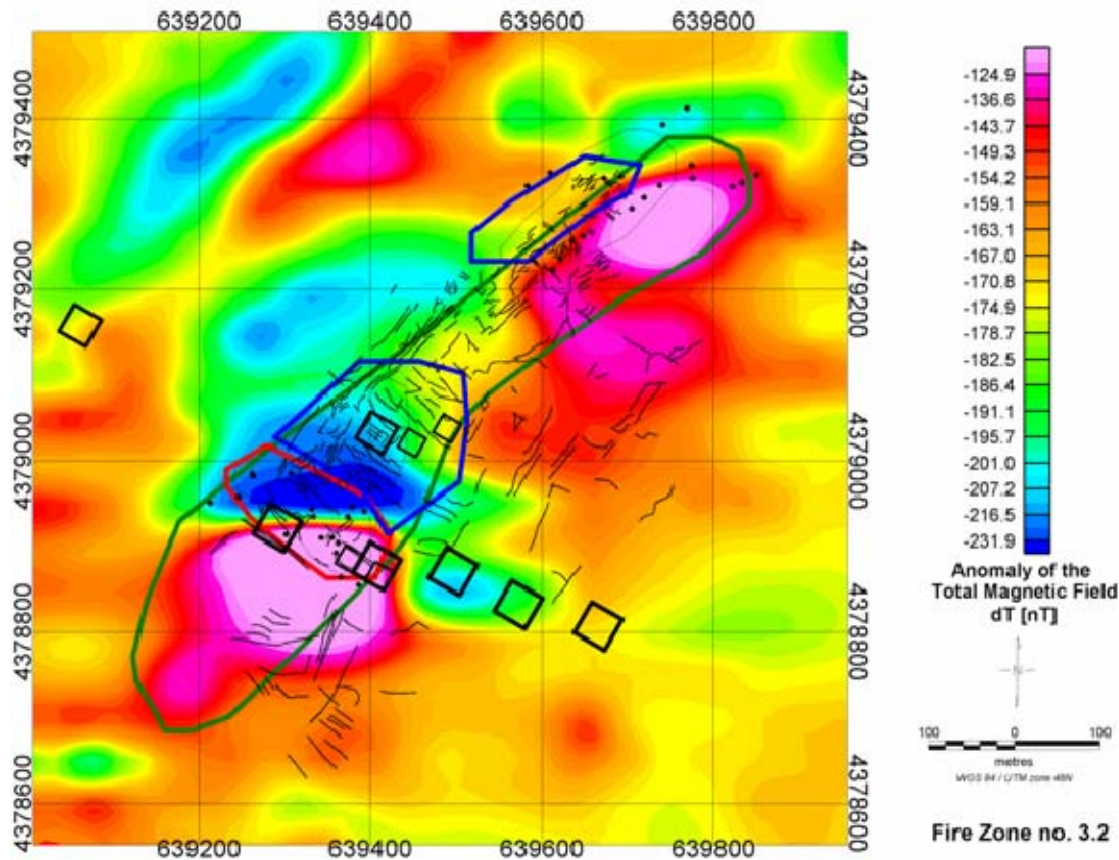


Figure 78: Section of the map of the anomalies of the total magnetic field dT [nT] for fire zone no. 3.2 derived from the airborne magnetic data at an average flight altitude of 60 m and a line separation of about 50 m. Blue and red polygons indicate the burning zones in 2004, black dots indicate the burning zones in 2005, green lines mark the burning zone in 2002 and light black lines in 2003 (mapped by DLR). The sites of the TEM ground survey are shown by black squares.

4.4 Results from fire zones within the southern surroundings of fire zone no. 3.2

The region with enhanced values of the total magnetic field intensity extends at several areas from north to south, including parts of fire zones no. 1, no. 2, no. 3, no. 4, no. 5, no. 6, no. 15, no. 16 and no. 18 (Fig. 79).

While fires no. 2, no. 4, no. 5, no. 15 and no. 16 are extinct, fires no. 3, no. 6 and no. 18 are still burning (Kuenzer et al. 2006).

A displacement of the mapped polygons from the magnetic anomalies is striking, especially at fire zones no. 3, no. 5 and no. 15.

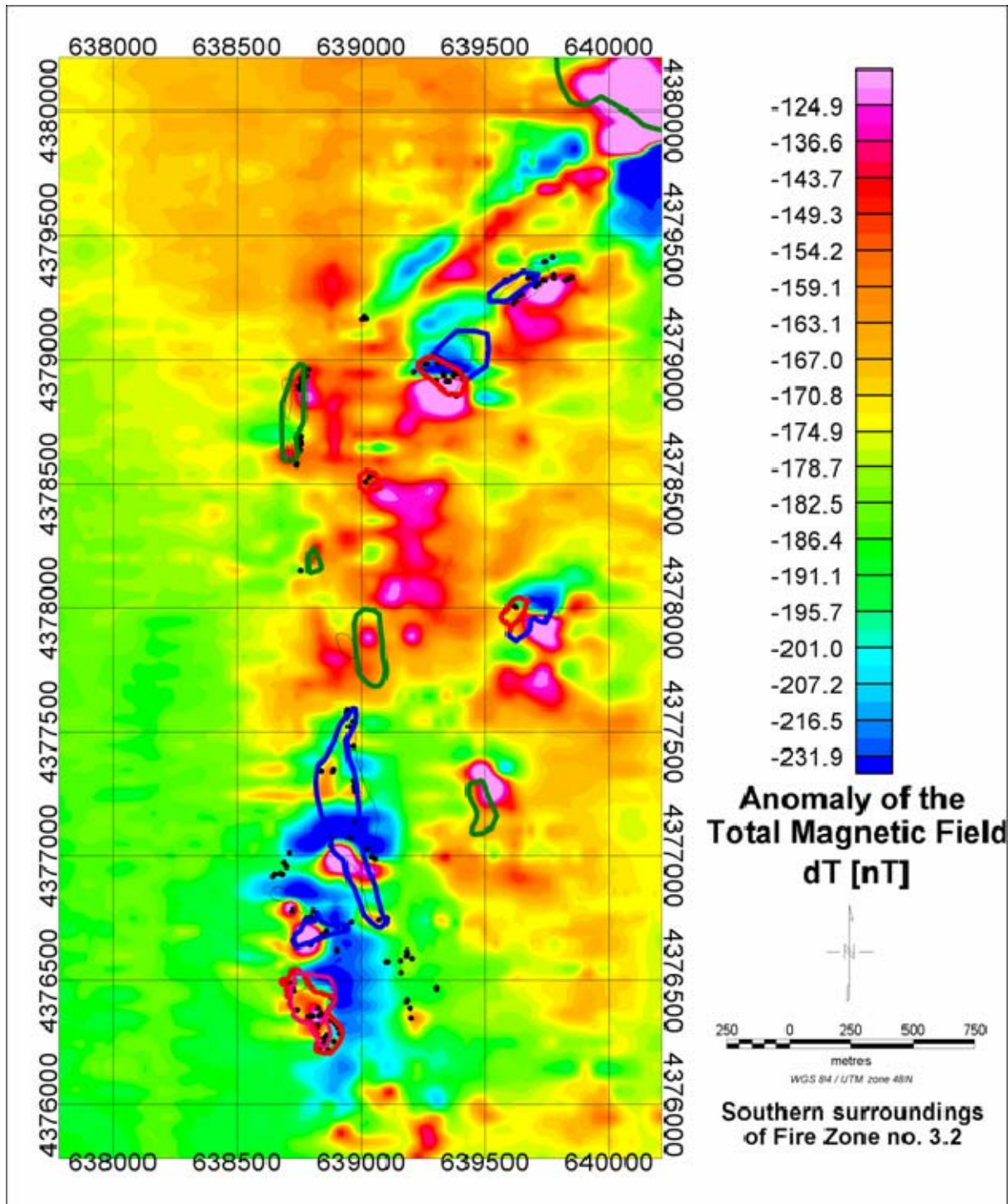


Figure 79: Section of the map of the anomalies of the total magnetic field dT [nT] for the southern surroundings of fire zone no. 3.2 derived from the airborne magnetic data at an average flight altitude of 60 m and a line separation of about 50 m. Blue and red polygons indicate the burning zones from 2002 to 2004, violet polygons and black dots indicate the burning zones in 2005, green lines mark the burning zones in 2002 and light black lines in 2003 (mapped by DLR).



4.5 Results from fire zone no. 7 in the centre of the syncline

Fire zone no. 7 is located about 1 km east of fire zone no. 8 towards the centre of the syncline. A striking anomaly on the map of the apparent resistivities gave reason for a detailed investigation of this fire zone, see chapter 5 for the VLF ground survey. Figure 80 shows the map of the anomalies of the total magnetic field at this fire zone. In the south-eastern part this fire zone extends along the geological structure. Similar to the other fire zones, the anomalous regions of the magnetic field fit to the mapped polygons, although not very exactly.

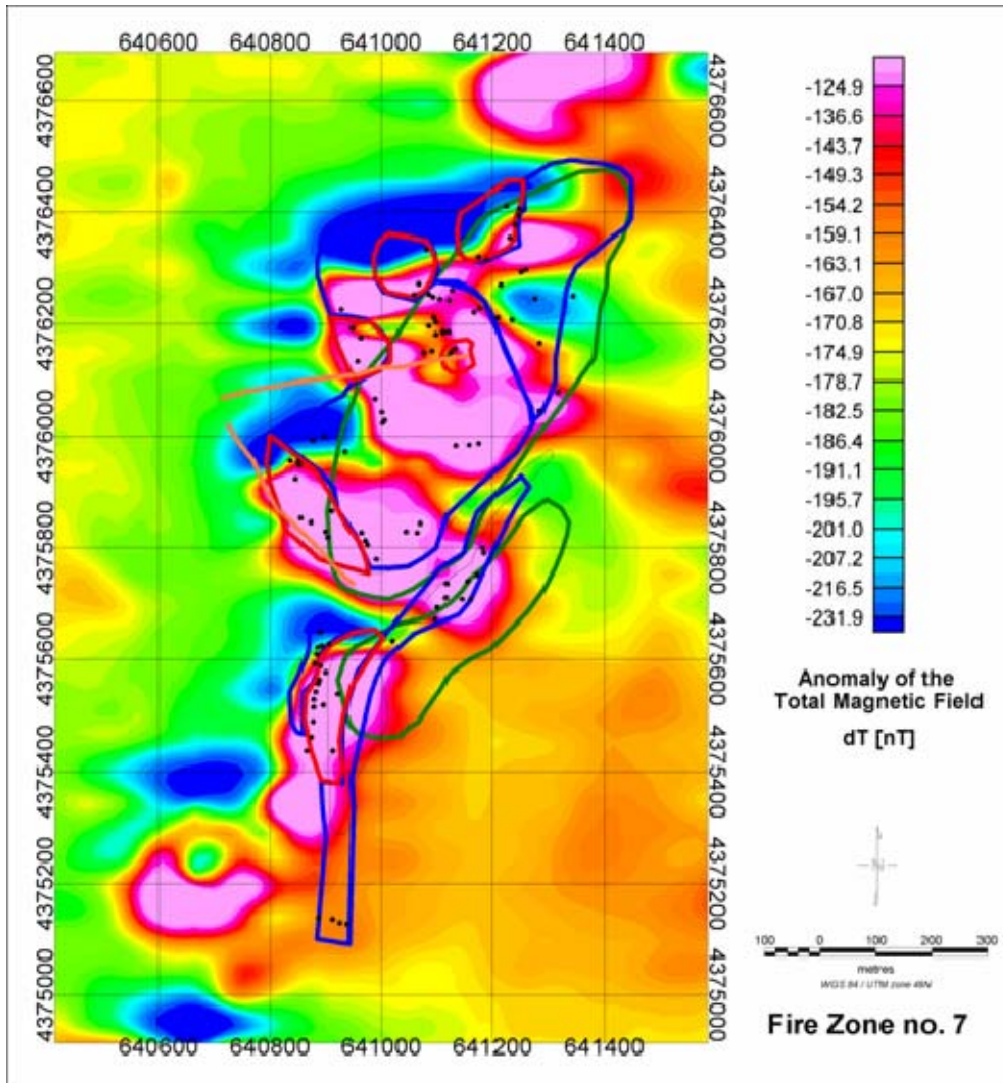


Figure 80: Section of the map of the anomalies of the total magnetic field dT [nT] over fire zone no. 7 derived from the airborne magnetic data at an average flight altitude of 60 m and a line separation of about 50 m. Blue and red polygons indicate the burning zones from 2004, black dots indicate the burning zones in 2005, green lines in 2002 and light black lines in 2003 (mapped by DLR). Profiles no. 6 and no. 7 from the VLF and ground magnetic survey are shown as orange lines.



4.6 Results from fire zone no. 11 and the southern part of the syncline

Within the southern part of the syncline several fire zones occur. These are the southern extension of fire zone no. 8, fire zones no.11, no. 12, no. 13 and no. 14. All fire zones are still active, besides that at fire zones no. 11 and no. 14 accelerating fires are burning (Kuenzer et al. 2006). The map of the anomalies of the total magnetic field (Fig. 81) shows areas of enhanced values of the magnetic field intensity, corresponding to the mapped polygons from 2004 (blue and red lines), although they do not fit very precisely. Especially the lateral extension of the mapped polygons at the southern part of fire zone no. 8 contradicts to the well concentrated anomalous regions. For that reason also polygons from 2002 (green lines) and 2003 (light black lines) were drawn within this map to get an idea about the progress of the burning front over the years. Fires no. 11 and no. 14 were classified as “slowly burning out fires” in 2002, but became active again one resp. two years later (Kuenzer et al. 2006).

All mapped polygons show variations of the burning areas in the course of the years, fire zone no. 11 was shrinking, fire zone no. 8 extends more to the south and no. 14 shows a progress northwards. The area of anomalous values of the total magnetic field mapped in 2002 correspond well to the fire zones, although not very precisely.

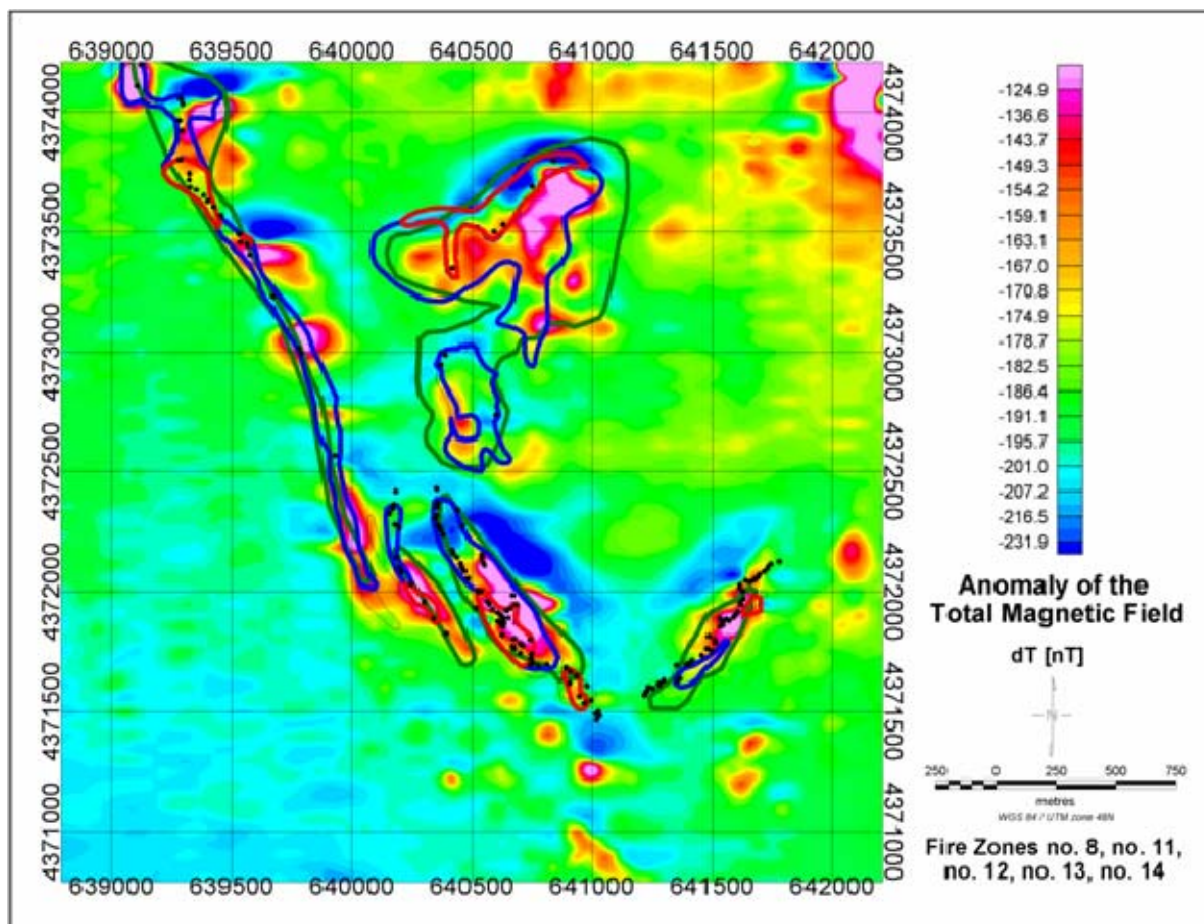


Figure 81: Section of the map of the anomalies of the total magnetic field dT [nT] for fire zone no. 11 and the southern part of the syncline derived from the airborne magnetic data at an average flight altitude of 60 m and a line separation of about 50 m. Blue and red polygons indicate the burning zones in 2004, green



polygons mark the burning zones from 2002 and black dots indicate the burning zones in 2005. Green lines show the burning zones in 2002 and light black lines in 2003 (mapped by DLR).

5 Ground electromagnetic surveys

Complementing the helicopter-borne electromagnetic and airborne magnetic surveys ground geophysical measurements were performed in the summer campaign 2005. For the ground geophysical survey the following methods were used: Transient Electromagnetics (TEM), Horizontal-Loop-Electromagnetics (HL) and Very Low Frequency (VLF) -Electromagnetics. All three methods provide information about the distribution of the electrical conductivity of the subsurface. The measurements yield the apparent resistivity (R_{ho}) and after data inversion one obtains the resistivity (Rho) distribution. In addition to the electromagnetic methods ground magnetic surveys were carried out.

The distinct localities for the ground geophysical surveys were chosen by help of the results of the HEM survey. For all areas of interest apparent resistivities for all frequencies of that survey were calculated, screened and examined in detail, especially across the fire zones no. 8 and no. 3.2. For selected flight lines a 1-D inversion yielded vertical resistivity sections which supplied the basis information for choosing the survey lines for the ground geophysical surveys. Besides that the surveys covered the selected test areas where investigations from different scientific fields were carried out.

In May and June 2005 numerous ground electromagnetic measurements were performed across the fire zones and were extended to areas not affected by coal seam fires. The transient electromagnetic method was mainly applied, only a few survey profiles were measured using other electromagnetic methods, i.e. HL and VLF.

5.1 Transient electromagnetics ground survey

The transient electromagnetic (TEM) method uses transmitter and receiver coils with different sizes and configurations. A changing current in the transmitter loop produces a changing primary magnetic field. The change of this primary field is produced by a rapid current shut-off in the transmitter loop. Due to these primary field changes currents are induced in the subsurface. Their decay induces a secondary magnetic field in the earth. Its decay is detected as a transient voltage induced in the receiving coil on the surface. This decaying voltage is recorded over a certain time window and contains information about the resistivity distribution in the subsurface. The resulting exploration depth depends on the local noise level (King 1987; Greinwald & Schaumann 1997).

By increasing the coil size and/or extending the time window to later times the ground borne TEM system is able to give information about the resistivities of layers at greater penetration depths. Because the velocity of expansion of the induced current system in the ground depends on the resistivity of the subsurface, the uppermost layers influence by this way the diffusion depth of the current system at the time when the first data for the decay curve is measured. If the resistivity of the uppermost layer is very high, the current system spreads very fast and has reached a greater depth when measuring of the decay curve starts. A layer of lower resistivity delays the current system and therefore information about more shallow layers can be gained. The apparent resistivities from the HEM survey in general allow investigations at smaller depths than TEM measurements provide. By this way the



combination of both methods will lead to results from very small to lower investigated depth. TEM measurements were performed along profile lines across the fire zones or at single localities selected. Because of the inductive coupling of the current flow at this method, TEM could be carried out successfully in the Wuda area, which is of semi-arid type with sand cover or dry hard rock surface.

The spacing of the TEM sites was adapted to the terrain. A loop size of 50 m by 50 m was applied at most sites. The mostly used inloop configuration places the receiver coil in the centre of the transmitter loop. The sounding point is considered to be directly below the centre of the loops. Below a transmitter coil size of 40 m by 40 m a separate loop configuration is appropriate. At this configuration the receiver coil is placed outside the transmitter coil by a certain distance. The sounding point is assigned to the centre between the two coils. A number of 65 transient electromagnetic soundings on 12 profile lines were carried out using the PROTEM47 system manufactured by Geonics, Canada. For each site one-dimensional modelling was carried out without a-priori-information using an iterative Marquardt algorithm (Weidelt 1984) to determine resistivities (ρ) and depths of the model layers, these are vertical resistivity sections. For adapting the 1D models to the data the criterion within the inversion process was a deviation value of less than 3% between several models found. That means that equivalent models within a deviation of less than 3% may also fit the data. Besides that typical deviation errors for the data and model parameters within one model fitted to the data vary roughly between 1% and 5%. Especially if the subsurface structure is not a layered one, the deviation can become very big and sometimes no fitting of any 1D-model to the data can be yielded.

5.1.1 Results from fire zone no. 8

Figures 82 and 83 show the location of the TEM sites (black squares) crossing fire zone no. 8 (profiles no. 3 to no. 9) and at various other sites in the desert, west and east of one of the big hills in the south and over coal seams 6 and 7. Profiles no. 1, 2, 3 and 4 (orange lines) show the profile lines of the HL and the VLF measurements. The polygons of the burning zones (blue resp. light blue for colder fires and red resp. violet for hotter fires) were mapped in 2004 resp. 2005 by DLR. Fig. 83 with the quickbird satellite image of fire zone no. 8 in the background (by DLR 2003, Gielisch & Kuenzer 2003) shows also the numbers of the TEM ground survey sites (within the black squares). Black dots mark burning spots in 2005 (mapped by DLR). Cracks are marked by light black lines.



Innovative Technologies for Exploration, Extinction and Monitoring of Coal Fires in North China
Final Report Phase A Part B

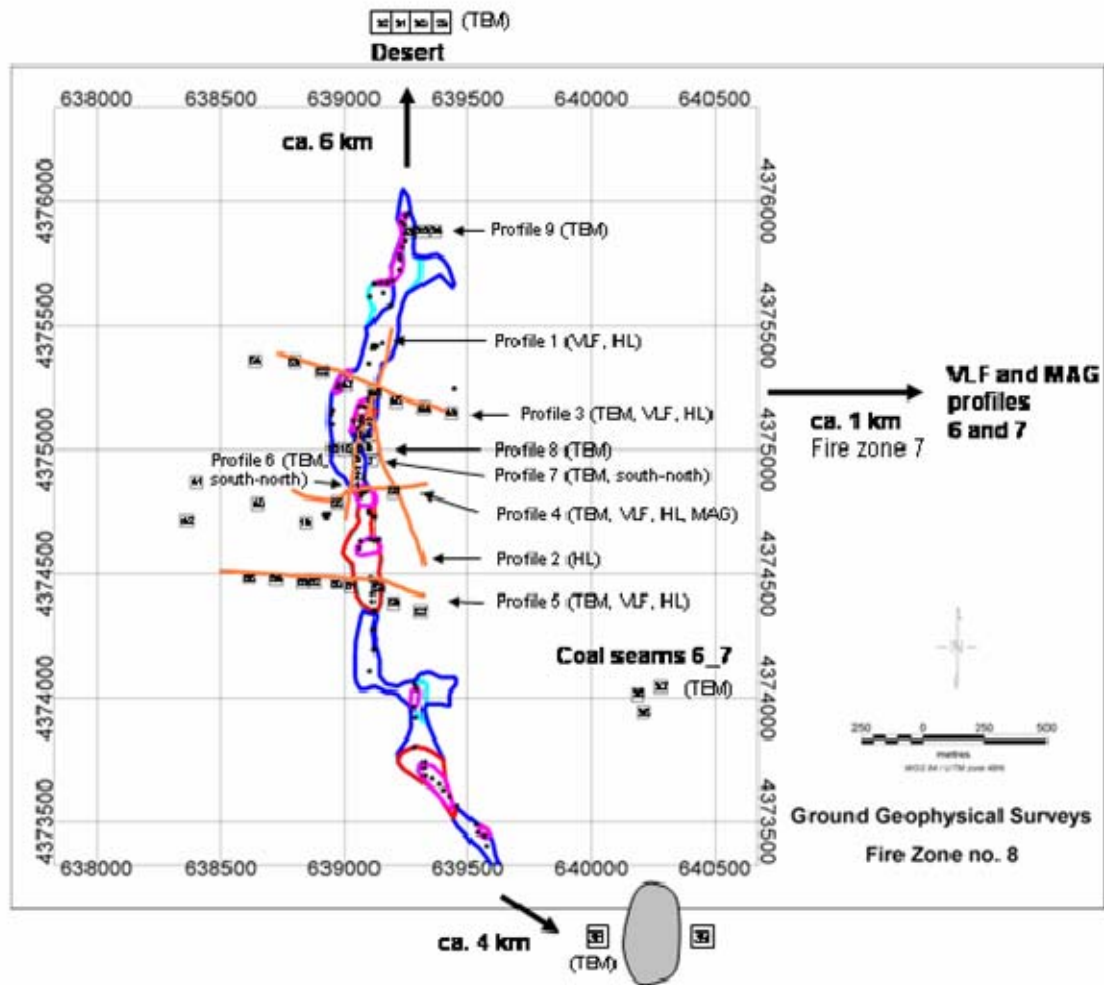


Figure 82: Map of the location of the TEM sites (black squares) crossing fire zone no. 8 (profiles no. 3 to no. 9) and at various other sites in the desert, west and east of one of the big hills in the south and over coal seams 6 and 7. Profiles no. 1, 2, 3 and 4 (orange lines) show the sites of the HL and the VLF measurements. The polygons of the burning zones (blue resp. light blue for colder fires and red resp. violet for hotter fires) were mapped in 2004 resp. 2005 by DLR.

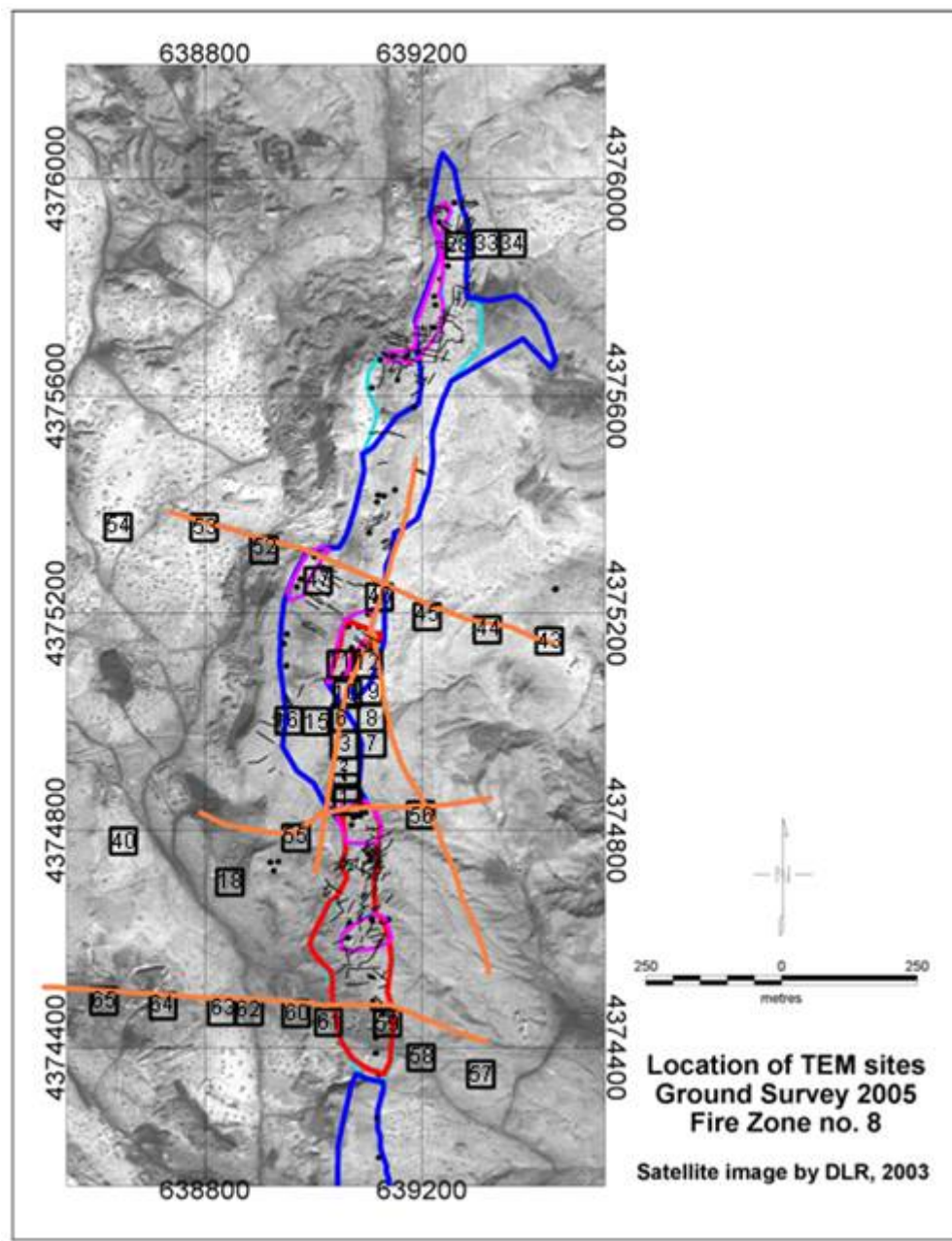


Figure 83: Quickbird satellite image of fire zone no. 8 (DLR, 2003) with location of the TEM ground survey sites (black squares). Orange lines show the profile lines of the HL and the VLF measurements. Blue and red polygons show the burning zones in 2004 and light blue and violet polygons show the burning zones in 2005. Black dots mark burning spots in 2005 (mapped by DLR). Cracks are marked by light black lines.

The apparent resistivity curves at all survey sites are shown in Fig. 84, 87, 90, 92, 93, 96, 98, and 100. They provide an overview of the resistivity structure to be expected at the subsurface below that point by assuming a homogeneous half-space model. The 1-D inversion yields layered resistivity models. Although the diffusion depth is theoretically independent of the transmitter loop size, it is restricted by energy losses because of the resistivity of the subsurface. Thus, the diffusion depth of the transient current system is about three times the



side length of the transmitter loop leading to investigation depth for most soundings of about 150 m with a 50 m by 50 m loop. But it has to be considered that the resistivity structure influences the investigation depths, too. Besides that the investigation depth can be restricted by the local noise level. For three profiles (no. 3, no. 6 and no. 5) apparent resistivity versus apparent depth is shown (Fig. 85, 88 and 94). This gives a quick overview of the apparent resistivity distribution for soundings located along a survey line with an appropriate distance.

The vertical resistivity sections include all soundings along a profile line and show the 1-D models calculated at each sounding site (Fig. 86, 89, 91, 95, 97, and 101). It has to be kept in mind that the TEM soundings, mostly carried out with the inloop configuration, provide information about the subsurface directly below the sounding point, although the current system spreads with depth. The graphical display of several sounding sites close together neglects especially in inhomogeneous terrain the fact that the modelled resistivity values between two measured points are interpolated. For an one-dimensionally layered earth it can also be expected that for greater depths neighbouring soundings sites should yield the same model. As it can be seen e.g. at the northern part of profile no. 6 this is not obtained. The neighbouring sites 10 and 11 show different apparent resistivity curves and the curve from site 11 cannot be explained by a 1-D model. This fact gives reason for the assumption that the subsurface structure is inhomogeneous and needs three-dimensional interpretation (Fig. 87).

At fire zone no. 8 TEM profiles no. 3 to no. 9 were carried out. The profiles no. 3, no. 4, no. 5, no. 8 and no. 9 cross this fire zone from west to east. Profiles no. 6 and no. 7 start at the northern end of the collapsed area, i.e. directly at the southern end of the plateau at fire zone no. 8 (profile no. 6) or about 50 m further to the north (profile no. 7, located 50 m east of profile no. 6), see Fig. 82 and 83.

The loop sizes at sites 17 and 18 on profile no. 4 have to be reduced to 12.5 m by 12.5 m due to little space. The results of both measurements are similar, they used the same transmitter loop but different locations of the receiver coil (separate loop configuration). Site 18 yielded data of better quality and is shown in the vertical resistivity section.

In the central part of profile no. 6 a 100 m by 100 m transmitter loop was used, including the area of the transmitter loops of the sites 6, 8, 9 and 10. As the results do not differ significantly from the soundings of the smaller loops from sites 6 and 9, it is not shown here. Site 5 of profile no. 6 on the plateau was carried out with the separate loop configuration. The result is similar to that from site no. 4 but of less quality; it is also not shown. For profile no. 4 it has to be considered that the sounding sites do not follow a straight line from west to east, especially site 42 is situated south of site 41.

The vertical resistivity section of profile no. 6 displays a northwards dipping conductor (Fig. 89) at depths of 23 m (site 1) down to about 50 m (site 6). The southern collapsed part of this fire zone was not accessible on ground as numerous cracks pass through the area (see Fig. 83). Therefore, no data could be obtained from that region. At a drilling site about 50 m north of site 1 on profile no. 6, the top coal seam (seam no. 9) was found at a depth of about 20 m below surface (Gielisch et al. 2006). With increasing distance from the cracks (in northerly direction) the depth of this conductor increases and its resistivity increases (from 10 Ohm*m to 23 Ohm*m), too. In the northern part of profile no. 6 (sites 10 and 11) the resistivity structure of the subsurface is more complicated and one-dimensional modelling may not be sufficient to explain the data. The northwards dipping conductor at profile no. 6 continues to the east on profile no. 7 (Fig. 91), which is situated 50 m east of profile no. 6 (see Fig. 83).



**Innovative Technologies for Exploration, Extinction and Monitoring of Coal Fires in North China
Final Report Phase A Part B**

Investigations of the gas temperature of this fire zone predict a propagation of the fire front in north-easterly direction (Schloemer et al. 2006). This corresponds to the continuation of this conductor. Kus et al. (2006) describe the changes in the properties of coal samples collected along the outcropping seams no. 9 and no. 10 at fire zone no. 8.

Sites 15 and 16 from profile no. 8 do not show highly conductive layers at greater depth (Fig. 99). Profile no. 9 was chosen because of a low resistive area found by the HEM survey. TEM site 33 shows a layer with lower resistivity at a depth of about 30 m (Fig. 101).

Profile no. 3 crosses the fire zone further to the north. In this part of the area several burning spots can be found. Also several anomalies of the total magnetic field occur, which coincide with them (see Chapter 6). Low resistive layers (Rho below 30 $\text{Ohm}\cdot\text{m}$) can be found at sites 47, 45 and 44 on that profile. Site 47 shows a low resistive layer (Rho about 26 $\text{Ohm}\cdot\text{m}$) below 30 m depth (Fig. 86). The location of this site coincides with a coal seam affected by fire and an anomaly found by the ground magnetic survey (Fig. 133). Sites 46 to 44 display a conductive layer close to the surface. The locations of these sites coincide with a low resistive area derived from the helicopter survey for the medium frequency (Fig. 28).

Profile no. 5, crossing fire zone no. 8 in the south, shows different apparent resistivity curves along the course of the profile. Crossing the part of the area where the hot burning zone can be found (sites 60 and 61), these curves change their shape clearly (Fig. 92 and 93). The vertical resistivity section shows a low resistive layer, starting at site 60 and dipping to the east (Fig. 95). The dipping of burning coal seam no. 9 coincides with that site. The vertical resistivity section displays a good spatial correlation of these shallow conductors with the burning zone. The eastwards dipping conductive layer coincides with the thermally affected coal seam at sites 60 to 57. The area of low apparent resistivities derived from the helicopter-borne electromagnetic survey (Fig. 26, 28 and 30) also corresponds to the location of the thermally affected coal seams. At greater depth a highly resistive basement can be found, showing the generally dipping of layers in the Wuda syncline.

The areas of low apparent resistivity (Rho_a below 50 $\text{Ohm}\cdot\text{m}$), determined by the helicopter survey, coincide with areas showing low resistive layers (Rho below 30 $\text{Ohm}\cdot\text{m}$) determined by the TEM survey as demonstrated in the eastern part of profile no. 3 (fig 86), the southern part of profile no. 6 (Fig. 89), and the central and eastern part of profile no. 5 (Fig. 95). In particular, low resistive layers (Rho below 30 $\text{Ohm}\cdot\text{m}$) close to the surface can be found at sites 47, 46, 45 and 44 on profile no. 3, sites 1, 4, 2, 3 and 6 on profile no. 6 and sites 62 to 57 on profile no. 5. Site 47 shows a low resistive layer (Rho about 26 $\text{Ohm}\cdot\text{m}$) below 30 m depth. The location of this site coincides with a coal seam affected by fire and anomalies of the total magnetic field can be found at the same sites or within a little distance.



Innovative Technologies for Exploration, Extinction and Monitoring of Coal Fires in North China
Final Report Phase A Part B

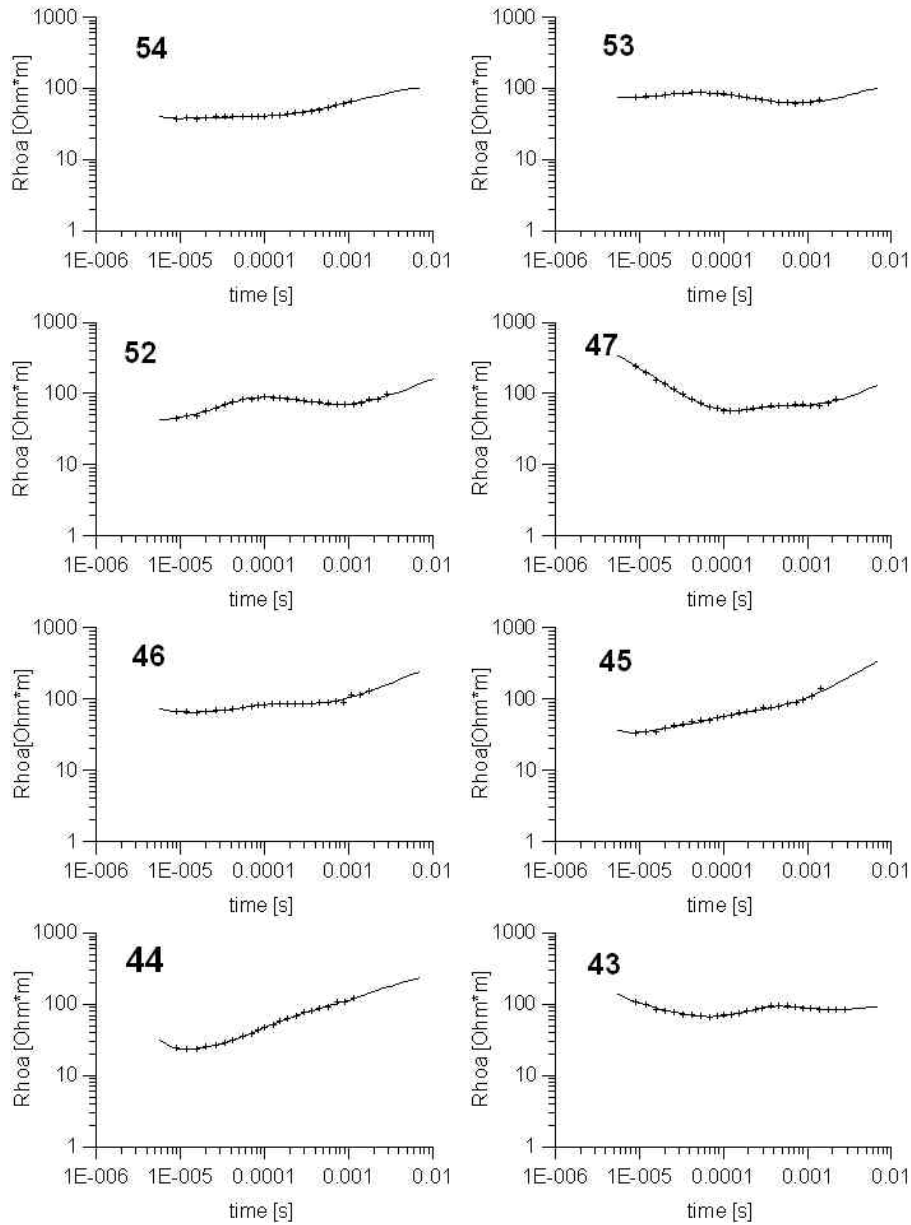


Figure 84: Apparent resistivity curves from TEM data along profile no. 3. Crosses: data, lines: model curve.



Innovative Technologies for Exploration, Extinction and Monitoring of Coal Fires in North China
Final Report Phase A Part B

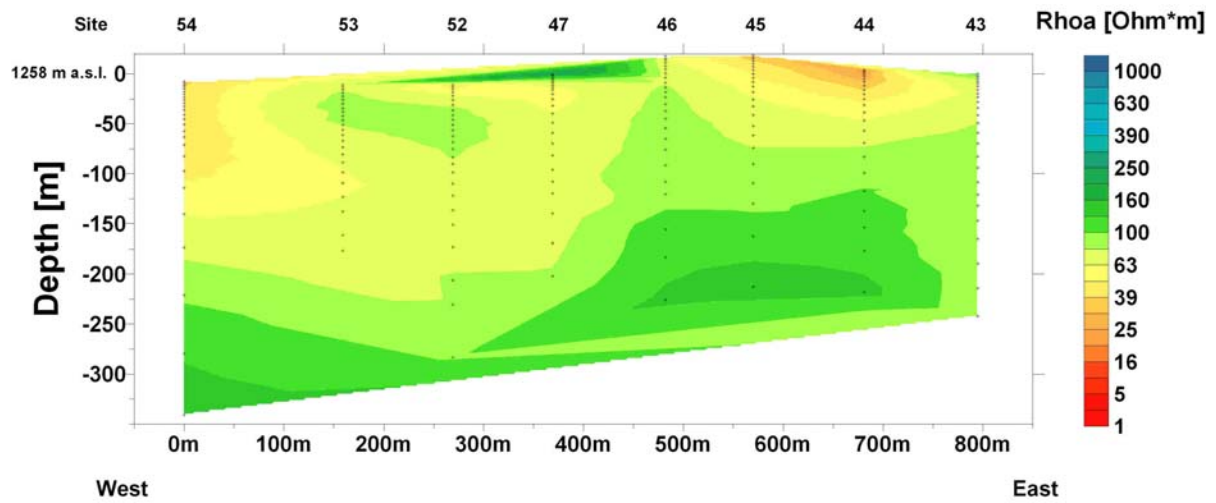


Figure 85: Apparent resistivity versus apparent depth from TEM data along profile no. 3.

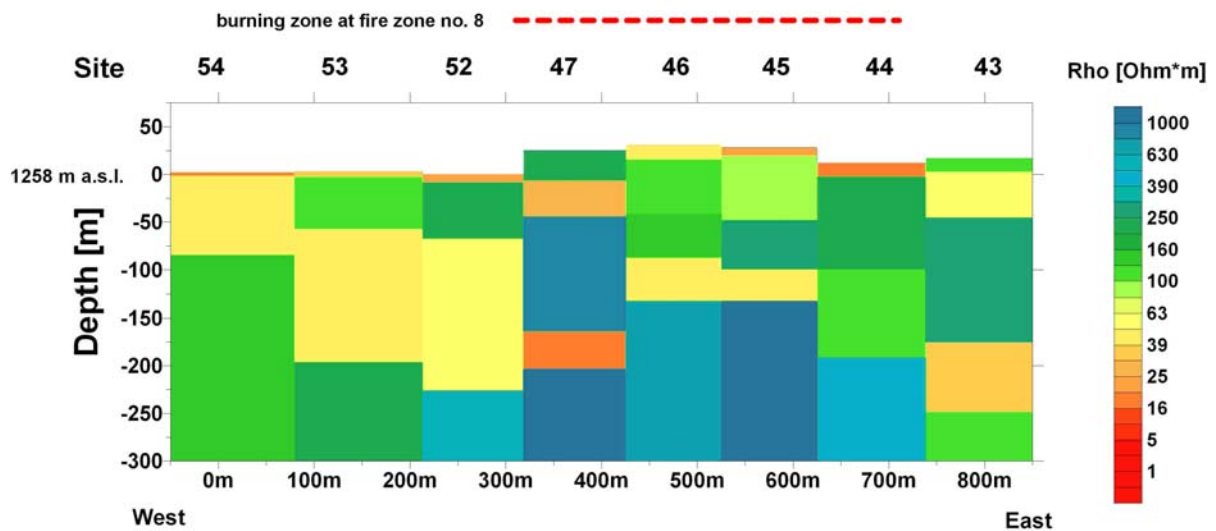


Figure 86: Vertical resistivity section derived from TEM data along profile no. 3. The burning zone is marked by a dashed red line.



**Innovative Technologies for Exploration, Extinction and Monitoring of Coal Fires in North China
Final Report Phase A Part B**

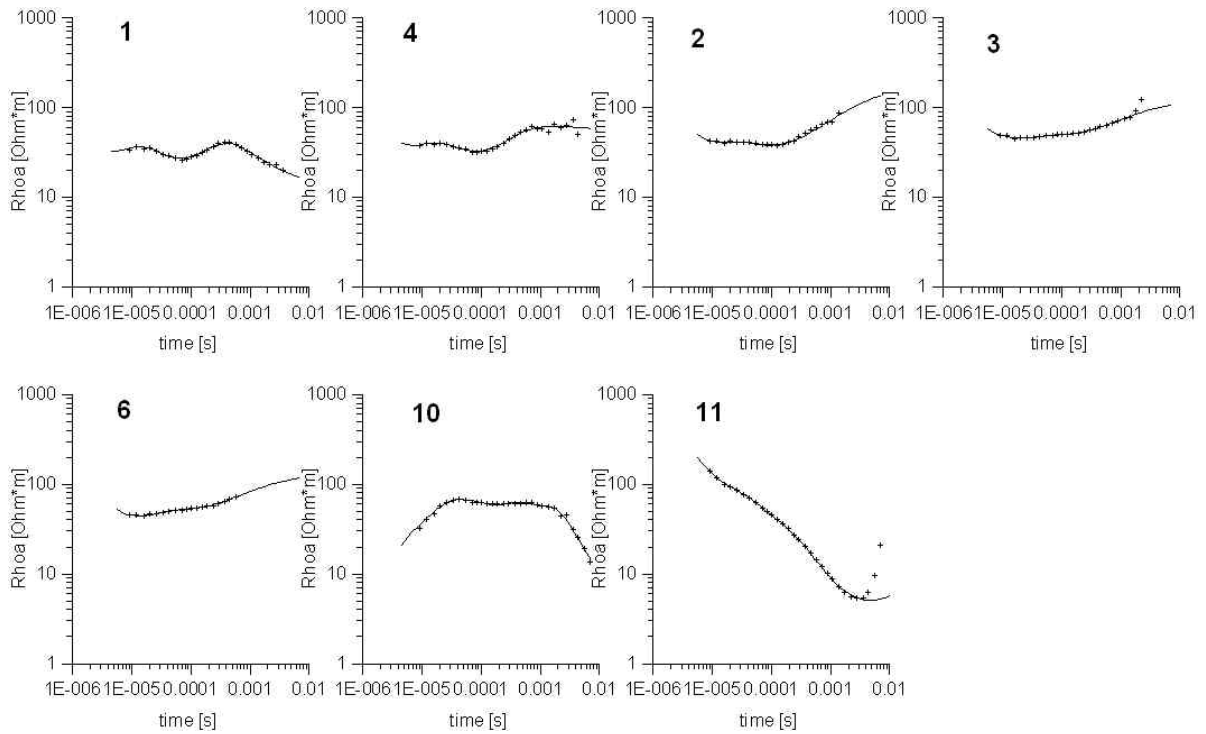


Figure 87: Apparent resistivity curves from TEM data along profile no. 6. Crosses: data, lines: model curve.

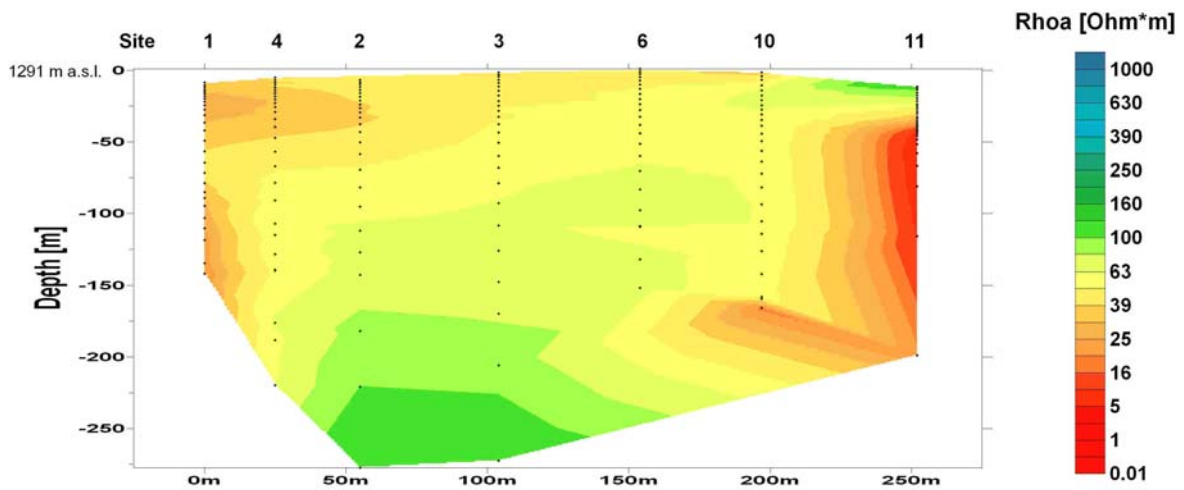


Figure 88: Apparent resistivity versus apparent depth from TEM data along profile no. 6.



**Innovative Technologies for Exploration, Extinction and Monitoring of Coal Fires in North China
Final Report Phase A Part B**

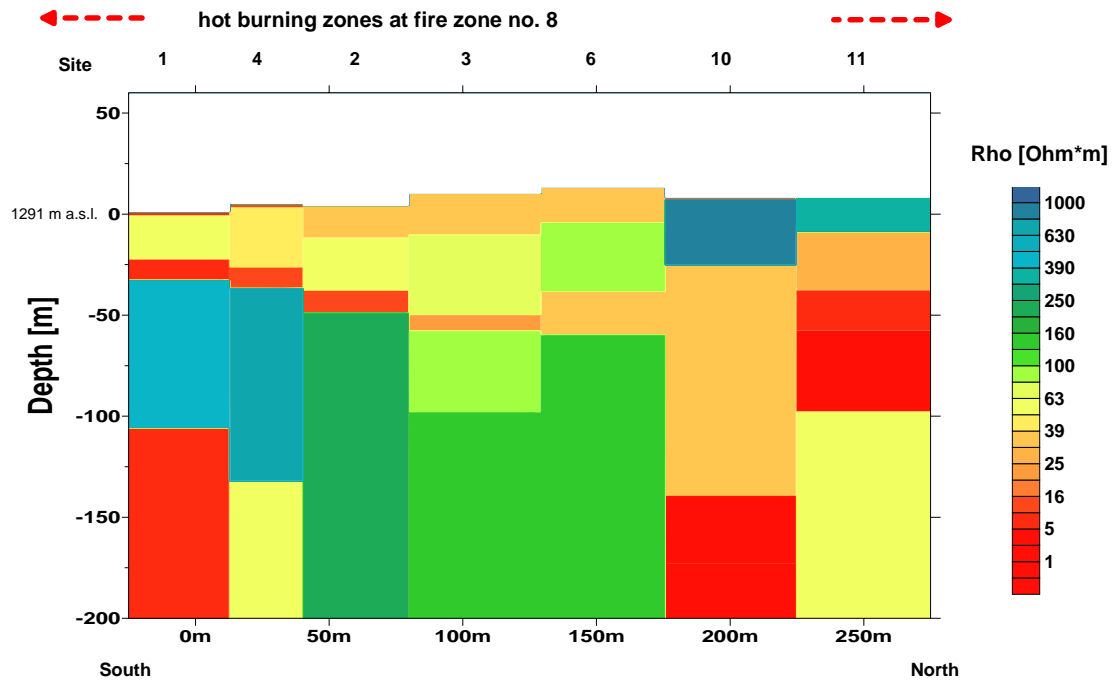


Figure 89: Vertical resistivity section derived from TEM data along profile no. 6. The burning zone is marked by a dashed red line. The conductor is dipping northwards from about 25 m to 50 m depth.

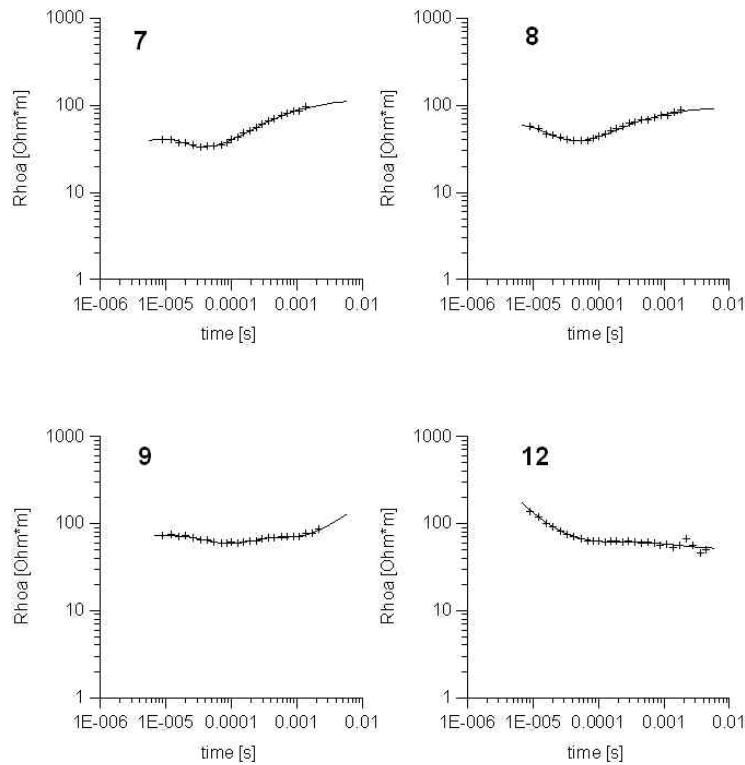


Figure 90: Apparent resistivity curves from TEM data along profile no. 7. Crosses: data, lines: model curve.



Innovative Technologies for Exploration, Extinction and Monitoring of Coal Fires in North China
Final Report Phase A Part B

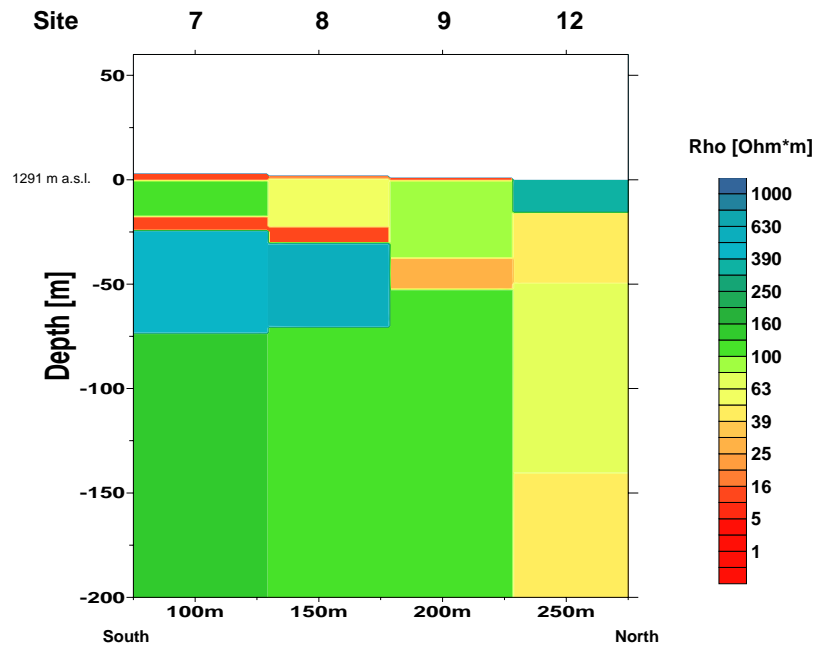


Figure 91: Vertical resistivity section derived from TEM data along profile no. 7.

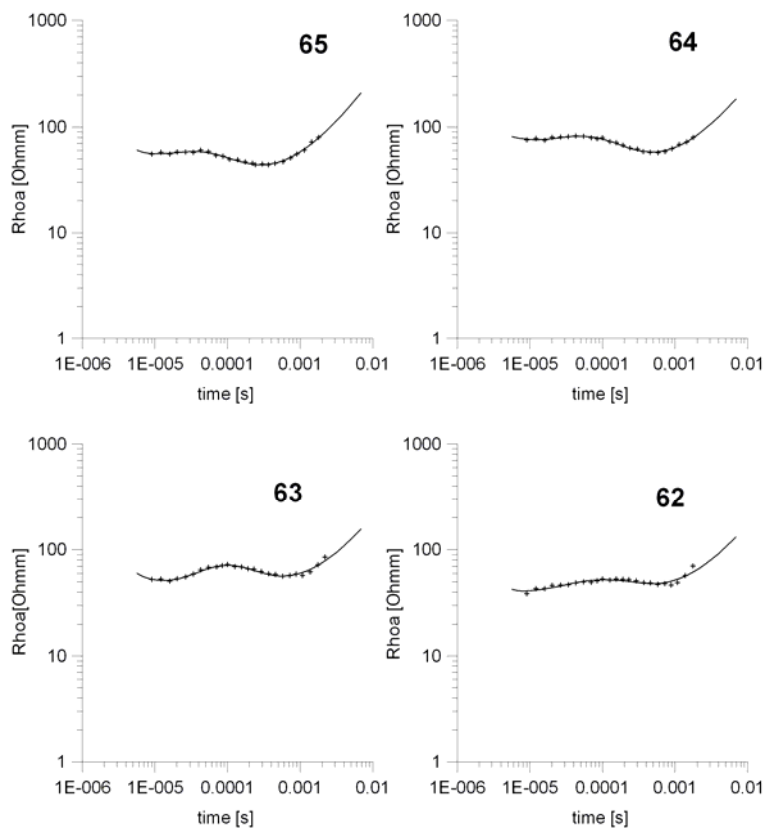


Figure 92: Apparent resistivity curves from TEM data along the western part of profile no. 5. Crosses: data, lines: model curve.



Innovative Technologies for Exploration, Extinction and Monitoring of Coal Fires in North China
Final Report Phase A Part B

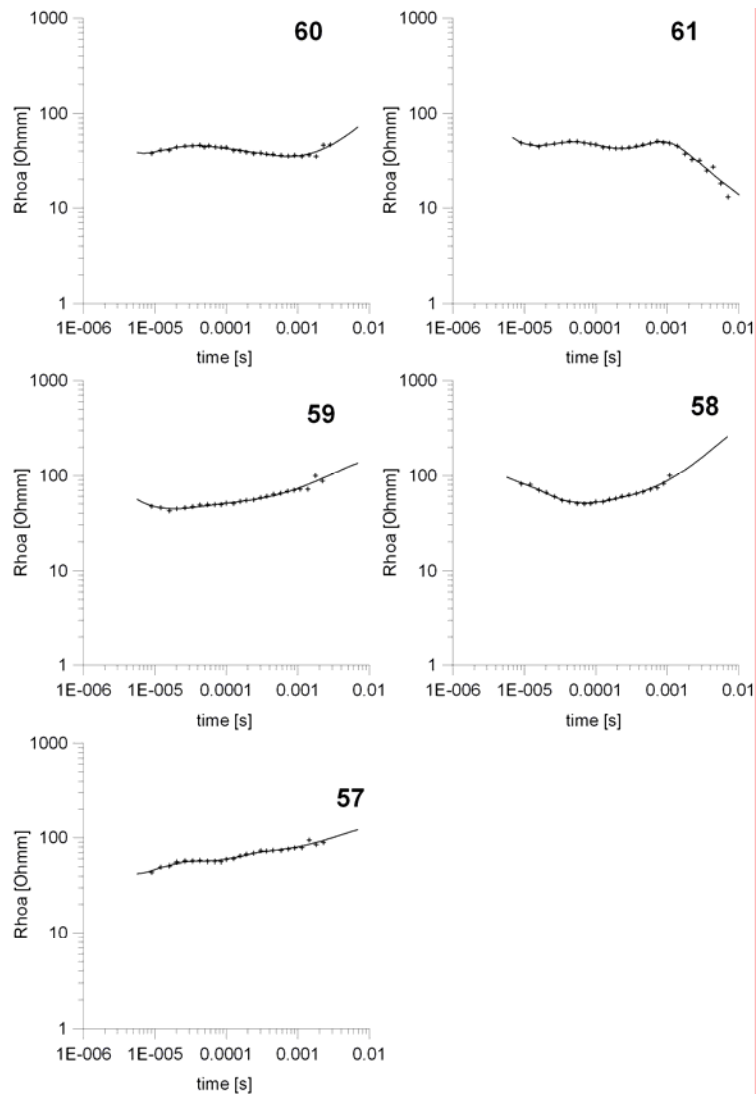


Figure 93: Apparent resistivity curves from TEM data along the eastern part of profile no. 5. Crosses: data, lines: model curve.



Innovative Technologies for Exploration, Extinction and Monitoring of Coal Fires in North China
Final Report Phase A Part B

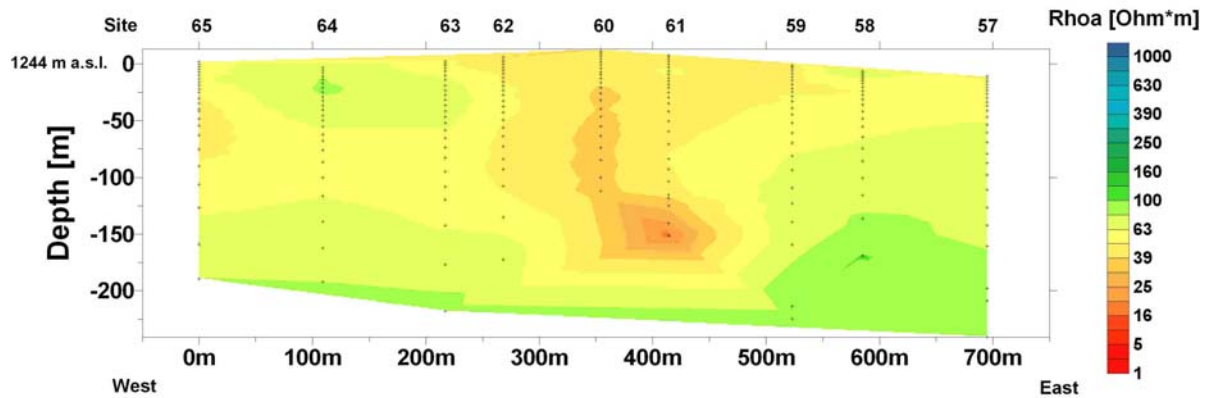


Figure 94: Apparent resistivity versus apparent depth from TEM data along profile no. 5.

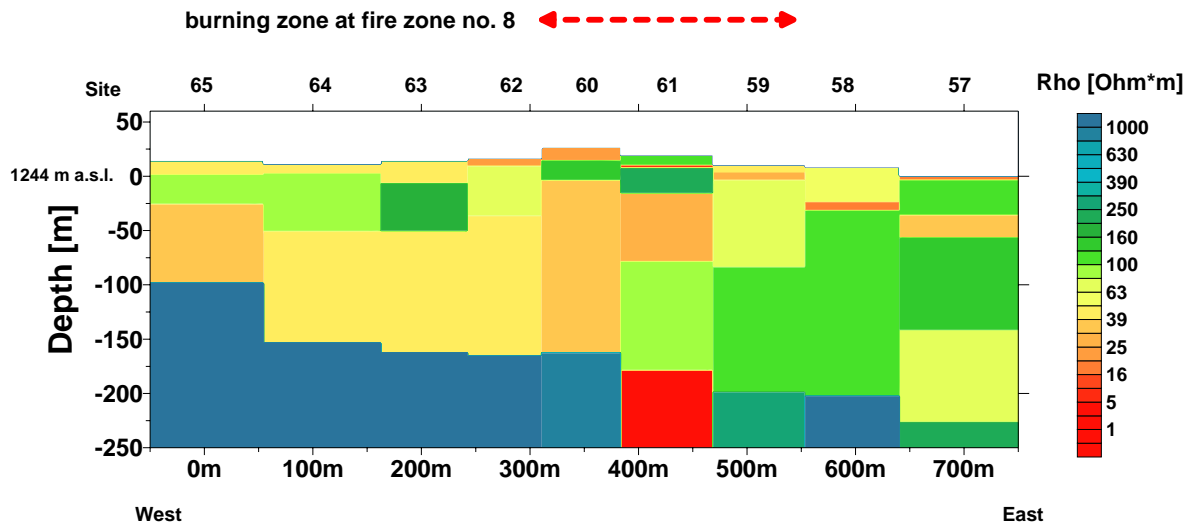


Figure 95: Vertical resistivity section derived from TEM data along profile no. 5. The burning zone is marked by a dashed red line. The eastwards dipping shallow conductor correlates with the burning part of fire zone no. 8.



Innovative Technologies for Exploration, Extinction and Monitoring of Coal Fires in North China
Final Report Phase A Part B

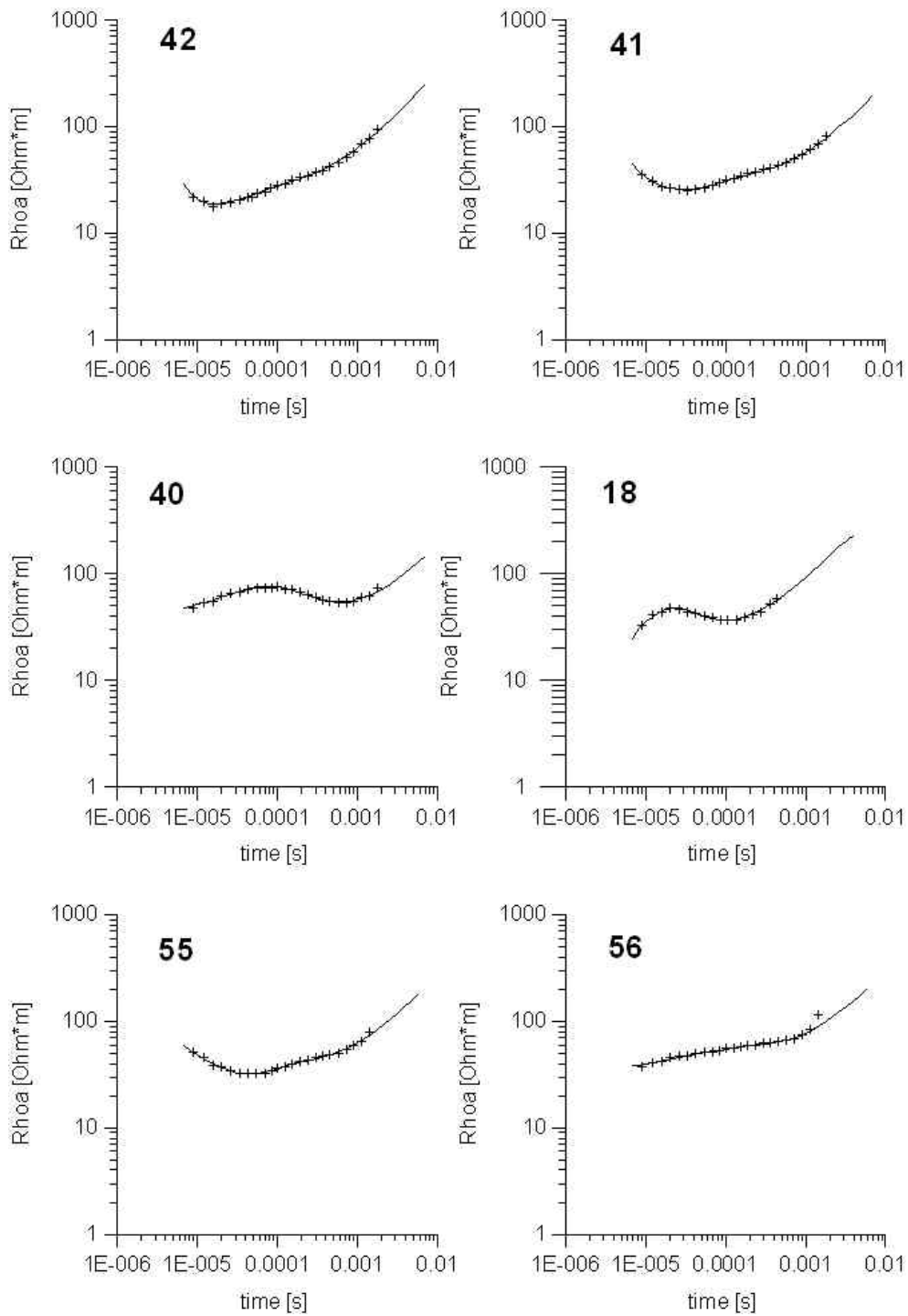


Figure 96: Apparent resistivity curves from TEM data along profile no. 4. Crosses: data, lines: model curve.



**Innovative Technologies for Exploration, Extinction and Monitoring of Coal Fires in North China
Final Report Phase A Part B**

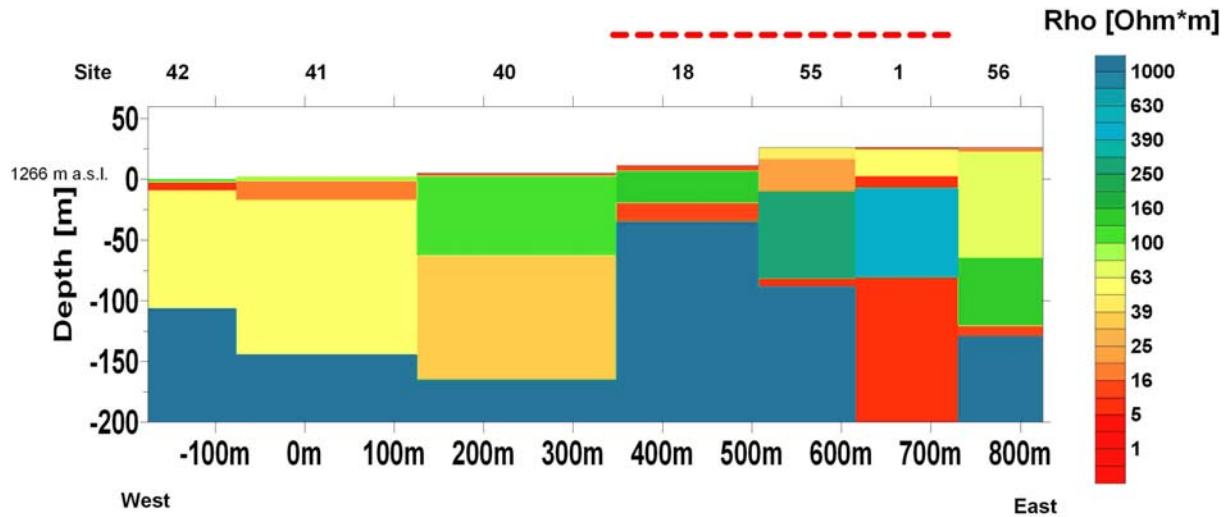


Figure 97: Vertical resistivity section derived from TEM data along profile no. 4. The burning zone is marked by a dashed red line. This profile crosses profile no. 6 at site 1.

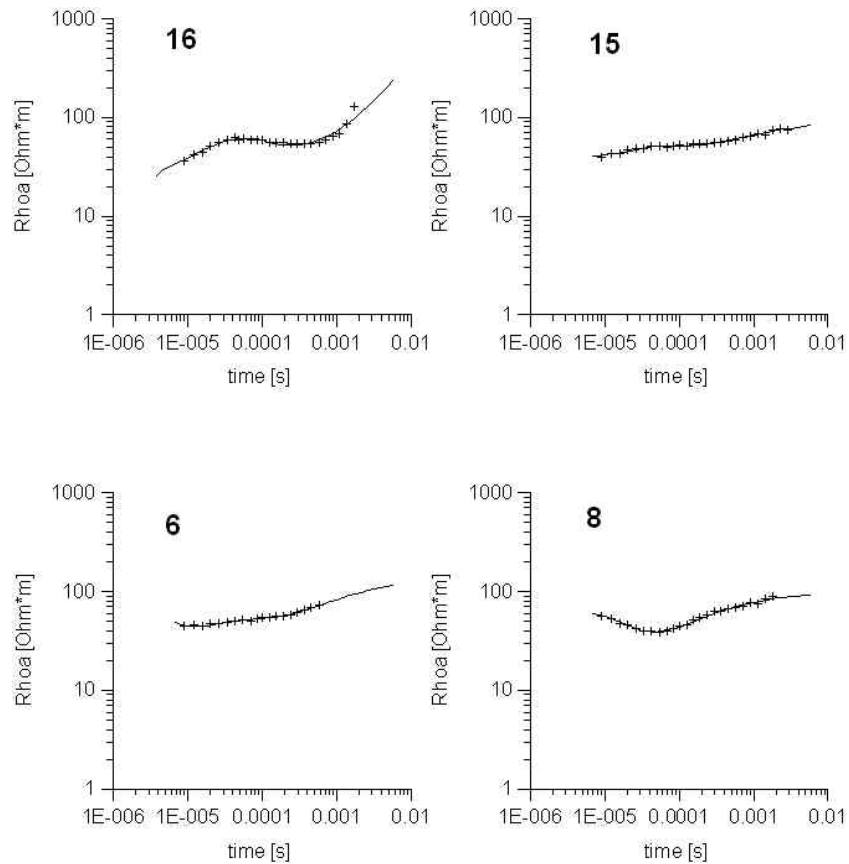


Figure 98: Apparent resistivity curves from TEM data along profile no. 8. Crosses: data, lines: model curve.



**Innovative Technologies for Exploration, Extinction and Monitoring of Coal Fires in North China
Final Report Phase A Part B**

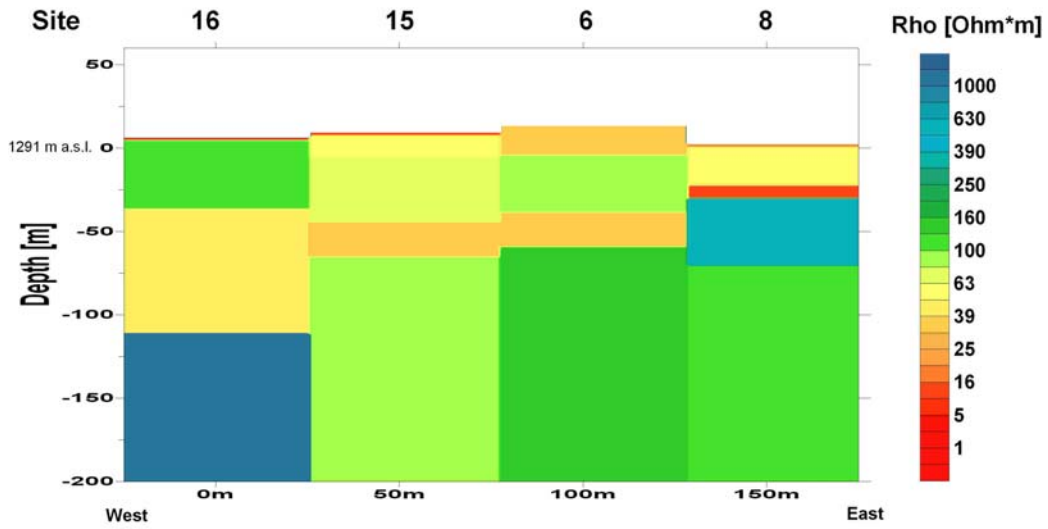


Figure 99: Vertical resistivity section derived from TEM data along profile no. 8. This profile crosses profile no. 6 at site 8.

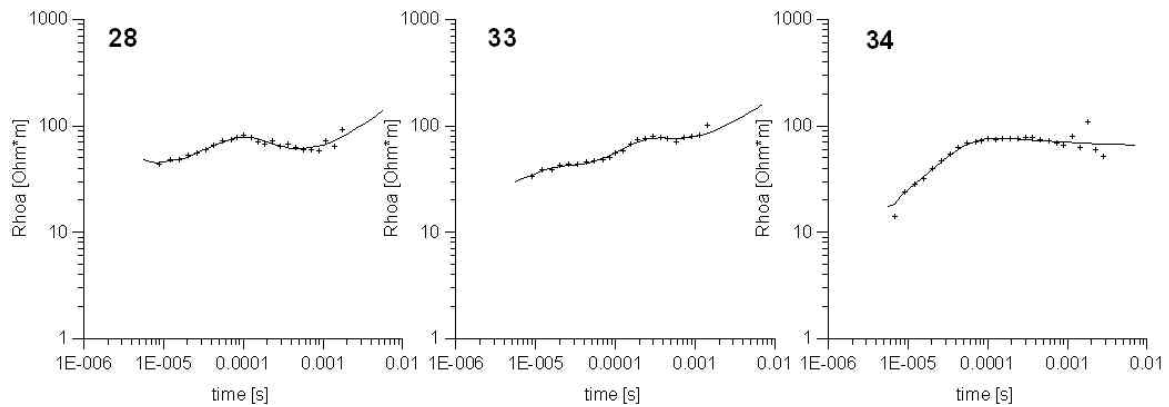


Figure 100: Apparent resistivity curves from TEM data along profile no. 9. Crosses: data, lines: model curve.



Innovative Technologies for Exploration, Extinction and Monitoring of Coal Fires in North China
Final Report Phase A Part B

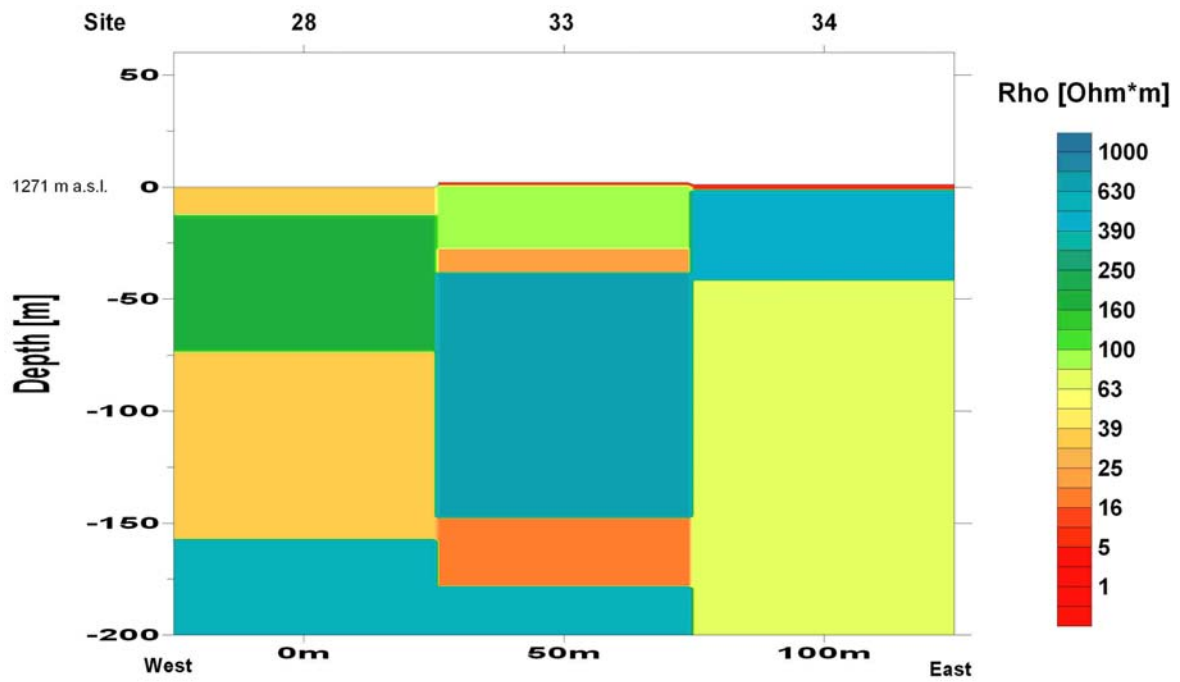


Figure 101: Vertical resistivity section derived from TEM data along profile no. 9 in the northern part of fire zone no. 8.



5.1.2 Results from fire zone no. 3.2

The central part of fire zone no. 3.2 was object of investigation for the ground survey. Several TEM soundings were carried out over this fire zone. It is situated in the north-western part of the Wuda syncline, close to a small mining factory, which is located north-west of it. The whole fire zone extends from south-westerly direction a few hundreds of metres to the north-east. In the northern part a sandstone covered valley is situated with a pillar remained in the central part after mining. Coal seam no. 9 is burning at this test site.

Due to topographic conditions the coil spacing varies from 12,5 m by 12,5 m (sites 19, 20, 21, 22, 26 and 27) to 40 m by 40 m (sites 24 and 25) and 50 m by 50 m (sites 23, 48, 49, 50 and 51). At site 24 (Fig. 102) it was heavily burning, the transmitter coil covered an area with collapsed structure and smoking cracks. Fig. 103 shows the location of the TEM sites.



Figure 102: TEM survey at fire zone no. 3.2, site no. 24. View to the south-east.

Sites 19 and 20 have the same transmitter loop as well as sites 21 and 22. Here the separate loop configuration was used. The transmitter to receiver distance was 18 m for sites 19 and 20 and 25 m for sites 21 and 22 (not shown). These sites are situated at profile no. 11. Profile no. 10 is situated along the same survey line, but extends to the east and bigger coil sizes with the inloop configuration were used (sites 24, 23, 48, 49 and 50).

Profile no. 12 (sites 51, 25, 26 and 27) crosses fire zone no. 3.2 about 150 m north of the mentioned survey lines in the valley depression. It coincides nearly with a flight line of the HEM survey (Fig. 51 and 63) and crosses the remained pillar, which is partly burning, in the centre (at TEM site 26).

Site 51 was situated about 400 m north-west of the fire zone. No coal seam fire was noticed directly at that sounding point by the authors, but within a little distance collapsed structures were found.

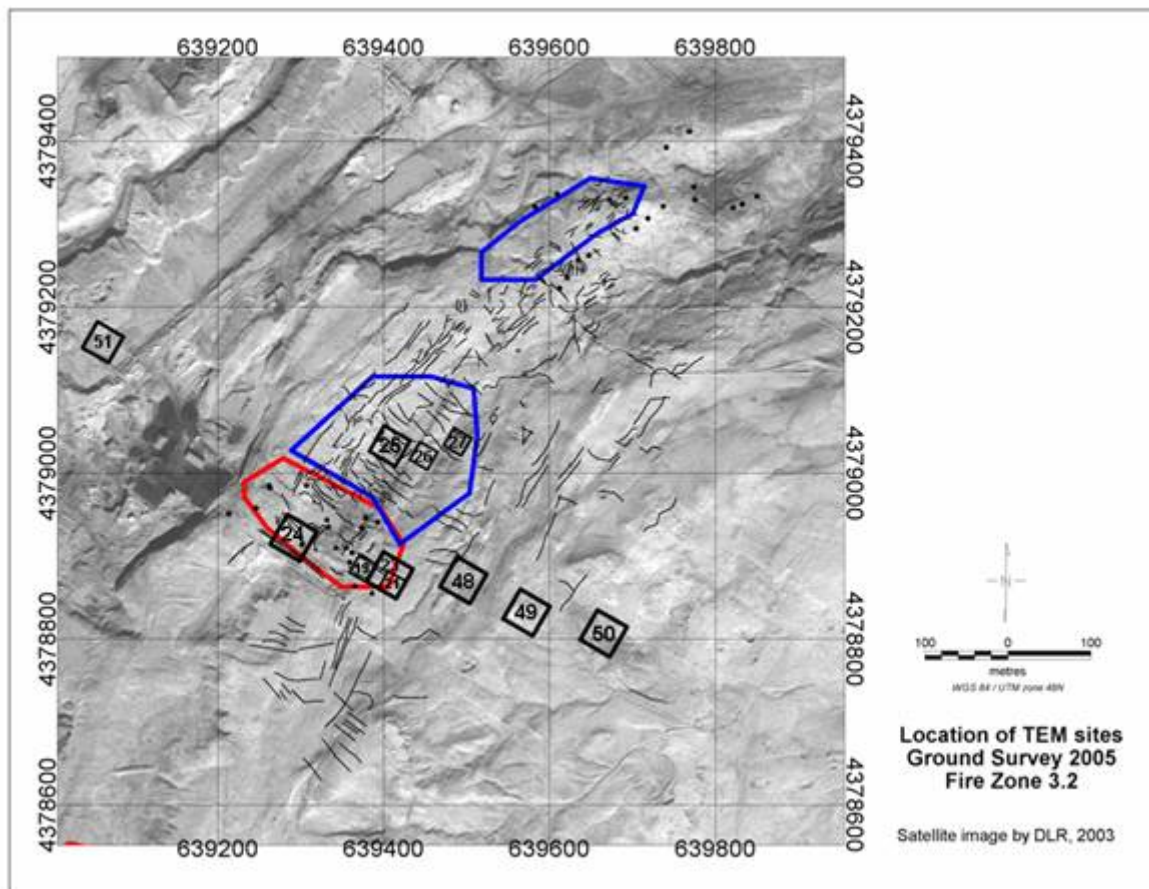


Figure 103: Quickbird satellite image of fire zone no. 3.2 (DLR, 2003) with location of the TEM ground survey sites (black squares). The red and blue polygons show burning zones in 2004 and black dots show the burning spots in 2005 (mapped by DLR). Cracks are marked by light black lines.

Figures 104, 106 and 108 show the apparent resistivity curves for all sites. It is evident that the curves differ a lot from each other, even neighbouring sites show different apparent resistivities. This is a hint for the inhomogeneous structure of that test site. For a few sites it was not possible to adapt sufficient one-dimensional models, these are sites 20, 21, 22 and 23. The resulting vertical resistivity section for profile no. 11 is therefore only estimated (Fig. 107). Nevertheless site 20 shows similar results to site 23 at the same location, but measured with a bigger transmitter coil size.

Sites 24, 23 and 48 from profile no. 10 show conductive layers at different depths (Fig. 109). The resistivity structure gives reason for the assumption of a very inhomogeneous subsurface. This can be confirmed by the bad adaptation of 1-D models to the sites measured with small coil sizes (profile no. 11). Beyond the fire zone in the south-east (sites 49 and 50) no fires were observed by the authors, but the area was interspersed by cracks and collapsed structures.

Site 26 at profile no. 12 (Fig. 105) is situated on top of the pillar in the centre of the valley. This site shows a conductor at a depth below 25 m. Site 51 outside the fire zone does not show a layer with low resistivity in the upper tens of metres.



**Innovative Technologies for Exploration, Extinction and Monitoring of Coal Fires in North China
Final Report Phase A Part B**

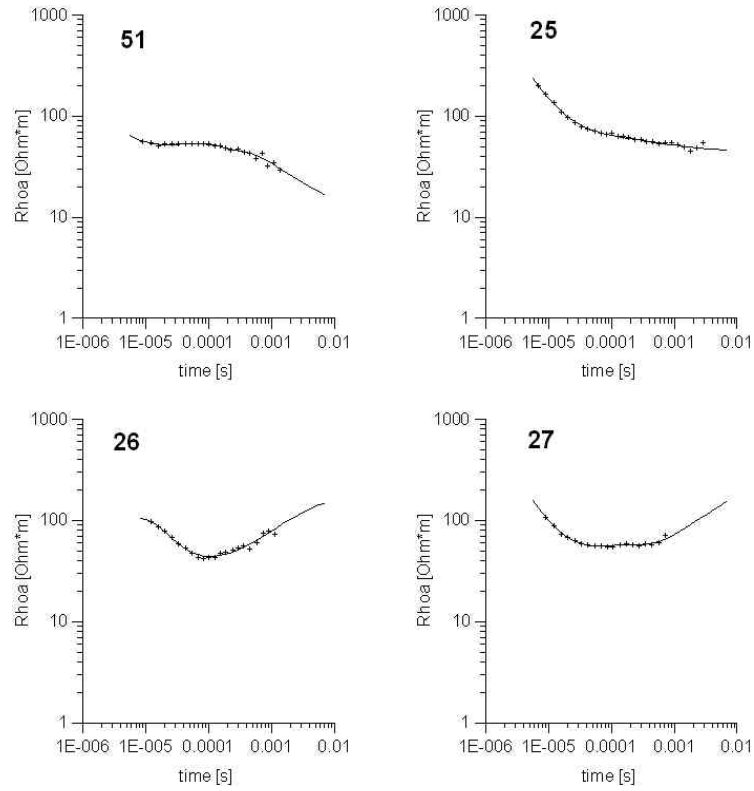


Figure 104: Apparent resistivity curves from TEM data along profile no. 12. Crosses: data, lines: model curve.



**Innovative Technologies for Exploration, Extinction and Monitoring of Coal Fires in North China
Final Report Phase A Part B**

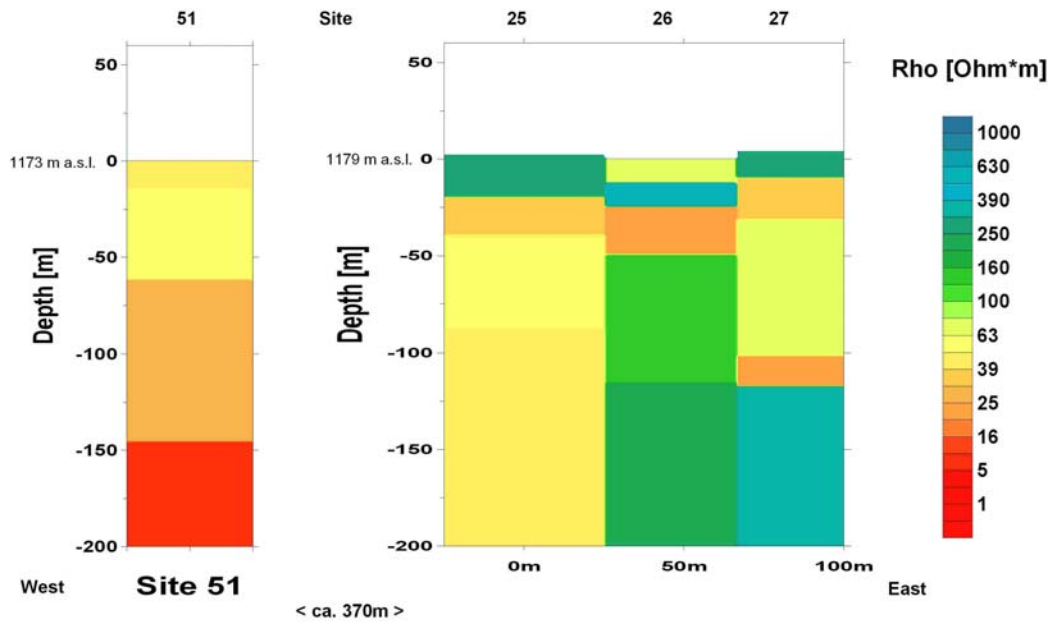


Figure 105: Vertical resistivity section derived from TEM data along profile no. 12. Site 51 is situated about 370 m apart west of profile no. 12.

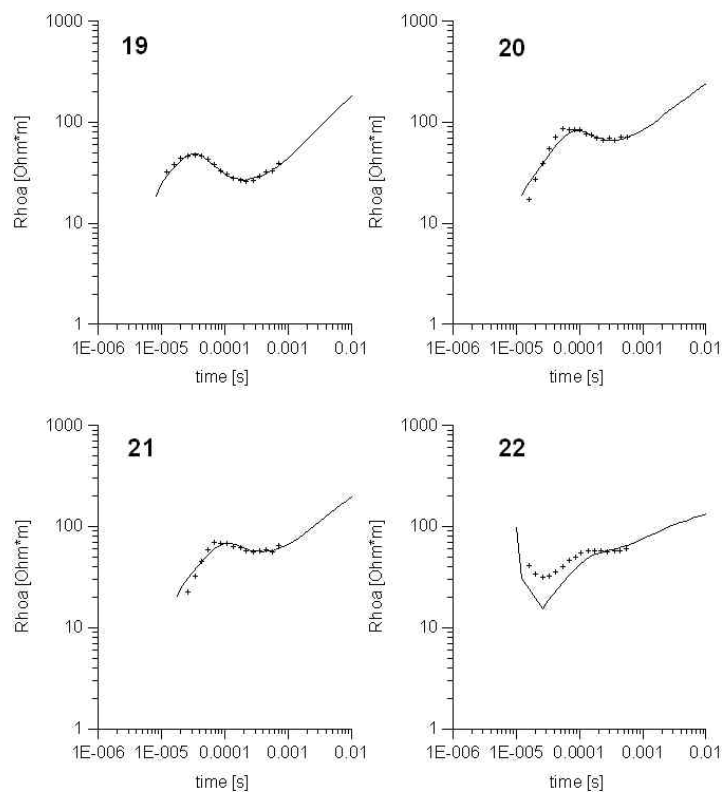


Figure 106: Apparent resistivity curves from TEM data along profile no. 11. Crosses: data, lines: model curve.



Innovative Technologies for Exploration, Extinction and Monitoring of Coal Fires in North China
Final Report Phase A Part B

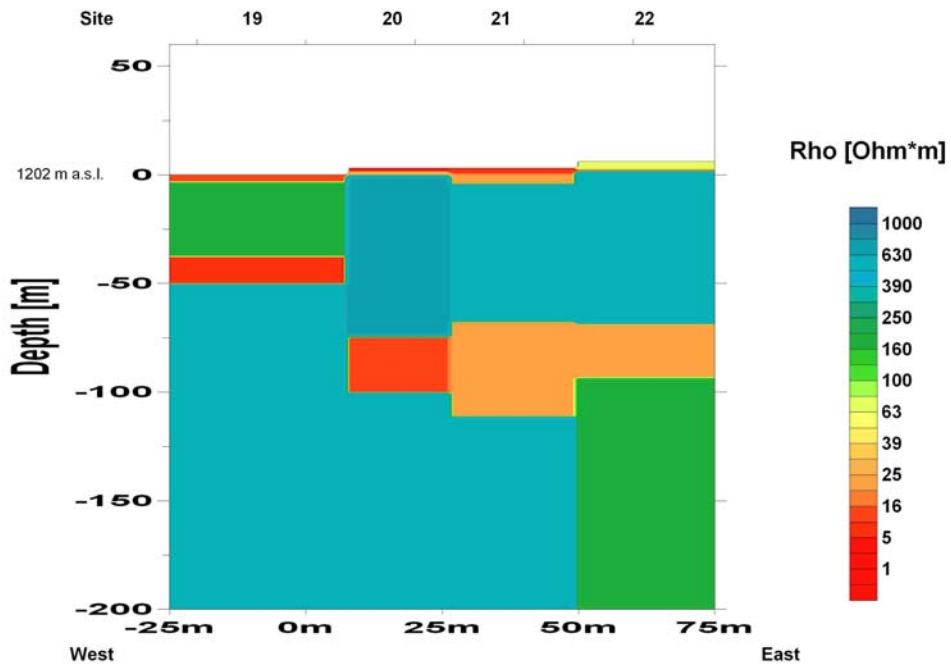


Figure 107: Vertical resistivity section derived from TEM data along profile no. 11.



Innovative Technologies for Exploration, Extinction and Monitoring of Coal Fires in North China
Final Report Phase A Part B

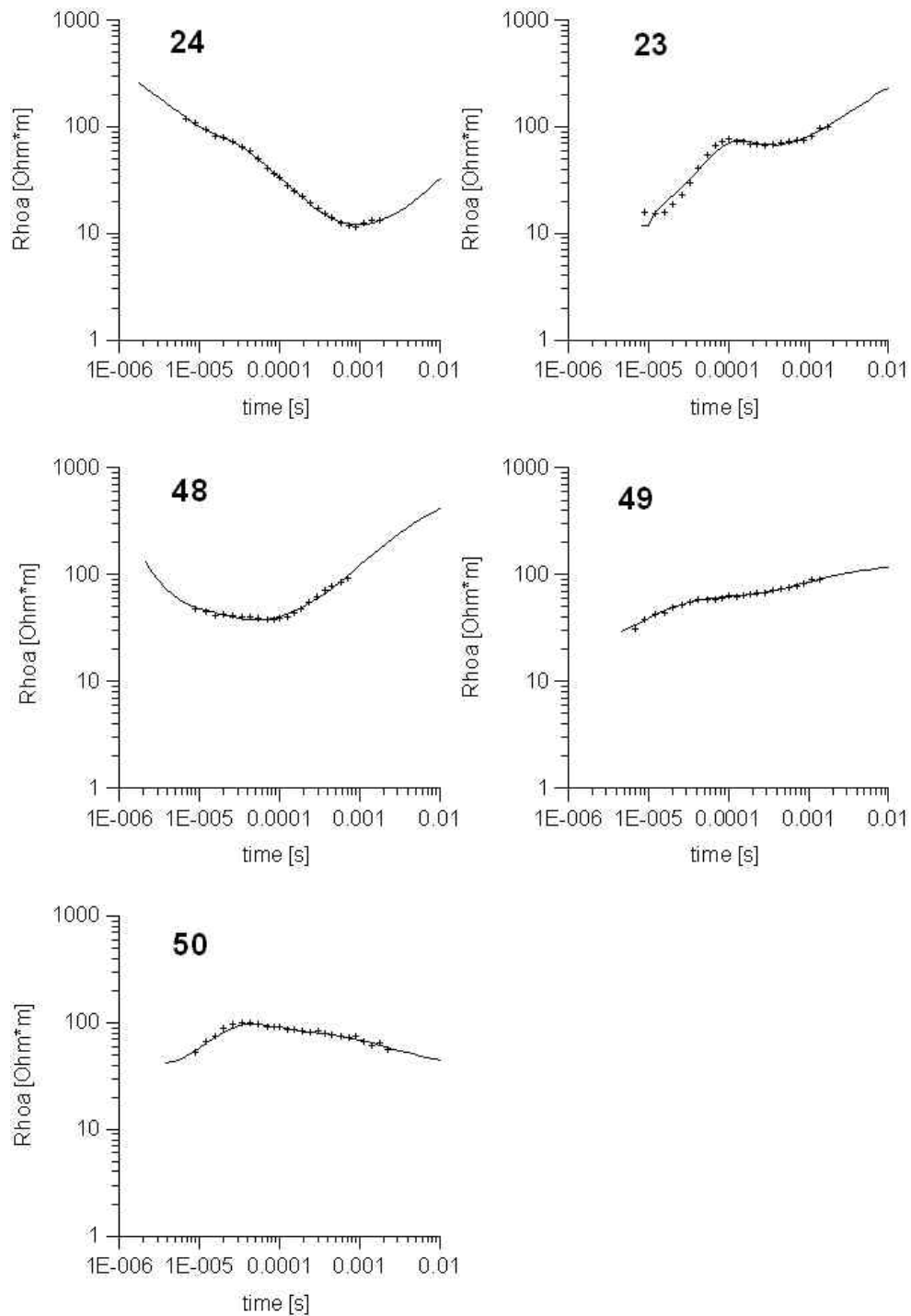


Figure 108: Apparent resistivity curves from TEM data along profile no. 10. Crosses: data, lines: model curve.

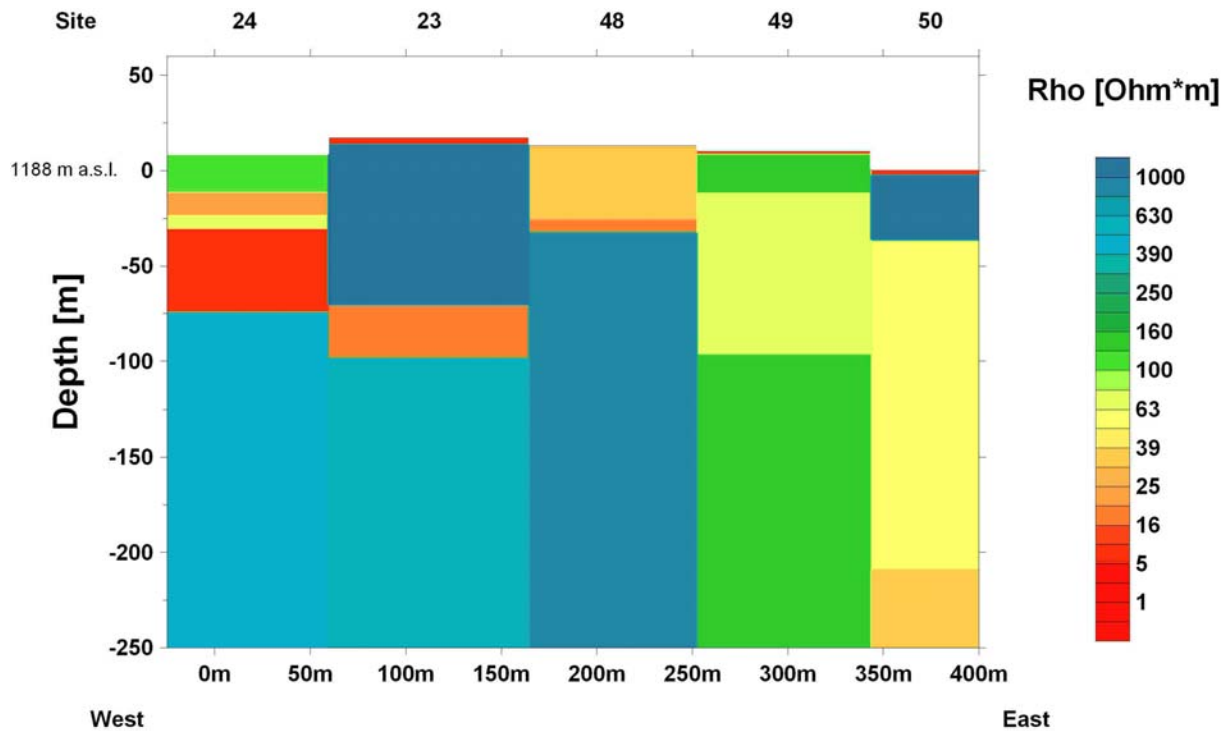


Figure 109: Vertical resistivity section derived from TEM data along profile no. 10.

5.1.3 Results from other sites

TEM soundings at the sites 35, 36 and 37 were performed above unaffected coal seams (seams no. 6 and no. 7) about 1 km south-east of fire zone no. 8 (Fig. 82) in order to investigate possible changes in electrical conductivity in the subsurface at sites where intact coal seams are located. The one-dimensional modelling results do not reveal conductive layers at the depth of these intact coal seams. Figure 110 shows the apparent resistivity curves derived from TEM data at this three sites, gained over the two intact coal seams no. 6 and no. 7, situated at a depth of about 8 m. At this depth no resistivity low occurred. The medium part of the apparent resistivity curve of site no. 36 was disturbed. Nevertheless a sufficient approximation by a 1D inversion model was achieved. Site no. 37 was not interpreted by a layered model, but the resistivity curve clearly shows no low resistive layer for the uppermost metres below surface (Fig. 111).



**Innovative Technologies for Exploration, Extinction and Monitoring of Coal Fires in North China
Final Report Phase A Part B**

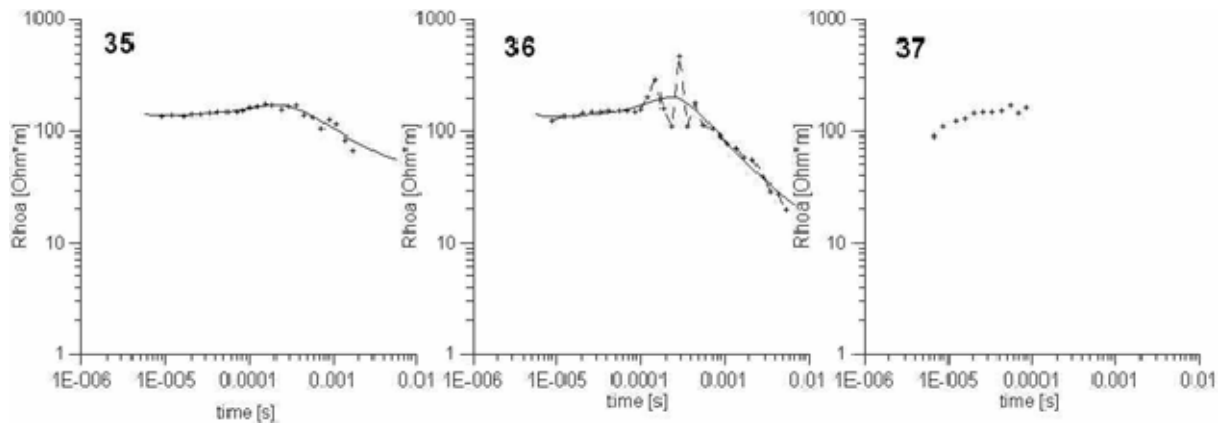


Figure 110: Apparent resistivity curves from TEM data at coal seams no. 6 and no. 7.

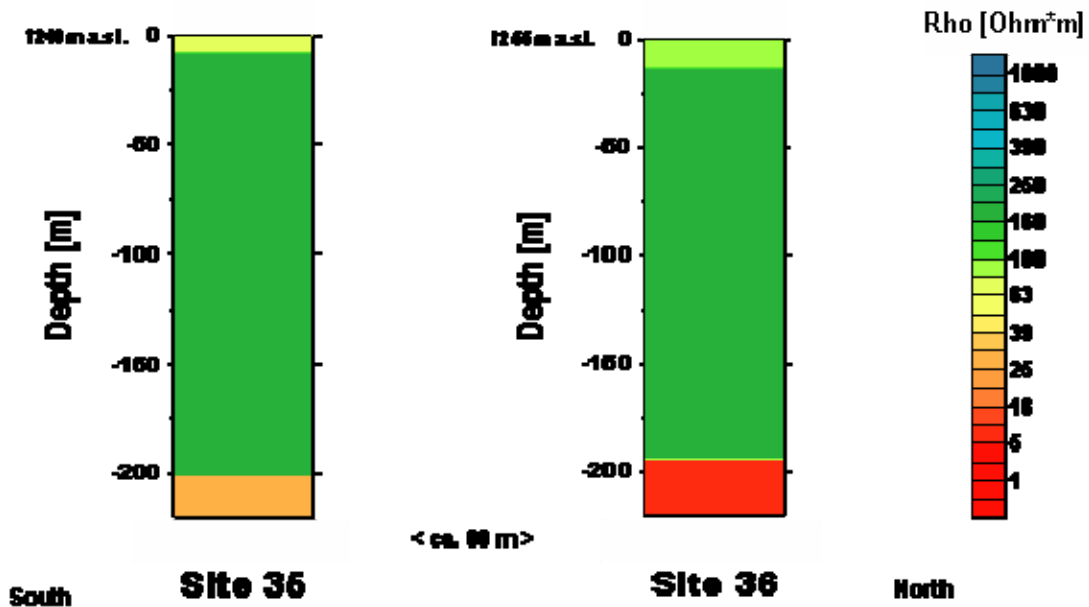


Figure 111: 1D inversion models derived from TEM data for two sites outside the burning zones over the not burning coal seams no. 6 and no. 7 in the central part of the Wuda syncline.

North of the Wuda syncline towards the Gobi desert four TEM sites had been placed to compare the results from an area unaffected by coal seam fires with those sampled over the burning zones. Figure 112 shows the apparent resistivity curves for these measurements. At no site highly conductive layers were found. The 1-D inversion models (Fig. 113) reveal two or three layers with resistivity values in the range from 20 to 60 Ohm*m for the upper layers and more than 400 Ohm*m for the base layer. The low conductive base layer is ascending from west to east. The low resistivity of the upper layers can be explained by the eolian quicksands of the Gobi desert, which cover most parts west and north outside the Wuda syncline. These quicksands could contain a high content of minerals, which might contribute to a lower resistivity of the upper layers.



**Innovative Technologies for Exploration, Extinction and Monitoring of Coal Fires in North China
Final Report Phase A Part B**

Two soundings were done at sites 38 and 39 in the southern part of the Wuda syncline. They are situated west and east of one of the big hills in the south (Fig. 82). It was intended to get data from zones without fire and to yield more information about the geology within the Wuda area. Figure 114 and 115 show apparent resistivity curves and the results of 1-D modelling. No low resistive layers could be found to a depth of about 200 m.

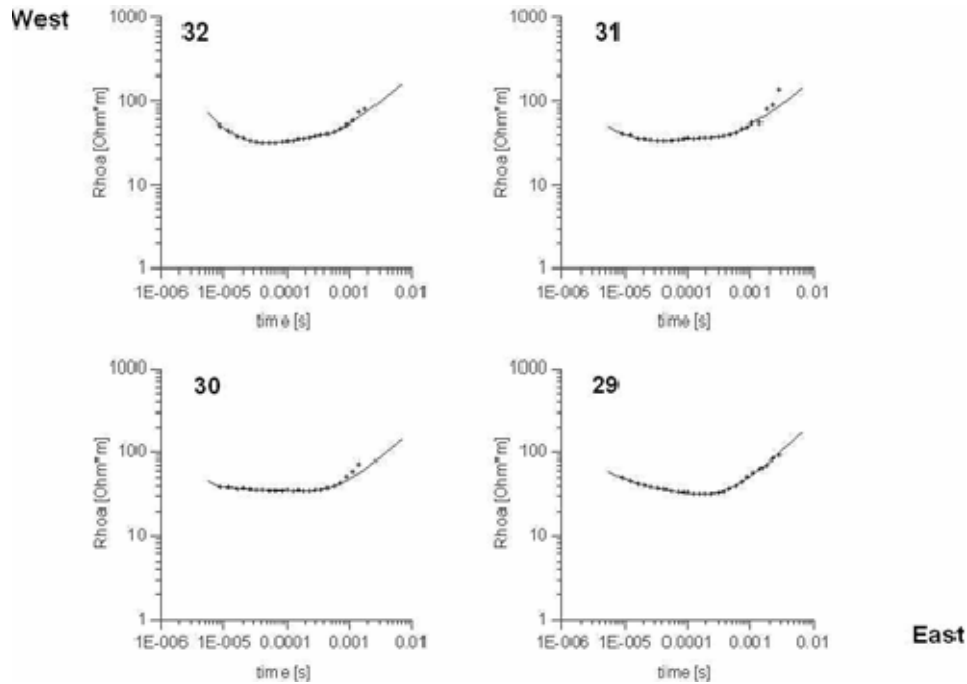


Figure 112: Apparent resistivity curves from TEM data at sites in the desert north beyond the Wuda syncline.

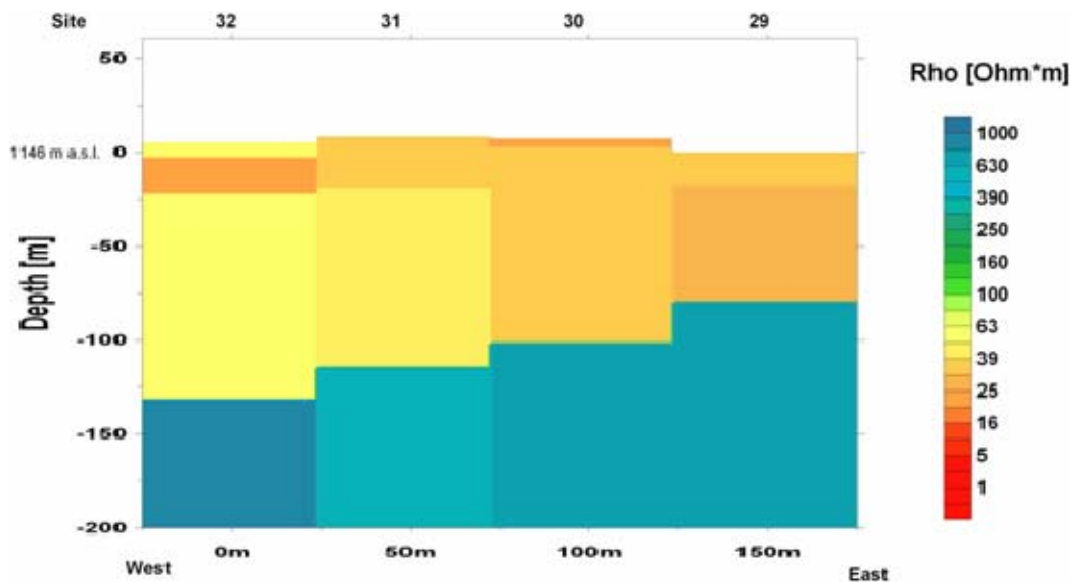


Figure 113: Vertical resistivity section derived from TEM data outside the burning zones in the desert area north of the Wuda syncline.



Innovative Technologies for Exploration, Extinction and Monitoring of Coal Fires in North China
Final Report Phase A Part B

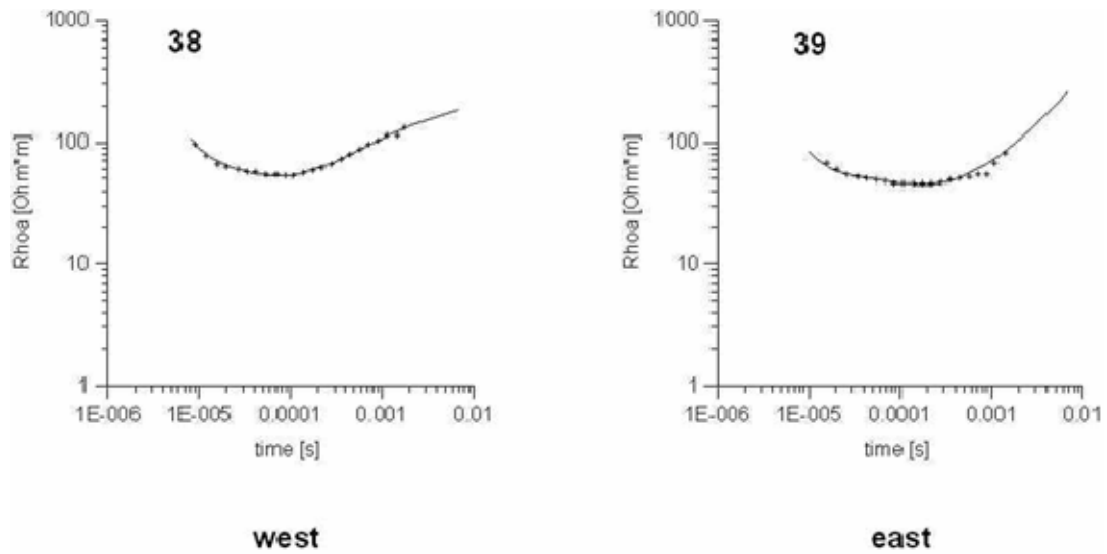


Figure 114: Apparent resistivity curves from TEM data at two sites in the southern part of the Wuda syncline.

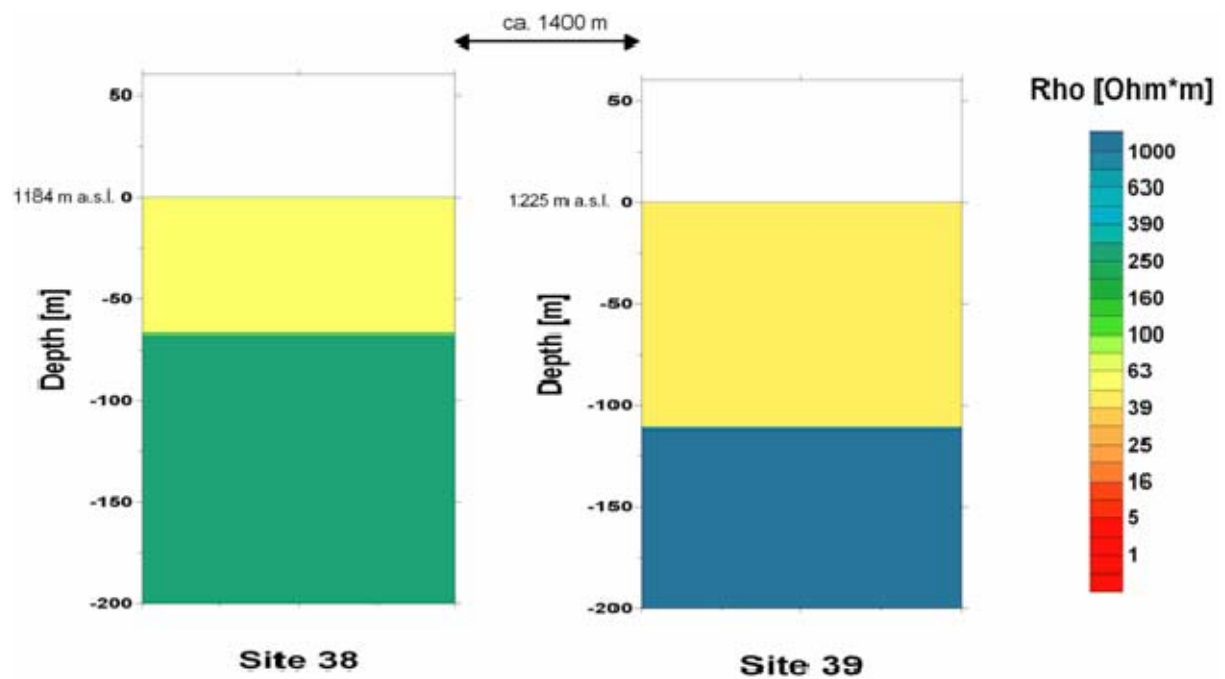


Figure 115: Vertical resistivity section from TEM data outside the burning zones in the southern part of the Wuda syncline. Site 38 is located west of one of the big hills in the south and site 39 east of it.



5.2 Horizontal Loop and VLF ground surveys

The Horizontal-Loop method (HL) is a frequency electromagnetic method (EM). Such measurements, similarly as TEM measurements, provide information on the distribution of the electrical resistivities in the subsurface. By varying the frequencies of the EM signals or the separations of the transmitter and receiver coils it is possible to get information on changes of resistivity with depth. Lateral changes such as dykes, gaps and faults can be studied by this method as well.

For the HL survey the instrument Apex Max-Min was used. The coil separation was 100 m for all measurements and the point separation 25 m. Up to eight frequencies were used, these are 28160 Hz, 14080 Hz, 7040 Hz, 3520 Hz, 1760 Hz, 880 Hz, 440 Hz and 220 Hz. The signal response is plotted as In-phase and out-of-phase curves along the profile measured. No HL profiles were measured at fire zone no. 3.2.

With the VLF method magnetic field components of the signals of military radio transmitters in the very low frequency range (15 to 30 kHz) are utilized. VLF gives information about lateral changes of the electrical resistivity within the ground. It is preferably chosen to detect steeply dipping conductors or contacts, but does not give valuable information about the depth of the structures. In a modification of this VLF method, called VLF-R, the horizontal components of the electrical field as well as the orthogonal magnetic field components of such radio signals are measured. By this also the resistivities of the subsurface can be calculated. VLF frequencies are rather high for geophysical applications and so the penetration depth of the method is less than for the TEM and the HL method, too.

For our VLF measurements the reasonably strong signals of a transmitter situated in an easterly direction with a frequency of 22.2 kHz could be used. The distance of the sampling points was about 10 m for all profiles measured (no.1, no. 3, no. 4 and no. 5). Profiles no. 6 and no. 7 were chosen at fire zone no. 7 in order to compare VLF results with those from the helicopter electromagnetic survey. No VLF measurements were carried out at fire zone 3.2.

For the location of the HL and the VLF profiles see Fig. 82. All presented measurements were performed over fire zones no. 8 and no. 7. The TEM profiles no. 6 and no. 7 at fire zone no. 8 are not identical with the VLF profiles no. 6 and no. 7 from the VLF-R survey. These are situated at fire zone no. 7. Along the VLF profiles no. 4 (fire zone no. 8), no. 6 and no. 7 (fire zone no. 7) also the total magnetic field was measured.

Figure 116 shows the results of the VLF and the HL measurements along profile no. 1. This profile starts in the south and takes its course west of the plateau close to the active burning part of fire zone no. 8 in the southern part. It moves slightly eastwards and continues then along the plateau further to the north.



Innovative Technologies for Exploration, Extinction and Monitoring of Coal Fires in North China
Final Report Phase A Part B

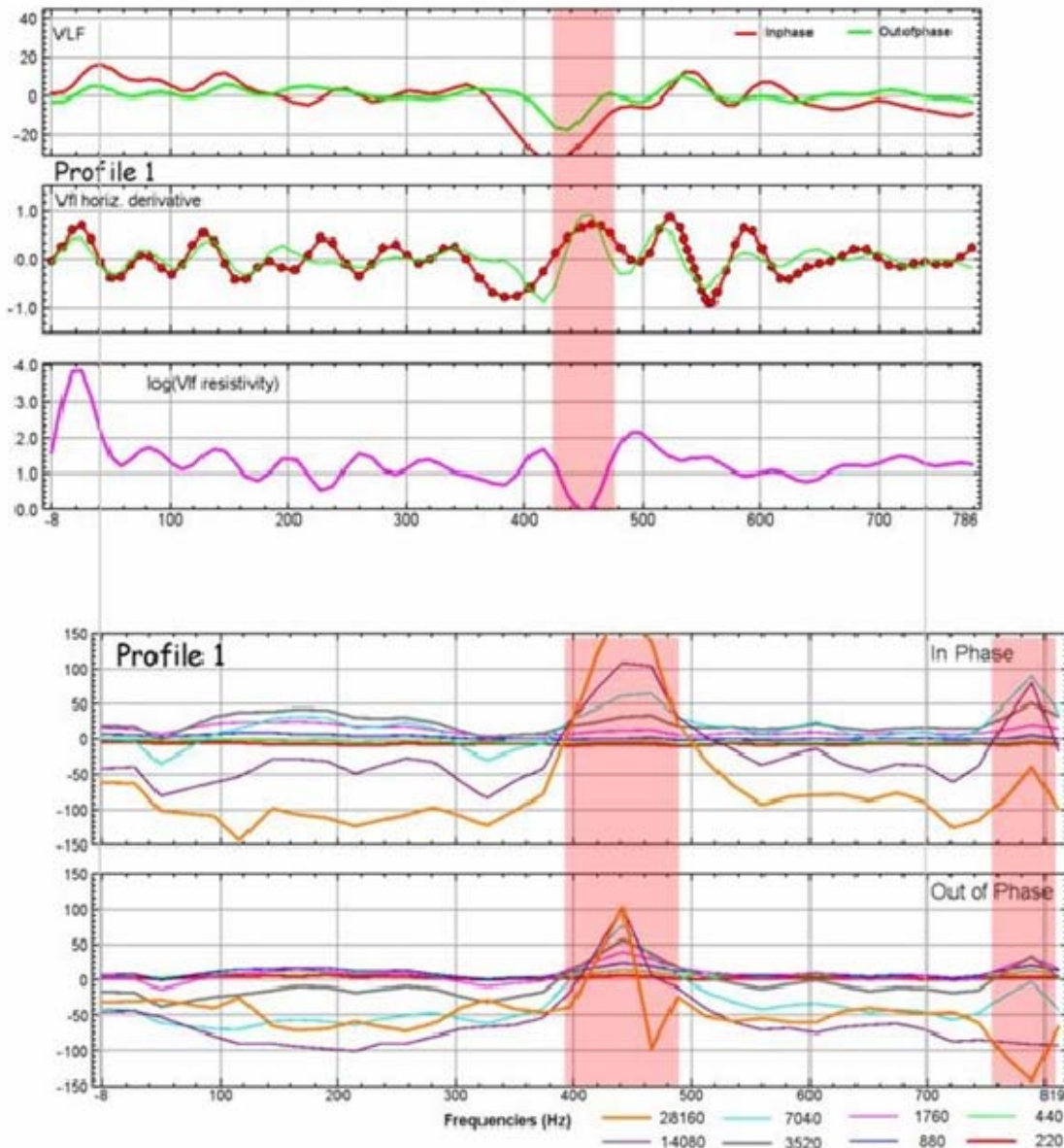


Figure 116: VLF and HL data along profile no. 1 in the western part of the Wuda syncline, fire zone no. 8. The red marked parts of the profile line show the data over burning spots within the fire zone.

The variations of the resistivity from the VLF-R measurements are not very remarkable along the profile. Except at the sites from 420 m to 480 m (distance from the southern starting point) a distinct low of the resistivity can be identified. This part of the profile can again be found south of the east-west crossing profile no. 3. Active burning parts of fire zone no. 8 were crossed by this profile.

The HL measurements show for all frequencies remarkable variations in the in-phase and the out-of-phase curves at the same part of the profile. Profile no. 1 shows no distinct variations to the north and the south of this section.



Innovative Technologies for Exploration, Extinction and Monitoring of Coal Fires in North China
Final Report Phase A Part B

In the southern part profile no. 2 takes its course east of the plateau close to the active burning part of fire zone no. 8. There are no remarkable variations in the HL data (Fig. 117). Along this profile no VLF measurements were carried out.

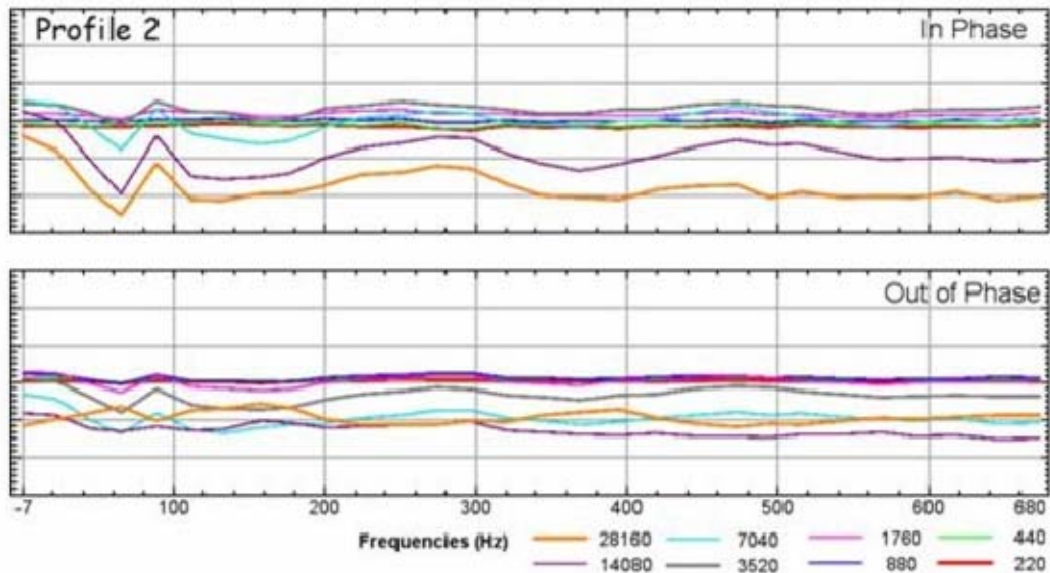


Figure 117: HL data along profile no. 2 in the eastern part of fire zone no. 8.

Figure 118 shows a point-wise one-dimensional interpretation of the HL data along the profiles no. 1 and no. 2. At profile no. 1 the data are remarkably varying between 350 m and 600 m. One-dimensionality obviously does not exist here. Profile no. 2 can be reasonably interpreted with a two-layer-case: top layer of 30 to 60 Ohm*m and a thickness of around 40 to 80 m, and a second highly resistive layer about 5000 Ohm*m at least.



Innovative Technologies for Exploration, Extinction and Monitoring of Coal Fires in North China
Final Report Phase A Part B

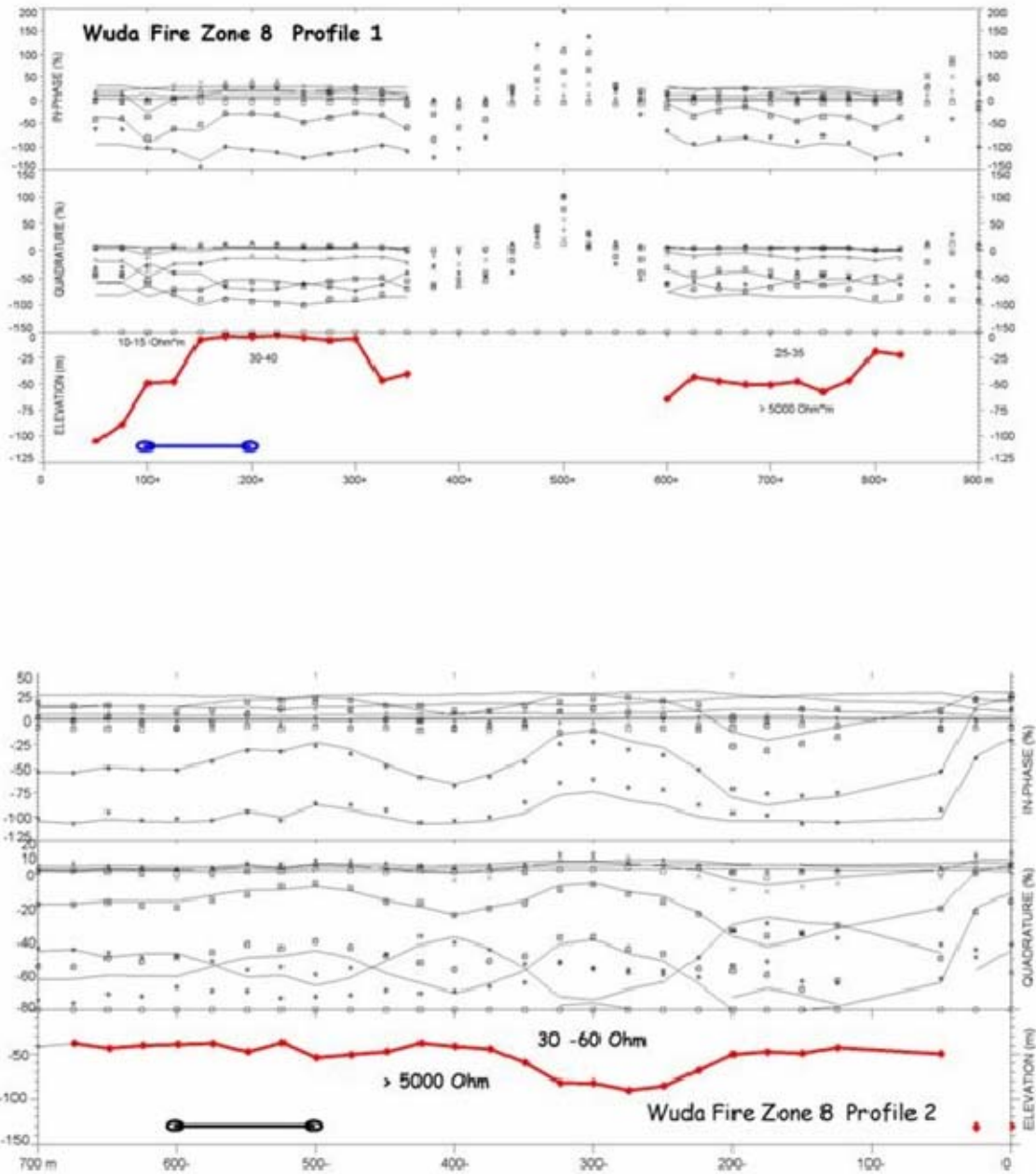


Figure 118: 1-D model from HL data for profiles no. 1 and no. 2.



Innovative Technologies for Exploration, Extinction and Monitoring of Coal Fires in North China
Final Report Phase A Part B

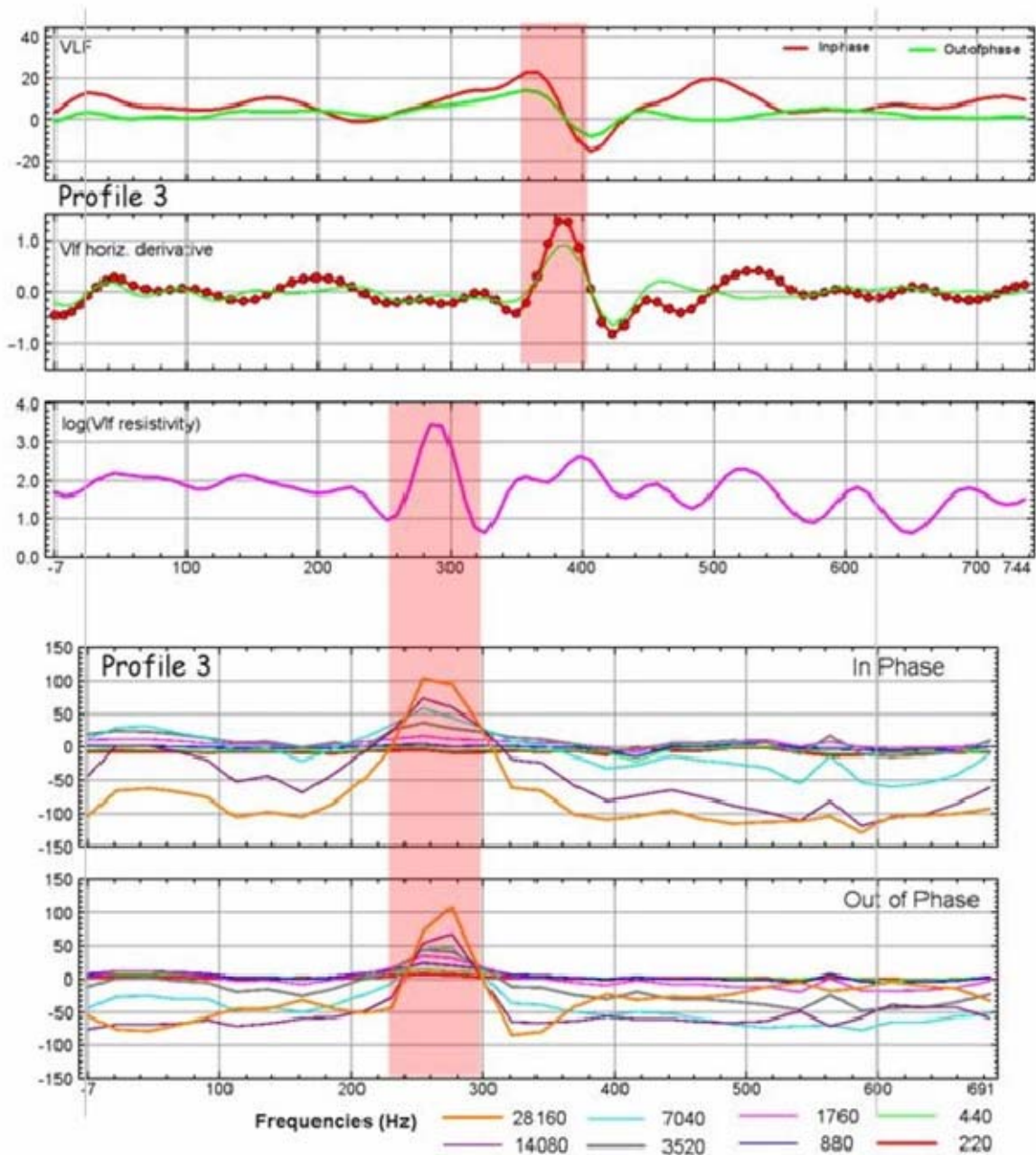


Figure 119: VLF and HL data along profile no. 3, crossing fire zone no. 8. The red marked parts of the profile show the data over active parts of the fire zone.

Profile no. 3 crosses the northern part of fire zone no. 8 from west to east. Conspicuous variations in the VLF resistivity can be seen between points 260 and 320 m. This section coincides with an active part of fire zone no. 8. It is also mentioned in the chapter about the interpretation of the TEM results from this profile, especially at site no. 47. Further to the north additional slight variations of the resistivity occur (Fig. 119).

Distinct variations of the in-phase and the out-of-phase HL data occur at the same sites as a VLF resistivity anomaly. This latter anomaly is also not interpretable with one-dimensional



**Innovative Technologies for Exploration, Extinction and Monitoring of Coal Fires in North China
Final Report Phase A Part B**

models which are only available in the program disposable to us. The parts of the profile north and south of this section do not show distinct variations in the parameters.

Figure 120 displays the VLF and HL data along profile no. 4. This profile crosses fire zone no. 8 from west to east very close to the southern end of the plateau. Directly south of this profile the collapsed area extends further to the south. Over the active burning part of fire zone no. 8, the VLF resistivities are varying between several hundreds of Ohm*m and about 10 Ohm*m. Outside the hot burning part the resistivity changes become much smoother. The in-phase and out-of-phase HL data are changing only slightly along the profile, however, two very small anomalies, ruddily marked, deserve to be mentioned. They correspond with the crossed active part of fire zone no. 8.

In addition to these two methods measurements of the total magnetic field carried out along this profile are plotted in Fig. 120. Over the active burning part in the centre of the profile the magnetic field is generally lower and more turbulent than outside.

Figure 121 shows VLF and HL results along profile no. 5, crossing fire zone no. 8 south of the collapsed area. The VLF resistivity varies slightly only. The red stripe marks the actually burning part of this fire zone. Here a small and narrow resistivity low is visible. The HL data do not reveal any distinct changes along this profile.



Innovative Technologies for Exploration, Extinction and Monitoring of Coal Fires in North China
Final Report Phase A Part B

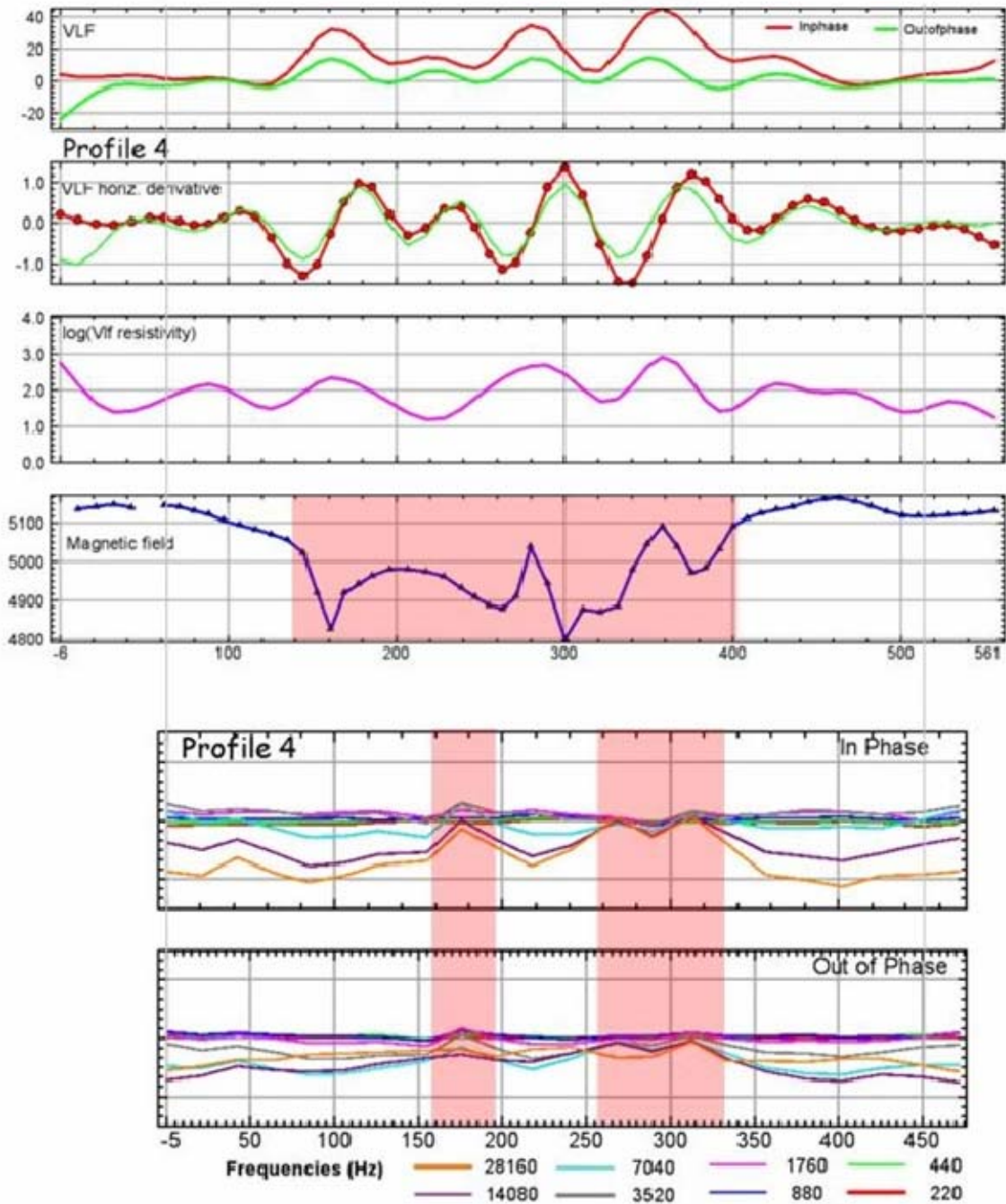


Figure 120: VLF and HL data along profile no. 4, crossing fire zone no. 8 close to the hot burning part at the southern end of the plateau. The red tagged sections mark anomalies.



Innovative Technologies for Exploration, Extinction and Monitoring of Coal Fires in North China
Final Report Phase A Part B

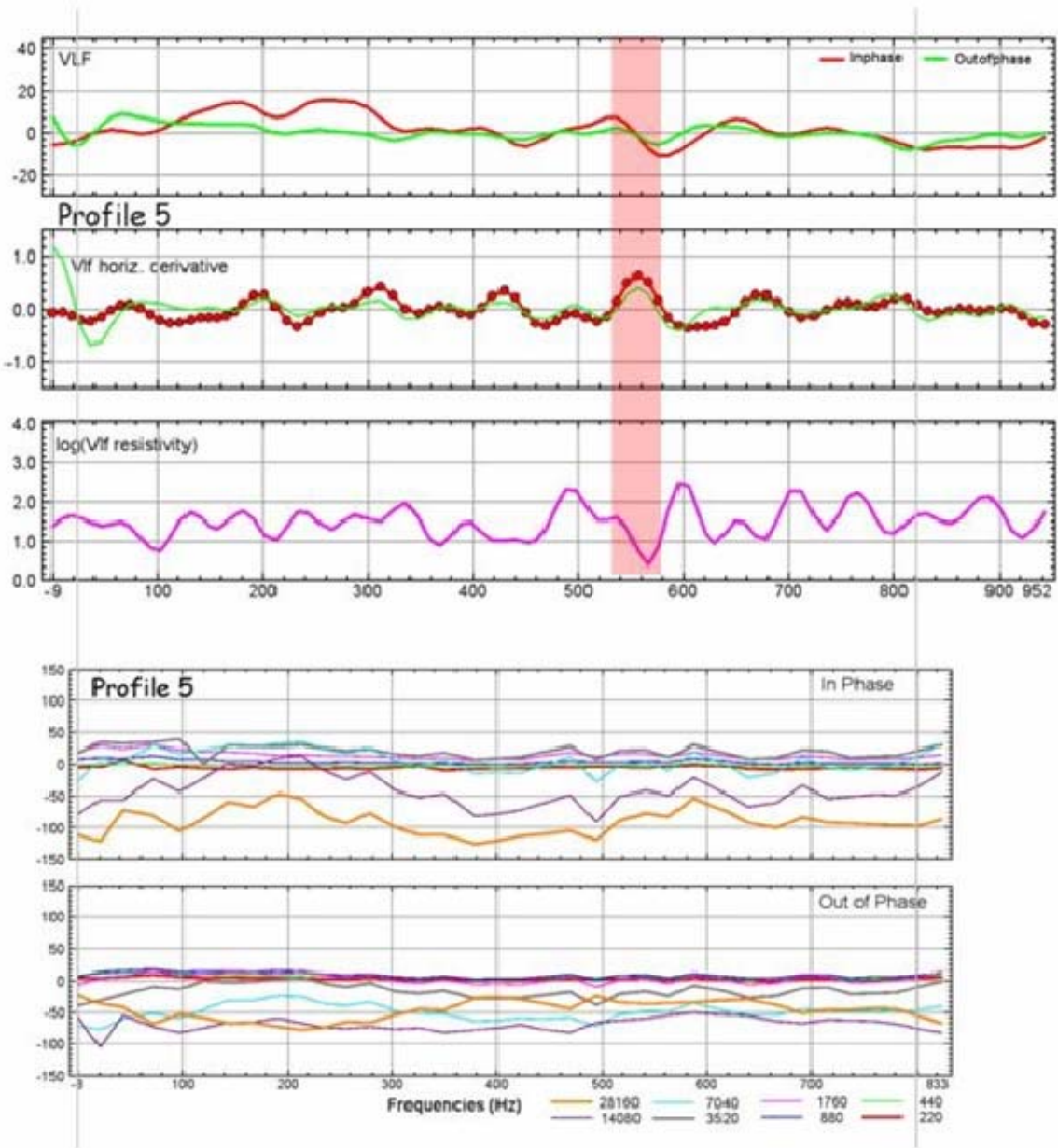


Figure 121: VLF and HL data along profile no. 5, crossing fire zone no. 8 south of the collapsed area. The red coloured sections mark areas over the burning part of this fire zone.

Fire zone no. 7 extends into the centre of the syncline. It was proven due to a resistivity low derived from helicopter electromagnetic data. This fire zone was apparently not longer heavily burning and showed some burning parts only at a few scattered places. Most parts of the fire zone were filled and covered by unknown stone material. Profile no. 6 extends into the vicinity of fire zone no. 7 (Fig. 122). The VLF-R resistivity does not show any notable variations. The total magnetic field along this profile, however, becomes again conspicuously disturbed when crossing this fire zone (Fig. 123). The values decrease and become bumpy. Profile no. 7 crosses fire zone no. 7 from west to east (Fig. 122). When entering the already burnt zone the VLF-R resistivities increase considerably (more than 1000 Ohm*m). The total



Innovative Technologies for Exploration, Extinction and Monitoring of Coal Fires in North China
Final Report Phase A Part B

magnetic field once more changes clearly its attitude in the characteristic manner described over the burnt area (Fig. 124).

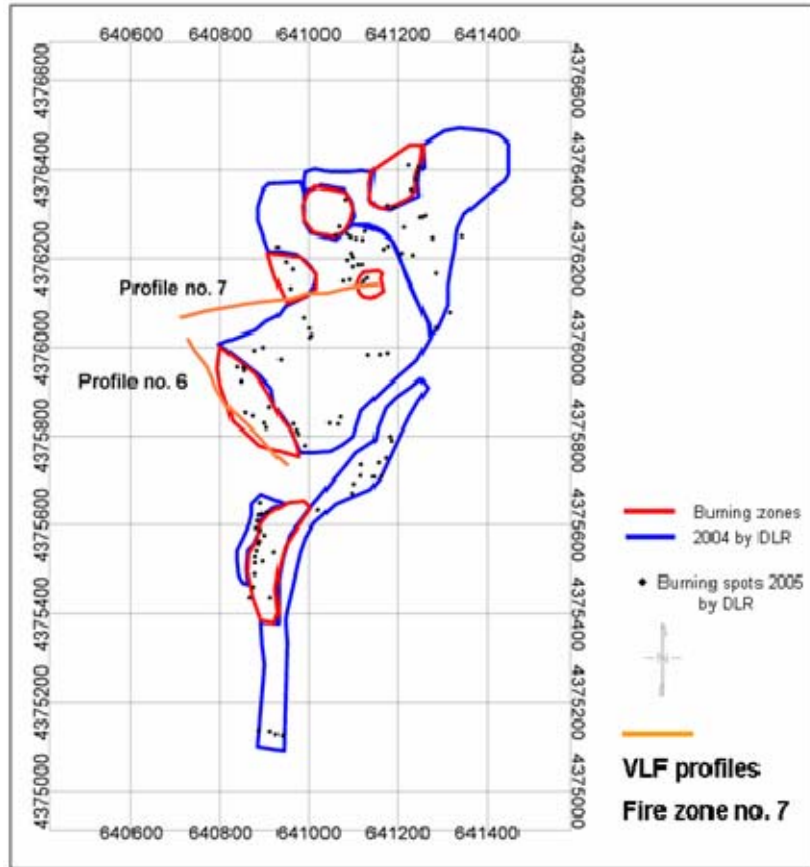


Figure 122: Location of the VLF profiles no. 6 and no. 7 at fire zone no. 7.



Innovative Technologies for Exploration, Extinction and Monitoring of Coal Fires in North China
Final Report Phase A Part B

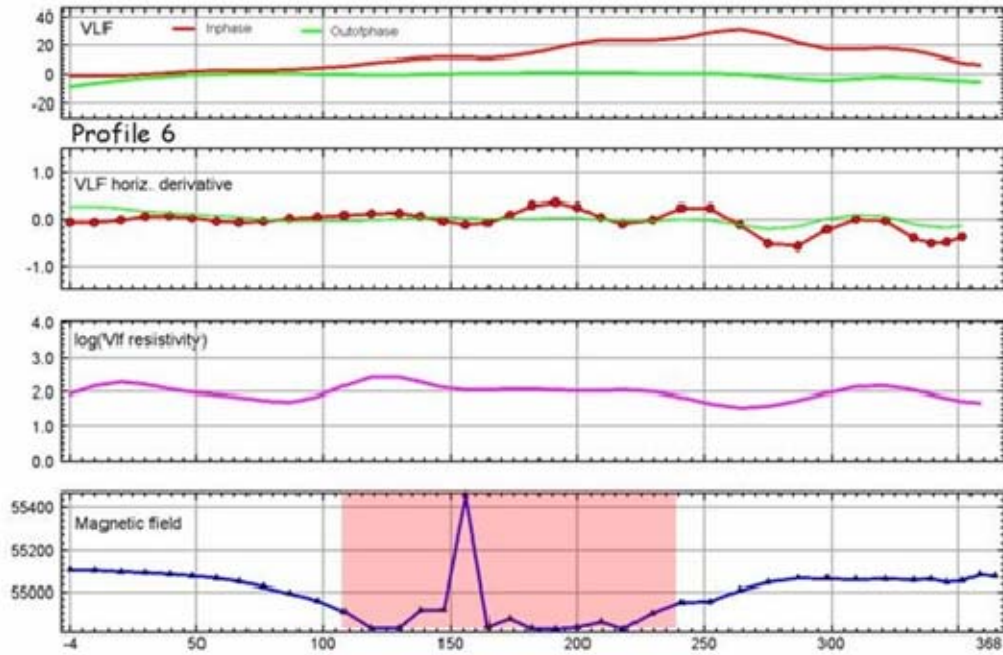


Figure 123: VLF and magnetic data along profile no. 6 within the central part of the Wuda syncline in the vicinity of fire zone no. 7, marked in red.

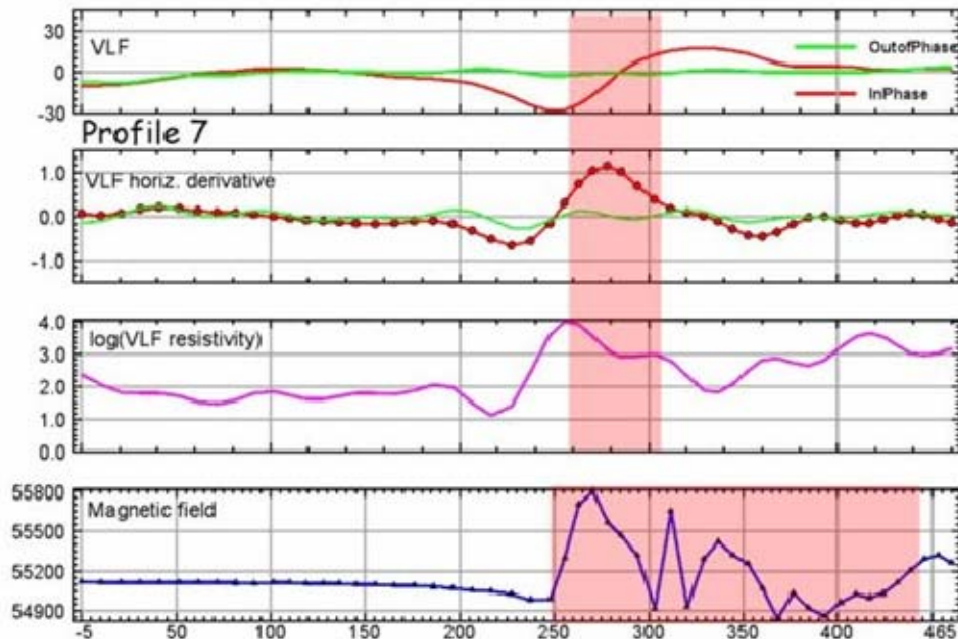


Figure 124: VLF and magnetic data along profile no. 7 over fire zone no. 7 within the central part of the Wuda syncline. The red stripes again mark the burnt fire zone.



6 Ground magnetic surveys over fire zones no. 8 and no. 3.2

A ground magnetic survey was carried out in May and June 2005 by AGRS and covers most parts of fire zones no. 8 and no. 3.2. In October 2005 another ground magnetic survey was performed by the Deutsche Montan Technologie (DMT) in order to supplement the measurements over fire zone no. 8 (Elsen 2006). In selected parts of this area the survey lines were narrowed and extended to places of interest.

The ground magnetic survey done by AGRS (Fig. 125) used a HC-95 ground helium optically-pumped magnetometer. The line direction was mainly E-W and the nominal line spacing and sampling distance were of the order of 10 m for most of the measurements. The data were corrected by subtracting an average value for the normal total intensity of the earth's magnetic field for that area, no further corrections (including sun-vary and an IGRF correction) were made (Yu 2006, pers. comm.). Figure 126 shows the anomalies of the magnetic field for fire zone no. 8 from that survey. Clearly visible are a great anomaly in the southern part of the area and a few smaller anomalies in the northern part.

At fire zone no. 3.2 only a few ground magnetic measurements were carried out. Two big anomalies were found, one is located south-west of the area zoned by mapped polygons and one north-east of it (Fig. 127). The survey lines did not cover the entire area and were of greater distance. So it was intended to narrow these lines in another survey to get more information in detail, see below.

Currently burning zones were derived from temperature and satellite data (Gielisch & Kuenzer 2003, Kuenzer et al. 2006). The polygons in Fig. 126 and 127 show the fire zones mapped by DLR in 2004 (blue and red) and 2005 (light blue and violet). Blue resp. light blue lines, which coincide in most parts with the blue lines, outline areas of colder coal seam fires and red resp. violet lines outline areas of hotter coal seam fires. Spots also burning in 2005 were mapped and are shown by black dots. Polygons from former years, e.g. 2002, are not shown. They cover a greater part of this fire zone extending from the plateau to the east, but do not show correlations to the magnetic ground survey measurements in that region.



**Innovative Technologies for Exploration, Extinction and Monitoring of Coal Fires in North China
Final Report Phase A Part B**



Figure 125: Areas with baked rocks at fire zone no. 8: 1) Area south of the hot burning zone with collapsed overburden, view to the east, 2) Western slope below the water basin, view to the north. TEM site no. 18 was situated in the small flat area below the hill.

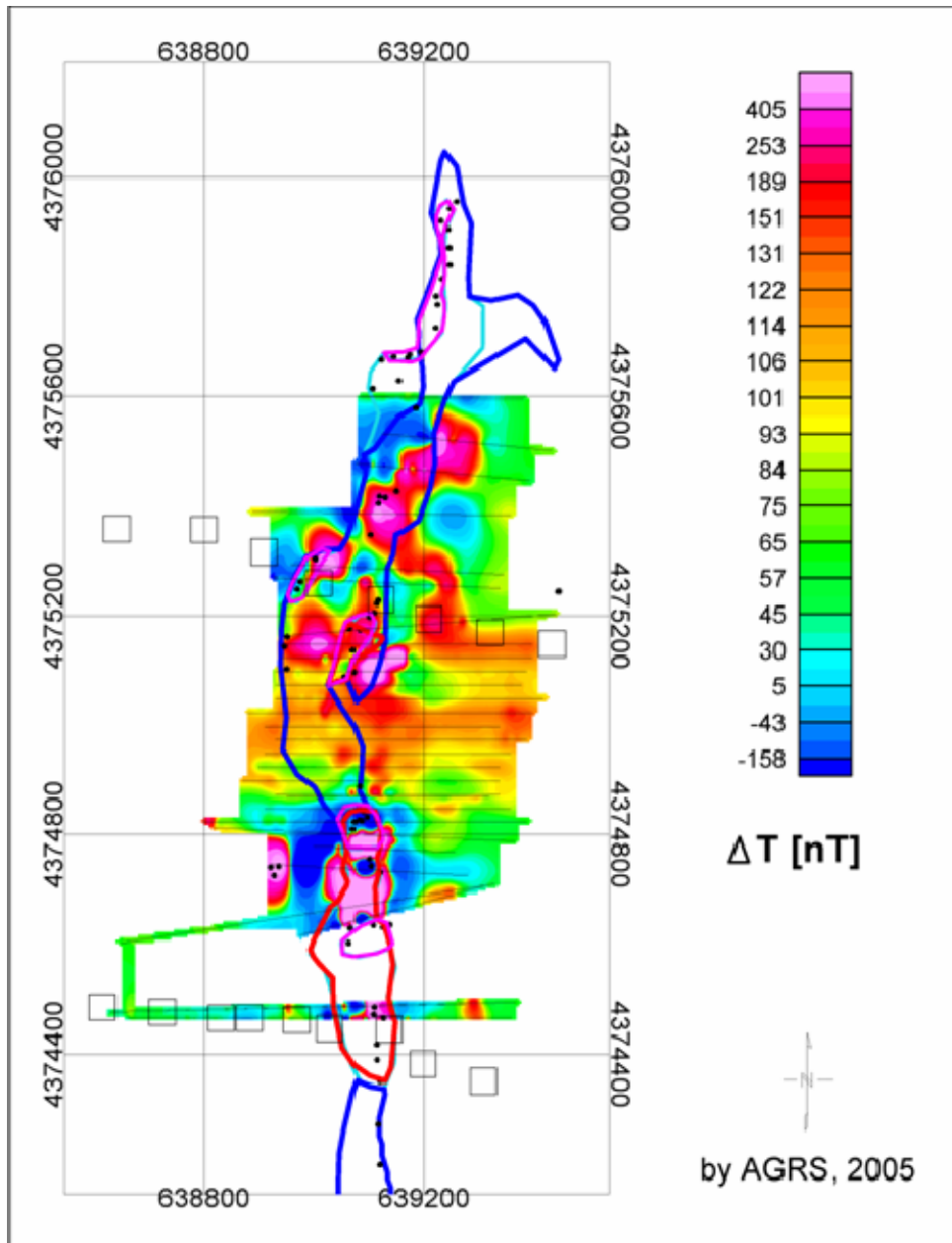


Figure 126: Anomalies of the magnetic field ΔT derived from the ground magnetic survey, conducted by AGRS in 2005 over fire zone no. 8. Blue resp. light blue and red resp. violet lines outline areas of colder and hotter coal seam fires, mapped by DLR in 2004 and 2005. Black dots mark burning spots mapped in 2005. For a better orientation the TEM survey sites from profiles no. 3 and no. 5 are shown as light black squares. Light solid black lines show the survey lines.

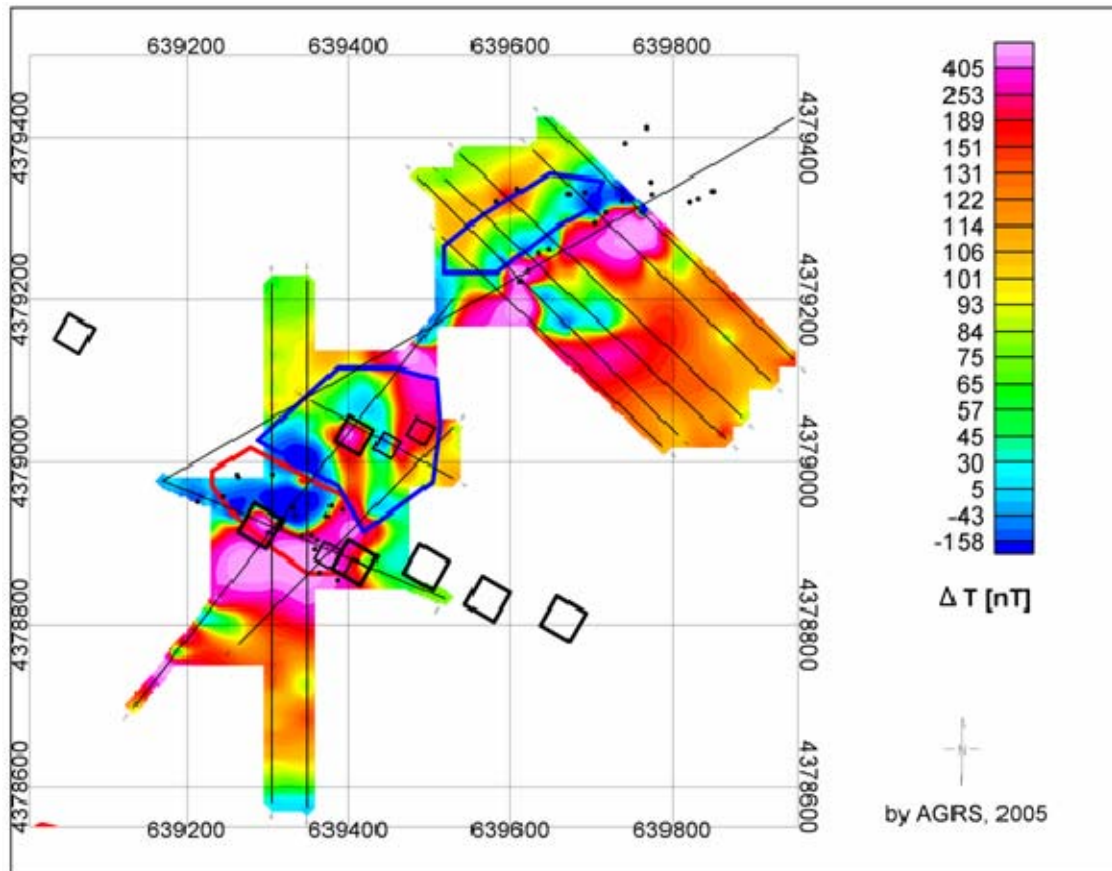


Figure 127: Anomalies of the magnetic field ΔT derived from the ground magnetic survey, conducted by AGRS in 2005 over fire zone no. 3.2. Blue and red lines outline areas of colder and hotter coal seam fires, mapped by DLR in 2004. Black dots mark burning spots mapped in 2005. For a better orientation the TEM survey sites from profiles no. 10, 11 and 12 are shown as black squares.

Inspecting the local geology of fire zone no. 8, siltstones can be found at the burning areas, see Fig. 5. In this area, high amplitudes of the magnetic field intensity were measured over the baked stones. Figure 125 shows an example of baked rocks close to fire zone no. 8.

Figure 128 shows ground magnetic measurements taken close to the collapsed area at fire zone no. 8.



**Innovative Technologies for Exploration, Extinction and Monitoring of Coal Fires in North China
Final Report Phase A Part B**



Figure 128: Ground magnetic measurements at fire zone no. 8: 1) at the southern end of the plateau close to the cracks, view to the west, 2) within the southern part of the collapsed zone, view to the north (Photos by AGRS).

The second ground magnetic survey was carried out by DMT a few months later. A GSM-19 instrument from GEM systems, Canada, was used for this survey (Elsen 2006). The survey did not follow straight lines. In this way the survey lines could be denser at sites of interest and widened at areas with no distinct variations of the total magnetic field intensity. Diurnal variations were corrected by help of registration of the total magnetic field intensity at a base



**Innovative Technologies for Exploration, Extinction and Monitoring of Coal Fires in North China
Final Report Phase A Part B**

station. By this the reduced total magnetic field intensity is the investigated parameter. No IGRF corrections were applied because of the small extension of the investigated area.

Most measurements were carried out above the well investigated fire zones no. 8 and no. 3.2, but also a few measurements were gained at other sites for comparison with areas unaffected by coal seam fires. One of them is a sandstone plateau located about 1.5 km south-east of fire zone no. 8. Here coal seams no. 6 and no. 7 are located and no coal seam fires have been detected up to now. Another survey line along a path extending about 2 km eastwards from fire zone no. 8, passing at coal seams 7, 6, 5 and 4 shows various anomalous magnetic field intensities. This is an indication for sites with still burning or burnt coal seams along that survey line, but actually burning coal seams do not show heavily striking magnetic anomalies. At the sandstone plateau no magnetic field anomalies were found (Elsen 2006).

Figure 129 shows the map of the anomalies of the magnetic field at fire zone no. 8. It is evident that in the northern part of this area numerous anomalies with small extension about a few metres up to tens of metres occurred. Most of these anomalies are situated along the western edge of this fire zone. Here coal seams 9 and 10 are partly outcropping. In the middle part (the so called plateau at fire zone no. 8) no anomalies were found. In the southern part, which represents the collapsed area, a big anomaly of greater extend is outlined, about 300 m to 400 m extension from north to south and 200 m to 300 m from west to east. Fire zone no. 8 extends further southwards (see Fig. 82). The survey lines were not continued into that region. It can be expected that ongoing measurements would show a continuation of anomalous total magnetic field values into that region. A lack of the data exists in the centre of the collapsed area because of bad accessibility (see Fig. 129).

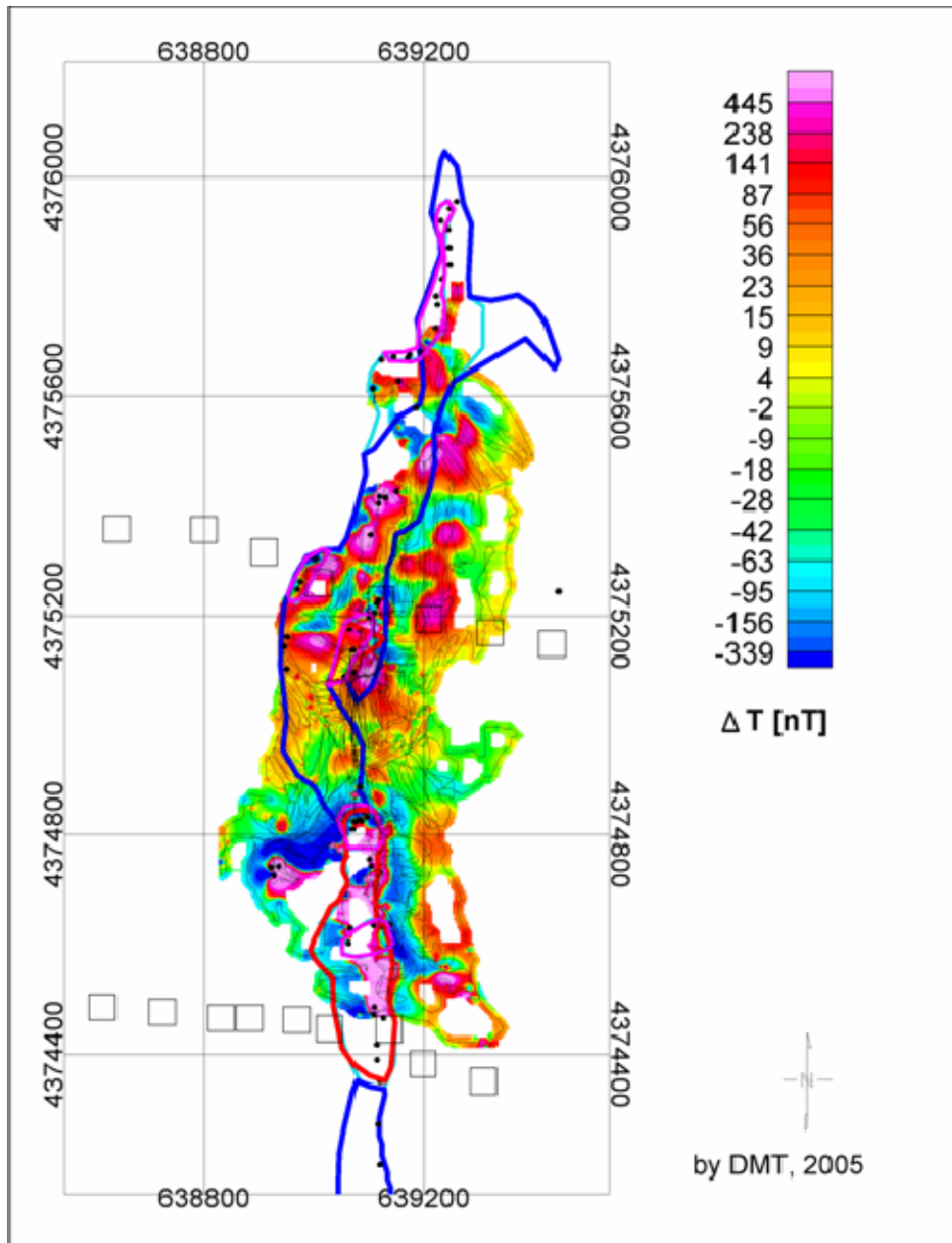


Figure 129: Anomalies of the magnetic field ΔT derived from the ground magnetic surveys, conducted by DMT in 2005 over fire zone no. 8. Blue resp. light blue and red resp. violet lines outline areas of colder and hotter coal seam fires, mapped by DLR in 2004 and 2005. Black dots mark burning spots mapped in 2005. The light black lines show the route of the survey. For a better orientation the TEM survey sites from profiles no. 3 and no. 5 are shown as light black squares.

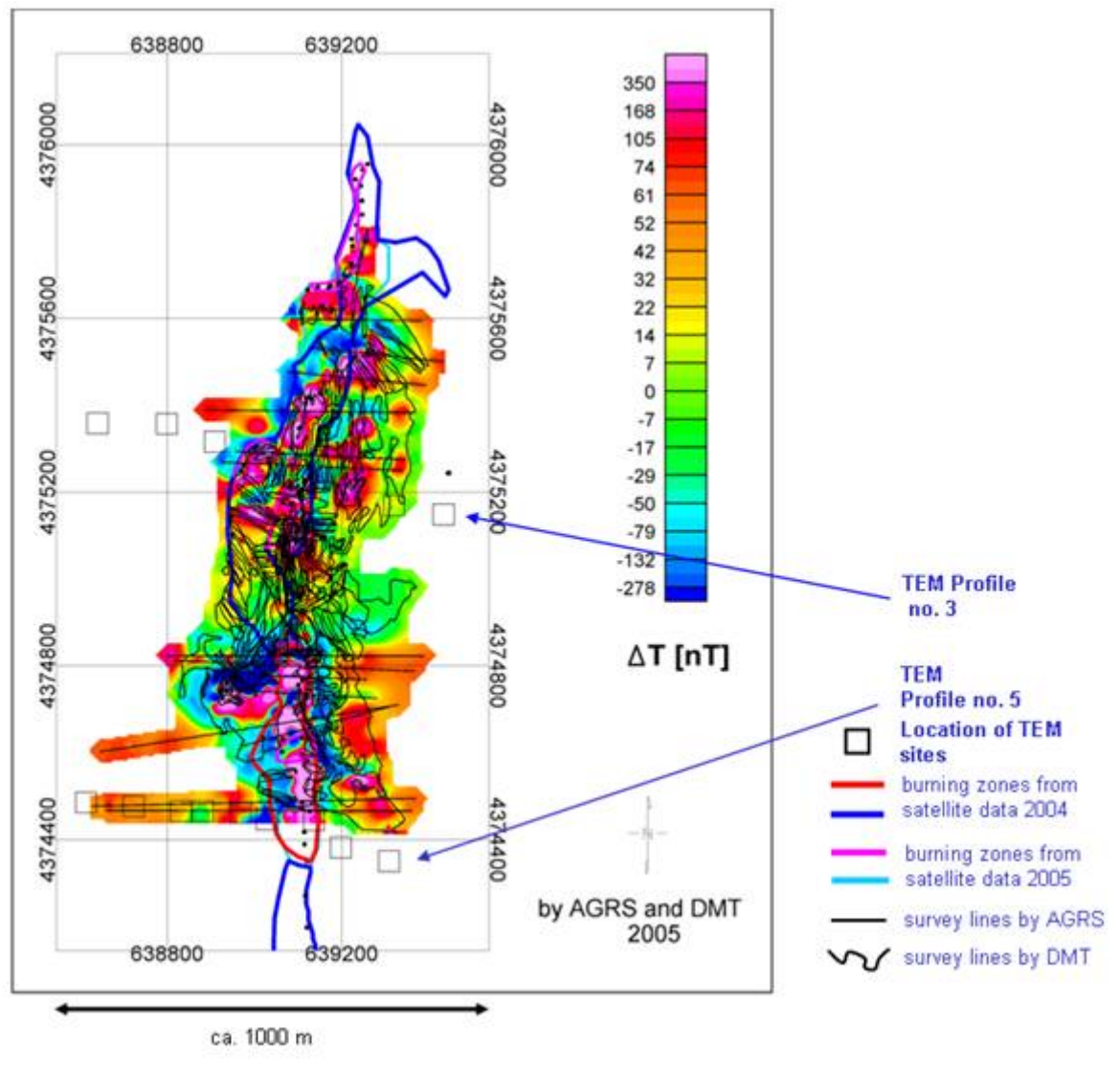


Figure 130: Anomalies of the magnetic field ΔT derived from the ground magnetic surveys, conducted by AGRS and DMT in 2005 over fire zone no. 8. Blue resp. light blue and red resp. violet lines outline areas of colder and hotter coal seam fires, mapped by DLR in 2004 and 2005. Black dots mark burning spots mapped in 2005. For a better orientation the TEM survey sites from profiles no. 3 and no. 5 are shown as light black squares. The light black lines show the route of the surveys.

The results of both surveys do not reveal distinct differences, but the latter shows more details due to the increased density of survey sites and a thorough data processing. So for an appropriate extending both data sets have been merged. Figure 130 shows the result. The survey lines of both surveys are indicated and for a better orientation and comparison with the results of the electromagnetic methods, the TEM survey sites are shown.

The map of the anomalies of the magnetic field derived by the ground magnetic surveys within fire zone no. 8 shows strongly enhanced positive amplitudes in the area of burnt and burning coal seams as described above. The mapped polygons give some help by locating the burning parts of the area.

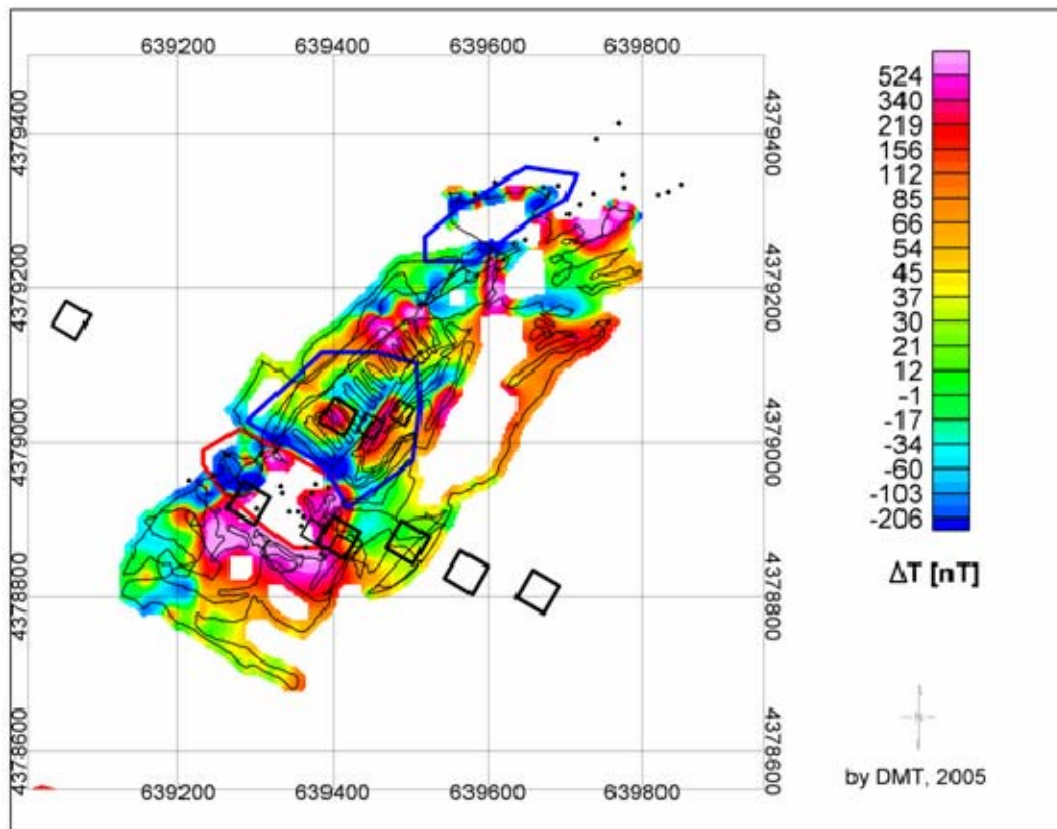


Figure 131: Anomalies of the magnetic field ΔT derived from the ground magnetic survey, conducted by DMT in 2005 over fire zone no. 3.2. Blue and red lines outline areas of colder and hotter coal seam fires, mapped by DLR in 2004. Black dots mark burning spots mapped in 2005. The light black lines show the route of the survey. For a better orientation the TEM survey sites from profiles no. 10, 11 and 12 are shown as black squares.

Figure 131 shows the anomaly of the magnetic field at fire zone no. 3.2. The whole fire zone extends along a valley with a pillar remained in the central part after mining. A big anomaly occurs in the south-western part of this area, similar to that of the former survey. Due to the narrowed survey lines the big anomaly in the north-east, revealed by AGRS, divides into a few ones of smaller extend. Because of inaccessibility a lack of data is given in the central part of the anomaly in the south-west at hot burning sites. Parts of the pillar in the centre of the fire zone are also burning, observed by the authors. The mapped polygons coincide roughly with the places of the anomalous field intensities. It has to be considered that the polygons had been mapped one year before the magnetic surveys were carried out.

The ground magnetic surveys reveal zones of anomalous magnetic field intensities which correspond to places of burning and burnt coal seams. While the correlation to still burning seams is not as strong, there is a clearly relation to the burnt areas. At fire zone no. 8 siltstones can be found in the area concerned. Enhanced iron oxide content within the sandstones can be expected due to the observation of higher electrical conductivities close to the surface in the surroundings of fire zone no. 8 (Gielisch, 2006, pers. comm.). This area is mainly covered by sand and sandstone. At fire zone no. 3.2 siltstone is located very close to the coal seams no. 9 and no. 10 (see Fig. 5 and 6 about the geology of the test areas).



The anomalies of the magnetic field T derived from the airborne magnetic survey (Fig. 76 and 78) are smaller than those measured on ground. Therefore the correlation of the fire zones with airborne magnetic anomalies is not as strong as with those of the ground magnetic surveys.

7 Conclusions

The objective of the geophysical surveys was to detect and delineate areas affected by coal seam fires by means of physical parameters, such as the electrical conductivity and the magnetic susceptibility. That is possible, if these parameters are altered above burning and already burnt coal seams. The electromagnetic methods outline areas of lower resistivity and the magnetic surveys clearly reveal increased amplitudes and rapid changes of the magnetic field intensity in the areas affected by coal seam fires. Therefore these methods can be used as a tool for detection of burning and burnt coal seams.

As the changes of the physical parameters measured over the fire zones are obviously rather small in most cases, ground geophysical surveys are more sensitive to locate coal seam fires than airborne geophysical surveys. However, areas of coal seam fires are not always accessible on ground, so that airborne surveys are essential. Because of the small signals to be expected caused by coal seam fires, high resolution and high quality data are necessary. That requires a low survey altitude and very dense coverage as well as high-precision measuring devices and sophisticated processing and interpretation tools.

8 References

- Bartel, L.C., 1982. Evaluation of the CSAMT geophysical technique to map abandoned coal mine fires: Department of Energy, Contract DE-AC04-76DP00789, Sandia National Laboratories, Albuquerque, New Mexico. Society of Exploration Geophysicists, 52nd Annual International Meeting: p. 419-421.
- Cheeseman, S., 1988, HEMRES2 GX documentation (online Help for the amplitude-altitude resistivity inversion algorithm in Oasis montaj software): Geosoft Inc. Toronto, Canada.
- Duba, A., 1977. Electrical conductivity of coal and coal char. *Fuel* 56: 441-443.
- Duba, A., 1983. Electrical conductivity of Colorado oil shale to 900° C. *Fuel* 62: 966-972.
- Elsen, R., 2006. Geophysikalische Messungen zur Erkundung der Brandzonen 8 und 3, Wuda, Magnetik. Ergebnisbericht Deutsche Montan Technologie. Unpublished Report, Federal Institute for Geosciences and Natural Resources, Hannover, Germany.
- Fraser, D.C., 1978. Resistivity mapping with an airborne multicoil electromagnetic system. *Geophysics*, 43, 144-172.
- Gielisch, H., 2005. Innovative Technologies for Exploration, Extinction and Monitoring of Coal Fires in North China, Work Package 2240 – Investigation of the Hydrogeological Situation (Wuda, Rujigou, Gulaben). Unpublished project report. Deutsche Montan Technologie GmbH, Essen, Germany.
- Gielisch, H. & Kahlen, E., 2003. Innovative Technologies for Exploration, Extinction and Monitoring of Coal Fires in North China, Work Package 2210 – General Geological



**Innovative Technologies for Exploration, Extinction and Monitoring of Coal Fires in North China
Final Report Phase A Part B**

Description of Helan Shan Mountain Area with Emphasis on Coal Fire Areas; Geology of the Helan Shan – Field Report. Unpublished project report. Deutsche Montan Technologie GmbH, Essen, Germany.

Gielisch, H. & Kuenzer, C., 2003. Innovative Technologies for Exploration, Extinction and Monitoring of Coal Fires in North China, Work Package 2220 – Structural Pattern of the Coal Deposits (Wuda, Rujigou, Gulaben); Analysis of Linear Pattern (Air Photos, Satellite Images), Cracks and Crack Systems of the Test Areas. Unpublished project report. Essen, Germany: Deutsche Montan Technologie GmbH; Oberpfaffenhofen, Germany: German Aerospace Center (DLR).

Greinwald, S. & Schaumann, G., 1997. Transientelektromagnetik, in: Knödel, K., Krummel, H. & Lange, G., Handbuch zur Erkundung des Untergrundes von Deponien und Altlasten, Band III: Geophysik; Berlin, Heidelberg (Springer).

Heffern, E.L. & Coates, D.A., 2004. Geologic history of natural coal-bed fires, Powder River basin, USA. *International Journal of Coal Geology*, 59, 25-47, Elsevier.

Hooper, R.L., 1987. Factors affecting the magnetic susceptibility of baked rocks above a burned coal seam. *International Journal of Coal Geology*, 9, 157-169, Elsevier.

Jödicke, H., 1991. Zonen hoher elektrischer Krustenleitfähigkeit im Rhenoharzynikum und seinem nördlichen Vorland. Dissertation, University of Münster. ISBN 3-89473-152-4.

Jongmans, D., Hemroulle, P., Demanet, D., Renardy, F. & Vanbrabant, Y., 2000. Application of 2D electrical and seismic tomography techniques for investigating landslides. *European Journal of Environmental and Engineering Geophysics*, 5: 75-89.

King, A., 1987. Cindered Coal Detection Using Transient Electromagnetic Methods. *Geoexploration*, 24, 4/5, 367-379.

Kuenzer, C., Zhang, J. & Hirner, A., 2005. Multitemporal coal fire dynamics – combining thermal remote sensing analysis and temperature field mappings to assess coal fire development in Wuda coal mining area. In: *ISPMSRS Beijing 2005 conference proceedings*, pp. 805-809.

Kuenzer, C., Zhang, J., Hirner, A., Jia, Y., Sun, Y., 2006. Multitemporal In-Situ Mapping of the Wuda Coal Fires from 2000 to 2005: Assessing Coal Fire Dynamics. *ERSEC Ecological Book Series - 4 on Coal Fire Research*, ERSEC UNESCO Office Beijing.

Kus, J., Hiltmann, W., & Balke, A., 2006. In situ gasification of coal, a natural example: micropetrography of coal oxidation, carbonisation and combustion. *ERSEC Ecological Book Series - 4 on Coal Fire Research*, ERSEC UNESCO Office Beijing.

Powell, R.W. & Schofield, F.H., 1939. The thermal and electrical conductivities of carbon and graphite to high temperatures. *Proc. Phys. Soc.*, 51, 153-172.

Roux, A.T., 1978. The magnetic method. *Geophysical field manual for technicians*, no. 1. South African Geophysical Association.

Schloemer, S., Teschner, M., Poggenburg, J. & Seeger, C., 2006. Gas and Temperature Monitoring of a Natural Coal Fire in Wuda (Inner Mongolia Autonomous Region, PRC). *ERSEC Ecological Book Series - 4 on Coal Fire Research*, ERSEC UNESCO Office Beijing.

Sengpiel, K.P., 1988, Approximate inversion of airborne EM data from multilayered ground: *Geophysical Prospecting*, 36, 446-459.



**Innovative Technologies for Exploration, Extinction and Monitoring of Coal Fires in North China
Final Report Phase A Part B**

- Sengpiel, K.P. and Siemon, B., 2000. Advanced inversion methods for airborne electromagnetics. *Geophysics*, 65, 1983-1992.
- Siemon, B., 2001. Improved and new resistivity-depth profiles for helicopter electromagnetic data. *Journal of Applied Geophysics*, 46, 65-76.
- Sternberg, R. & Lippincott, C., 2004. Magnetic surveys over clinkers and coal seam fires in Western North Dakota. Presented at Denver Annual Meeting, Geological Society of America.
- Thomas, L., 2002. *Coal Geology*. John Wiley & Sons Ltd, Chichester, England.
- Valleau, N. C., 2000. HEM data processing a practical overview, *Exploration Geophysics*, 31, 584-594.
- Van Krevelen, D., W., 1981. *Coal. Typology – Chemistry – Physics – Constitution*. Coal Science and Technology 3, Elsevier.
- Voigt, S., Tetzlaff, A., Zhang, J., Künzer, C., Zhukov, B., Strunz, G., Oertel, D., Roth, A., van Dijk, P. & Mehl, H., 2004. Integrating Satellite Remote Sensing Techniques for Detection and Analysis of Uncontrolled Coal Seam Fires in North China. *International Journal of Coal Geology*, No. 59, pp. 121-136.
- Weidelt, P., 1984. Bericht über Inversion transient-elektromagnetischer Messungen über geschichtetem Untergrund. Archives-no. 96720, Federal Institute for Geosciences and Natural Resources, Hannover, Germany.
- Whitehead, N., Musselman, Ch., 2002. Euler 3D Deconvolution. Processing, Analysis and Visualisation System for 3D Inversion of Potential Field Data. Geosoft Inc. Toronto, Canada.
- Whitehead, N., 2002. HEM System, Helicopter Electromagnetic Data Processing, Analysis and Presentation System for Oasis montaj. Geosoft Inc., Toronto, Canada.

Suggested Additional Reading

Geosoft Technical Note: Microleveling using FFT Decorrugation. Geosoft Inc., Toronto, Canada.

Acknowledgements

We gratefully acknowledge Bernd Röttger, Hans-Joachim Rehli and the Chinese airborne team, who performed the airborne geophysical survey under leadership of AGRS. Special thanks are due to Chen Bin, who managed the airborne survey and supported the field activities. Hanno Schmidt and Yu Chang Chun participated in the ground geophysical survey and contributed with their experience in the field. We also wish to express our gratitude to our German and Chinese colleagues, who assisted the field trips and provided many useful comments for the data interpretation. Rolf Elsen (DMT) performed a ground magnetic survey by order of BGR.